



HAL
open science

Combining spectroscopy, diffraction and imaging (Raman, neutron) for investigating synthetic and natural gas hydrates in marine clay media: formation kinetics, composition and spatial distribution.

Charlène Guimpier

► **To cite this version:**

Charlène Guimpier. Combining spectroscopy, diffraction and imaging (Raman, neutron) for investigating synthetic and natural gas hydrates in marine clay media: formation kinetics, composition and spatial distribution.. Other. Université de Bordeaux, 2022. English. NNT : 2022BORD0263 . tel-04220513

HAL Id: tel-04220513

<https://theses.hal.science/tel-04220513>

Submitted on 28 Sep 2023

HAL is a multi-disciplinary open access archive for the deposit and dissemination of scientific research documents, whether they are published or not. The documents may come from teaching and research institutions in France or abroad, or from public or private research centers.

L'archive ouverte pluridisciplinaire **HAL**, est destinée au dépôt et à la diffusion de documents scientifiques de niveau recherche, publiés ou non, émanant des établissements d'enseignement et de recherche français ou étrangers, des laboratoires publics ou privés.

THÈSE PRÉSENTÉE
POUR OBTENIR LE GRADE DE
DOCTEUR DE
L'UNIVERSITÉ DE BORDEAUX

ÉCOLE DOCTORALE DES SCIENCES CHIMIQUES

SPÉCIALITÉ : CHIMIE - PHYSIQUE

Par **Charlène GUIMPIER**

Combinaison de la spectroscopie, de la diffraction et de l'imagerie (Raman, neutron) pour l'étude des hydrates de gaz synthétiques et naturels dans les milieux argileux marins : cinétique de formation, composition et distribution spatiale.

Sous la direction de : **Arnaud DESMEDT**
(co-encadrant : **Livio RUFFINE**)

Thèse soutenue publiquement à Bordeaux, le 26 Septembre 2022

Membres du jury :

M. MICHOT, Laurent	Directeur de Recherche	PHENIX, FR	Président du jury
Mme SCHICKS, Judith	Professeure	GFZ, GE	Rapporteur
M. SILVESTRE-ALBERO, Joaquin	Professeur	LMA, SP	Rapporteur
Mme JIMÉNEZ-RUIZ, Mónica	Chargée de Recherche	ILL, FR	Examineur
Mme LECOMTE, Sophie	Directrice de Recherche	CBMN, FR	Examineur
Mme DUCASSOU, Emmanuelle	Maître de Conférence	EPOC, FR	Examineur
M. RUFFINE, Livio	Chargé de Recherche	GEOOCEAN, FR	Examineur
M. DESMEDT, Arnaud	Directeur de Recherche	ISM, FR	Directeur de thèse

Unité de recherche

Groupe de Spectroscopie Moléculaire – Institut des Sciences Moléculaire

UMR 5255 CNRS – Université de Bordeaux

Bâtiment A12, 351 cours de la Libération

33405 TALENCE Cedex

FRANCE

À mon Papi,
À mon Kiki,
À Natalia,
À ma Famille,
À ma Belle-Famille,
À Ouby,
À Marc,

Remerciements

Durant ces trois années de thèse, j'ai eu la chance d'être accompagnée, soutenue, et formée par de nombreuses personnes afin de mener à bien mon projet doctoral. Il me tient à cœur de les remercier.

Je souhaite dans un premier temps remercier mes deux directeurs de thèse : Arnaud DESMEDT et Livio RUFFINE. À la fin de mon master, le choix de la thèse n'était pas évident, la rencontre avec Arnaud lors du cours de Master 2 'Large Scale Facilities' et des nombreuses conversations m'ont pourtant convaincue et je suis heureuse d'avoir fait ce choix. J'avais pour objectif de travailler sur un sujet en lien avec des problématiques environnementales, de travailler sur les grands instruments de recherches et de compléter mon expérience multidisciplinaire et internationale, grâce à vous, mes objectifs ont été remplis et bien au-delà de mes espérances. Je souhaite alors vous remercier de m'avoir accordée votre confiance. Ensemble nous avons appris à travailler, chacun avec nos domaines d'expertises et nos caractères bien affirmés, on ne s'est pas ennuyé. Merci de m'avoir guidée, encadrée, tout en me donnant la possibilité de faire mes propres choix et de suivre mes intuitions. La thèse restera à jamais une expérience inoubliable à la fois de par sa richesse scientifique, technique et humaine mais aussi de par le déroulement original forcé par une certaine 'pandémie'. Les réunions Zoom ou encore les réunions sur les parkings de supermarchés ont compliqué sont déroulement normal, abaissé ma motivation mais grâce à vous aujourd'hui je suis en train de rédiger les remerciements : j'ai réussi à finir ma thèse !

Plus particulièrement, je tiens à vous remercier individuellement pour l'aide que vous m'avez apportée chacun à votre manière. Arnaud, merci de m'avoir ouvert les portes des grands instruments de recherches, je n'oublierai pas ma première expérience neutronique à Saclay avec Sylvain Petit. Après celle-ci, 38 jours d'expériences à l'Institut Laue-Langevin (ILL) à Grenoble, des changements d'échantillons à des heures tardives, des oublis de démarrer les acquisitions, des problèmes techniques en tout genre, mais surtout des longs trajets en voiture. On a testé beaucoup de voiture de location, des grosses, des moins grosses, bizarrement jamais de décapotable ! Et on a passé des heures à parler, à refaire la vie, à se plaindre sur la playlist aléatoire qui nous joue toujours le même artiste ou encore à chercher la meilleure aire de repos sur le chemin. On a aussi eu la chance d'avoir de nombreux déplacements professionnels. Objectif numéro 1 : la science, objectif numéro 2 : trouver un bon restaurant, du grand air, un bon cocktail - ou peut-être l'inverse. Scientifiquement et humainement, je me suis éclatée ! Je

te remercie. Livio, merci de m'avoir fait découvrir ton domaine d'expertise, la géochimie. J'étais très loin d'imaginer la complexité et diversité des milieux marins des hydrates de gaz. J'ai pris beaucoup de plaisir à les découvrir. La chance unique de participer à la campagne GHASS2 m'a permis d'observer et d'étudier des phénomènes géochimiques qui auparavant étaient pour moi que de simples notions théoriques issues de la littérature. Livio, Arnaud, merci pour votre soutien au cours de ces trois années de doctorat, merci pour toutes nos discussions parfois trop longues à mon goût mais pour autant bénéfiques. Merci aussi pour votre gentillesse et votre bienveillance. Je ne sais pas de quoi l'avenir est fait, mais il se pourrait que l'on puisse travailler ensemble à nouveau.

Je souhaite également remercier les membres du Jury pour avoir pris le temps d'évaluer mes travaux de thèse. Je suis fière de la constitution de ce Jury international, et de sa nature pluridisciplinaire. Laurent Michot je te remercie d'avoir accepté de tenir le rôle de président du jury au cours de la soutenance, merci aussi d'avoir été présent sur IN1-LAGRANGE, les mains dans l'azote liquide, une expérience neutronique sportive, comme on les aime. I also would like to thank Dr. Judith Schicks and Dr. Joaquin Silvestre-Albero for their critical and attentive reading and evaluation of my PhD manuscript and the scientific conversation/debate that we were able to share during and after the defense. Je remercie aussi Mónica Jiménez-Ruiz d'avoir accepté d'assister à ma soutenance de thèse en tant qu'examinatrice. J'ai aussi pris beaucoup de plaisir sur IN1-LAGRANGE, des expériences inédites et dynamiques, je te remercie d'avoir accepté de partager tes connaissances et de m'avoir introduite à la spectroscopie inélastique des neutrons. Enfin, je souhaite remercier Sophie Lecomte et Emmanuelle Ducassou, d'avoir accepté d'assister à ma soutenance de thèse en tant qu'examinatrices et d'avoir fait partie de mon comité de suivi de thèse.

Un merci particulier revient à Cédric Crespos. J'ai rencontré Cédric lors de ma première année de licence. J'ai passé la porte de son bureau pour râler, je ne peux pas compter combien de fois cela s'est reproduit par la suite. J'ai ensuite eu la chance d'intégrer le master PCCP, et plus encore de partir étudier aux Etats-Unis durant un an dans le cadre d'un double diplôme avec la Colorado School of Mines encadré par Cédric et Frédéric Castet. Voici l'expérience qui m'a convaincue que j'aimais la science et que je souhaitais travailler dans le domaine de l'environnement. Cédric, Frédérique, je vous remercie pour cette expérience, PCCP Forever ! Cédric, je te remercie pour ton accueil amical et tes conseils à chaque fois que j'ai pu passer la porte de ton bureau (si par chance pour une fois, tu t'y trouvais).

Durant ma thèse, j'ai eu accès à trois laboratoires de recherche. Tout d'abord, je remercie l'ensemble du Groupe de Spectroscopie Moléculaire (GSM) de l'Institut des Sciences

Moléculaires (ISM) à Bordeaux, au sein duquel j'ai principalement effectué mes travaux de thèse. En particulier, je remercie Jean-Luc Bruneel et David Talaga pour leur aide avec les appareils de spectroscopie Raman. Je remercie également Christian Aupetit pour avoir veillé au remplissage du réservoir d'azote liquide et maintenu mes précieux échantillons à froid, ainsi que Julien Sanchez pour m'avoir aidé à ouvrir mes cellules sous-pression lorsque je n'y parvenais pas (et d'avoir sauvé mon BMS). Je tiens également à remercier Marie-Anne Dourges, du groupe C2M de l'ISM pour la caractérisation des matrices argileuses. D'autre part, je souhaite remercier l'Ifremer à Brest pour leur accueil ainsi que pour l'unique opportunité de participer à une campagne scientifique en Mer Noire à Bord du Pourquoi Pas?. Cette expérience m'a permis de rencontrer de nombreux scientifiques dans le domaine des géosciences ainsi que la récupération d'échantillons d'hydrates naturels. Je souhaite alors remercier Vincent Riboulot et Nabil Sultan les responsables de missions et Sandrine Cheron et Audrey Boissier pour la caractérisation des sédiments naturels récoltés. Je souhaite aussi remercier Olivia Fandino Torres, avec qui j'ai eu la chance de collaborer sur un projet portant sur la Mer de Marmara. Enfin, je souhaiterais remercier les responsables d'instruments et les techniciens rencontrés à l'Institut Laue-Langevin (ILL) à Grenoble, durant les expériences neutroniques. Je remercie donc Vivian Nassif, Thomas Hansen and Monica Jimenez-Ruiz, les responsables de D1B, D20 et IN1-LAGRANGE respectivement, pour leur aide au cours des expériences ou pour l'analyse de données. Je remercie ensuite Simon Baudoin, Sofien Djellit les techniciens qui ont contribué au bon déroulement des expériences neutroniques.

Je suis reconnaissante d'avoir eu la chance de rencontrer et de partager des moments précieux avec d'autres doctorants au cours de ma thèse. Je souhaite les remercier pour leur présence, leur soutien, et leurs conseils dans les pires moments comme les meilleurs. C'est en partie ce qui rend la thèse aussi riche scientifiquement qu'humainement. En particulier, je souhaite remercier ce qui sont devenus des amis aujourd'hui. Natalia, je ne peux même pas imaginer comment ma thèse se serait déroulée si je ne t'avais pas rencontrée ! Patronne et super patronne. La distance a rendu notre amitié d'autant plus forte, de par les heures au téléphone à raconter nos vies mais surtout à planifier notre prochaine expérience commune afin d'allier science et plaisir : les expériences à Grenoble et le ski de fond accompagné d'une bonne raclette, ou encore des conférences à Fréjus ou à Anglet accompagnées de balades sur la côte avec un bon cocktail, sans oublier de tester les spécialités culinaires. Quel plaisir de partager ton énergie, tu es un soleil, tu me fais grandir et je t'en remercie. Constant, je ne savais pas à quel point travailler avec toi serait aussi génial et je ne pouvais pas imaginer un meilleur collègue de thèse ! À chacun notre rythme (je n'ai pas réussi à ralentir le mien), chacun notre

expertise, nous avons tiré le meilleur de cette collaboration. Tu m'as beaucoup appris, tu es ma super source bibliographique, je te remercie. Mais notre amitié ne peut se résumer qu'à la science. Comment pourrais-je oublier ma semaine à Brest, et notre repas aux saveurs de ton pays la Côte d'Ivoire. Du bon rhum, de la musique et une réunion manquée le lendemain, oups. Merci Constant pour ta gentillesse et ton soutien. Bon courage, c'est toi le prochain ! Dans le reste de la team 'hydrate', je souhaite remercier Cyrielle, pour sa rigueur, et sa douceur. Nous avons partagé de très bons moments à Grenoble, scientifiques mais toujours accompagnés d'un bon thé ou d'un verre de vin. Sophie, la reine des clathrates d'acide, toujours partante pour démarrer un nouveau projet, je te remercie pour ton énergie et ton soutien ! Enfin je souhaite remercier Clara et Lara, les inséparables, avec qui j'ai partagé mon bureau pendant ces trois dernières années ainsi que nos fameuses séances de sport en plein air. Je vous souhaite à tous le meilleur pour la suite.

Comment ne pas remercier également mes amis les plus anciens Romain, Maxime, Anice, sans qui les années de fac n'auraient pas été aussi folles, merci d'avoir été présents pour ma soutenance. Merci aussi à tous mes amis rencontrés durant la thèse, Manon, Flo, Guillaume, Charlotte, Popeye, Elo, Juju, Toto, Marcelle, Pips, Pierrick et toute l'équipe. Déjà de nombreux moments inoubliables avec vous, merci pour votre énergie, votre amour. Merci aussi à Charles et les copains de CSM, une belle aventure qui a permis à chacun d'entre nous de donner le meilleur aujourd'hui, et de trouver notre propre voie.

Enfin, je souhaiterais remercier ma famille pour leur soutien depuis toujours. Merci à mes parents de m'avoir fait confiance pour faire mes propres choix. Maman, Papa, Sylvie, Michèle, Alain, merci de votre présence le jour de la concrétisation de toutes mes années d'étude. Un merci plus particulier à mon kiki, ma sœur, merci pour ton énergie, ta folie. Je suis fière de toi, finalement tu es devenue une petite scientifique toi aussi ! Merci à ma tatie, de m'avoir ouvert la voie des sciences avec nos expériences des petits débrouillards, les cours particuliers et surtout ton plus grand soutien, à toute heure, quel que soit le pays dans lequel je me trouvais, qui m'a donnée de la force à chaque fois que je pensais en manquer ! Il me faut aussi remercier mon papi, merci d'avoir contribué à faire de moi la personne que je suis aujourd'hui. Merci pour tout l'amour que vous me donnez. Keke, Florent, Echcha, Océane, Jade, Diego, Coco et toutes les personnes de ma famille qui n'ont pas pu être présents pour ma soutenance, merci pour votre soutien à distance.

Mon dernier remerciement va à la famille que je commence à construire. Mon mari, Marc, celui qui m'a maintenue en forme durant toute la thèse, qui ma soutenue et surtout déstresser lorsque je ne pensais plus rien maîtriser, que j'étais complètement sous-l'eau mais

aussi celui qui râlait lorsque l'on ne pouvait pas partir en van-trip et dormir dans un super spot au bord de l'océan car je n'avais pas fini d'écrire mon manuscrit ! Merci pour tout ton amour, ton énergie et ton humour. Sans oublier notre petit chat, Ouby, un soutien indéfectible durant la thèse (qui a dit que l'on ne pouvait pas citer son chat dans son manuscrit de thèse ?).

Content

RESUME	7
ABSTRACT	9
GENERAL INTRODUCTION	13
CHAPTER 1: GAS HYDRATES	21
I. GENERALITIES.	23
a. Structural properties and Raman signatures	23
b. Mechanism and kinetics of formation	28
c. Cage occupancy.....	33
II. NATURAL GAS HYDRATES.....	36
a. Occurrence, gas origin and challenges	36
b. The Black Sea case.....	38
c. The Sea of Marmara case	40
III. FORMATION IN SEDIMENTS.....	43
a. Natural sediments	44
i. Chemical and structural properties	44
ii. Sedimentary environment of the Black Sea	49
b. Sedimentary surrogates	51
c. Impact of the sedimentary media on hydrate formation	53
i. Distribution.....	53
ii. Thermodynamics	55
iii. Kinetics.....	59
iv. Cage occupancy.....	65

CHAPTER 2: EXPERIMENTAL METHODOLOGY 69

I. GAS HYDRATE SYNTHESIS..... 71

 a. Gas hydrate formation without sedimentary media 71

 i. From liquid water 71

 ii. From ice..... 73

 b. Gas hydrate formation in sedimentary media 74

 i. Preparation of the water-sediment premix 74

 ii. Hydrate formation 76

II. RECOVERY OF NATURAL GAS HYDRATES FROM THE BLACK SEA. 77

III. EXPERIMENTAL TECHNIQUES. 79

 a. Neutron scattering 79

 i. Neutron diffraction 82

 ii. Inelastic Neutron Scattering 83

 b. Raman spectroscopy 84

IV. EXPERIMENTAL STRATEGY..... 88

 a. Kinetic study 88

 b. Structural analysis 89

 i. Le Bail and Rietveld refinements 89

 ii. Raman signatures 91

 c. Cage occupancy..... 93

 d. Gas hydrate distribution at the nano- and micro- scales 95

**CHAPTER 3: RAMAN AND NEUTRON DIFFRACTION OF PURE AND MIXED
GAS HYDRATES. 99**

I. INTRODUCTION..... 101

II. PURE GAS HYDRATES.....	104
a. Methane hydrate (sI)	104
b. Ethane hydrate (sI)	109
c. Propane (sII).....	111
d. Iso-Butane (sII)	116
e. Carbon dioxide (sI).....	120
III. MIXED GAS HYDRATES.....	123
a. Methane – Ethane (sII).....	123
b. <i>n</i> -Butane – Methane (sII)	127
IV. CONCLUSION.....	133

CHAPTER 4: KINETICS OF METHANE HYDRATE FORMATION: IMPACT OF SEDIMENTARY MEDIA AND SALINITY. 137

I. INTRODUCTION.....	139
II. KINETICS OF METHANE HYDRATE FORMATION IN MONTMORILLONITE: SALINITY EFFECT (NaCl).....	142
a. Abstract	142
b. Materials and methods	143
c. Experimental results.....	145
d. Conclusion.....	156
III. KINETICS OF METHANE HYDRATE FORMATION IN SYNTHETIC AND NATURAL SEDIMENTS FROM BLACK SEA: EFFECT OF CLAY PROPERTIES. ...	157
a. Abstract	157
b. Materials and methods	157
i. Sediment.....	157
ii. Experimental procedure.	159
c. Experimental results.....	160
i. Monitoring the methane hydrate formation.	160

ii. Quantifying the methane hydrate formation kinetics.....	163
iii. Modeling the methane hydrate formation kinetics.....	165
d. Conclusion.....	167

CHAPTER 5: HYDRATE FORMATION IN CLAYS: INVESTIGATION OF CONFINEMENT SIGNATURES. 171

I. INTRODUCTION.....	173
II. MATERIALS AND METHODS.	176
a. Sample preparation.....	176
b. Techniques	179
III. RESULTS AND DISCUSSION.....	180
a. Structural analysis and cage occupancy	180
b. Hydrate distribution from micrometer to nanometer scales.....	188
IV. CONCLUSION.....	198

GENERAL CONCLUSION & PERSPECTIVES 199

APPENDIX 199

REFERENCES 199

Résumé

Titre : Combinaison de la spectroscopie, de la diffraction et de l'imagerie (Raman, neutron) pour l'étude des hydrates de gaz synthétiques et naturels dans les milieux argileux marins : cinétique de formation, composition et distribution spatiale.

Résumé : Les hydrates de gaz sont des matériaux cristallins dans lesquels des molécules d'eau forment des cages pouvant piéger des molécules gazeuses. Dans la nature, les hydrates de gaz existent dans le pergélisol des régions polaires et dans les sédiments marins des marges continentales. Ces hydrates possèdent une très grande capacité de stockage de gaz et constituent le plus grand réservoir de méthane existant sur Terre. A l'état naturel, les hydrates marins se trouvent principalement dans des sédiments riches en argile – systèmes à porosité multi-échelle. Cependant, l'évaluation de la quantité de gaz stockée dans les hydrates sédimentaires est basée sur des modèles géophysiques supposant d'une part un remplissage en méthane constant et homogène au sein des cages aqueuses de l'hydrate et d'autre part, une distribution macroscopique des hydrates dans les sédiments, ne prenant pas en compte la formation potentielle dans les espaces micrométriques ou nanométriques des argiles. Quelques études (principalement théoriques) consacrées aux hydrates de méthane au sein d'argiles gonflantes suggèrent une formation potentielle dans les espaces nanométriques (inter-feuillet) des argiles, s'accompagnant d'une variabilité du taux de remplissage des cages aqueuses. Ce travail de doctorat propose une étude expérimentale des facteurs physico-chimiques influençant la formation d'hydrates de gaz en milieu naturel. Ce travail se base sur une approche multi-échelle où les expériences de laboratoire sont comparées aux mesures d'échantillons naturels collectés en mer Noire.

Des hydrates de gaz naturels et synthétiques mimant l'environnement naturel (composition des gaz, salinité et minéralogie des sédiments) ont été caractérisés à l'échelle microscopique et nanoscopique par spectroscopie Raman, diffraction des neutrons et diffusion inélastique des neutrons. L'influence de l'environnement naturel sur les structures résultantes, l'occupation des cages, la cinétique de formation et les mécanismes de dissociation ont été étudiés. En considérant une large gamme de mélanges gazeux rencontrés en mer de Marmara, les signatures spectrales des hydrates de gaz (formant les structures dites sI et sII) sont rapportées. Des études de la cinétique de formation des hydrates de méthane dans des argiles gonflantes (Montmorillonite), non gonflantes (Illite) et des sédiments naturels montrent une forte influence de la nature du sédiment sur la cinétique de formation de l'hydrate de méthane. L'imagerie spectrale Raman montrent la formation d'hydrate de méthane à l'échelle micrométrique et une variabilité du taux de remplissage en méthane à cette échelle. De plus, les spectres de diffusion inélastique des neutrons montrent des signatures de formation d'hydrates en milieu argileux comparable à celles des hydrates massifs (c'est-à-dire sans matrice sédimentaire). Ces résultats expérimentaux ne permettent pas de mettre en évidence un confinement dans les pores des argiles à l'échelle nanométrique. L'ensemble de ces données apportent des informations nouvelles quant à l'estimation des quantités de gaz stockées dans les fonds marins à l'échelle géologique.

Mots clés : Hydrates de gaz, diffraction des neutrons, spectroscopie Raman and neutronique, cinétique de formation, distribution spatiale, argiles.

Abstract

Title: Combining spectroscopy, diffraction and imaging (Raman, neutron) for investigating synthetic and natural gas hydrates in marine clay media: formation kinetics, composition and spatial distribution.

Abstract:

Gas hydrates are crystalline materials in which water molecules form cages, which can trap gaseous molecules. In nature, gas hydrates exist in the permafrost of polar regions and in the marine sediments of continental margins. These hydrates have a very large gas storage capacity and constitute the largest methane reservoir on Earth. In their natural environment, marine hydrates are mainly found in clay-rich sediments - multi-scale porosity systems. However, the assessment of the amount of gas stored in sedimentary hydrates is based on geophysical models assuming on one hand, a constant and homogeneous methane filling within the aqueous cages of the hydrate and on the other hand, a macroscopic distribution of hydrates in the sediments, not taking into account the potential formation in the micrometric or nanometric spaces of clays. Some studies (mainly theoretical) dedicated to methane hydrates in swelling clays suggest a potential formation in nanometric spaces (interlayer) of clays, with a variability of the filling rate of aqueous cages. This PhD work offers an experimental study of the physicochemical factors influencing the formation of gas hydrates in natural media. This work is based on a multi-scale approach where laboratory experiments are compared with measurements of natural samples collected in the Black Sea.

Natural and synthetic gas hydrates mimicking the natural environment (gas composition, salinity and sediment mineralogy) were characterized at the microscopic and nanoscopic scales by Raman spectroscopy, neutron diffraction and inelastic neutron scattering. The influence of the natural environment on the resulting structures, cage occupancy, formation kinetics and dissociation mechanisms have been studied. Considering a wide range of gas mixtures encountered in the Marmara Sea, the spectral signatures of the gas hydrates (forming the so-called sI and sII structures) are reported. Studies of methane hydrate formation kinetics in swelling (Montmorillonite), non-swelling (Illite) clays and natural sediments show a strong influence of sediment nature on methane hydrate formation kinetics. Raman spectroscopy imaging shows methane hydrate formation at the micrometer scale and a variability in methane filling rate at this scale. In addition, inelastic neutron scattering spectra show signatures of hydrate formation in clay media comparable to those of bulky hydrates (i.e., without a sedimentary matrix). These experimental results do not allow us to demonstrate confinement in the pores of clays at the nanometric scale. All these data provide new information for the estimation of the quantities of gas stored in the seabed at the geological scale.

Keywords: Gas hydrates, neutron diffraction methane, Raman and neutron spectroscopy, formation kinetics, spatial distribution, clays.

General introduction

Gas clathrate hydrates (also named gas hydrates) were first mentioned in 1934 by Hammerschidt, who discovered that these materials composed of ice and gas were at the origin of the plugging of pipeline.¹ Since the middle of the 20th century, many works have been devoted to the study of the crystalline structure of these nanoporous materials made of 85 % of water molecules arranged in nanometer cages in which gas molecules are trapped.² Later, natural gas hydrates were observed in the USSR Permafrost in 1960 and in Black Sea in 1972.³

Natural gas hydrates, found in marine sediments on continental margins are by far the largest reservoir of methane on the planet, accounting for about ~98- 99 % of hydrate on Earth.^{4,5,6,7} These large quantities place natural gas hydrates at the heart of current energy (large unexploited hydrocarbon sources) and environmental issues. This last point refers in particular to the climatic impact of methane hydrates. Today, with global warming, the increase of the water level and of the Earth temperature could lead to the destabilization of gas hydrates.^{8,9} In the short term, this could potentially cause underwater landslides and the formation of tsunami waves.¹⁰ In the longer term, the release of methane into the water column that may trigger ocean acidification and in the worst case scenario reach the atmosphere and contribute to climate change - methane being an important greenhouse gas.^{9,11,12} Currently, in the Black Sea, sedimentary methane hydrates deposit is undergoing dissociation¹⁰ and large uncertainties remains on the amount of methane trapped in these deposits, as well as the formation mechanism within the clay-rich sediments. However, assessment of the amount of gas stored in sedimentary hydrates is conducted on macroscopic considerations (primarily based on geophysics, geology, geochemistry and thermodynamics), assuming a constant rate of cage filling with the gas molecules and considering an effective sedimentary media.^{4,6,13-16} Recent findings show that many cages, up to 17%, can remain empty.^{17,18} Moreover, the nature of the sedimentary matrices (chemistry, structure, etc.) may impact the gas hydrate formation, and in particular, their cage filling. Very few studies have been conducted to determine the consequences of this microscale filling variability on the macroscopic properties of the hydrates, particularly on their methane storage capacity. Thus, understanding the formation of gas hydrates in natural environments becomes a priority.

The natural occurrence of gas hydrates in sediments and clay minerals raises questions about the influence of this sedimentary matrix on their physicochemical properties. It becomes crucial to determine which characteristics, specific to the sediments constituting their natural environment (structure, chemical composition, particle size, specific surface area, etc.), have a

significant impact on the formation of gas hydrates. Several studies have been conducted to investigate the influence of sediments on the thermodynamics, kinetics and physicochemical properties of gas hydrates, most of them focusing on amorphous materials (quartz, silica sand) or sedimentary porous analogs (MCM-41, porous activated carbons, ...).¹⁹ All the experiments carried out have largely advanced our physicochemical knowledge on the formation of hydrates. However, in order to go further, it is necessary to reproduce the natural environment more accurately, in particular by studying the influence of clayey sediments on the formation of hydrates and the related kinetics. Hydrate formation kinetics have already been addressed in the literature, with very few studies dedicated to the consideration of the influence of a sedimentary matrix. Many questions remain open because of the large range of parameters to be taken into account in these complex systems: the mineralogy, the size and the shape of the particles, the diameter of the pore diameter, specific surface, initial water saturation and interstitial water chemistry.

During this PhD work, several challenges related to natural gas hydrates are addressed. Initially, gas hydrates were treated independently of the sedimentary environment in which they are found in order to focus on the effects of gas composition on their structure. For this purpose, the wealth of natural gaseous species found in nature (e.g., CH₄, C₂H₆, C₃H₈, *iso*-C₄H₁₀, CO₂) yield to consider the formation of gas hydrates by considering various gas mixtures. Such a knowledge makes it possible to characterize and identify the formed hydrate structure gas hydrates systems composed of several gas species. In a second step, the study focuses on understanding the mechanisms that govern methane hydrate formation in natural porous media; in particular in identifying and determining the physic-chemical factors that most affect the methane hydrate formation – methane being the most abundant gas species on Earth.^{4,20} For this purpose, synthetic methane hydrate samples formed in the laboratory under thermodynamic conditions and sediments reproducing the Black Sea will be compared to natural gas hydrates collected on the Romanian sector of the Black Sea during a scientific campaign (GHASS2²¹, September 2021). Four clay-rich matrices were selected as sedimentary surrogates for the formation of the synthetic hydrates. They are constituted of 60 % clay and 40 % of other minerals (quartz and plagioclase). The prototypical clays met in marine environment are Illite, Kaolinite (both being non-swelling clays) and Montmorillonite (a swelling clay). The particle size, the specific surface area and the structural arrangement vary from one clay to another. Methane hydrates are synthesized with the same thermodynamics' conditions in all the matrices. The recovery of natural sediments and natural hydrates in the Black Sea allows the

direct comparison of the measured properties for natural and synthetic methane hydrates. Methane hydrate formation kinetics, dissociation mechanism, cage occupancy, structural properties and multi-scale distribution are detailed in the manuscript. This PhD work is thus a multiscale approach conducted at the boundary of physical chemistry (spectroscopy, thermodynamics) and geochemistry and ranging from the nanoscale to the microscale. Crucial issue at the core of the present PhD work concerns the potential formation of gas hydrate within pores of nanometer sizes, especially when considering the inter-layer spaces of clays. The study of these systems contributes to the improvement of the scientific knowledge of the hydrate formation mechanism in natural environment and thus should contribute to a better estimation of the methane reservoir trapped into hydrates. For this reason, this work constitutes a priority in terms of preventing geological and environmental risks; the destabilization of methane hydrates could lead to the release of underestimated quantities of methane (greenhouse gas) into the water column and potentially in the atmosphere. Such phenomena may have a significant impact on deep-sea living organisms and on climate change.¹⁰

This manuscript is divided into four main parts. Chapter 1 and Chapter 2 present the state of the art and the methodology used during this PhD work. The analysis of the structural and vibrational signatures of the pure and mixed gas hydrates are reported in chapter 3. The results of experimental studies of the formation kinetics and dissociation mechanisms of methane hydrates formed in the presence of sediment and salt rich matrices are detailed in chapter 4. Chapter 5 is dedicated to the comparison of structural and spectroscopic signatures of synthetic and natural methane hydrates formed within sedimentary matrices; it addresses the crucial question of the potential formation of methane hydrate under nano-confinement (i.e., in the inter-layer space of clays).

Chapter 3 is dedicated to the analysis of the structural and vibrational signatures of the structure sI and the structure sII adopted by pure (CH_4 , C_2H_6 , C_3H_8 , *iso*- C_4H_{10} , CO_2) and mixed gas hydrates ($\text{CH}_4+\text{C}_2\text{H}_6$, $\text{CH}_4+n\text{-C}_4\text{H}_{10}$) synthesized in the laboratory. This study contributes to the evaluation of the effects of gas composition on the structure and occupancy of the resulting hydrate cages. In some geological sites, natural gas sources are composed of complex mixtures of several gas species. This is particularly the case in the Marmara Sea, where hydrates are derived from thermogenic gases, resulting from thermal cracking of organic matter at depth.²²⁻²⁵ The study of gas hydrates from small to larger hydrocarbons gas molecules is required to characterize natural gas hydrates especially to explore the structures formed in presence of complex natural gas mixture and the possible variation of gas compositions and

coexisting phases.²⁶⁻²⁸ In this chapter, Raman spectroscopy and Neutron diffraction experiments are detailed for selected gas hydrates of interest in natural environments.

In Chapters 4 and 5, detailed studies focus exclusively on methane hydrate and the effects of the sedimentary environment (sediment mineralogy, salinity) on formation kinetics, dissociation mechanisms, structural properties, cage occupancy, and distribution of methane hydrates.

Experimental studies of methane hydrate formation kinetics and dissociation within clay-rich sedimentary matrices and in the presence of salt are detailed in Chapter 4. Neutron diffraction technique was used to investigate both processes. The selected substrates are made of 60 % clay and 40 % of other minerals (quartz and plagioclase) constituted by a mixture of Montmorillonite and Fontainebleau sand (denoted MS), commercially available Illite (IS), and the natural Black Sea sediments collected during the scientific cruise GHASS2²¹. In the first part of Chapter 4, the effect of NaCl and swelling clay (MS) on the kinetics of formation and dissociation mechanism of methane hydrate are investigated. In the second part, the formation kinetics in IS and BS are compared to the data collected in MS to investigate the effect of the sediment nature on the formation process. Several physicochemical parameters are taken into account for these studies: the particle size effect, the specific surface area and the clay chemical composition.

Chapter 5 is dedicated to the study of the influence of the nature of the clay sediment on the structure of the formed hydrate, the cage occupancy and the distribution from the micro- to the nano-scale. Neutron diffraction, Raman spectroscopy and Inelastic Neutron Scattering are selected in this work to provide new original data on synthetic and natural methane hydrate. In particular, a major effort has been devoted in this chapter to the search for vibrational and structural signatures that might indicate the formation of methane hydrates in the nanoscale spaces of swelling clays. These spaces, which are not considered in geophysical models dedicated to estimating the amount of methane trapped in hydrates, represent extremely large areas where gas hydrates could be intercalated.²⁹⁻³² Their presence in these spaces could therefore considerably increase the current estimates and environmental concerns. However, in the current literature, experimental studies of methane hydrate formation in the interlayer space of swelling Montmorillonite are inconsistent.³³⁻³⁵ Additional evidence for the hypothetical formation of methane hydrate within this nano-space is investigated in this Chapter. Moreover, collected information on the synthetic samples made in IS, kaolinite and Fontainebleau sand (KS), MS and BS are compared to the natural sample collected in Black Sea in September 2021 during the GHASS2 cruise.²¹

CHAPTER 1:

Gas Hydrates

Introduction

The study of gas hydrates is at the center of a multidisciplinary research field where the combination of numerous experimental and theoretical techniques covers the multi-scale exploration of these systems. In this first chapter, a bibliographical study is presented, including a description of the various crystal structures met for gas hydrates, as well as their thermodynamic and kinetic properties. The second part of this chapter will be devoted to natural gas hydrates and their sedimentary environments. The latter will be the subject of an in-depth study detailing in particular the various physicochemical impacts of the sedimentary environment on hydrates. Finally, the scientific approach adopted for this thesis will be detailed and positioned with respect to the published results. The systems and the techniques envisaged to carry out this project will also be presented. Throughout this chapter, the questions addressed during this PhD work are highlighted.

I. GENERALITIES.

a. Structural properties and Raman signatures

Gas hydrates are crystalline structures consisting of cages resulting from the hydrogen bonding of water molecules (host) enclosing relatively small gas molecules (guest), such as hydrogen, carbon dioxide, methane and other small hydrocarbons.^{3,36} Van der Waals interactions between the host and guest molecules ensure the stability of the structures.³⁷ Gas hydrates formed from only one type of gases are considered as pure gas hydrates. They can also be synthesized from a gas mixture where the structure hosts multiple molecules inside the cages, and these hydrates are called mixed hydrates.

The nature of the guest molecules determines the type of network formed by hydrogen-bonded water molecules and thus, the hydrate structure³ and its thermodynamics stability conditions (p, T). The phase diagram of methane hydrate is presented in **Figure 1**. It describes the thermodynamics conditions required to form methane hydrates. In the figure, I is used to denote ice, H is for hydrate, L_w is for liquid water and V is used for vapor. The hydrate region is on the left of (H-L_w-V) and (H-I-V) lines. On the right of these lines, liquid water or ice phases with the methane gas co-exist. Two methods allow forming hydrate. The first method consists of the fixing the temperature and increasing the pressure to reach the equilibrium thermodynamics conditions – it corresponds to the isothermal method. The second methods is

consists of fixing the pressure and varying the temperature until the p-T stability line of the selected hydrate is crossed – it is the isobaric method.

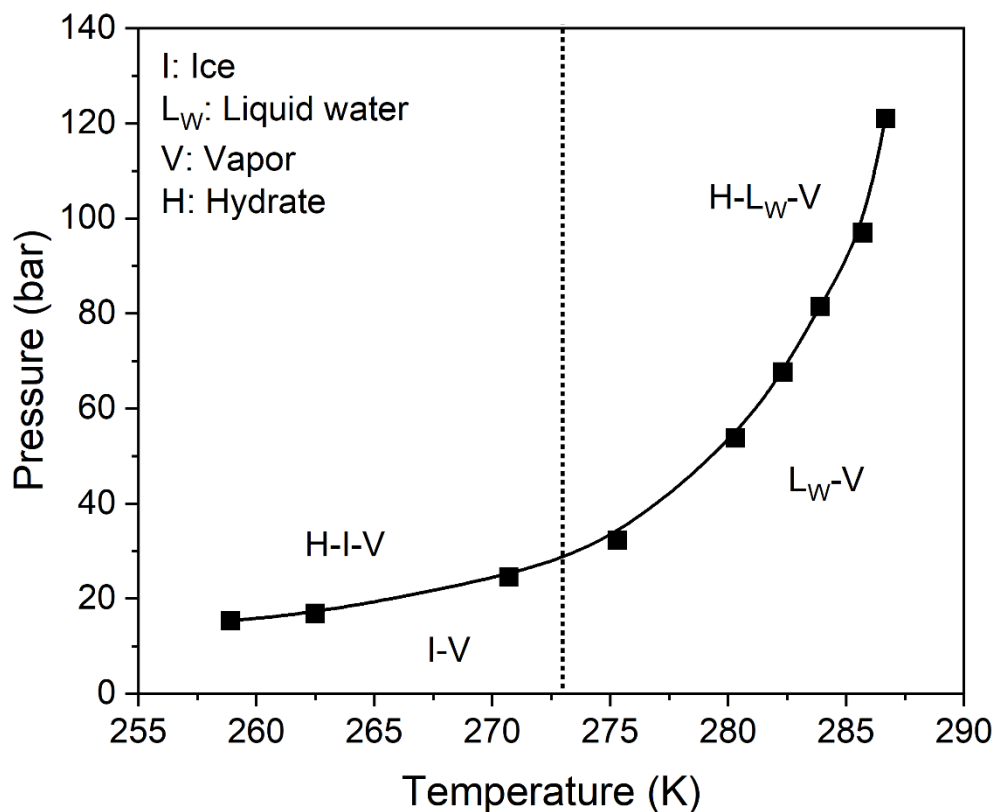


Figure 1. Methane hydrate formation thermodynamics conditions (Black squares). The dotted line represents the ice equilibrium curve (adapted from Goel³⁸).

In nature, two different spatial organizations are mainly found: the structure I (termed sI) and the structure II (termed sII), with a cubic structure parameter $a \approx 12 \text{ \AA}$ and $a \approx 17.2 \text{ \AA}$ respectively. These structures are defined by the arrangements of particular polyhedron composed by water molecules, which constitute the cages. There are two types of cages: The small cages (SC) are made by the arrangements of the hydrogen-bonded water molecules network describing a dodecahedron 5^{12} (12 pentagons compose the cage). It is the most stable cage. The large cages (LC) are composed by a mixed of hexagons and pentagons giving rise to two types of LC: $5^{12}6^2$ (12 pentagons and 2 hexagons compose the cage) and $5^{12}6^4$ (12 pentagons and 4 hexagons compose the cage). These types of cages possess a larger volume to host guest molecules than the SC. The structure sI is composed of 2 SCs 5^{12} and 6 LCs $5^{12}6^2$, and the structure sII contains 16 SCs 5^{12} and 8 LCs $5^{12}6^4$ (Figure 2). There is another structure – less frequently found in nature – called structure H (termed sH).^{3,39} It could be formed by encaging large size hydrocarbons (such as neohexane) molecules together with a small-size

hydrocarbon help-gas molecules (generally methane). This structure is constituted from an hexagonal unit cell, which contains three types of cavities, three regular dodecahedral SCs 5^{12} , two irregular dodecahedral $4^35^66^3$ and one irregular icosahedral $5^{12}6^8$ (Figure 2).⁴⁰

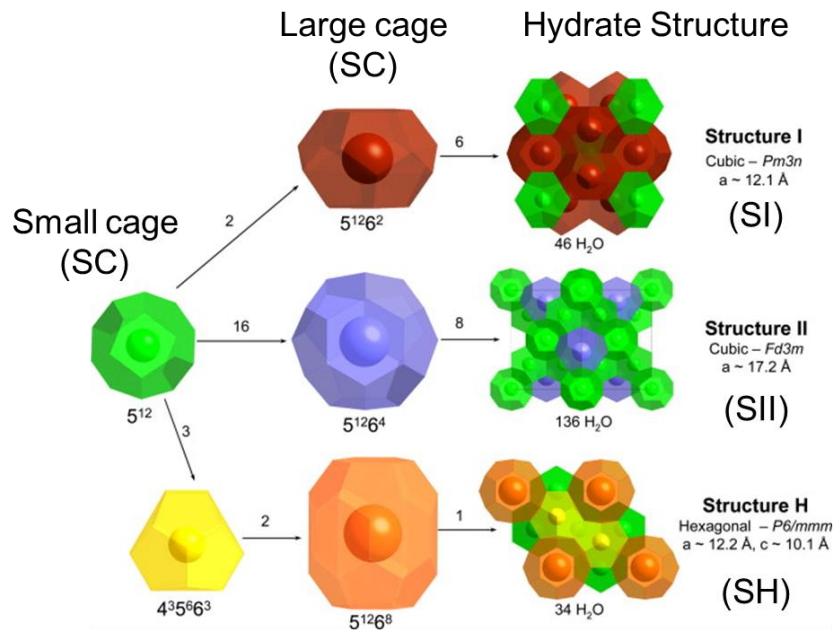


Figure 2. Description of the three main gas hydrate structures. (Adapted from Strobel *et al.*⁴¹)

The structure analysis of the resulting hydrate can be done by using various techniques (X-ray diffraction, neutron diffraction, Nuclear Magnetic Resonance, Infrared absorption, Raman scattering, etc.).³⁶ Among them, Raman spectroscopy appears to be a very attractive one, because of its chemical sensitivity, its non-destructive character and its lab “easy-access”.⁴² Regarding Raman spectroscopy, the spectra of the hydrate sI and sII show characteristic signatures for low frequency intermolecular modes, also called lattice modes, and O-H elongation modes, which differ from the hexagonal ice structure Ih and liquid water, and thus allows the distinction between the four systems. Indeed, the ice Ih has a perfect hexagonal lattice consisting of water molecules forming tetrahedral sites via hydrogen bonds (Figure 3).

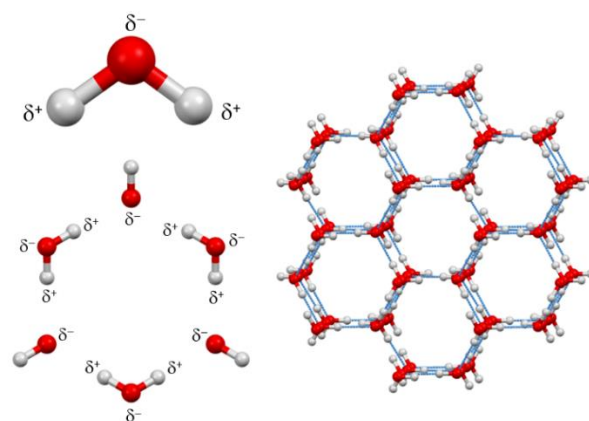


Figure 3. Crystal lattice and molecular arrangement of hexagonal ice Ih.⁴³

The structure sI hydrate consisted of 6 LCs ($5^{12}6^2$) and 2 SCs (5^{12}) has a predominance of hexagons to pentagons. The water molecules orientate likewise to those in Ice Ih, which explains the similarities between the two spectra.⁴⁴ However, the hydrogen-bonding network of a hydrate structure sI is distorted and weakened. Thus, the lattice mode of a gas hydrate will possess a lower vibrational frequency than that of ice Ih (**Figure 4**).⁴⁵ The intermolecular modes of liquid water and the lattice mode of structure sII hydrate are broader compared to ice Ih and structure sI hydrate. Structure sII hydrates are composed of 16 SCs (5^{12}) and 8 LCs ($5^{12}6^4$). Molecular dynamics studies on the arrangement of water molecules in liquid water proposed a model organizing the water molecules in similar complex 5^{12} cavities.⁴⁶⁻⁴⁹ The similar shape between the water and sII spectra could be explained by the predominance of the SCs (5^{12}) in both systems.⁴⁴ In addition, the lattice mode of structure sII hydrate is at a higher frequency than structure sI hydrate.^{50,51} This can be explained by the difference in size of SC 5^{12} . Indeed, the small cage of structure sII hydrate is slightly smaller than that of type I.⁵²

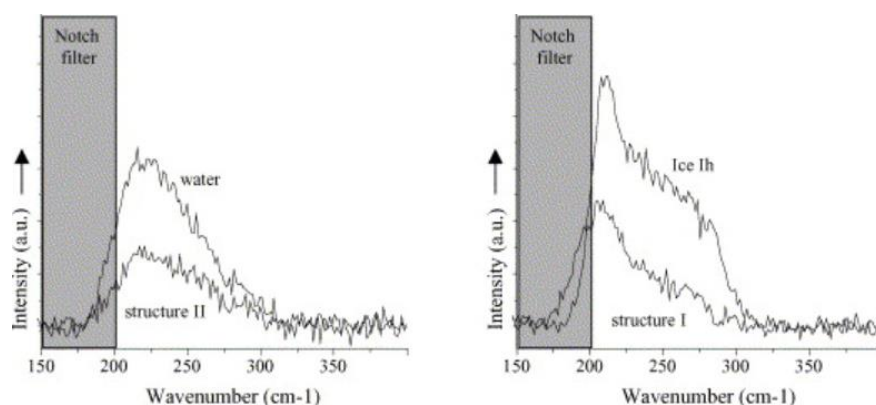


Figure 4. Intermolecular hydrogen bonded stretching band of water and water lattice mode of hexagonal ice, structure sI and structure sII methane hydrates (From Schicks *et al.*⁴⁴).

Similar observation can be done for O-H stretching regions (3000-3700 cm^{-1}). On one side, the spectrum of liquid water shows two broad bands at 3190 cm^{-1} and 3450 cm^{-1} and a weak shoulder at 3630 cm^{-1} assigned respectively to the Fermi resonance between O-H stretching and bending mode overtone, the symmetric stretching and the asymmetric stretching of water molecules.^{53,54} The spectrum of the structure sII hydrate shows signatures similar to those of liquid water, except for the band attributed to O-H stretching at 3450 cm^{-1} which has a lower intensity⁴⁴. On the other side, the O-H elongations of ice Ih and sI hydrate again demonstrate similarities with a strong band at around 3100 cm^{-1} . According to Hare and Sorensen⁵⁵, this signature is attributed to the in-phase symmetric stretching vibrations of water molecules. Moreover, the signatures of structure sI hydrates are observed at higher frequencies compared to ice Ih; the distortion of the hydrogen-bonding network enhances the force constant of O-H (Figure 5).^{50,51}

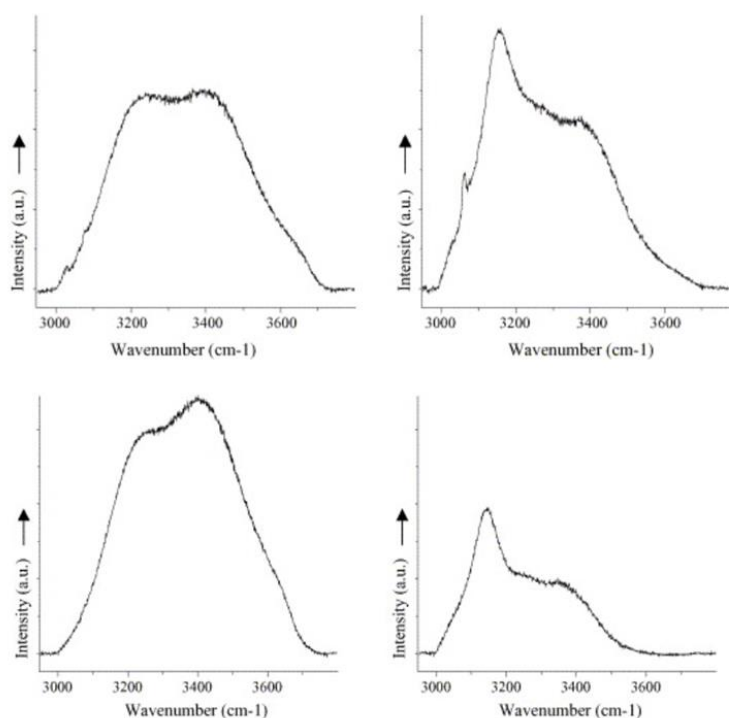


Figure 5. On the top, O-H stretching modes of structure sII methane hydrates (left) and structure sI methane hydrates (right). On the bottom, O-H stretching modes of liquid water (left) and hexagonal ice Ih (right). (Adapted from Schicks *et al.*⁴⁴).

However, it is important to note, that experimentally, hydrate formation rarely reaches the complete conversion of water or ice into hydrate. Thus, the presence of "residual" ice signatures Ih can create difficulties when assigning vibrational frequencies.

In parallel to the analysis of the aqueous substructure, the determination of the type of hydrate structure formed can be made from the vibrational signatures of the guest molecules trapped in the LCs and SCs. The example of methane hydrate is presented here. Since the Raman intensity is proportional to the variation of polarizabilities and the concentration of the species, it is possible to determine the filling rate of hydrate cages by assuming that the polarizabilities of the guest molecule in LCs and SCs are identical (detailed in Chapter 2). Therefore, the relative Raman intensity ratios for LCs and SCs occupancy are equal to 3 and 0.5 for structure sI (6 LCs and 3 SCs) and structure sII (8 LCs and 16 SCs), respectively, as shown in **Figure 6**. Moreover, the frequencies of methane in LCs and SCs in structure sI differs from that of structure sII, respectively 2905 cm^{-1} and 2910 cm^{-1} for structure sI and 2904 cm^{-1} and 2915 cm^{-1} for structure sII. Note that the CH_4 signature in the gas phase is at a higher frequency (2917.6 cm^{-1}).

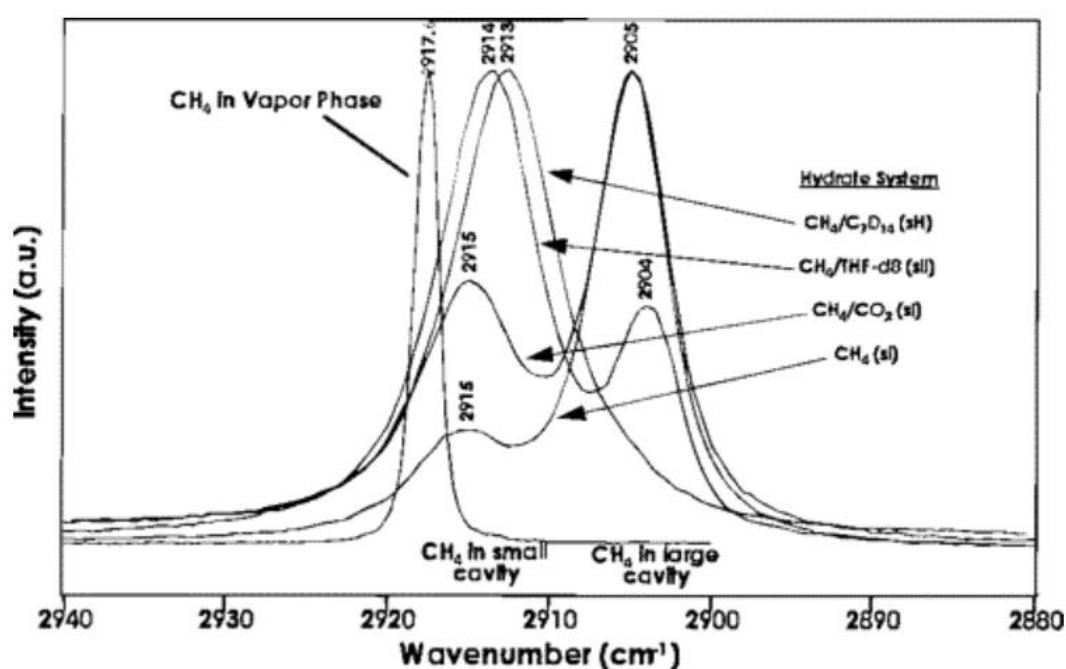


Figure 6. Raman signatures of CH_4 in vapor phase and in structures sI, sII, and sH hydrates. (From Sum *et al.*⁵⁶).

b. Mechanism and kinetics of formation

One of the questions that persists within the hydrate community deals with the mechanisms of gas hydrate formation, and in particular the understanding of the phenomena of *nucleation* and *growth* mechanisms. These processes involve many properties such as the thermodynamics conditions (p , T) and kinetics. **Figure 7** illustrates the formation process of gas hydrates with a typical curve representing gas consumption. It is necessary to distinguish the formation of

hydrates from liquid water and from crystalline ice. Indeed, it turns out that the solubility in liquid water of the guest molecules would favor the formation of hydrate. At 295 K and 1bar, CH₄ has a solubility of 0.023 g.L⁻¹ in water; the methane hydrates form in the range of several hours.^{3,57} In contrast, in the same p, T conditions, CO₂ has a solubility of 1.69 g.L⁻¹ and, the hydrate typically forms in one hour.^{56,58,59} In this PhD work, the two methods will be used to form methane hydrates.

Figure 7 illustrates the formation process of gas hydrates from liquid water with a typical curve representing gas consumption. The gas consumption could be assimilated to the rate of hydrate formation.⁶⁰ The first step called nucleation of hydrates is characterized by an induction time, which corresponds to the elapsed time between when the gas/ water systems reach the favorable (p, T) conditions (stability region of gas hydrates) and the beginning of the growth. During this period, the gas molecules are dissolved in the aqueous phase until the first hydrate crystals appear, i.e. the water molecules form hydrogen-bonding cages around the gas molecules. They begin to clump together to increase the volume. However, hydrate does not accumulate within this period because of metastability (i.e., the ability of a nonequilibrium state to persist for a long period of time). Then, three periods follow and are related to the growth of the hydrate. In the second period, the adsorption phase begins, it corresponds to the fast growth of gas hydrate, and a large amount of gas is incorporated into the hydrates, thus the crystal size increases. As the hydrate grows, water and gas molecules are consumed; the rate of gas consumption begins to decrease and then flattens out. This is the third region: the system tends to reach a thermodynamically stable state. This final step can be explained by either the complete consumption of one of the hydrate-forming components (i.e., water or gas) or by the limitation of mass or heat transfer from the molecular species (i.e., water or gas) to the hydrate-forming interface, resulting in low driving forces and an almost negligible rate of hydrate formation.⁶⁰

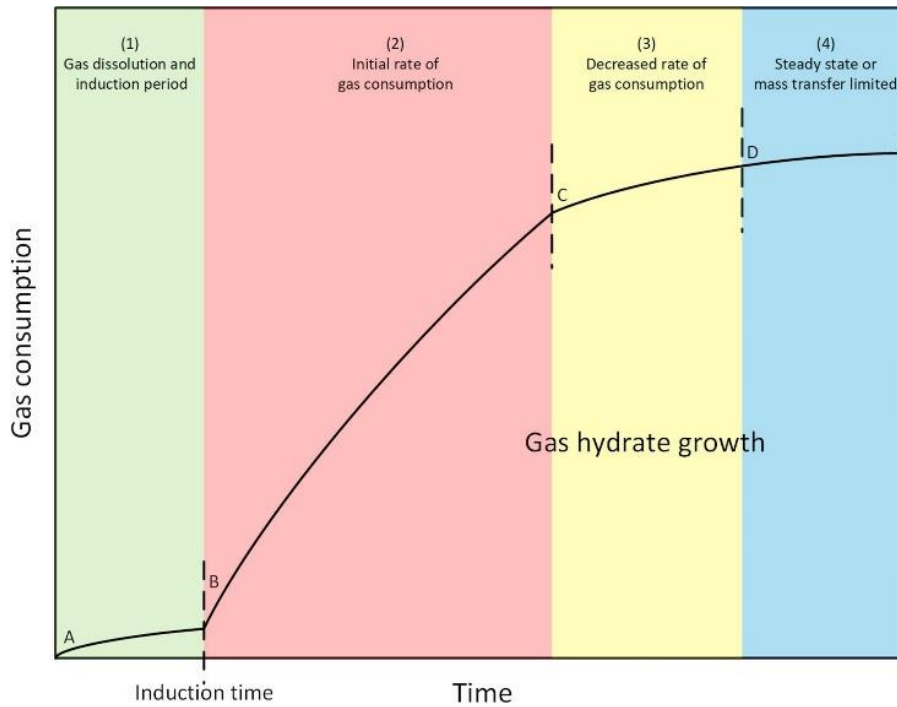


Figure 7. Typical curve representing gas consumption during hydrate formation from a liquid water (From Yin *et al.*⁶⁰).

Numerous theoretical and experimental studies have been conducted to investigate the nucleation and growth mechanisms of gas hydrates in order to contribute to the understanding of their formation kinetics.^{60–65} The various models and advances are detailed in this section.

Hydrate nucleation is a stochastic and dynamical mechanism, which takes place at the molecular level.⁶⁶ It is extremely difficult to observe hydrate nucleation: it occurs on a time and space scale too small to be characterized with existing experimental technologies. Subsequently, molecular simulation is a powerful and essential technique to help understand this mechanism.^{62,65} Hydrate nucleation is characterized by the induction time, which drastically depends on experimental set-up and procedures⁶⁷ (e.g., driving force, medium geometry, etc.) and the thermodynamics history of the system (“memory effect”: a shorter nucleation time would be observed for the formation of hydrate for water that has very recently experienced hydrate formation^{68,69}). It exists two types of nucleation phenomenon classified as homogeneous nucleation and heterogeneous nucleation. Gas hydrates homogeneous nucleation would rarely be observed in nature, since it occurs when only two phases are involved: the aqueous solution and the nuclei/growing crystal.⁷⁰ In real systems, the hydrate nucleation is expected to be heterogeneous. Hydrate crystals initiates at the surface of impurities, particles, gas-liquid interfaces, grains boundaries, etc. Therefore, heterogeneous nucleation would require

far fewer molecules to collide and aggregate to form the critical size nuclei.⁶² Moreover, the site of initial nucleation and later growth were investigated. Experimental and Molecular Dynamics (MD) simulations studies have shown that hydrate formation was initiated at a surface, usually at the water-gas interface.^{71,72} MD simulations on methane hydrate formation indicates that due to the low solubility of methane in water, a significant concentration gradient for either phase exists at the interface, thus, initial hydrate preferentially occurs at the water–methane interface.⁷²

Four models of hydrate nucleation have been established from molecular dynamic simulations: the labile model, the local structuring nucleation, the interfacial nucleation and the “blob mechanism”.³⁶

The labile model, developed by Sloan *et al.*⁷⁵ in 1991 and extended by Christiansen *et al.*⁷⁶ in 1994 focuses on hydrate formation from pure water. The hypothesis of this model is based on the presence of transient, labile ring structures of pure water molecules without guest. These rings arrange as pentamers or hexamers. When these water structures are in contact with guest dissolved molecules, they would immediately form labile cluster – approximating 5¹² cages – which would grow, and agglomerate into nuclei to initiate the subsequent growth.

An alternative to this model is the local structuring theory, which assumes that nucleation is initiated by dissolved guest molecules.^{72,73} In this model, thermal fluctuations cause a local organization of the guest molecules that induces the structuring of the water molecules around them. When the number of ordered guest molecules is sufficiently large, the host-guest clusters will rearrange and trigger the crystallization of the hydrate.

The interfacial nucleation model is based on the nucleation from the gas side of the gas-water interface.^{74,75} In this model, four steps characterize cluster formation. First, the transport of gas molecules to the interface and their adsorption onto the interface. Then, the migration of the adsorbed gas molecules to suitable locations where water molecules would trap the gas and form partial or complete cages. Finally, the addition of more gas and water molecules to join the formation of the cavities until critical nuclei form and grow.

The most recent model is probably the “blob mechanism”, developed by Jacobson *et al.*, describes a multiple hydrate crystallization process (**Figure 8**).⁷⁶ A blob is a gas-rich amorphous reversible precursor within which amorphous hydrate cages form and dissolve continuously until a cluster of cages reaches a critical size. It is thus a two-step nucleation mechanism, with the formation of amorphous and metastable nuclei, and the crystallization of the hydrate.

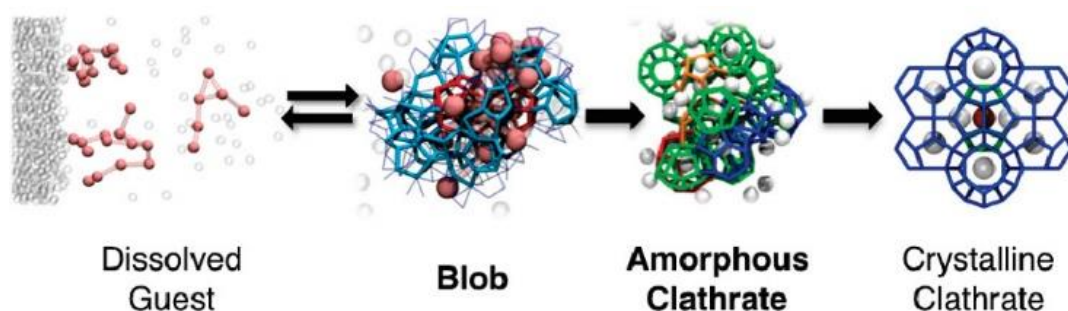


Figure 8. Schematic of the "blob" formation mechanism proposed by Jacobson *et al.*⁷⁶.

Once the hydrate nuclei is formed, the growth process begins. This stage consists of a significant incorporation of molecular species (gas and/or water) into the hydrate phase and the agglomeration of the growing particles.⁶² The growth of gas hydrates is also considered as a complex interfacial phenomenon, which involves a multi-phase distribution (water, gas and hydrate) at several levels (molecular and macroscopic scale).⁶¹ The growth of hydrate may be detected macroscopically either from pressure and temperature measurements (i.e. gas consumption is directly proportional to the pressure drop during hydrate growth) allowing the measurement of its rate of gas consumption, or by other techniques allowing direct visualization of the hydrate layer properties (thickness, morphology, structure, etc.). The growth of hydrates is governed by three major controlling mechanisms or their combination: the intrinsic growth kinetics, at the hydrate surface; the mass transfer of water and gas molecules to the growing surface; the limited heat transfer of hydrate formation. Numerous models, at the microscopic scale, have been developed to describe hydrate growth phenomenon and are detailed in the two major reviews of Yin *et al.*⁶⁰ and Ke *et al.*⁶². The models developed depend on the experimental conditions (type of hydrate, type of reactor, type of formation technique), the technique used to quantify the rate of hydrate formation (p or T measurement, gas saturation, thickness of the hydrate layer, etc...) and the type of growth model chosen (thermodynamic, surface phenomenon, molecular diffusion, etc.).^{60,62} Thus, there is no universal model and the models developed are far too numerous to be detailed in this manuscript. A summary of hydrate growth models is detailed in Yin *et al.*⁶⁰. The majority of these models consider a growth of hydrate from liquid water.

Models of hydrate kinetics formation from ice have also been developed over the past two decades.⁷⁷⁻⁸² Formation from ice and more precisely from ice powders or particles has an advantage over liquid water. First of all, ice surface is known as a nucleator of hydrate as it provides a much greater concentration of heterogeneous nucleation sites compared to microscopic impurities in bulk water.⁸³ Moreover, from a practical point of view, the ice surface

can be more easily quantified than the water-gas interface in a model. The formation of hydrate from ice is also "facilitated" because of the greater stability of hydrogen bonds compared to liquid water; this leads to kinetics different from those obtained from liquid water.⁸⁴ Furthermore, it is generally accepted that at temperatures close to the melting point of ice, a layer of quasi-liquid water (QLL) is found on the surface of the ice⁸⁵, making possible the adsorption of molecules like nitrogen⁸⁶ or alkanes⁸⁷ similar to that which occurs on the surface of liquid water. The Shrinking Core Model (SCM) has been developed to describe the growth of hydrate from ice particles or water droplet.^{77,78} In this model, individual ice particles or droplets behave as independent gas hydrate reactor, guest molecules react at the ice particle surface to form an outer hydrate shell. The formation of additional hydrates requires the diffusion of guest molecules through the existing hydrate shell, the hydrate kinetics is then limited by the diffusion. Alternatives to this model have been developed. Falenty *et al.* proposed an improvement by considering the non-spatially uniform formation of hydrate layers (i.e. presence of patches of hydrate) around ice particles limited either by clathration reaction itself or by gas/water mass transfer through the hydrate shells.⁸¹ Staykova *et al.* developed another model taking into account that the kinetics could be controlled either by the diffusion of molecular species through the hydrate layer or by the kinetics of the clathration reaction, depending on the corresponding formation steps.⁷⁹ This model has been extended and improved by Kuhs *et al.* to study the kinetics of methane hydrate formation from polydisperse spherical ice particles.⁸⁰ It takes into account the size of the particles, and the effect on the rate of conversion of ice to hydrate. The Johnson-Mehl-Avrami-Kolmogorov (JMAK) equation, commonly named the Avrami equation^{88,89}, was used by Susilo *et al.*⁹⁰ to fit the data corresponding to the fast hydrate growth phase and the SCM developed by Henning *et al.*⁷⁷ for the diffusion-controlled growth phase. All these studies have confirmed the applicability of an SCM to describe the growth rate of gas hydrates under a regime controlled by mass transfer.

c. Cage occupancy

Gas hydrates are non-stoichiometric compounds that can be stable even with a few vacant cages: to stabilize the hydrate, a sufficient number of its cages must be occupied. However, in 2014, a new ice structure (so-called ice XVI) were obtained by removing all guests molecules from a structure sII neon hydrate.⁸² This structure exhibits negative thermal expansion and is more stable than the filled hydrate. It is the first observation of a metastable empty water-based hydrate. Thus, the composition of a hydrate can varies. The ratio of water molecules to guest molecules varies from one guest molecule to another, but also according to the conditions of

formation (P-T) of the hydrate. In addition, a hydrate can be either pure (a single guest species) or mixed (several guest species).

The structure formed from a given guest molecule will depend mainly on the steric hindrance. Indeed, the Van Der Waals diameter of the guest molecule will determine the preferential occupation of one or more types of cages (**Figure 9**). All molecules with a diameter between 3.8 Å (e.g. diameter of Argon) and 6.5 Å (e.g. diameter of cyclobutane) will be able to participate in the formation of a hydrate structure sI and structure sII.⁹¹ On the other hand, certain molecules only fit into one type of cage. It is notably the case of propane and iso-butane, which fit only in the LCs $5^{12}6^4$ of structure sII.³ Small molecules such as argon, krypton, oxygen and nitrogen will also favor the formation of structure sII not only because of the large number of SCs (16) that constitute the cubic unit cell allowing a better stability^{92,93} (as a reminder, the structure sI contains only 2 SCs), but also because of a multiple cage occupant (i.e. more than one guest molecule per cage) that is possible in the LCs.³⁶ Moreover, some gases are able to form several types of structures (sI, sII, sH), but these will be stable under different p, T conditions.

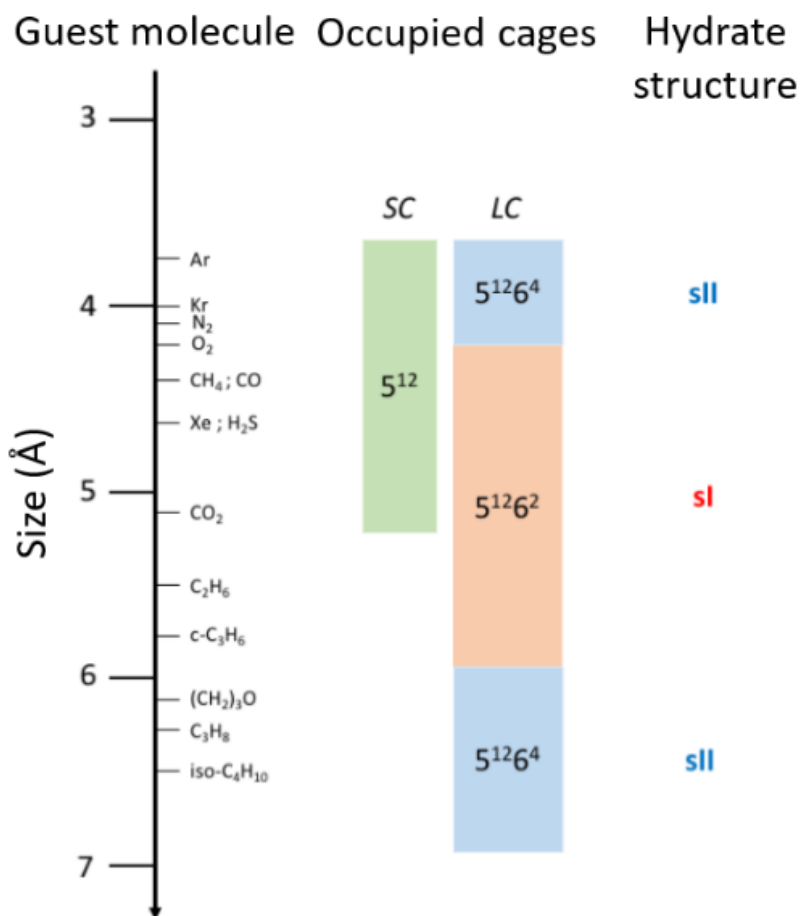


Figure 9. Diagram relating the size of the guest molecule with the type of cage it occupies. Considering pure hydrates, the preferred structure formed for each species is shown on the right. (From Métais *et al.*⁹⁴, adapted from Sloan *et al.*³).

The formation of mixed hydrates from gas mixtures makes more complex the determination of the formed structure, for which molecular selectivity comes into play. The molecular selectivity is the preferential encapsulation of one molecule over another or of one type of cage over another. In particular, the example of the CH₄-C₂H₆-C₃H₈ mixture can be used to understand the effect of steric hindrance on molecular selectivity. The molecular diameters of methane, ethane and propane are respectively: 4.36 Å, 5.5 Å and 6.28 Å. ¹³C NMR experiments⁹⁵ allowed the evidence of the occupation of the LCs of structure sII by the three types of gas whereas the SCs are filled exclusively with methane at 90%. Raman spectroscopy experiments on this same mixture have also shown a preferential enclathration of these gas species: CH₄ < C₂H₆ < C₃H₈ in the 5¹²6⁴ cages.^{95,96} Moreover, during the formation of the mixed hydrate, Kumar *et al.* reported an increase in the amount of methane in the gas phase and

showed an increase in the equilibrium pressure, thus reducing the driving force, which turns in reducing the rate of hydrate growth.⁹⁵

Consequently, it is important to note that the composition of the gas influences the occupation of the cages, and thus the structure of the hydrate formed.

II. NATURAL GAS HYDRATES.

a. Occurrence, gas origin and challenges

Natural gas hydrates are found in the permafrost regions and the continental margins where the the pressure and temperature conditions are favorable to ensure their stability.^{3,97,98} They accumulate in sediment that contains or is supplied by natural gases. **Figure 10** shows the worldwide gas hydrate distribution according to the U.S. Geological Survey.⁹⁹ One can clearly see that the hydrate deposit distributions all along the continental margins, representing around 97 % of the total natural hydrate reservoirs on Earth.¹⁰⁰ Methane-rich hydrates are mostly encountered deposits, and only 10 % of the natural gas hydrates are constituted with other small gas molecules (ethane, propane, H₂S, CO₂, N₂...) and larger hydrocarbons (butane, iso-pentane...).^{4,20}

Thus, the hydrate-bound gases are composed of light hydrocarbons and other low-molecular weight composed such as carbon dioxide. The natural gases are either of microbial or thermogenic origin. Microbial gases are generated at low temperature (e.g., low sedimentary depth) from a biogeochemical process, and consist of mainly methane. Thermogenic gases are the results of thermal cracking of organic matter at depth.²²⁻²⁵

Besides methane, heavier hydrocarbons such as ethane or propane are also present in thermogenic gas sources.^{101,102}

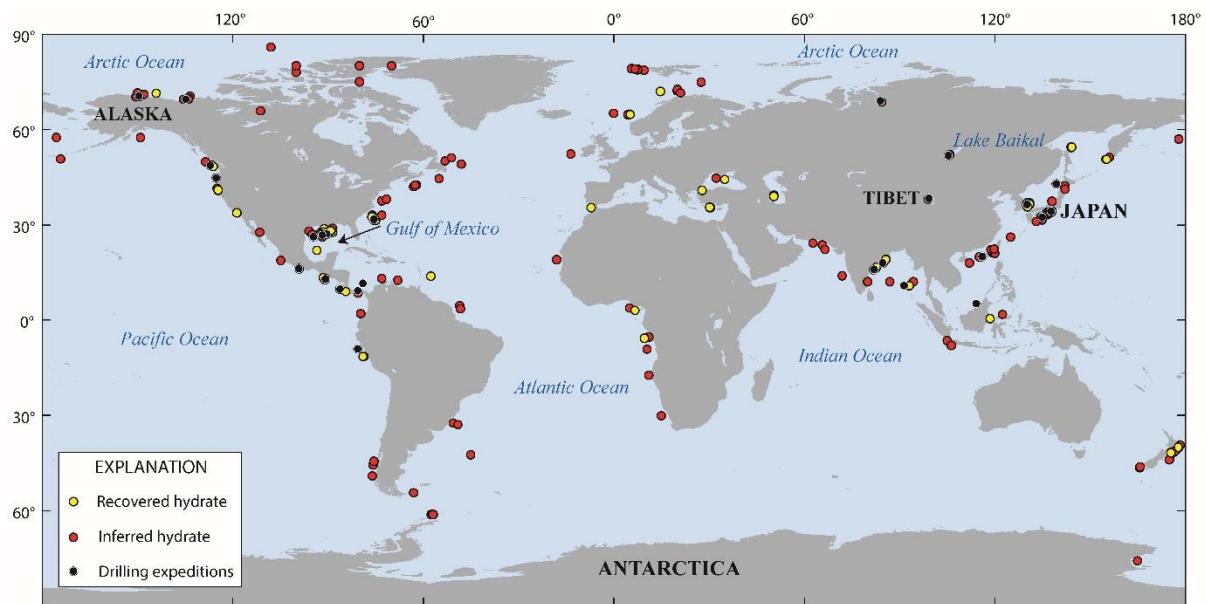


Figure 10. Map of the distribution of onshore natural gas hydrates, showing deposits where hydrates have been recovered (yellow), where gas hydrates are suspected based on seismic data (red), where drilling expeditions have been conducted in permafrost or deep marine environments leading to the recovery of gas hydrates (black).⁹⁹

Natural gas hydrate deposits represent one of the largest methane reservoirs on Earth⁹, and one volume of hydrate could contain 160 to 180 volumes of gas under standard conditions of temperature and pressure.¹⁰³ Recent estimates of methane bound in hydrates range between $[600-3000] \times 10^3$ Tg of CH₄.^{6,104} The IPCC report (2013) estimated that 600 to 10 000 billion tons of methane are trapped for millennia to millions of years in the world's deposits.¹⁰⁵ Thus, due to the huge amount of methane trapped, natural gas hydrates constitute both an energy and environmental threats. Due to the world energy demand, numerous research groups around the world are working to develop innovative methods to produce methane from hydrate deposits, notably based on thermal stimulation, depressurization, injection of chemical inhibitors or gas exchange processes such as CH₄ shifted to CO₂.^{100,106-108} Besides, most of the hydrate deposits are located on the continental margins, where their accumulation within the marine sediment modified the morphology of the seafloor, leading to the development of pockmarks, the build-up of carbonates or the occurrence of gassy sediments. All these geological features change the mechanical properties of the seafloor and can trigger seafloor instabilities. Accordingly, natural gas hydrates can be seen as a geohazard.¹⁰⁹⁻¹¹² Marine hydrate deposits are often associated with the discharge of free and dissolved gas into the water column; most of the discharge is oxidized or dissolved away in the water masses, potentially causing local ocean acidification, whereas the remains portion may enter into the atmosphere.¹¹² Thus, although climate change

may threaten some shallow hydrate deposits, the resulting release gases may contribute to the climate positive feedbacks. The aforementioned examples illustrate that, beside the scientific interests for natural gas hydrates, natural gas hydrates represent both a societal issue considering their potential environmental impacts and their geohazard features, and a possibility to meet the world energy (by recovering this unexploited natural gas reservoir) demand in the future for several countries.¹¹³

Addressed questions of this work: It is necessary to understand the formation of natural gas hydrate, their role in the deep carbon cycle and their gas storage capacity. This work is applied to two hydrate deposits located in the Sea of Marmara where thermogenic hydrates have been recovered on the Western High, and in the Romanian sector of the Black Sea characterized by microbial methane hydrates.

b. The Black Sea case

The Black Sea is a land-locked basin of ca 432.000 km², connected to the Sea of Marmara by the Bosphorus Strait (**Figure 11**). It represents the largest methane-rich and anoxic water body on Earth characterized by widespread gas emissions from the shelf to the deep basin^{114–117} and has huge energy resources.^{118,119} The Black Sea basin is also characterized by an accumulation of a significant amount of sediments constituting a thickness of ~19 km at its northwestern margin since the Late Cretaceous (~ 99.6 Ma–65.5 Ma Before Present (BP)).¹²⁰ Black Sea sediments have an average mineralogical composition of 60–65 % clay (predominantly illite), 35 % quartz and feldspars and 5 % calcium carbonate.¹²¹

In the Romanian sector, gas hydrates have been inferred from seismic surveys^{13,122–124}, and recovered for the first time¹²⁵ during the GHASS¹²⁶ cruise in 2015 in the Danube fan, located in the western part of the Black Sea. In the Black Sea, the upper limit of the hydrate stability zone is at a water depth of around 700 m, corresponding to a pressure close to 70 bar, and a water temperature of about 9 °C.¹²⁷ During the GHASS2¹²¹ cruise in 2021 (in which I participated for recovering natural gas hydrates), a large amount of hydrate samples have been collected and stored in liquid nitrogen for onshore analyses. Gas hydrates collected in clay-rich sediments, are mainly methane hydrates. They contained >99% of microbial methane.

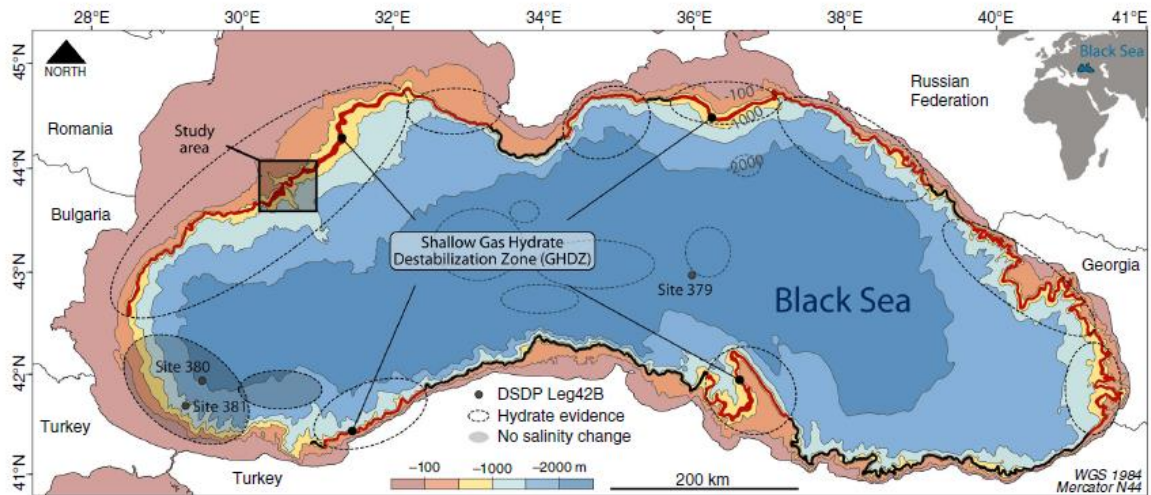


Figure 11. Bathymetric map of the Black Sea with the delimitation of Gas Hydrate Destabilization Zone (GHDZ) where gas hydrate are expected to decompose due to salinity diffusion through the sediment. (From Riboulot *et al.*¹⁰).

The recent geological history is characterized by its reconnection to the Marmara Sea, and thus indirectly to the Atlantic Ocean. Indeed, during the late Quaternary Period, the Black Sea was disconnected from the world oceans.¹²⁸ This geological event caused a general drop in sea level (-100 to -150 m compared to the actual level) as well as a drop in average temperatures (4 °C).¹³ The water salinity was affected by this lake environment, and dropped to 2 mg/L until the reconnection via the Bosphorus Strait, where water salinity increased again to 22 mg/L and remained stable for the last 2500 years of the reconnection.^{10,128}

Addressed questions in this work: Analyses carried out in the Black Sea, currently indicate the dissociation of methane hydrates, showing in particular the decrease of the hydrate stability zone during the next years (Figure 12).¹⁰ In this work, interest is focused on the influence of the sediment mineralogy on the formation and dissociation mechanisms, distribution of methane hydrates, with the aims of providing elements of answer on the hydrate formation, and dissociation processes in the Black Sea.

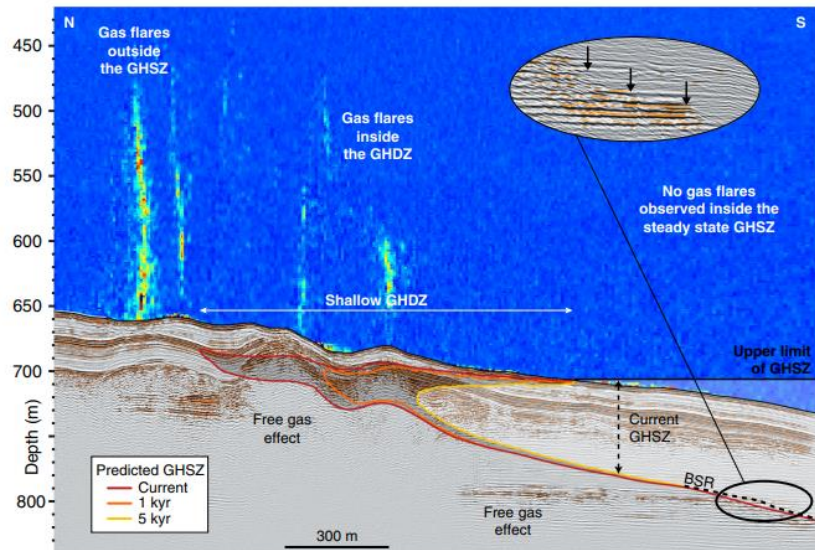


Figure 12. GHSZ on the Romanian sector of Black Sea and the location of the gas flares outside the current GHSZ. The colored lines simulate the model-predicted evolution of the GHSZ at two different time steps. (From Riboulot *et al.*¹⁰)

c. The Sea of Marmara case

The Marmara Sea is located in the Turkish territory and connects the Mediterranean Sea and the Black Sea. It covers an area of about 11,000 km², it is made of four deep basins (Tekirdag Basin, Central Basin, Kumburgaz Basin and Çınarcik Basin) separated by two pressure highs (Western High and Central High) (**Figure 13**). The Sea of Marmara is crossed lengthwise by the North Anatolian Fault (NAF), which corresponds to one of the most dangerous seismically-active faults on Earth.

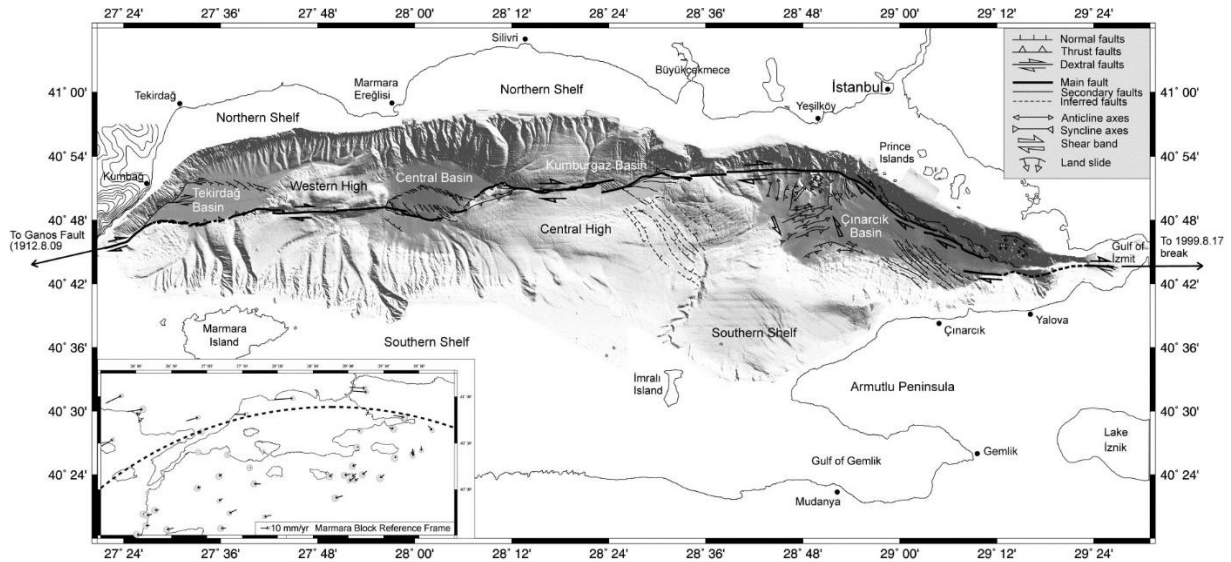


Figure 13. Bathymetric map of the Sea of Marmara showing the tectonic framework. NAF: North Anatolian Fault. (From Le Pichon *et al.*^{129,130})

It has been shown that the North Anatolian Fault and its inherited fault network correspond to the main pathway for the migration and mixing of fluids before their emission into the seafloor.^{131–133} In recent years, gas emissions from the seafloor into the water column of the Sea of Marmara have been investigated.^{134–136} During the MARNAUT¹³⁷ cruise in May–June 2007, the Western High area was explored. Gas bubbles were collected and analyzed to determine their molecular and isotopic compositions. The released gases were characterized by gas chromatography and the isotopic analyses were focused on the determination of the stable carbon ($\delta^{13}\text{C}$) isotope ratios. The studies revealed a complex thermogenic gas containing a large part of none-methane hydrocarbons. Thermogenic gas hydrates were also collected at the same location. The gas hydrates are supplied by gases coming from the hydrocarbon reservoirs of the Thrace Basin.¹³⁴ The encapsulated gas in the hydrates were analyzed and presented a isotopic composition similar to that of the gas bubbles collected in the area (**Table 1**).²⁶ However, their molecular composition are different from each other due to the fractionation processes that occur during complex thermogenic gas-hydrate formation. Indeed, the hydrate formation in presence of thermogenic gas mixture is a selective mechanism, which conducts to a preferential encapsulation of some gas molecules in the hydrate phase.⁴⁴

Component	Western High Gas Bubbles		Western High Gas hydrate	
	Composition (%)	$\delta^{13}\text{C}$ (‰ PDB)	Composition (%)	$\delta^{13}\text{C}$ (‰ PDB)
CH ₄	90.90	-44.4	66.10	-44.1
C ₂	1.23	-25.7	1.23	-23.4
C ₃	2.50	-21.1	18	-21.8
i-C ₄	0.93	-28	8	-27.6
n-C ₄	0.15	-20.1	9.50	-22.9
neo-C ₅	0.0034	-	0.19	-25.6
i-C ₅	0.31	-25.3	0.048	-25.7
n-C ₅	0.010	-18.9	0.0002	-
C ₆₊	0.0017	-	0.041	-
N ₂	0	-	0	-
CO ₂	3.90	29.1	4.0	-25.6
C ₁ /(C ₂ +C ₃)	24.4	-	3.3	-

Table 1. Molecular and isotopic composition of gas bubbles and gas hydrate collected in Marmara Sea. (Adapted from Bourry *et al.*²⁶)

The variation of the molecular composition of the gas released as gas bubbles and encapsulated in gas hydrates is puzzling and required an in-depth study to understand the parameters governing the gas selectivity during hydrate formation. UV-Raman spectroscopy was used to investigate natural gas hydrate from the Western High.²⁶ The vibrational signatures observed at ~ 2903 and $\sim 2913 \text{ cm}^{-1}$ are characteristic of methane hydrate that crystallizes in the structure sII. Similarly, the C₂, C₃, i-C₄ and CO₂ gas species were found to be co-clathrated with methane in structure sII (**Figure 14**).

Addressed questions of this work: In the present work, High-resolution Raman spectroscopy will be employed to disclose information about the hydrate structures formed from the different gas species encountered in the complex thermogenic gas (see chapter 3). These results will allow the comparison of the vibrational signatures of natural gas hydrates and synthetic gas hydrates formed from the natural gas mixture (collected during the scientific cruise) in order to determine the structures adopted.

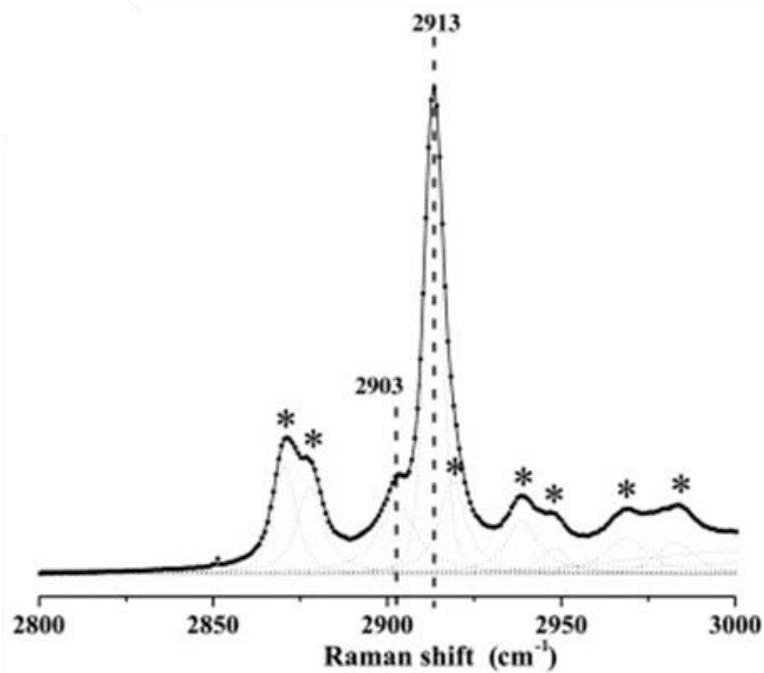


Figure 14. Raman C–H stretching signatures of natural gas hydrate (133 K and 1 bar). The bands at ~ 2903 and $\sim 2913 \text{ cm}^{-1}$ are attributed to CH_4 encapsulated in the large cages ($5^{12}6^4$) and small cages (5^{12}) of the sII hydrate. The bands attributed to C–H stretching modes of C_2H_6 , C_3H_8 and $i\text{-C}_4\text{H}_{10}$ are marked by asterisk (Adapted from Bourry *et al.*²⁶)

III. FORMATION IN SEDIMENTS.

Natural gas hydrates can be located on the uppermost layer of the permafrost or embedded in clay-rich marine sediments. These sediments can be of different nature, size and composition depending on the region where they are found and their origin. Their physicochemical properties can have an impact on the stability conditions of gas hydrates, their formation mechanisms and their distribution, from the micrometer to the geological scale. The objective of this section is to detail the characteristics of marine sediments on continental margins and to review the state of the art of studies concerning the impacts of sediments on gas hydrates.

a. Natural sediments

i. Chemical and structural properties

Sediment build-up in marine environment results from the deposition of granular materials in suspension in the water column. These particles have two major origins. They can be either created *in-situ* from the precipitation of dissolved chemicals by biogenic means or because of biological activity or they are carried out to the ocean in solid form.¹³⁸ They are mainly characterized by their particle size distribution, chemical composition, mineralogy, origin, deposition rate and geographic distribution.

Grain diameter is used to classify sediments according to Udden-Wentworth grain-size scale.^{139,140} This size classification scheme only takes into account the diameter of the particles and does not reveal any information regarding the mineral composition of the particles. The particles are classified as clay, silt, sand, and larger particle size (**Table 2**). Most sedimentary particles are of the size of sand, silt, or clay. Sand particles are characterized by a size ranging between 63 μm and 2 mm. In addition, the Udden-Wentworth scale distinguishes fine sand from medium to coarse grain. Generally speaking, sand is considered as fine when the size of its grains is lower than 250 μm . Between sand and clays, we find the silts with a particle size ranging from 2 to 63 μm . Clays are the finest sediment particles with a grain size of less than 2 μm .

Millimeters (mm)	Micrometers (μm)	Phi (ϕ)	Wentworth size class	Rock type
4096		-12.0	Boulder	Conglomerate/ Breccia
256		-8.0	Cobble	
64		-6.0	Pebble	
4		-2.0	Granule	
2.00		-1.0	Very coarse sand	
1.00		0.0	Coarse sand	Sandstone
1/2	0.50	1.0	Medium sand	
1/4	0.25	2.0	Fine sand	
1/8	0.125	3.0	Very fine sand	
1/16	0.0625	4.0	Coarse silt	
1/32	0.031	5.0	Medium silt	Siltstone
1/64	0.0156	6.0	Fine silt	
1/128	0.0078	7.0	Very fine silt	
1/256	0.0039	8.0	Clay	
0.00006	0.06	14.0		Claystone

Table 2. Size scale of natural sediments according to the Udden-Wentworth classification (From Gallagher *et al.*¹⁴¹ after Wentworth¹⁴⁰)

The sediment can be described according to its mineralogy. The most common minerals in marine sediments are silicates in which Si and O form a repeating tetrahedral basic unit. Other common minerals in marine sediments are carbonates and sulfates.

The crystalline unit of silicates is a tetrahedron that has an O^{2-} anion at each of its four corners and a Si^{4+} cation in the center. According to the arrangement of the silicate tetrahedra, a variety of crystalline silicate minerals arises. The phyllosilicates (clay minerals) are constituted of silica sheets and tectosilicates (as quartz and feldspar) are constituted of silicates three-dimensional silica framework where every corner O^{2-} anion is shared by an adjacent silicate tetrahedron.

Granite constitutes a large proportion of earth's crust and is largely composed of oxygen atoms held together with silicon and aluminum atoms. These atoms are organized in two main mineral types, quartz and feldspar. The alteration of these granitic rocks due to the action of water transport and other agents, transforms quartz into sand and feldspar into clay.

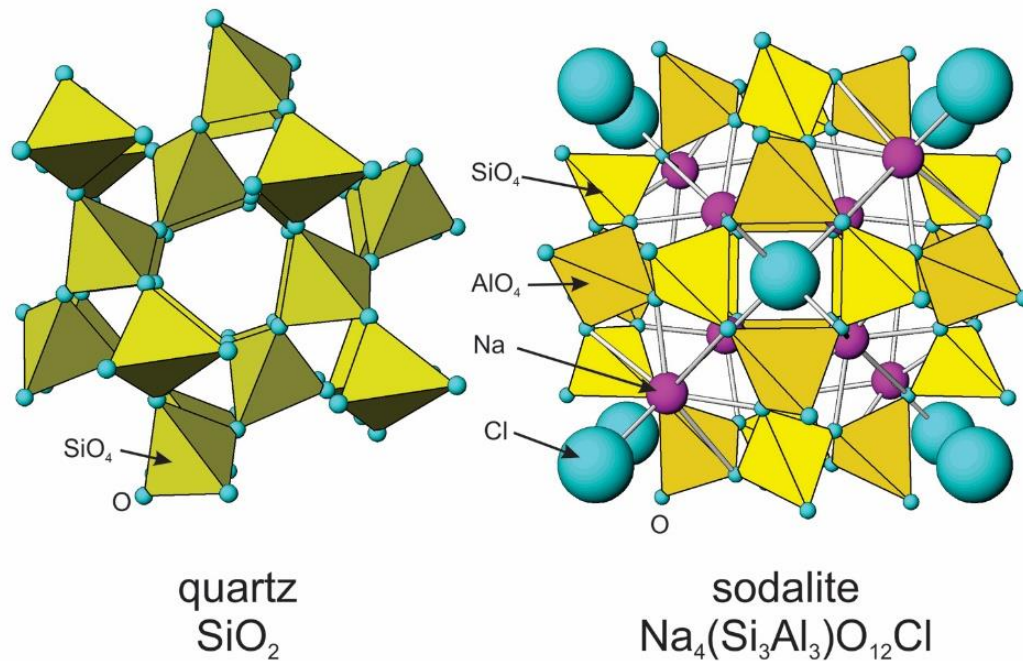


Figure 15. Mineral structure of quartz (SiO_2) and feldspar (Sodalite). (From Perkins¹⁴²)

Quartz has a three-dimensional crystalline structure composed of silicon and oxygen atoms (SiO_2) described in **Figure 15**. The weathering of quartz results in the formation of sand grains characterized by a chemical composition close to quartz, which can be mixed with a small amount of micas and feldspars of potassium. There are several varieties of sands: the black sands composed of volcanic minerals like olivine ($(\text{Mg,Fe})_2\text{SiO}_4$) or pyroxene ($(\text{Mg,Fe})_2\text{Si}_2\text{O}_6$), and pink to white sands composed mainly of calcite (CaCO_3), which is derived from the alteration of mollusks and corals, and feldspars. The distribution of the size of the grains of a sand is rather wide since it varies from $63\ \mu\text{m}$ to $2\ \text{mm}$. In natural sands, this change in grain size is accompanied by a change in the mineral composition of the sand.¹⁴³ Although quartz remains the majority compound regardless of the size of the sand grains, the quartz content decreases with decreasing grain size, which implies that the proportion of mineral impurities increases.

Feldspars are the most abundant mineral group in the Earth's crust. They are aluminosilicate minerals with a structure composed of corner-sharing AlO_4 and SiO_4 tetrahedra linked in an infinite three-dimensional arrangement (**Figure 16**). The general chemical formula of feldspars is MT_4O_8 , where T is Al and Si, M is a cation that occupies the large irregular cavities in the tetrahedral framework. It can be Na and/or K for alkali feldspars [$(\text{K,Na})\text{AlSi}_3\text{O}_8$] (ex. Sodalite **Figure 15**) or Ca for plagioclase ($\text{CaAl}_2\text{SiO}_8$).

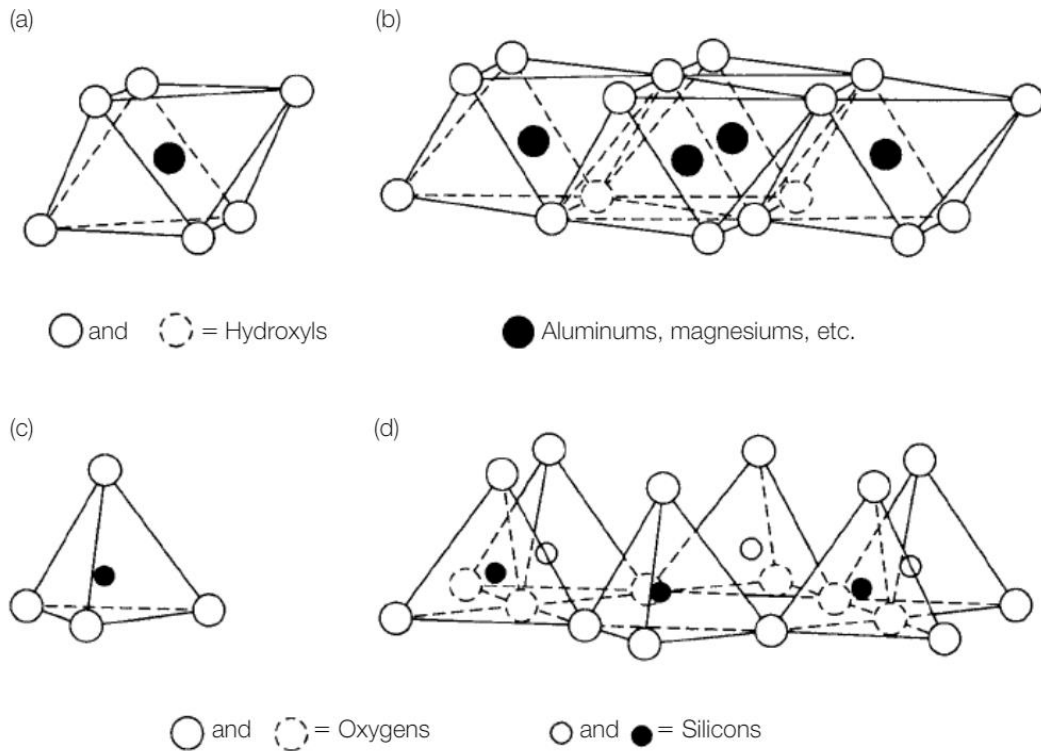


Figure 16. Structural arrangement and composition of octahedral sheet (top) and tetrahedral sheet (bottom) of clay minerals.¹³⁸

Clay minerals are the most abundant phyllosilicates. They participate in several biogeochemical processes.^{144–146} For example, the chemical alteration reactions responsible for their formation are accompanied by the absorption and release of cations that contribute to the long-term control of the pH of seawater and, consequently, to the regulation of CO₂ levels in the atmosphere.¹⁴⁷ The most abundant clay minerals are illite, kaolinite, montmorillonite and chlorite and their distributions in marine sediments are spatially variable. Clays are crystalline materials consisting of planes of atoms arranged in silicate layers. The composition and structure of the layers is used to classify clay mineral. Two types of aluminosilicate sheets constitute clay layers, the tetrahedral and octahedral sheets. The tetrahedral sheets are built up from the assembly of tetrahedra where the silicon atoms are surrounded by four oxygen atoms. The silicon atom shares its three oxygen atoms with adjacent tetrahedra to form a continuous tetrahedral sheet. The unshared oxygen atoms all point in the same direction. Hence, one side of the tetrahedral sheet consists of a hexagonal mesh of shared oxygens and the other side is formed by the remaining oxygen atoms, called "apical" oxygen (**Figure 16.c and Figure 16.d**). The octahedral sheet is built up from two planes of close packed oxygens and/or hydroxyls. In the center of such a sheet, and adjacent to every anion, there are three octahedral sites, which

may be occupied by cations such as aluminum, iron and magnesium, each cation being surrounded by six anions (**Figure 16.a and Figure 16.b**).

The modular assembly of these two types of sheets classify phyllosilicate clay minerals in two categories, the 1:1 layer and the 2:1 layer. The 1:1 layer constitute the kaolin-serpentine group where clay layers are composed of one tetrahedral sheet with one octahedral sheet. Layers are uncharged and the bonding between them is ensure by hydrogen bonding involving hydrogen atoms of one layer and the basal oxygen atoms of the adjacent layer.¹⁴⁸ Kaolinite clay is part of this group and is the simplest marine clay minerals with a chemical composition of $\text{Al}_2\text{Si}_2\text{O}_5(\text{OH})_4$ (**Figure 17**). The spacing between two layers, which corresponds to the 001 X-ray diffraction peak, is 7.2 Å.¹⁴⁹ Kaolinitite is characterized by a low water adsorption-ability, which classifies kaolinite as a non-swelling clay mineral.¹⁵⁰

The 2:1 clay layers are constituted of an octahedral sheet sandwiched between two tetrahedral sheets. This group includes micas, smectites and vermiculites; and the properties of the clay, the charge of the layers and the nature of the bonding between them depends on the type of clays.

Illite is part of the mica group (**Figure 17**). It can be identified by X-ray diffraction with a spacing of 10 Å between two layers corresponding to its (001) Bragg peak. The general chemical composition of illite clay is $(\text{K,H})\text{Al}_2(\text{Si,Al})_4\text{O}_{10}(\text{OH})_{2-x}\text{H}_2\text{O}$, where x represents a variable amount of water. The substitution of Al^{3+} for Si^{4+} in every fourth tetrahedral site and (Mg, Fe^{2+}) for Al in the octahedral sheet result in an excess of negative charge per formula unit. The negative charge is balanced by nonexchangeable potassium cation K^+ that reside on interlayer sites between the 2:1 layers. The interlayer cation forms a strong bond between adjoining tetrahedral sheets and limits expansion of the mineral. Like kaolinite, illite is a non-swelling clay mineral.

Montmorillonite is a 2:1 clay mineral part of the smectite group. Its general chemical composition is $X_{0.3 \cdot n}\text{H}_2\text{O} [(\text{Al}_{1.5} \text{Fe}^{3+}_{0.2}\text{Mg}_{0.3})\text{Si}_4\text{O}_{10}(\text{OH})_2]^{0.3}$, where X corresponds to exchangeable cations such as Na^+ and Ca^{2+} , n is the number of interlayer water molecules, which can vary between 1 and 5; Al, Fe, and Mg are the octahedral cations and Si is a tetrahedral cation (**Figure 17**). The tetrahedral substitutions of Al^{3+} for Si^{4+} develop a negative 2:1 layer charge. Interlayer cations, such as Ca^{2+} and Na^+ , compensate the negative charge of the clay. The presence of interlayer cations located between water molecules in the interlayer allows for swelling of the crystal lattice. The spacing between two layers varies from 10 Å under dry

conditions to 20 Å when the mineral is saturated with water. Van der Waals bonds and weak cation-to-oxygen linkages hold the 2:1 layers in montmorillonite together.

Chlorite is a 2:1 clay with a structure consisting of a negatively charged 2:1 layer and a positively charged “interlayer” octahedrally coordinated hydroxide sheet (Figure 17).¹⁵¹

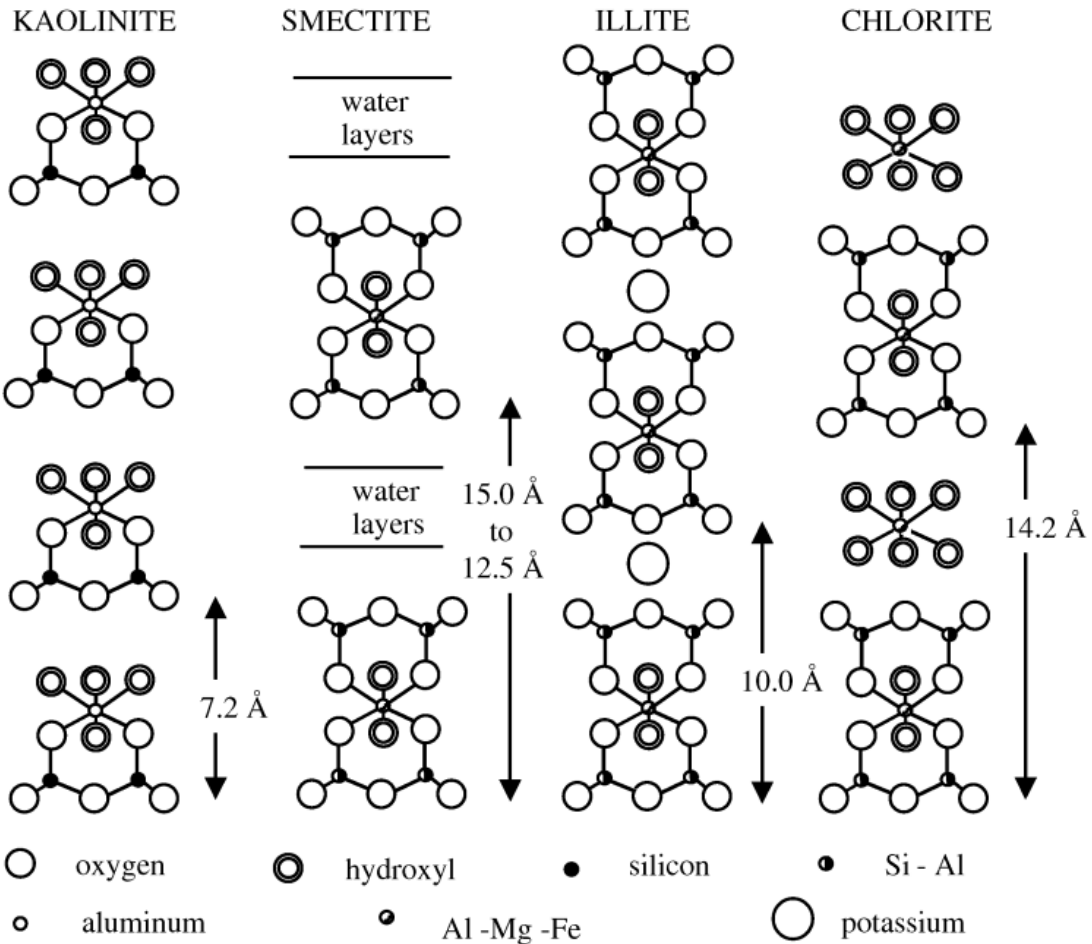


Figure 17. Structural layer arrangement and composition of different clay minerals.¹⁵²

ii. Sedimentary environment of the Black Sea

During the scientific cruise GHASS¹²⁶ in 2015 in the Romanian waters of the Black Sea, GAS-CS14 core was collected at 738 m water depth and 9°C bottom water. The core analysis reveals the presence of small carbonates concretions on the first 10 centimeters followed by methane hydrate pieces at 4.2 m below the seafloor (Figure 18).¹⁵³ Analysis by X-ray diffraction on the sediment gave an average mineralogical composition of 60-65 % clay, 35 % quartz and

feldspars and 5 % calcium carbonate.^{121,154} Illite is the most abundant clay mineral, followed by kaolinite, smectites and chlorite.

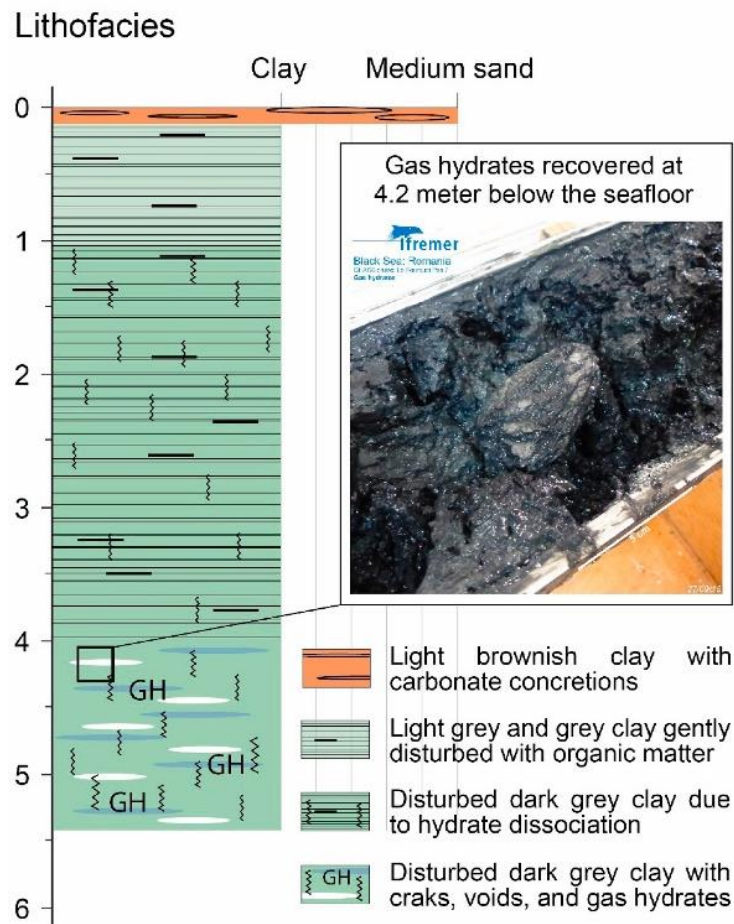


Figure 18. Representation of a typical core collected on the Romanian sector of the Black Sea. Methane hydrate are found in clay-rich sediments. (Adapted from Chazallon *et al.*¹²⁵)

The geochemical analyses of the pore water reveal a pronounced variation in the depth-concentration profiles of the major dissolved elements, indicating the occurrence of reactive-transport processes within sediments (**Figure 19**). Ruffine *et al.*¹⁵⁴ showed the effect of seawater infiltration on the reverse weathering processes involving clays, causing change in their composition.

Sulfate reduction coupled with methane oxidation take place within the first five meters of sediment and cation exchange down to 25 m below the seafloor. The horizon where sulfate is depleted whereas methane increases when moving downwards is called the sulfate-methane transition zone (SMTZ). Cl^- concentration continuously decreases with depth, illustrating the infiltration of seawater to the limnic sediment since the reconnection of the Black to the Sea of

Marmara. Diffusion is the dominant transport process of pore water species at all investigated sites.

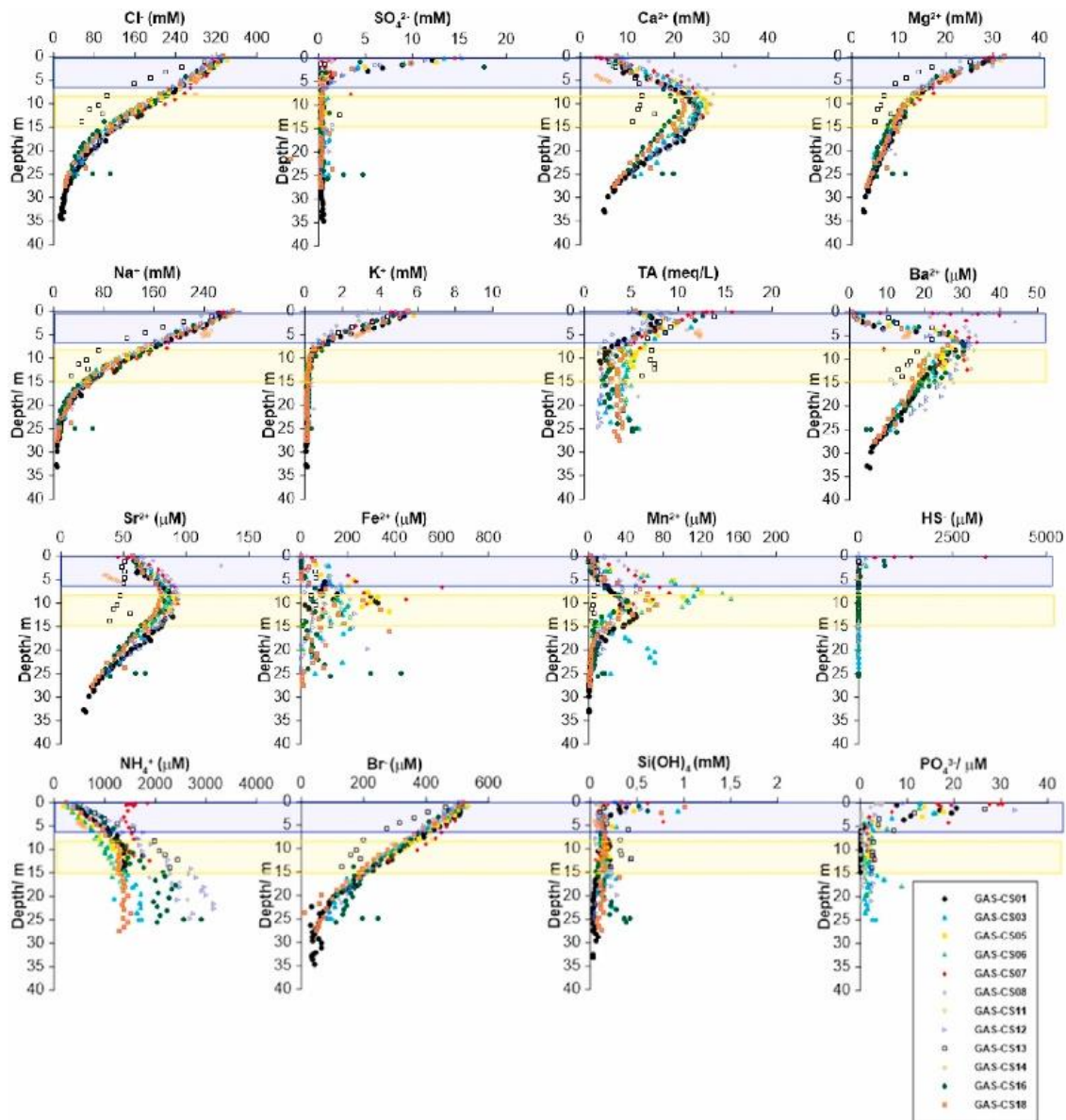


Figure 19. Pore water depth profiles of dissolved ion concentrations in Black Sea. (From Ruffine *et al.*¹⁵⁴)

b. Sedimentary surrogates

In natural environments, methane hydrates are mainly found in fine-grained clay-rich sediments mixed mainly with silica materials like plagioclase, quartz and feldspars.^{155,156} Initially, in order to study the formation of methane hydrates in natural environments, the scientific community

focused on the formation in the presence of amorphous materials or analogous porous materials.^{78,94,157–163}

Some studies dedicated to the investigation of the effect of a sandy environment on the formation of gas hydrates have used the Fontainebleau sand.^{164–167} It is a very polydisperse natural sand with a grain size ranging between 80 and 450 μm , which has the particularity to have a homogeneous composition with 97 to 99 % of silica. Other natural sands, silica powders and silica beads with controlled particle sizes have also been used as surrogates of natural sediments.^{158,161} The use of such systems allows working with homogeneous sediments in composition and/or size while minimizing the chemical interaction between the sediment and water or methane.

However, to get closer to natural porous clay systems, new material emerged resulting in original theoretical and experimental experiments devoted to the study of hydrate formation in porous media. Mesoporous MCM-41¹⁶⁸, activated carbons, carbon nanotubes^{162,169,170} and metal organic frameworks (MOFs)¹⁷¹ were used as nanoporous sedimentary surrogates. All these systems are crystalline nano-porous materials. As an example, microporous, mesoporous and macroporous carbon models with calibrated pore size of 0.2 nm, 10 nm and 25 nm were used to carry out theoretical methane hydrate formation (**Figure 20**).¹⁷² Unlike clays, these materials have a perfectly organized crystal lattice and a well-calibrated pore size distribution, which allows the investigation of hydrate formation in confined nanoporous spaces.

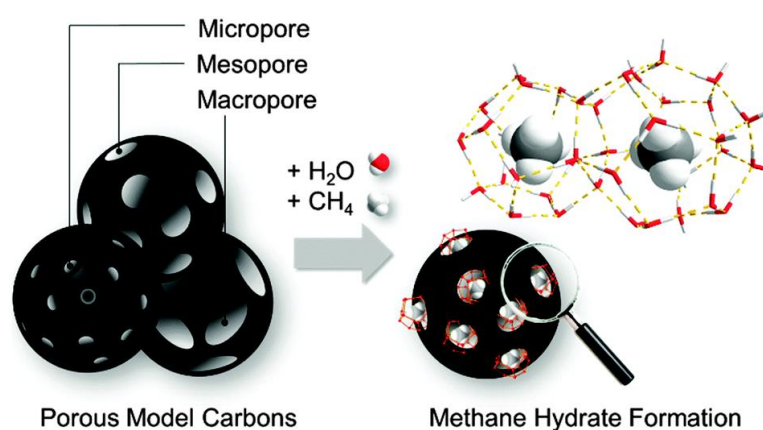


Figure 20. Methane hydrate formation in the confined spaces of porous model carbons covering the range from micro- to meso- and macropores. (From Borchardt *et al.*¹⁷²)

Addressed questions of this work: One of the objectives of this thesis is to better understand the mechanisms of gas hydrate formation in sedimentary environments, particularly in the presence of clays. Illite, kaolinite, montmorillonite and natural Black Sea sediments will constitute the porous media used at the core of the present investigations.

c. Impact of the sedimentary media on hydrate formation

i. Distribution

Natural gas hydrates are distributed in clay-rich sediments with various particle sizes and mineralogical compositions. These sediments, depending on the place where they are found, will present mixtures of different clays types, sand and other minerals in smaller quantities. Hence, the nature and grain size of the sediments will determine how hydrates will occupy this space. The location of hydrates at the pore scale exerts a strong control on the physical properties of hydrate-bearing sediments on a macroscopic scale.

Natural hydrates exhibit three main morphologies: lenses/veins, nodules and disseminated hydrate at the pore scale of sediments (**Figure 21**), resulting in hydrates size ranging from micrometers (interparticle spaces) to several centimeters (veins or nodules in sediments).^{98,100,173} In clay-rich sediments, hydrates are mostly found in the form of veins, lenses or nodules. These two types of morphologies are characterized by a very heterogeneous distribution of gas hydrates within the sedimentary matrix.

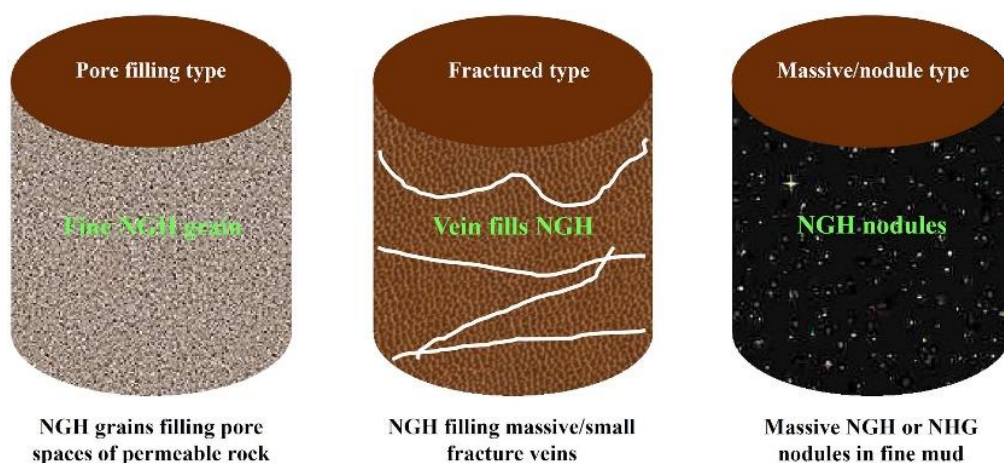


Figure 21. Natural gas hydrate (NGH) reservoir types: pore filling, fractured, and nodules. (From Yang *et al.*¹⁰⁰)

There are four arrangements of hydrate at the pore scale in sediment, referred as “pore habits”: “grain-grain contact cementing”, “mineral coating cementing”, “load-bearing” and “pore-filling” (Figure 22).¹⁷⁴ Pore-filling hydrates form by filling the pores between sediment grains. In this case, the nucleation of the hydrate takes place within the pore fluid within the pore, and it then grows freely in the pore space between the grains, without connecting the particles together. The formation of hydrates in these inter-grain spaces changes the size and geometry of the pores, and thus the inter-granular porosity, which directly affects the fluid flow properties in the latter.⁹⁸ When the hydrate saturation in the pore space reaches 40%, then the pore space becomes naturally load-bearing.¹⁷⁵ Hydrates aggregate to form part of the sediment skeleton and contribute to the mechanical stability of the sediments.^{98,176} When the hydrate concentration in the pore space exceeds 50 %, hydrates form at the intergranular contacts; it refers to cementing.^{176,177} The last pore habit refers to hydrate growing on the surface of grains and enveloping the sand particles, it is the grain-coating habit.¹⁷⁸

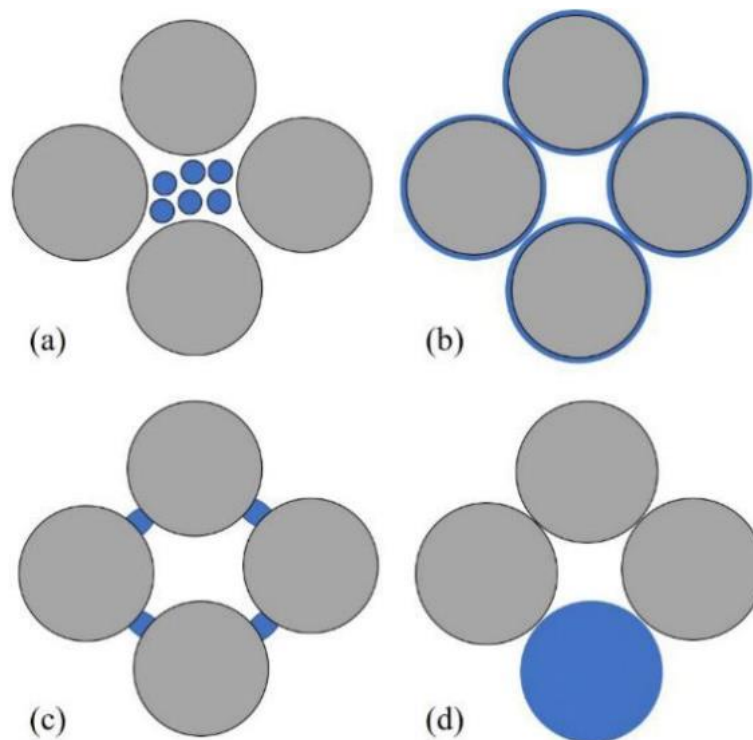


Figure 22. Description of hydrate pore habits. Grey circles represents sand particles and hydrates are represented in blue. (From Lv *et al.*¹⁷⁹)

The composition of the sediment matrix will influence the hydrate morphology. When the concentration of fines in sand increases, the sediment properties can dramatically change as well as the hydrate saturation and pore habit (Figure 23). In coarse sediments in the Nankai Trough and Gulf of Mexico, pore-filling hydrate saturation can exceed 70 %. However, in fine-

grained sediments there is low hydrate saturation and hydrates are typical in the form of lenses and nodules (natural hydrates are found in abundance in fine-grained sediments with a predominantly clay component)^{4,96,180}. Because of their abundance, fine-grained marine sediments collectively contain more gas hydrates than any of the coarse-grained reservoirs, even though the saturation of disseminated gas hydrate in the pore space of fine-grained sediments is generally less than 10 %.⁹⁸

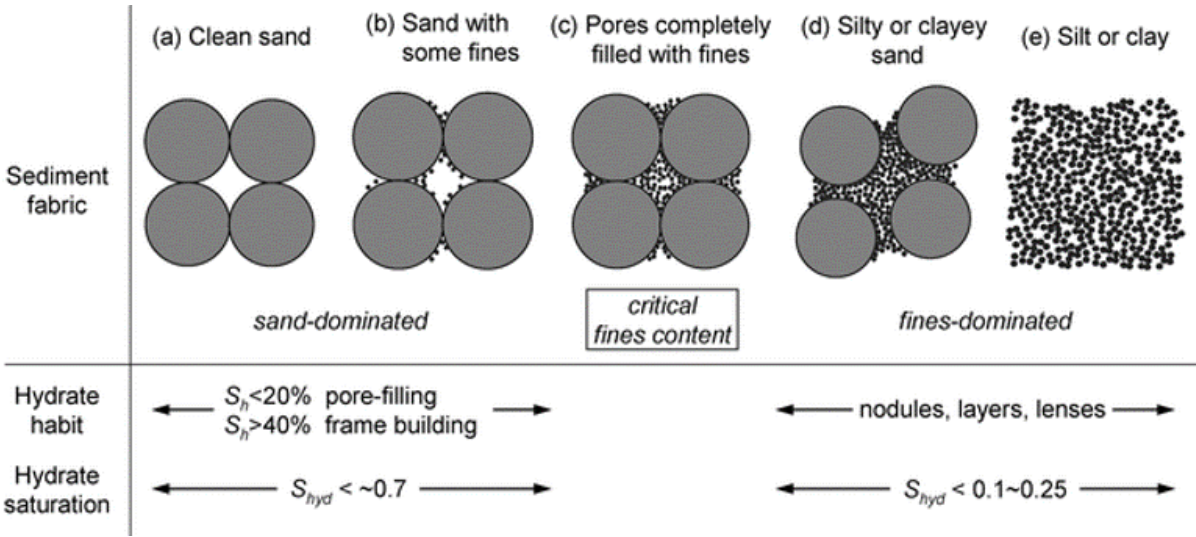


Figure 23. Estimation of hydrate pore habit and saturation of the pore as function of the evolution of the presence of fines in sand (Adapted from Jung *et al.*¹⁸¹).

ii. Thermodynamics

Several studies have been carried out to investigate the influence of the sedimentary environment on the thermodynamic equilibrium of gas hydrate.¹⁸²⁻¹⁸⁶ First, these studies have shown that pore size plays an important role in the thermodynamic equilibrium of hydrates within a sedimentary matrix. In porous media, the different particle sizes result in different pore sizes, which will have a great influence on phase equilibrium conditions mostly due to the capillary effect. According to several studies, coarse-grained sediments, larger than 250 μm , have no effect on the phase equilibrium of hydrates.^{183,184,187} However, in fine-grained sediments ($< 250 \mu\text{m}$), the capillary effect, generated by pores, has an inhibitor effect of the activity of water and improves the solubility of methane gas. Hence, higher pressure or lower temperature is needed to initiate the hydrate formation.¹⁸⁸ Under mesoporous conditions, Zang *et al.* summarized literature data and found that the phase equilibrium conditions required for

the formation of hydrate would shift to the left with a more obvious effect when decreasing particle size (**Figure 24**).¹⁸²

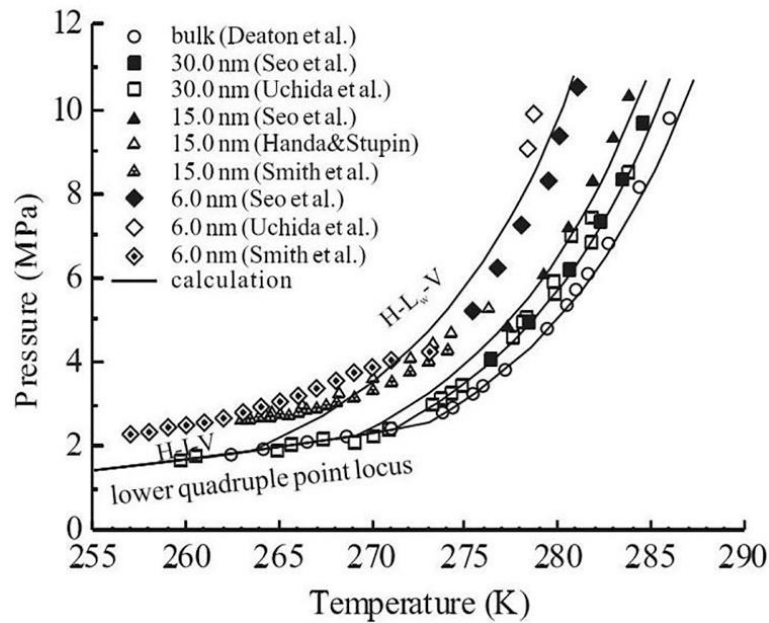


Figure 24. Comparison of experimental and theoretical phase equilibrium for methane hydrates formed in the presence of pure water and in the presence porous media with pore sizes ranging between 6 and 30 nm (From Li *et al.*¹⁸⁵).

Other studies focused on the thermodynamic effect of natural sediments on methane hydrate formation. Experiments on methane hydrate formation were conducted in presence of different concentrations of Krishna-Godavari (KG) sediments at (10, 20, and 35 wt % in the system).¹⁸⁶ These sediments mostly laid in the category of silt, with particle sizes ranging from 0.0039 to 0.0625 mm. The equilibrium conditions obtained were shifted toward the lower temperatures and higher pressures compared to the pure water system.¹⁸⁶ KG basin sediments showed an inhibition effect during methane hydrate formation, which increases with the increase of sediment concentration.¹⁸⁶ The effect can be attributed to the combination of two effects: the presence of small pores in this clay-rich sediments and a minor contribution from the salt present in the pore water of the KG basin sediments.¹⁸⁶ Indeed, Sun *et al.* observed a reduction in the activity of water in fine sediment especially in clay and in silt.¹⁸⁷ Bhawangirkar *et al.* suggests that most of the nanopores of the KG sediments are filled with water molecules avoiding gas molecules to enter in this nanospace.¹⁸⁶ Gas molecules remain in the vapor phase instead of being trapped in water cages to form hydrates. When the concentration of the sediment in the aqueous solution increases, the inhibition effect increases (**Figure 25**).

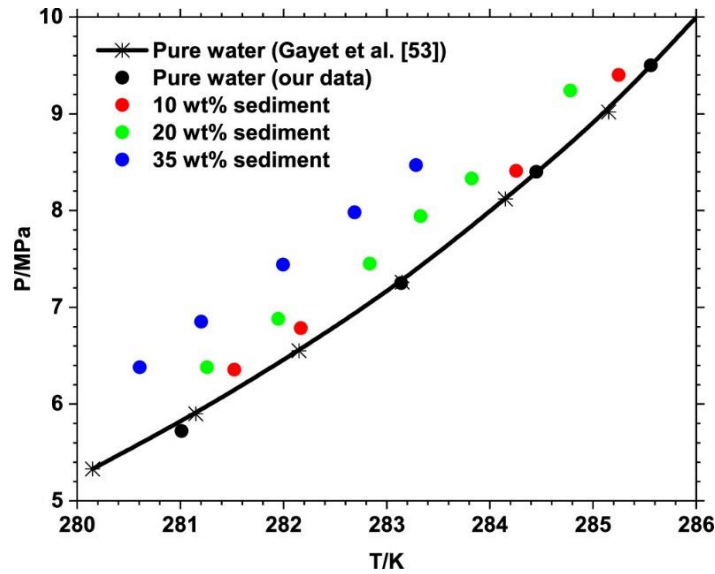


Figure 25. Comparison of Experimental phase equilibrium for methane hydrates formed in the presence of pure water and in the presence of 10, 20, and 35 wt % sediment solutions (From Bhawangirkar *et al.*¹⁸⁶).

Similarly, studies conducted by Yakushev *et al.*¹⁸⁹ show the inhibition effect of clay on hydrate formation and observed that clays and silts with fine particle size hold water molecules in their pores, which cannot be used for hydrate formation. However, they affirm that wet clay surface is a good surface to form hydrate. Based on these findings, it can be concluded that the hydrate can be formed either in the freely available water space or on the surface of the wet clay.¹⁸⁶

The effect of swelling clay on methane hydrate formation has also been evaluated. By using molecular simulations, Park and Sposito³² described the thermodynamic promoting effect of the surface of montmorillonite on methane hydrate whereas there the confinement effect of the interlayer space would have an inhibitor impact.

It is therefore necessary to consider the effect of particle size on the phase equilibrium of gas hydrates. In porous media, the surface tension and capillary effect generated by the porous media decrease the activity of water, increasing the critical solubility of methane in the hydrate-water system and hydrates are formed at lower temperature or higher pressure.¹⁸⁷ Furthermore, this effect increases with decreasing pore size, up to critical size. No pressure and temperature shift was observed in pores larger than about 60 nm.¹⁹⁰ Moreover, the effect of surface chemistry and chemical interaction between water, gas and sediments needs to be taken into account when considering clay and natural sediments. These considerations are even more important on hydrate kinetics.

When considering the study of natural gas hydrates, depending on the location of interest, the thermodynamic conditions and sediments may vary as well as the salinity level of the water and the nature of the salts present. The seawater salinity is of 3.5 %. Numerous studies focused on the effect of salt on hydrate stability in bulk water.^{191–195} All of them show the thermodynamic inhibition of salt on hydrate stability. As the concentration of salt increases the phase equilibrium curve is shifted to higher pressure and lower temperature (**Figure 26**). The type of salt also influences the phase equilibrium conditions. Experiment conducted with the same amount of NaCl, MgCl₂ and CaCl₂ in water solution show that the inhibiting effect of MgCl₂ is stronger than that of NaCl and the inhibiting effect of NaCl is stronger than that of CaCl₂.^{195,196}

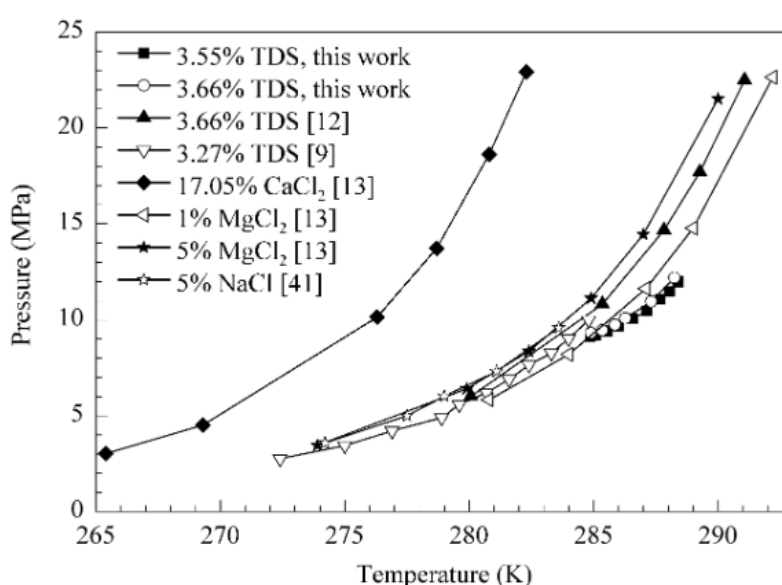


Figure 26. Comparison of experimental phase equilibrium data with previously reported experimental data for methane hydrate in presence of different salt and concentration. TDS means Total Dissolved Salt and is related to NaCl salt (From Saw *et al.*¹⁹⁵).

To go further, some studies were devoted to the study of the combine effect of sediments and salts. It is notably the case of the study conducted by Maiti *et al.*¹⁹⁷ on hydrate formation and dissociation behavior in KG sediments with NaCl. They observed an inhibition effect on using sediments, and colloidal sediment solution with NaCl shows greater inhibition effect on hydrate formation.¹⁹⁷ The influence of montmorillonite and NaCl concentration on methane hydrate stability have also been evaluated.¹⁹⁸ They observed that salt ions have a significant influence on the hydration properties of montmorillonite with the inhibition of swelling when brine solution concentration increases. This is explained by the decrease of the bound water in the sample.¹⁹⁸ Moreover, all studies observed a competitive effect between montmorillonite and

NaCl on hydrate formation. Tao *et al.*¹⁹⁸ observed a decrease of phase equilibrium temperature of hydrate with increasing brine solution concentration. The change of initial water content and the influence of salt ions on the stability of methane hydrate together affect the phase equilibrium condition of methane hydrate.¹⁹⁸ Therefore, the thermodynamic stability of natural gas hydrates is not only influenced by sediment properties and salt content, but also by the competition between these two elements, involving many physicochemical properties.

iii. Kinetics

The understanding of hydrate formation also requires also the investigation on the kinetics properties, including the impact of the sediment. Numerous studies have been carried out to evaluate the influence of various sedimentary surrogates and natural sediments on the kinetics of gas hydrate formation.^{35,143,170,199,200} In general, these studies show that the presence of sedimentary analogues improves the formation kinetics compared to a bulk hydrate.^{200–202}

In the lab, most researches devoted to study the influence of sediments on gas hydrate formation kinetics focus on sandy matrices¹⁴³, complemented by the use of artificial sediments such as silica gels, silica beads^{203,204}, activated carbons^{169,170} and metal organic frameworks (MOFs)¹⁷¹. These studies have highlighted the importance of matrix composition, particle size, pore structure, water and gas transport, and hydrate morphology on gas hydrate formation kinetics.⁹⁸

The effect of particle size has been highly explored on quartz sand. However, it is observed that the different studies do not observe the same effect. On one side, it seems that induction time and hydrate saturation decreases with increasing particle size.^{187,203} Wang *et al.* reported that the amount of methane hydrate formed and the initial rate of formation decrease gradually when the quartz sand particle increases when using particle size ranging from 75 to 3000 μm .²⁰³ Inversely, for sand quartz particle with sizes ranging between 610 and 1880 μm , Zhao *et al.* observed a shorter induction time and a higher hydrate saturation with smaller particle size.²⁰⁵ This effect can be explained by the increase of the specific surface area when the particle size decreases. This provides a greater water-gas reaction surface to improve hydrate formation. However, for natural sand, decreasing the particle size modifies its mineralogy leading to a larger concentration of clay and feldspar. These mineral have a greater chemical reactivity with water compared to pure silica.¹⁴³ On the other hand, other experimental studies devoted to the study of the kinetics of methane hydrate formation in a sandy matrix show that the effect of particle size on the kinetic rate is less obvious and presents a great variability.^{164,165} The review

of Qin *et al.*²⁰⁶ summarizes the effect of particle size on hydrate formation in porous media. Moreover, differences between these three results could be explained by the differences in the sample preparation methods employed for each study. One main difference is the size of the vessel used to form methane hydrates. Zhao *et al.*²⁰⁵ synthesized methane hydrate-bearing sediments in a small X-ray transparent cell with an inner diameter of 10 mm while Wang *et al.*²⁰³, Ruffine *et al.*¹⁶⁴ and Benmesbah *et al.*¹⁶⁵ used a large vessel ranging between 500 and 800 mL.

In addition to the effect of particle size on hydrate formation, experiments in porous media analog to natural systems have explored the effect of porosity on the kinetics. In particular, the surface of porous materials provides new nucleation sites and ensures a better gas–water contact resulting in a better hydrate formation kinetics compared to other matrices (quartz, sand).^{19,201} A study compared the formation kinetics of CO₂ hydrate in presence of pumice, red clay (FHRC), silica gel and sand. It has been reported that pumice favors hydrate formation and increases the rate of hydrate conversion (**Figure 27**).²⁰⁷ Also, methane hydrate formation in aqueous solution with activated carbons or silica nanoparticles in suspension shows shorter induction time with activated carbon particles.¹⁶⁹ Moreover, when the pore size reaches a critical value (such as 2nm), the confinement effect increases and thermodynamically inhibits hydrate formation (as seen above).

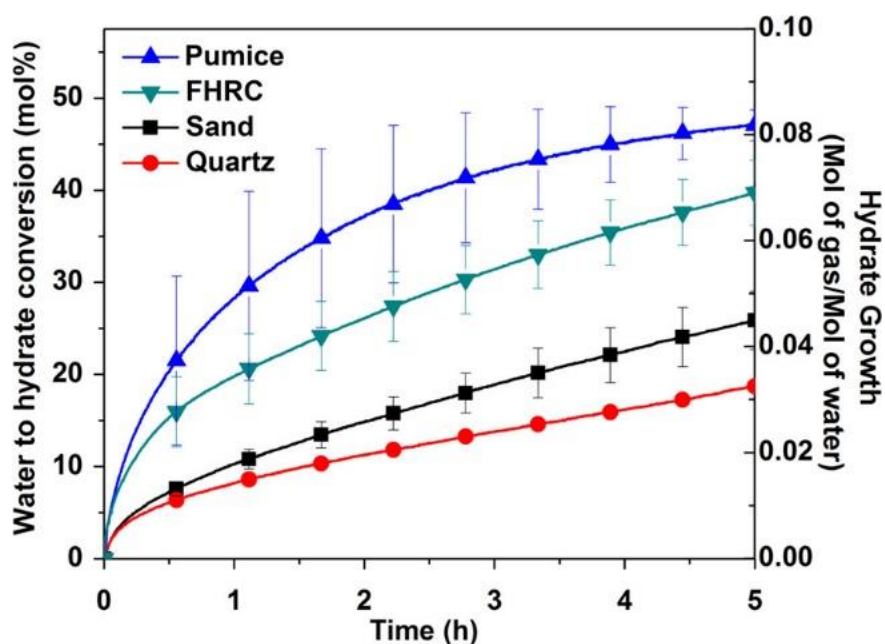


Figure 27. Comparison of the rate of conversion of water to hydrate and the rate of growth of hydrate in the presence of different porous media at constant water volume: pumice in blue, fire hardened red clay ("FHRC") in green, sand in black, and quartz in red (From Bhattacharjee *et al.*²⁰¹).

Thus, it appears that a substrate accelerating the formation of gas hydrates must be composed of relatively fine particles, but not with too small pores. Several studies on the formation of hydrates in porous media (activated carbon, silica sand, silica gel) have shown that the pore space, and the corresponding interconnectivity, plays an important role in the formation of hydrates. Indeed, a smaller grain size leads to a more regular stacking, to a greater interconnectivity of the pores, and thus to a greater water-gas contact surface.^{170,208,209}

Another factor to consider on hydrate formation is the water saturation of the sedimentary medium, *i.e.* the quantity of water initially present for the formation of the hydrate. Depending on the hydrophilic/hydrophobic character of the sedimentary particles and the water saturation, there are several scenarios for water-gas contact in packed beds of particles. Casco *et al.*¹⁷¹ have shown that the use of hydrophilic MOFs favors the nucleation and growth of hydrate in the internal cavities of the material with a low water/hydrate ratio, whereas hydrophobic MOFs do not allow water to access the internal porosity, thus favoring the formation of hydrates in the interparticle space with a high hydrate yield. Moreover, partial water saturation of the interstitial space of hydrophilic particles can provide optimal conditions for the formation of gas hydrates. Water films cover the solid particles and water bridges can form between the particles, as sufficient inter-particle spaces are still available for the gas phase. Thus, in a system

undersaturated with water, the pores remain interconnected and create channels dedicated to the gas circulation, which allows to increase the contact surface between water and gas, and consequently the formation of gas hydrates.^{201,210} Several experiments have indicated that gas hydrates form more favorably in hydrophilic beds under 40-75 % water saturation.^{203,207,210-212} Experiment conducted on sand or silica gel demonstrated that the rate of conversion of water to hydrate can reach more than twice that obtained with 100 % saturation.²⁰⁷ An optimal value of water saturation around 70 % was found from work on the formation of methane hydrates in silica sand²¹², in fine sand²¹¹ and glass beads²⁰³.

To go further on the understanding of hydrate natural sedimentary media, some studies are devoted to the analysis of the kinetics of formation in clay sand mixtures. The effect of particle size has been mentioned by Heeschen *et al.*¹⁴³. They have shown that sediment particle size has a strong effect on the kinetics of gas hydrate formation. Indeed, medium or coarse sands conducted to slower gas hydrate formation compared to a high concentration of fine grains <125 μm .¹⁴³ However, other studies have demonstrated the promotor effect of clay surfaces on hydrate nucleation. It was shown that suspensions of bentonite swelling clay shortened the induction time by providing a larger driving force.^{195,213} Yan *et al.*²¹⁴ brought one evidence of this phenomenon. They believed that the rapid nucleation of hydrate is due to the hydroxylated edge sites on the clay surface.²¹⁴ Experimental studies on methane hydrate formation in presence of montmorillonite swelling clay emphasized this result by revealing the promoting effect of the clay surface. However, they underlined that confinement in the nano-pores of clay have a stronger inhibition effect compared to the bulk phase (**Figure 28**). Indeed, Wu *et al.* insist on the fact that it is much easier to form hydrate in bulk phase than in pores.²¹⁵ This suggests that hydrate formation may favor the formation in larger pore sizes.²¹⁵

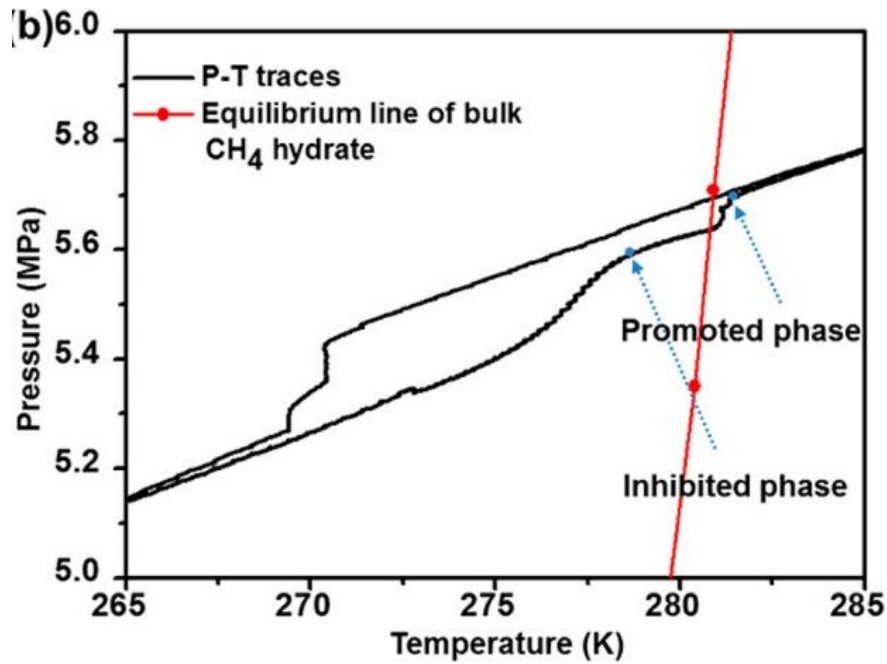


Figure 28. Pressure and temperature trace curve of CH₄ hydrate in crystalline-swelled Na-montmorillonite (Kim *et al.*³⁵).

These last results underline the effect of the multiscale distribution of pores in clay provided by their layered structure. This provides to the clays a large specific surface area and raises questions about the impact on gas hydrate formation. The majority of the projects dedicated to this study used molecular simulation techniques and only a few studies have investigated the formation of methane hydrates in the presence of non-swelling clay. MD simulations focusing on the kaolinite effect shows that hydrate nucleation is affected by water and gas contacts with the surfaces of the clay layers, resulting in two nucleation events: in the bulk phase and near clay surfaces.²¹⁶ The adsorption of cations on the clay surface would be involved in the formation of methane nanobubbles at the liquid water/hydrate interface during decomposition. Molecular dynamics simulations conducted by Fang *et al.* have identified this effect.²¹⁷

The combine effect of salt and sediments have also been explored. Chong *et al.* studied the influence of MgCl₂, KCl and NaCl on methane hydrates in sands with particle size ranging between 0.1–0.5 mm.^{218,219} They observed the kinetic inhibitor effect of salts on hydrate nucleation and growth, which resulted in a lower gas uptake and water conversion. Moreover, with a same concentration of MgCl₂, KCl and NaCl salts, NaCl as the stronger kinetic inhibitor effect.²¹⁸ In a very recent study, the effect of montmorillonite, sand and NaCl concentration on methane hydrate has been investigated.²²⁰ Zeng *et al.* observed for a low NaCl concentration of 0.2 mol/L and a low montmorillonite content range of 10–25 wt% the

induction time of hydrate formation was reduced (Figure 29). Inversely, when the concentration of NaCl and montmorillonite were increased, the induction time significantly increased. They suggested that the effect of montmorillonite content on the induction time is smaller than NaCl.²²⁰

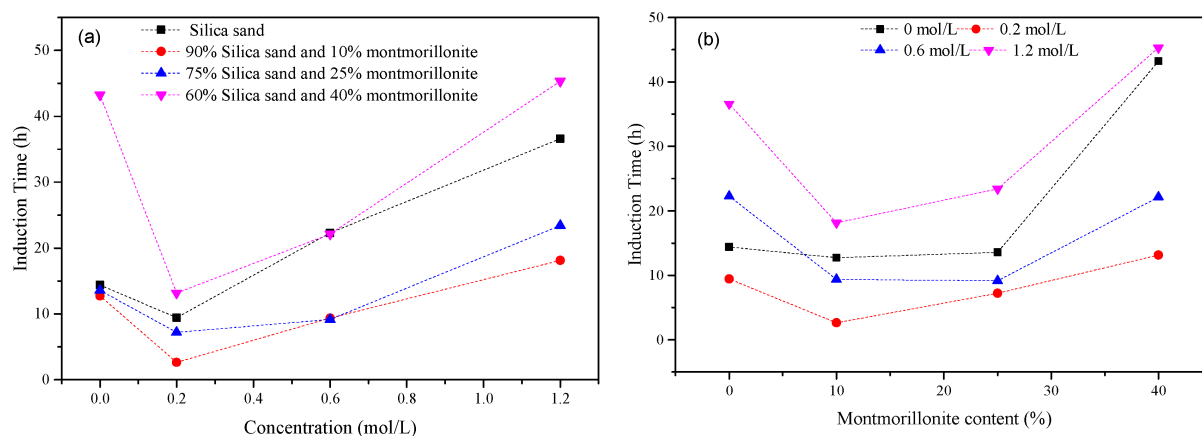


Figure 29. Comparison of the effect of NaCl concentration and montmorillonite content on the induction time of methane hydrate. (From Zeng *et al.*²²⁰)

All these studies are devoted to investigating the origin, stability and kinetics of natural gas hydrates in an environment mimicking marine sediments where large quantities of natural gas are present and mechanism of formation remains unknown. In general, hydrate formation in sedimentary media is a faster process than in bulk water, which leads to higher conversion of water to hydrate. This formation is mainly related to the size of the particles, the arrangement of the pore space or inter-particles and the initial water saturation of the sedimentary bed. When combined, these three parameters allow to increase considerably the specific surface of water-gas reaction and consequently to promote the formation of hydrate in sedimentary medium. However, when the concentration of fines (clays) become too high in the sandy media, hydrate formation may be slow down.¹⁴³ Moreover, at the microscale, molecular simulation highlighted the promotion effect of clay surfaces on hydrate formation kinetics.^{30–32,216} On the other side, the presence of salt in the water phase inhibit the gas hydrate kinetics.^{218–220}

iv. Cage occupancy

The estimation of methane resources from natural hydrates is at the heart of current environmental and energy issues. Natural methane hydrates adopt the structure sI where methane molecules occupy the SCs and LCs. As of today, the methods employed to estimate the amount of gas trapped in natural methane hydrates are based on a mean cage occupancy of 85%, which corresponds to $\sim 164 \text{ m}^3$ of methane for 1 m^3 of hydrate.^{4,5} Moreover, structural and spectroscopic analyses on natural gas hydrates reveal heterogeneities at the microscale on the absolute cage occupancy, with up to 17% of empty cages in methane hydrate samples.^{17,18} Analysis of natural methane hydrate samples collected in different locations show that methane cage occupancy vary significantly.^{221–223} Similarly, Yeon *et al.* reported abnormal cage occupancy with a low SCs occupancy level for natural methane hydrate collected in East Sea (located in the eastern part of the Korean Peninsula) compared to synthetic pure CH_4 -hydrate.¹⁷ They suggested that the presence of mobile ions (sodium cations) due to the presence of clay-rich sediments could significantly affect the cage occupancy with the hypothetical encapsulation of Na^+ in the SCs.¹⁷ This finding is supported by Seol *et al.* who first brought spectroscopic evidence of the enclathration of Na^+ in a SCs of structure sII propane hydrate stabilized with an enclathrated CH_3SO_3^- anion in a LCs.¹⁸ Another hypothetical explanation of reduced cage occupancy can be attributed to the effect of salinity more especially, the presence of NaCl salt. Molecular simulations conducted by Tung *et al.*²²⁴ suggested that individual ions or NaCl ion pairs could replace water molecules and participate to the cage's formation. This would result in the distortion of the water cages, which may reduce the fraction of methane occupation in the cavities.²²⁴ However, previous studies reported that salt ions are inhibitors and do not enter in the gas hydrate phase.^{209,218,225,226}

Addressed questions of this work: The influence of sediments and marine environment on the physicochemical properties of gas hydrates remains not well constrained. Numerous questions arise and it becomes necessary to collect more information that is reliable on the distribution of hydrates in clay sediments and the effect of clay interlayer cations and water salinity on cage occupancy and formation kinetics. The large uncertainty on the gas hydrate reservoir (600 and 10000 billion tons^{104,105,227}) highlights the need for a better understanding of the mechanisms of hydrate formation in natural environments in order to improve current geological models dedicated to estimating the amount of methane on earth.

Conclusion

The bibliographic work presented in this chapter reports on the studies carried out on synthetic and natural gas hydrates. It summarizes the main physicochemical properties of these crystalline systems (structure, distribution, thermodynamic stability, formation and dissociation mechanisms and cage occupancy). Then, these properties were studied for gas hydrates formed in the presence of natural sediments and sedimentary analogues to reproduce their natural environment. Selected gas hydrates in this work to deepen scientific understanding are formed from naturally occurring gases in the seabed (CH_4 , C_2H_6 , C_3H_8 , *iso*- C_4H_{10} , CO_2 , $\text{CH}_4+\text{C}_2\text{H}_6$, $\text{CH}_4+n\text{-C}_4\text{H}_{10}$) and have been the subject of numerous theoretical and experimental studies. The use of Raman micro-spectroscopy on gas hydrates formed from these gases will allow the collection of high-resolution Raman spectra and the assignment of vibrational bands to identify the formed structures and the type of occupied cages. The combination of Raman micro-spectroscopy imaging, neutron diffraction, and inelastic neutron scattering contributes to probing the micro- and nano-scales of natural and synthetic methane hydrate samples formed in the presence of salt and clay matrices to gain information on formation and dissociation mechanisms, structural properties, cage occupancy, and distribution in the sediments.

CHAPTER 2:

Experimental

methodology

Introduction

The protocols for the formation and characterization of gas hydrates and all the experimental methods used during this PhD work are detailed in this chapter.

I. GAS HYDRATE SYNTHESIS.

a. Gas hydrate formation without sedimentary media

i. From liquid water

The formation of gas hydrate requires a precise control of temperature and pressure, which vary depending on the used gas. To satisfy these conditions and investigate *in-situ* hydrate formation and structures, an optical pressure cell was designed with a volume of the sample chamber of 1 cm³. The optical cell is made of a lab-modified temperature-controlled stage (Linkam Scientific Instruments Ltd., UK) to maintain the temperature of the sample at the desired value (± 0.1 K) during the acquisition (**Figure 30**). The temperature can range between 150 K and 300 K. The sample pressure is controlled by a PM high-pressure pump (Top Industrie, Vaux-le-Penil, France) connected to the cell. Any type of gas can be added with a pressure up to 500 bar. A transparent optical sapphire window of 2 mm thick allows for microscopic investigation and *in-situ* Raman spectroscopic measurements.

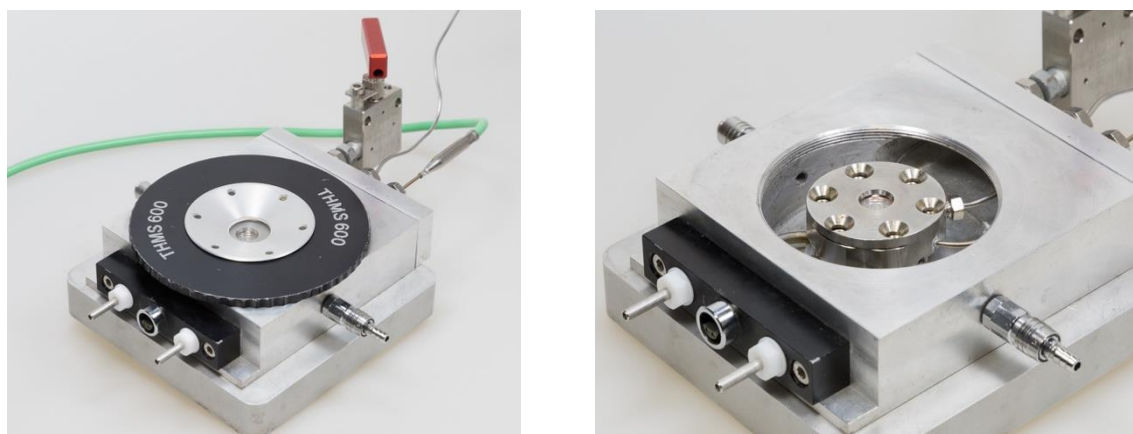


Figure 30. Pressure and temperature controlled Linkam cell.

To form gas hydrate, the cell is half-filled with Milli-Q water at room temperature and then the selected gas or gas mixture (prepared at the laboratory) is added at the desired pressure and start to dissolve into the aqueous phase. Then, the temperature is fixed to be in the hydrate stability zone according to the phase diagram of each gas species (represented in **Figure 31**) and the

hydrates start to growth. Hydrate formation can be observed inside the cell by the apparition of a white solid structure. The thermodynamic conditions selected for each gas species and the structure formed are summarized in **Table 3**.

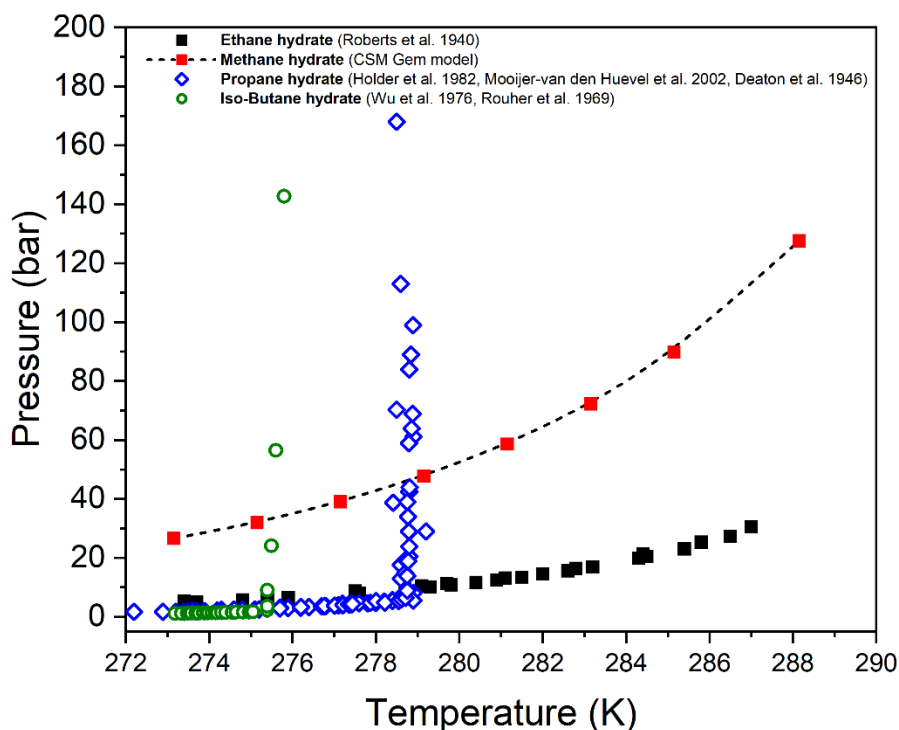


Figure 31. Phase diagram of various hydrocarbons studied in this work.

Gas species	Hydrate structure	P (bar)	T (K)
CH ₄	sI	66 bar	277 K
C ₂ H ₆	sI	10 bar	277 K
C ₃ H ₈	sII	6 bar	276 K
Iso-C ₄ H ₁₀	sII	1.5 bar	273 K
93 mol.% CH ₄ + 7 mol.% C ₂ H ₆	sII	84 bar	274 K
95 mol.% CH ₄ + 5 mol.% n-C ₄ H ₁₀	sII	20 bar	273K

Table 3. Summary of the thermodynamic conditions (P, T) applied for the formation of gas hydrates with various gas species.

In the case of iso-butane hydrate, the optical Linkam cell: Linkam CAP500 was used (**Figure 32**). Isobutane hydrate was synthesized inside a glass capillary with a diameter of 200 μm . ~2 cm of the glass capillary is filled by capillarity with Milli-Q water. The capillary is then sealed at the opposite side of water and centrifuged to force the water to go to the sealed side. Then, the capillary is glued on tube connected to a valve, which is connected to a syringe pump filled with iso-butane gas. All this equipment is placed on a heating–cooling stage of the Linkam cell

(CAP 500). This stage is composed of a silver block with a rectangular slot, where the capillary is inserted and which ensures good thermal homogeneity: over a lateral distance of ± 12.5 mm around the central observation hole, temperature T varies by less than 0.2 °C. The temperature is measured by means of a platinum sensor; its stability is ensured to within ± 0.1 °C by means of a Linkam T95 controller and a PE95 nitrogen pump. The temperature is set at 273K and the capillary filled with Milli-Q water is pressurized with iso-butane at 1.5 bar. These thermodynamics conditions ensure iso-butane hydrate formation. The use of this Linkam cell set-up with the optical window allows *in-situ* formation and characterization with Raman spectroscopy. Moreover, the motorized microscope stage connected to the spectrometer, on which the cell is placed, allows a precise control of the position along the two horizontal directions of the sample. Thus, the laser beam can focus on the sample, on the different phases (gas, water, hydrate) in the capillary.



Figure 32. Linkam cell CAP500.

ii. From ice

Pure methane gas hydrates have been used as reference system for the comparison with the synthetic methane hydrate formed in presence of clays and the natural methane hydrate samples collected in Black Sea. These pure methane hydrate samples have been synthesized in the laboratory inside high-pressure aluminum cells (5 cm^3) at constant pressure and temperature. A thermostatic bath controls the temperature, set at 253 K. The pressure is ensured by a high-pressure syringe pump (Top Industrie, Vaux-le-Pénil, France) controlled by a computer and regulating at 200 bar. The reference sample is form from crushed ice particles. MilliQ water (for hydrogen sensitive techniques: Raman and Inelastic Neutron Scattering) or deuterated water (for deuterium sensitive technique: neutron diffraction $\sigma_{coh}(D) > \sigma_{coh}(H)$) are crushed at 77 K in a liquid nitrogen bath to form fine ice grain particles. Ice powder is added into the cells at 77 K and the cells are closed with an indium gasket on top and screwed. The cells are

placed in the thermostatic bath at 273 K and pressurized with methane at 200 bar during 14 days. The indium gasket (1 mm diameter) is used to avoid pressure leakage once the cells are filled. After 14 days, the cells are depressurized and the samples are recovered at 77 K in a liquid nitrogen bath to avoid hydrate dissociation and stored in liquid nitrogen until analyses.

b. Gas hydrate formation in sedimentary media

i. Preparation of the water-sediment premix

Synthetic methane hydrate samples studied during my PhD work have been prepared in presence of four clay-rich matrices constituted of 60 % clay and 40 % of other minerals (mainly quartz and feldspar). The matrices are composed of Black Sea natural sediments, Illite, Kaolinite and Montmorillonite. A portion of Fontainebleau sand (Laboratoires Humeau, France) has been added to Kaolinite and Montmorillonite to reach the desired composition.

Black Sea sediments (BS) were collected during the GHASS¹²⁶ cruise in 2015 on the Romanian margin. These sediments, analyzed at Ifremer (Brest) by XRD, are mainly composed of clay (60 %) and 40 % of other minerals (mainly quartz, calcite and plagioclase) (**Figure 33**, left). The mineralogical analysis of the clay portion discloses the average presence of 66 % illite, <10 % smectite, 20 % kaolinite and <10 % chlorite (**Figure 33**, right).

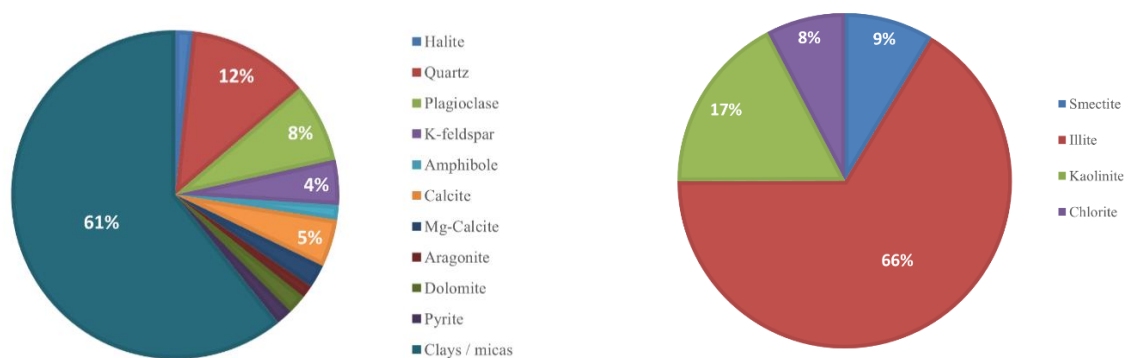


Figure 33. Average mineral composition of Black Sea natural sediment collected on core CS14 during GHASS onboard of Pourquoi Pas? in 2015.

The illite matrix (IS) is commercialized by Argiletz (FR). Its mineral composition makes this matrix an excellent sedimentary analogue of the natural sediments of the Black Sea since it is composed of 60 % clay and 40 % other minerals (quartz, calcite). Argiletz also commercializes

the kaolinite clay and the Montmorillonite clay is provided by Sigma Aldrich as Montmorillonite K10.

The mixture Montmorillonite + sand and Kaolinite + sand will be denoted respectively MS and KS in the manuscript. Black Sea natural sediments and Illite will be denoted BS and IS respectively. The main properties of each matrices are detailed in **Table 4**.

Properties	Montmorillonite (MS)	Illite (IS)	Kaolinite (KS)	Black Sea sediments (BS)
Particle size (D_{mean})	14 μm	4.5 μm	5.8 μm	2.75 μm
BET Surface area	240.8 m^2/g	66.5 m^2/g	17.5 m^2/g	63.1 m^2/g
Global mineralogy				
Quartz	30 %	25 %	40 %	14 %
Argiles / micas	60 %	60 %	60 %	60 %
Calcite	-	14 %	-	5 %
Plagioclase	10 %	-	-	8 %
Clay fraction mineralogy				
Smectite	82 %	< 5 %	-	5-10 %
Illite	15 %	77 %	< 5 %	60 %
Kaolinite	< 5 %	17 %	84 %	20 %
Chlorite	< 5 %	< 5 %	14 %	10 %

Table 4. Main physicochemical properties and mineral composition of the four clay-rich matrices used as methane hydrate substrates.

The water saturation is taken into account when considering the synthesis of gas hydrates in presence of a substrate. It corresponds to the quantity of water required to fill the inter-particle free volume of a sample of sedimentary analogues. In this work, the clay-rich matrices are under-saturated with water which means that the inter-particle spaces are not fully-filled and water and gas can circulate in the pore network.

The desired saturation level can be calculated from the following formula involving the volume of free space V_{free} between the particles and the calculated amount of water (in grams) to add:

$$Sat_{th} = \frac{(m_{H_2O})_{th}}{V_{\text{free}} \rho_{H_2O}} \quad (1)$$

Where Sat_{th} is the desired level of saturation ($Sat_{th} = 0.75$) and ρ_{H_2O} is the density of water ($\rho_{H_2O} = 1 \text{ g/cm}^3$). For the neutron diffraction experiments, deuterated water (D_2O) was used to form the hydrate samples. The density of deuterated water ($\rho_{H_2O} = 1.107 \text{ g/cm}^3$) is very closed to the density of hydrogenated water. The volume of deuterated water added into the sample is identical to the volume of MilliQ water.

The procedure followed to prepare the methane hydrate samples for this work consider as the reference system, to determine the amount of water to add in the sedimentary matrices to reach the saturation level, a matrix constituted only with Fontainebleau sand. A volume of 5 cm³ is filled with Fontainebleau sand. The volume of the free space between sand grains is approximated at 40 %, which corresponds to 2 cm³. With the equation (1), the amount of water to add in the system can be calculated: 1.5 cm³ of water are required to partially saturate the sandy matrix at 75 %. This same amount of water (H₂O or D₂O) is added onto 5 cm³ of each clay-rich matrix. Once added, the water and the sedimentary matrices are homogeneously mixed at room temperature. Note that the sample made with D₂O have been prepared under nitrogen atmosphere in a glove box. Moreover, in the frame of reproducing natural environment of natural gas hydrate, the impact of salinity on the formation of methane hydrate has been investigated. MilliQ and deuterated solution were prepared with a concentration of 2.2 mg/L of NaCl. A volume of 1.5 cm³ was added according to the same procedure onto the sedimentary matrices.

The mixtures of pure water or salted water (H₂O or D₂O) with sedimentary matrices constitute the premix used to reproduce the formation of methane hydrate in their natural environment.

ii. Hydrate formation

Synthetic methane hydrate samples have been prepared *in-situ* and *ex-situ*. *In-situ* methane hydrate refer to samples synthesized during data acquisition while *ex-situ* samples are prepared prior to experiments. In both scenarios, the premix (water – sedimentary matrices) is pressurized at constant pressure with methane at the required temperature to fulfill the thermodynamic conditions favorable for hydrate formation.

For *ex-situ* samples, the hydrogenated or deuterated / pure or salted premix are placed in a tightly sealed high-pressure cell (5 cm³) with an indium gasket that ensures tightness and prevents gas leakage. The cells are then placed in a thermostatically controlled bath set at 282 K. The gas is injected with a high-pressure syringe pump. The samples are pressurized at 200 bar for 1 to 110 days. Then, the samples are disconnected from the gas with a valve, placed in a liquid nitrogen bath and immediately depressurized to limit the condensation of the gas on the sample. The samples are crushed into powders under a nitrogen atmosphere created by the

liquid nitrogen bath to avoid water condensation from the room atmosphere deposits on the sample. Finally, all the samples formed ex-situ are stored in liquid nitrogen until their analysis.

In-situ methane hydrate formation has been recorded by neutron diffraction on the powder diffractometer D20. The pure and salted deuterated premix prepared in a glove bag under nitrogen atmosphere are put into an aluminum cell manufactured for neutron diffraction (3 cm³). An indium gasket to top of the cell ensure the tightness and prevents gas leakage between the cell and the neutron stick. The neutron stick, designed at Institute Laue Langevin, is made with a temperature sensor to record sample temperature during acquisition and a capillary connects the cell containing the sample to a high-pressure syringe pump to insert methane gas at the desired pressure. The temperature of the sample is controlled by an orange cryostat and set at 282 K. The pressure is fixed at 70 bar and the neutron diffraction experiment starts when pressure is added onto the sample. The formation of methane hydrate is recorded over time.

II. RECOVERY OF NATURAL GAS HYDRATES FROM THE BLACK SEA.

Natural methane hydrates samples studied during this PhD work were collected during a scientific cruise GHASS2²¹ onboard of the Pourquoi Pas? conducted by Ifremer on the Romanian sector of the Black Sea in September 2021. GHASS2 is focused on the northern sector of the Danube Canyon and aims to characterize the "fluid" system. The objectives were threefold: (1) to characterize the gas system as a whole, from the source through the migration pathways to the hydrosphere, (2) to quantify the gas flux at the water/sediment interface (methane and carbon balances) and to assess the transition to the atmosphere, and (3) to constrain the temporal evolution of the modelled gas hydrate stability zone from the last glacial episode (20 ka) to the present time and to make projections of the future evolution. This evolution is suspected to be responsible for the emplacement of several submarine slides discovered during GHASS (2015). The quantitative approaches envisaged following the acquisitions made during GHASS2 are multidisciplinary (geophysics, geotechnics, sedimentology, biogeochemistry, microbiology) in order to understand the processes involved in the methane cycle and the dissociation of gas hydrates. The methane cycle includes the formation, migration and dispersion of methane.

My contribution to this project is dedicated to the physicochemical investigations of natural gas hydrates from the nano-, microscale to the geological site. Samples investigated during my PhD work comes from one core CS05 collected on the crest area of the Romanian sector at 734 m

below sea level at around 9 °C. When the cores are lifted onto the boat's deck, they are cut into one-meter sections, opened lengthwise, photographed and labeled (**Figure 34**). Finally, hydrate samples are collected, indicating their position (depth) within the core. All samples were then stored in liquid nitrogen to ensure their stability until their characterization with micro-Raman and neutron spectroscopy. Then, the samples were crushed into small powder particles at 77 K under controlled atmosphere to avoid condensation and cold-transferred on the various experimental set-ups.

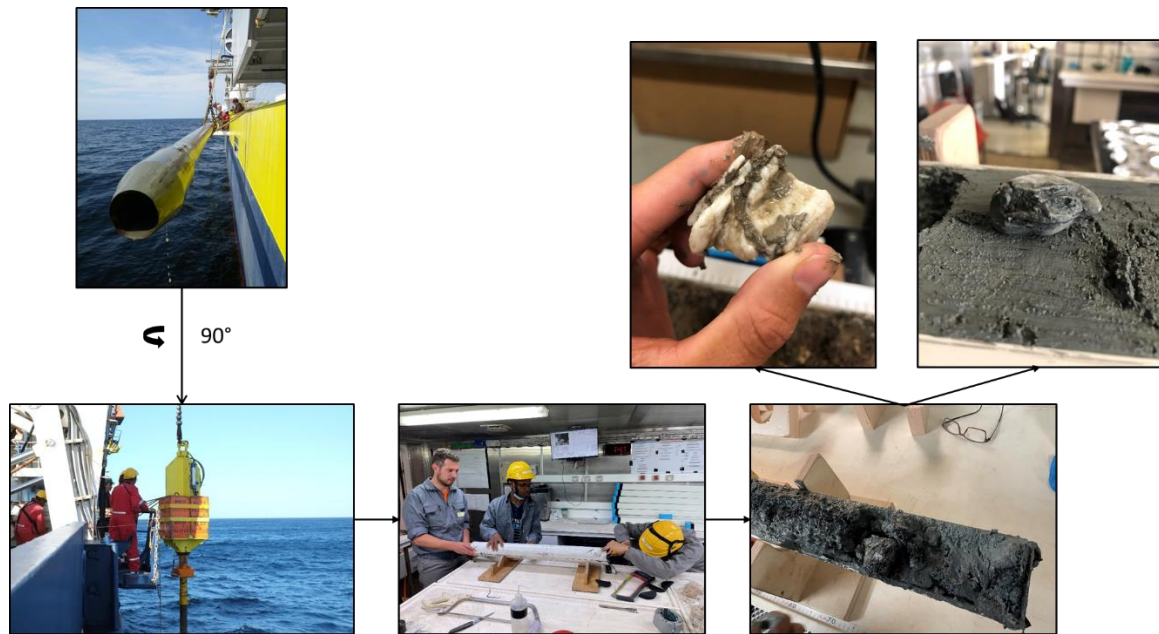


Figure 34. Schematic of the process of hydrate recovery on the Romanian sector of the Black Sea on board of the Pourquoi Pas? in September 2021 with pictures of two gas hydrate samples.

It is well-known that gas hydrates in the Romanian sector of the Black sea are mainly composed of methane and adopt the structure sI. They are found in natural clay-rich sediments (~60 % of clay). The structure of the collected hydrate samples and the rate of cage occupancy are investigated with micro-Raman spectroscopy and mapping at 150 K, and Inelastic Neutron Scattering at 10 K.

III. EXPERIMENTAL TECHNIQUES.

a. Neutron scattering

A neutron scattering experiment consists of *illuminating* a sample with a neutron beam with a wave vector \vec{k}_0 , a wavelength λ_0 and an energy E_0 . Neutrons are scattered by the sample with an angle, 2θ and a final wavevector \vec{k}_j and an energy E_f (**Figure 35**). The diffusion angle 2θ is defined as the angle between the vectors \vec{k}_0 and \vec{k}_j and the energy of a neutron with wavevector \vec{k} can be expressed as:

$$E = \hbar\omega = \frac{\hbar^2|\vec{k}|^2}{2m_n} \text{ and } k = \frac{2\pi}{\lambda} \quad (2)$$

Where m_n is the neutron mass and \hbar , the Planck constant divided by 2π . The momentum and energy conservation rules lead to:

$$\hbar\vec{Q} = \hbar\vec{k}_j - \hbar\vec{k}_0 \quad (3)$$

$$\hbar\omega = \hbar(\omega_j - \omega_0) \quad (4)$$

Where \vec{Q} is the scattering vector also called momentum transfer and $\hbar\omega$ is the neutron energy transfer.

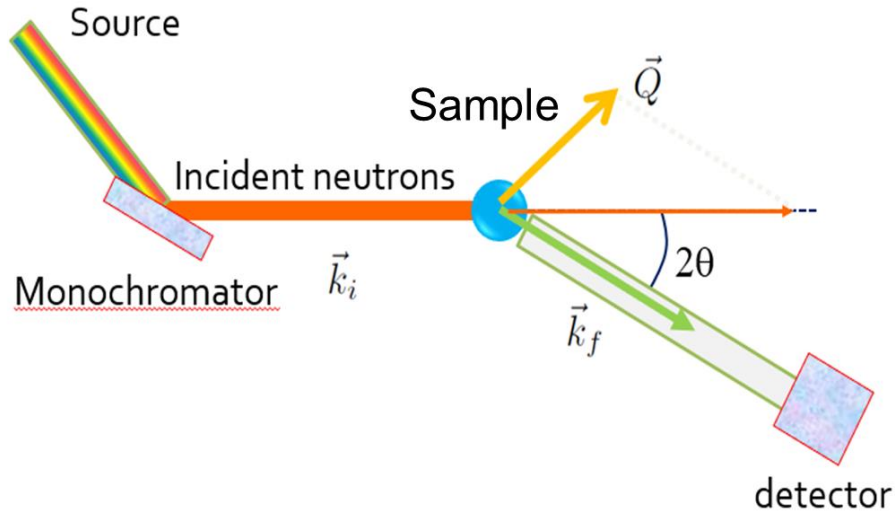


Figure 35. Principle of a neutron scattering experiment.

Experimentally, neutron scattering experiment give access to the differential scattering cross-section i.e., the number of neutrons scattered over a solid-angle $d\Omega$ and by elementary energy transfer $d\omega$. This quantity is determined by the scattering law defined as:

$$\left(\frac{d^2\sigma}{d\Omega d\omega}\right) = \left(\frac{d^2\sigma}{d\Omega d\omega}\right)_{coh} + \left(\frac{d^2\sigma}{d\Omega d\omega}\right)_{inc} \quad (5)$$

The terms of this equation are weighted by the neutron scattering σ_{coh} and σ_{inc} cross-sections:

$$\left(\frac{d^2\sigma}{d\Omega d\omega}\right)_{coh} = \frac{k_0}{k_j} \frac{\sigma_{coh}}{4\pi} S_{coh}(Q, \omega) \quad (6)$$

$$\left(\frac{d^2\sigma}{d\Omega d\omega}\right)_{inc} = \frac{k_0}{k_j} \frac{\sigma_{inc}}{4\pi} S_{inc}(Q, \omega) \quad (7)$$

In these expressions, the important terms are the coherent and incoherent dynamical structure factors, $S_{coh}(Q, \omega)$ and, $S_{inc}(Q, \omega)$ respectively. $S_{coh}(Q, \omega)$ provides information on collective phenomena met in matter (phonon, structure, etc.). $S_{inc}(Q, \omega)$ provides information on individual phenomena (Brownian motions, vibrations, etc.). These two parts contain an elastic and inelastic contribution that are different scattering processes: the elastic scattering is used for diffraction to determine the atomic of a material and the inelastic scattering is used to study atomic and molecular motion as well as phonon in condensed matter.

Moreover, the signature of coherent and incoherent neutron scattering will depend on the coherent and incoherent scattering cross sections of the atoms present in the studied system. Typical values of the various isotopes are summarized in **Table 5**. The hydrogen atom shows an incoherent scattering cross section 40 times higher than its isotope, the deuterium. It is clear that the incoherent contribution of hydrogen in hydrogenated materials will largely dominates the scattering signal. Hydrogenated compounds will be favor for neutron scattering techniques dedicated to the study of incoherent signatures of materials, such as Inelastic Neutron Scattering. For neutron diffraction techniques, the coherent signal of hydrogen atoms needs to be minimized to avoid a large background (incoherent background) which is scaled by the incoherent cross section of hydrogen. Deuterium is used to replace hydrogen, in order to enhance the coherent scattering (Bragg peaks).

Element	σ_{coh} (barn)	σ_{inc} (barn)	σ_{abs} (barn)
C	5.55	0.001	0.0035
N	11.01	0.50	1.90
O	4.232	0	0.000191
S	1.0188	0.007	0.53
H	1.7583	80.27	0.3326
D	5.592	2.05	0.000519

Table 5. Scattering cross sections of typical atoms (barn).²²⁸

The elastic scattering or diffraction happens when $k_0 = k_j$. The intensity of the signal I is proportional to $|Q^2|$ and can be expressed as:

$$I \propto |Q^2| = k_0^2 + k_j^2 - 2k_0k_j \cos(2\theta) = 2k_0^2 - k_j^2 \cos(2\theta) \quad (8)$$

$$|Q^2| = 2k_0^2 \cos(1 - (2\theta)) \quad (9)$$

We can simplify this by using these following equations:

$$\cos(2\theta) = \cos^2(\theta) - \sin^2(\theta) = 1 - 2\sin^2(\theta) \quad (10)$$

And,

$$\sin^2(\theta) = \frac{1 - \cos(2\theta)}{2} \quad (11)$$

Finally,

$$Q^2 = 4k_0^2 \sin^2(\theta) \quad (12)$$

With,

$$k_0 = \frac{2\pi}{\lambda} \quad (13)$$

$$\sqrt{Q^2} = Q = \frac{2\pi}{d} \quad (14)$$

We can combine these equations and get:

$$\frac{2\pi}{d} = 2 \frac{2\pi}{\lambda} \sin(\theta) \quad (15)$$

Thus, we can obtain the expression of the Bragg's law:

$$\lambda = 2d \sin(\theta) \quad (16)$$

Bragg's law gives the conditions for constructive interference.

The inelastic scattering is useful to study the interactions between atoms, can be used to perform vibrational spectroscopy and extract the vibrational density of states i.e., the distribution in energy of the vibrational modes of the system. It happens when $k_0 \neq k_j$:

- When $k_0 > k_j$, that means that the neutrons “give” energy to the crystal.
- When $k_0 < k_j$, that means that the crystal “gives” energy to the neutrons.

i. Neutron diffraction

Neutron diffraction (coherent elastic neutron scattering) is an experimental technique used to characterize the structure of crystalline or polycrystalline samples (powder) based on the phenomenon of diffraction. This technique can be used in addition to X-ray diffraction to characterize more precisely the structure of the studied material. Indeed, the X-ray diffraction probes the electron density of the crystalline system while neutron diffraction probes the density of scattering length (nuclear property). Therefore, neutron diffraction is more suitable to study systems rich in deuterium because of its essentially coherent scattering length (compared to hydrogen). Moreover, this difference of interaction with matter allows the neutron diffraction to implement complex sample environments due to the relative transparency of many materials to neutrons.

The neutron diffraction experiments were performed on the powder diffractometer D1B and D20 at the Institute Laue Langevin (ILL), Grenoble, FR. The incident wavelength used is $\lambda_0 = 2.52 \text{ \AA}$ on D1B and $\lambda_0 = 2.41 \text{ \AA}$ on D20. D1B is equipped with a high efficiency position sensitive detector (PSD) detector (PSD) that covers the angular range from 0.8 to 128.8° and allows probing very small samples in a volume of 2 cm^3 (**Figure 36**). The particularity of this instrument lies in its very good spatial resolution at small angles with a FWHM of up to 0.3° at 2.52 \AA (for a 5 mm diameter sample). D20 is a medium- to high-resolution diffractometer providing a very high flux at the sample position. It is equipped with a large microstrip detector. It has 1536 detection cells of a stationary and a curved linear position sensitive detector (PSD) covering a 2θ range of 153.6° . D20 is ideal for *in-situ* diffraction studies with acquisition times below 1 s allowing the investigation of fast changes in the sample (2 cm^3). The orange cryostat on both diffractometers allows the control of the temperature during the measurements.

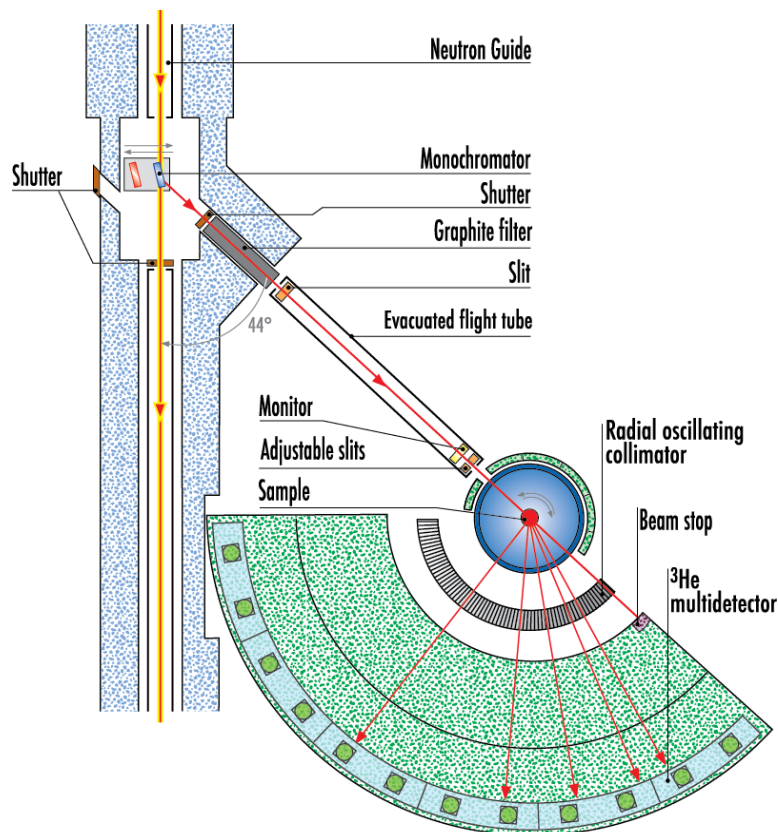


Figure 36. Layout of the neutron powder diffractometer D1B at ILL, Grenoble, FR (View from top).

The diffraction patterns of synthetic deuterated gas hydrate samples are analyzed in the range of scattering angles between 10° and 60° . In this angular range, enough Bragg peaks characteristic of gas hydrates are present to allow the identification of the formed structure.

ii. Inelastic Neutron Scattering

Inelastic neutron scattering (INS) (incoherent inelastic neutron scattering) is a well-established technique for vibrational spectroscopy. INS spectra have no symmetry selection rules and thus transitions that are otherwise forbidden (i.e., in Raman spectroscopy) can be observed. A wide range of energy can be explored, with energies ranging from that of the microwave region to the ultraviolet region of the electromagnetic spectrum. INS is mainly sensitive to the vibrations of hydrogen atoms because of their much higher incoherent cross section compared to other elements. This technique can be used to investigate hydrated compounds, as water vibrations can be observed on a wide spectral range providing information on the lattice dynamics and atomic molecular vibrations.²²⁹

The INS experiments carried out during the PhD were done at the Institute Laue Langevin (ILL) in Grenoble, FR on the IN1 neutron spectrometer (**Figure 37**). Gas hydrate samples were cold transferred to a new innovative sample changer manufactured at ILL, which can hold up to six samples and allows remote control of the sample change. This sample changer saves a considerable amount of time, avoiding multiple cold-transfers for each sample. The INS spectra from the synthetic and natural gas hydrates were measured at 10 K in the range of energy transfer from 1 to 140 meV, collecting the signatures of the rotational bands of methane, the translational and librational bands of water, with an energy of resolution of Δ/E 2%.

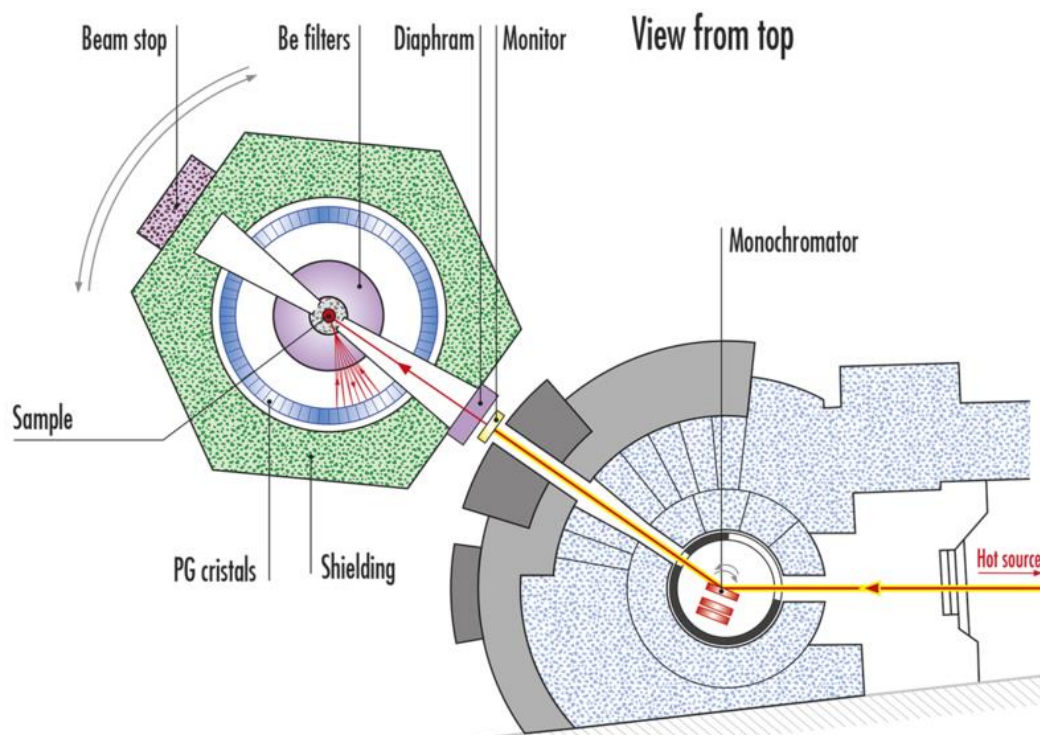


Figure 37. Layout of the neutron spectrometer IN1 at ILL, Grenoble, FR (View from top).

b. Raman spectroscopy

Raman spectroscopy is a technique based on the phenomenon of light scattering, which comes from a light-matter interaction. An incident photon transmits energy to the molecule and is scattered in all directions of space with a total intensity 10^{-3} to 10^{-4} times lower than the intensity of the incident radiation. The scattered radiation is composed of 99.99 % of intensity scattered at the same frequency, corresponding to the Rayleigh scattering (elastic). The tiny remaining part of the scattered radiation is polychromatic: it is the Raman scattering (inelastic).

In the classical model, an induced dipole \vec{P} , is created by applying an electric field \vec{E} of photons through the molecular polarizability tensor $\bar{\alpha}$ which depends on the geometry of the molecule:

$$\vec{P} = \bar{\alpha}\vec{E} \quad (17)$$

Indeed, a monochromatic incident radiation, characterized by a frequency ν_0 , is sent onto a molecule, and its electrons tend to move in the same direction as the electric field \vec{E} and the nuclei in the opposite direction. The medium is then polarized. The electric field is then defined by:

$$E = E_0 \cos(2\pi\nu_0 t) \quad (18)$$

And the polarizability is defined by:

$$\alpha(Q) = \alpha_0 + Q \cdot \left(\frac{\partial \alpha}{\partial Q} \right)_{Q=Q_0} \quad (19)$$

With α_0 , the static polarizability of the molecule and Q , the vibration coordinate defined by:

$$Q = Q_0 \cos(2\pi\nu_Q t) \quad (20)$$

The induce dipole is expressed as:

$$P = \alpha_0 E_0 \cos(2\pi\nu_0 t) + Q \cdot \left(\frac{\partial \alpha}{\partial Q} \right)_{Q=Q_0} Q_0 \cos(2\pi\nu_Q t) E_0 \cos(2\pi\nu_0 t) \quad (21)$$

In the quantum model, the molecule is excited by a photon of energy $h\nu_0$ to a virtual metastable level only to fall back, subsequently, to a permitted level. This allowed level can be the same as, higher than or lower than the starting level, and is referred as Rayleigh, Raman Stokes and anti-Stokes scattering, respectively **Figure 38**.

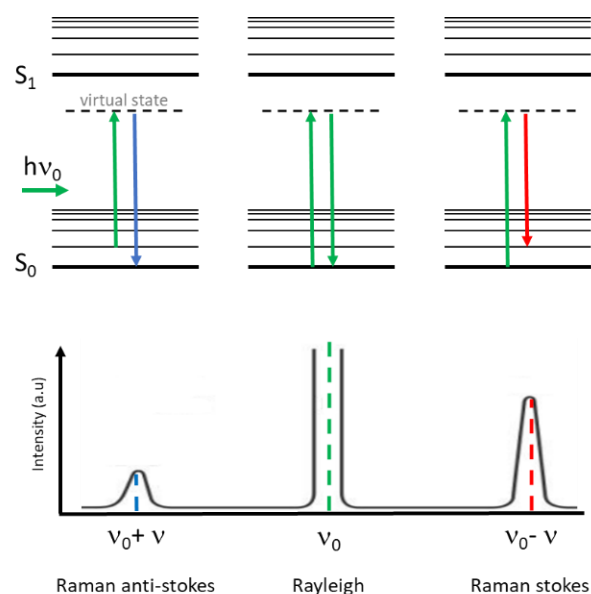


Figure 38. Schematic diagram of the energy transitions involved in Rayleigh scattering and Raman scattering when the interaction of an incident photon with a molecular vibration mode, gains (anti-Stokes scattering, blue-shifted) or loss (Stokes scattering, red-shifted) an amount of energy equal to that vibrational mode and the corresponding Raman band position.

Thus, the induced dipole can be expressed as follows:

$$P = \alpha_0 E_0 \cos(2\pi\nu_0 t) + \frac{1}{2} \left(\frac{\partial \alpha}{\partial Q} \right)_{Q=Q_0} Q_0 E_0 [\cos(2\pi(\nu_0 - \nu_Q)t) + \cos(2\pi(\nu_0 + \nu_Q)t)] \quad (22)$$

Where each part of the expression corresponds to a type of diffusion, as indicated by the colors. The low energy modes of vibration being the most populated, the Stokes lines are more intense than the anti-Stokes lines, and it is generally with these first that we work.

There are selection rules that define whether a vibrational mode is active in Raman. Thus, for the transition from one vibrational mode, with normal coordinate Q , to another state to be allowed, the polarizability of these two states must be different:

$$\left(\frac{\partial \alpha}{\partial Q} \right)_{Q=Q_0} \neq 0 \quad (23)$$

Finally, in the case of a vibrational spectrum in the harmonic oscillator approximation, the vibrational transition must occur between two vibrational states such that $\Delta\nu = \pm 1$, where ν is the vibrational quantum number. The vibrational coordinate must therefore induce a variation of the polarizability.

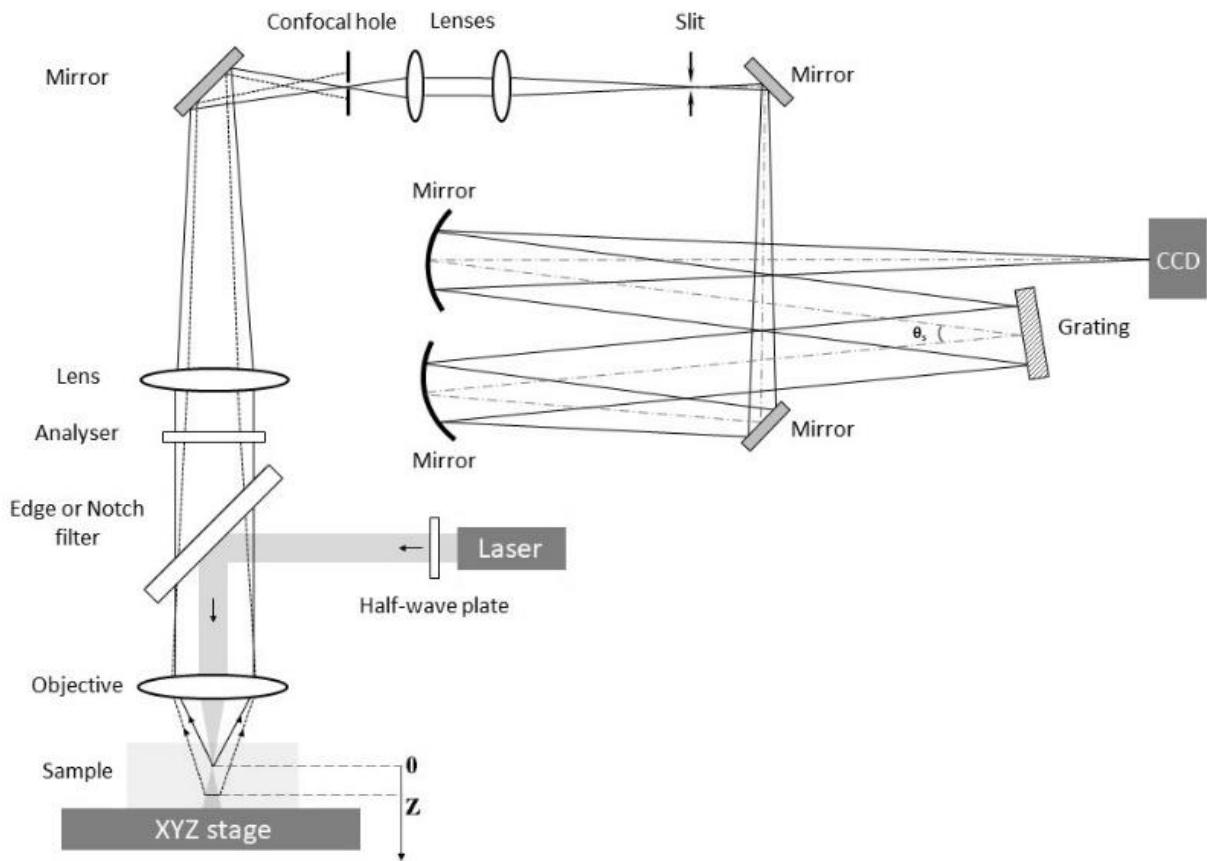


Figure 39. Schematic of a confocal Raman micro-spectrometer instrument with Z the distance of focalization.

The Raman spectrometer, LabRAM HR evolution (Horiba Jobin Yvon, France), was used during this thesis to probe natural and synthetic gas hydrate samples. The operating principle of the spectrometer is described in **Figure 39**. Two lasers were used $\lambda_0 = 405 \text{ nm}$ and $\lambda_0 = 532 \text{ nm}$. The laser is focused on the sample thanks to an optical confocal microscope for which the diameter of the hole (typically $150 \mu\text{m}$ or $300 \mu\text{m}$) and the objective (x50) are adjusted to improve radial and axial resolutions. The backscattered radiation is transmitted to the spectrometer through a Notch filter, which passes all wavelengths except λ_0 . A grating of 1800 lines/mm was used providing a spectral resolution with a “full width at half maxima” of $\sim 2.5 \text{ cm}^{-1}$ for $\lambda_0 = 405 \text{ nm}$ and $\sim 0.8 \text{ cm}^{-1}$ for $\lambda_0 = 532 \text{ nm}$. The calibration of the spectrometer is done using the characteristic vibrational mode of silicon at 520.7 cm^{-1} before each measurement. A CCD detector (charged coupled device) is used to recover the data by transforming the light signal into an electrical signal.

Raman micro spectroscopy allows probing micrometer-sized samples and volumes. The coupling with confocal microscopy improves the lateral and axial resolutions by the presence

of an adjustable diaphragm placed in the confocal image plane to collect only the Raman light scattered through this confocal hole. Thus, it is possible to choose different areas to be analyzed in the sample, at variable penetration depths.

IV. EXPERIMENTAL STRATEGY.

a. Kinetic study

In a first step, the kinetics of methane hydrate formation was studied *in-situ* by neutron diffraction. The main objective is to evaluate the time required for the formation of methane hydrate in the different matrices BS, MS and IS and to evaluate the effect of the matrix composition, the physicochemical properties of the clays, and the presence of salt (NaCl). The experiments were performed on D20 powder diffractometer at 282 K and 70 bar over 3 to 5 hours.

To overcome the very long formation times in the IS and BS matrices, methane hydrate samples formed *ex-situ* in the laboratory prior the experiments were analyzed by neutron diffraction on the D1B powder diffractometer at 150 K, at atmospheric pressure. Diffraction patterns of the samples pressurized over time scales ranging from 1 to 110 days were recorded. The evolution of the Bragg peaks of methane hydrate and ice not converted to hydrate over time allowed to estimate the rate of formation of methane hydrate in the BS and IS matrices over a time range of 1 to 110 days.

The kinetic curves obtained for the three matrices IS, BS, MS described the rate of methane hydrate formation as function of time. These curves are fitted with a kinetic model detailed in chapter 4. This model allows describing the nucleation and growth process involved in the formation of methane hydrate in presence of sediments. Comparison of the kinetic curves with this model provides information on the different methane hydrate formation mechanisms involved within the IS, BS, MS matrices.

b. Structural analysis

i. Le Bail and Rietveld refinements

The study of the diffraction patterns of gas hydrates allows to determine the types of hydrates formed, the fractions of hydrates, of ice (if the samples were studied at low temperature) and of the substrates (i.e., sand, clays, etc.) and sometimes even the gas occupancy in each type of cages. In order to determine the unit cell, during this thesis work, Le Bail refinements were performed on pure deuterated hydrate samples of carbon dioxide and propane. Deuterated samples of synthetic methane hydrates formed *in-situ* and *ex-situ* in the BS, IS and MS matrices were analyzed by Rietveld refinements.

The Rietveld method refers to the computation of Bragg peaks intensities from a structural model.²³⁰ In the Le Bail model, the Bragg peak positions are also determined from the space group and initial unit cell parameters, but the reflection intensities are treated as arbitrary unknowns.²³¹ Both methods were used on the Fullprof software.²³²

Le Bail refinements on propane and carbon dioxide hydrate respectively fit the intensity of the Bragg peaks of propane structure sII hydrates according to the space group $Fd\bar{3}m$ and of the Bragg peaks of carbon dioxide structure sI hydrates according to the space group $Pm\bar{3}n$. The intensity of the Bragg peaks of hexagonal ice Ih are fitted based on the space group $P6_3/mmc$. Other experimental parameters were refined: the zero offset, scale factors, the lattice parameters, and the peak shape parameters u , v , w . The background was fitted manually for each diffraction patterns. The refined lattice parameters (a , b , c , α , β and γ) of sI hydrate structure, sII hydrate structure and Ih ice are summarized in **Table 6**.

Structure	Space group	Lattice type	Crystal shape	a (Å)	b (Å)	c (Å)
sI hydrate	Pm $\bar{3}$ n	cubic	$\alpha = \beta = \gamma = 90^\circ$	11.87±0.008	11.87±0.008	11.87±0.008
sII hydrate	Fd $\bar{3}$ m	cubic	$\alpha = \beta = \gamma = 90^\circ$	17.18±0.03	17.18±0.03	17.18±0.03
Ih ice	P6 $_3$ /mmc	hexagonal	$\alpha = \beta = 90^\circ, \gamma = 120^\circ$	4.49±0.001	4.49±0.001	7.32±0.002

Table 6. Le BAIL refined parameters for sI, sII and Ih structures.

Rietveld refinements have been applied on the diffraction patterns recorded at 150K of the synthetic methane hydrate in IS, BS and MS. As with the Le Bail, experimental parameters were refined: the zero offset, scale factors, the lattice parameters, and the peak shape parameters u , v , w and the background were adjusted manually. The diffraction patterns are constituted of the Bragg peaks of sI methane hydrate, ice, quartz SiO₂ and the minerals which composed the matrices. Only the Bragg peaks of the methane hydrate and ice have been fitted for BS. In IS and MS, the Bragg peaks of quartz SiO₂, methane hydrate and ice are fitted. Furthermore, analysis of the ice Bragg peaks revealed the presence of both hexagonal (Ih) and cubic (Ic) ice. The average refined lattice parameters (a , b , c , α , β and γ) of sI hydrate structure, Ih and Ic ice, and SiO₂, determined for all the collected diffraction patterns, are summarized in **Table 7**. The structure models used for each phase are detailed in **APPENDIX 1**. The structural model used to refine methane hydrate is an effective model and did not allow the determination of methane cage occupancy (**APPENDIX 1, Table S1**). However, phase fractions (sI hydrate and ice) have been estimated according to the Rietveld refinement of the synthetic methane hydrate samples for each diffraction patterns and were used to obtain the hydrate conversion rates (details in chapter 4).

Structure	Space group	Lattice type	Crystal shape	a (Å)	b (Å)	c (Å)
sI hydrate	Pm $\bar{3}$ n	cubic	$\alpha = \beta = \gamma = 90^\circ$	11.90±0.03	11.90±0.03	11.90±0.03
Ih ice	P6 $_3$ /mmc	hexagonal	$\alpha = \beta = 90^\circ$, $\gamma = 120^\circ$	4.51±0.01	4.49±0.01	7.34±0.01
Ic ice	Fd $\bar{3}$ m	cubic	$\alpha = \beta = \gamma = 90^\circ$	6.37±0.01	6.37±0.01	6.37±0.01
SiO $_2$	P3 $_2$ 21	hexagonal	$\alpha = \beta = 90^\circ$, $\gamma = 120^\circ$	4.92	4.92	5.42

Table 7. Rietveld refined parameters for sI, sII and Ih structures.

ii. Raman signatures

Raman spectroscopy of gas hydrates provides detailed information on intramolecular vibrations. The assignment of internal vibrational modes (stretching and bending) due to water and guest molecules and their characteristic intensities can be used to determine the structures formed.

Raman spectroscopy was used to study substrate-free hydrates of several pure hydrocarbons (i.e., methane, ethane, propane and iso-butane) and gas mixtures (i.e. methane + ethane and methane + butane). These gas hydrates were formed *in-situ* in a high-pressure Linkam cell under the thermodynamic conditions detailed previously in **Table 4**. The experimental setup is detailed in **Figure 40**. The acquisition of the Raman spectra is done directly in the high-pressure cell, the laser with a wavelength $\lambda_0 = 532$ nm is focused on the sample. The spectra recorded inform on the type of hydrate formed according to the position of the Raman bands of the gas hydrate signatures and their intensities, and on the vibrational signatures of the water sub-structure (i.e., H $_2$ O lattice modes and OH-elongations). All the results are presented in the Chapter 3.

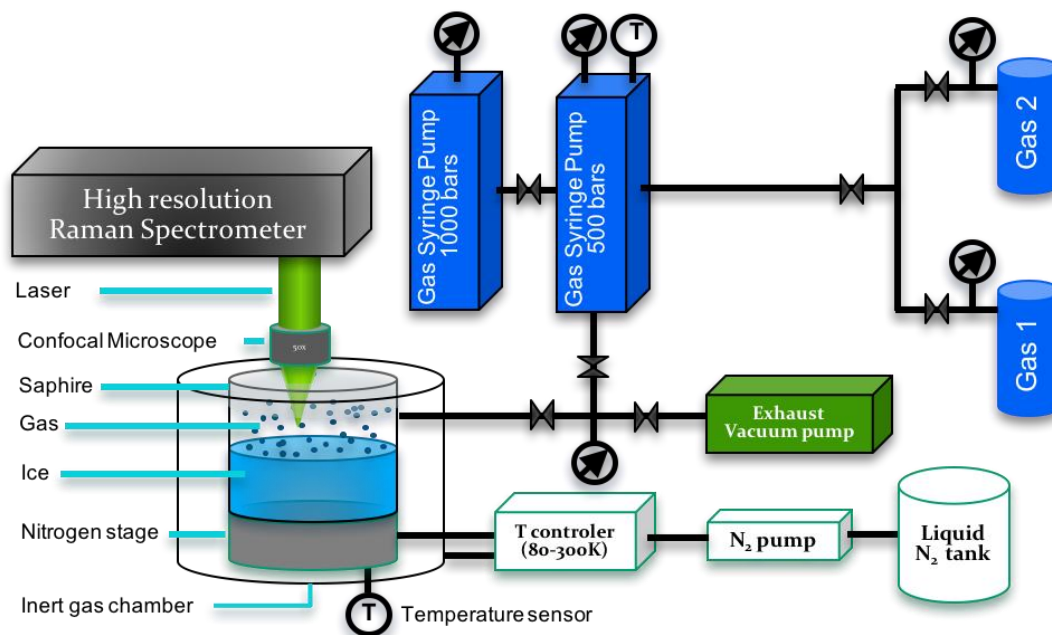


Figure 40. Schematic of the experimental *in-situ* high-pressure Raman set-up.

Crushed pure methane hydrate samples formed *ex-situ* from ice particles and crushed methane hydrate samples formed *ex-situ* within the IS, BS, KS and MS matrices and natural methane hydrates collected in the Black Sea were cold transferred and analyzed by Raman spectroscopy at 150 K in the Linkam cell. A controller connected to a liquid nitrogen tank regulates the temperature. The laser with a wavelength of $\lambda_0 = 405$ nm is focused on the sample. The laser wavelength is chosen to minimize the fluorescence related to the clays contained in the sedimentary matrices IS, BS, KS and MS and the organic matter contained in both synthetic and natural samples. Raman spectrum of pure methane hydrate are compared to spectra of synthetic and natural methane hydrates formed in clay-rich matrices. SC and LC Raman band positions, widths and intensities are measured.

c. Cage occupancy

Synthetic and natural methane hydrate samples were analyzed using Raman spectroscopy. Raman spectroscopy allows the quantitative analysis of hydrate cage occupancy from Raman scattering intensity. The Raman intensity of a species i is proportional to the square of the variation of polarizability α'_i , to the concentration C_i and to the instrumental factor F_i (objective, confocal hole, laser power). The ratio of Raman intensities R of species 1 and 2 can be expressed as:

$$R = \frac{I_1}{I_2} = \left(\frac{\alpha'_1}{\alpha'_2}\right)^2 \frac{C_1 F_1}{C_2 F_2} = \frac{\sigma_1 C_1 F_1}{\sigma_2 C_2 F_2} \text{ where } \sigma_i = |\alpha'_i|^2 \quad (24)$$

Where σ_i corresponds to the Raman cross-section of species i .

As the experimental conditions are kept identical, $F_1 = F_2$ and the equation (24) can be simplified as:

$$R = \frac{I_1}{I_2} = \frac{\sigma_1 C_1}{\sigma_2 C_2} \quad (25)$$

This equation can be used to determine quantitatively cage occupancy of methane hydrate considering the Raman signatures of methane molecules in SC ($\sim 2905 \text{ cm}^{-1}$) and LC ($\sim 2916 \text{ cm}^{-1}$) of the type I hydrate. Thus, the equation (25) can be written as:

$$\frac{C_{LC}}{C_{SC}} = \frac{A_{LC} \sigma_{SC}}{A_{SC} \sigma_{LC}} \quad (26)$$

Where A_i is the integrated intensity of the Raman bands of the SC and LC. Quantitative analysis on the variation of polarizabilities show a 4-5 % difference between σ_{SC} and σ_{LC} for a methane molecule encapsulated in a LC and in a SC.^{56,233} Thus, in this thesis the ratio $\frac{\sigma_{SC}}{\sigma_{LC}}$ is approximated to 1.

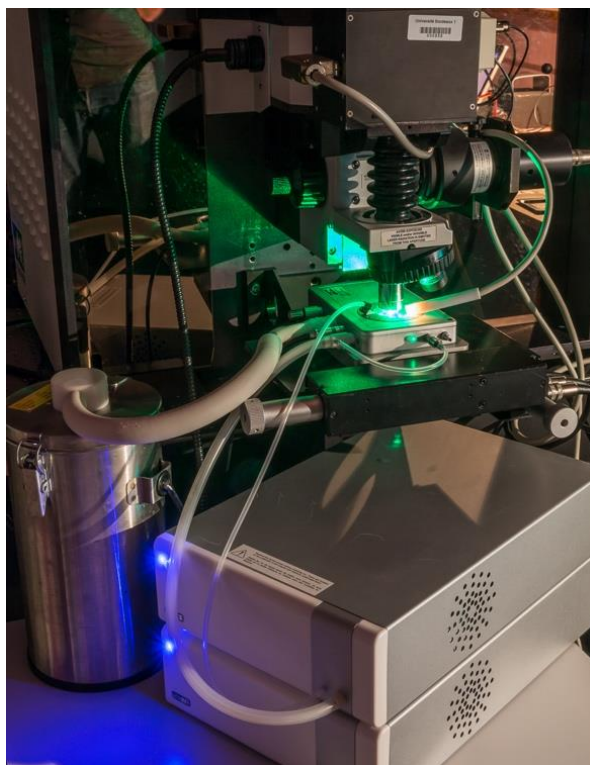


Figure 41. Setup configuration when using the Linkam capillary cell, for the study of ex situ samples. (The wavelength of the laser used on this picture is $\lambda_0 = 532$ nm)

In this work, the cage occupancy of *ex-situ* synthetic and natural methane hydrate has been determined and compared. The crushed samples have been cold-transferred on the thermostatic stage of the Linkam (**Figure 41**). A temperature controller connected to a liquid nitrogen tank controls the temperature of the cell and sample. The sample is injected at 150 K at atmospheric pressure. Raman spectra are recorded through the optical window with the laser beam ($\lambda_0 = 405$ nm) focused on the sample. The Raman bands of SC and LC are integrated by a pseudo-voigt function (included in the software Origin of the spectrometer) between 2850 and 2950 cm^{-1} (**Figure 42**). A linear background is subtracted manually. Raman mapping allows probing an area of several micrometers by recording a Raman spectrum every 5 to 10 μm . Hence, average cage occupancy and cage occupancy variation at the microscale are measured.

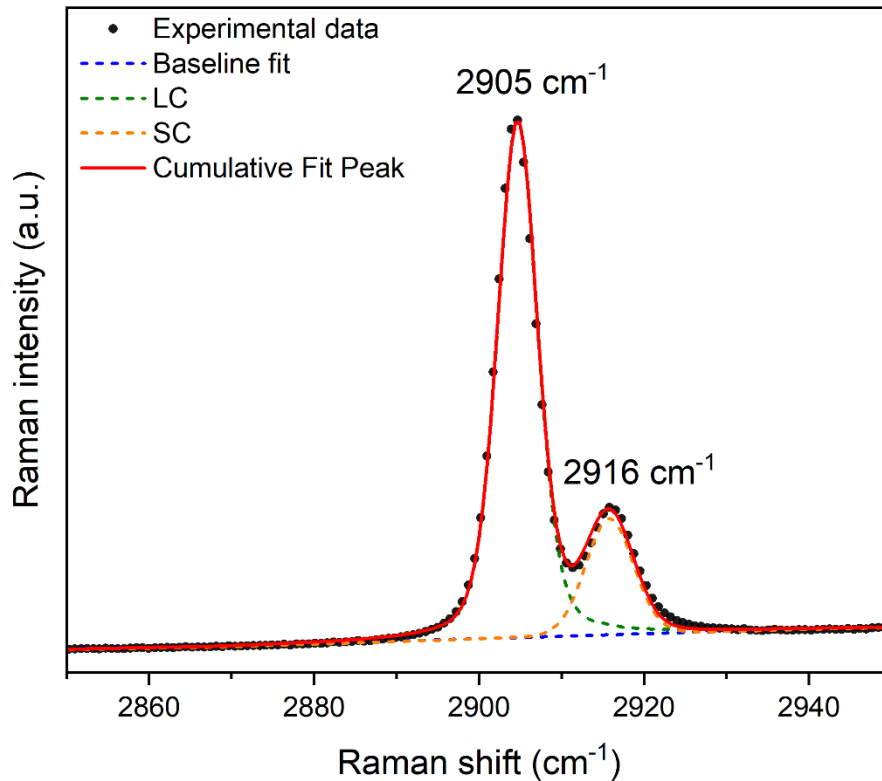


Figure 42. Pseudo-voigt fitting of two Raman bands of methane hydrate attributed to the LC (2905 cm^{-1}) and SC (2916 cm^{-1}) at 150 K and 1 bar ($\lambda_0 = 405\text{ nm}$).

d. Gas hydrate distribution at the nano- and micro- scales

In order to help improve current geophysical models dedicated to the estimation of gas trapped in gas hydrates on Earth, nano- and microscopic pores of the sediments were investigated to question whether methane hydrates could form in such spaces. To date, geophysical models do not incorporate these spaces, which could significantly modify the amount of gas trapped as clay minerals have extremely large specific surface areas. Indeed, the multi-scale distribution of pores in clay minerals provide intriguing spaces where hydrate could form.

Two strategies have been explored: Raman spectroscopy imaging to probe the microscale and Inelastic Neutron Scattering to probe the nanometric spaces. For this purpose, synthetic and natural methane hydrate samples were analyzed.

The synthetic and natural samples after being ground are inserted into the Linkam CAP500 cell at 150 K. The laser with the wavelength $\lambda_0 = 405\text{ nm}$ is used. Once an area of the sample where an intense Raman signal related to the presence of methane hydrates is identified, a perimeter

to be mapped is determined with a size ranging between 15-400 μm by 15-400 μm . A Raman spectrum is recorded every 3 to 7 μm depending of the sample. Probing the sample at the micrometer scale allows to identify the distribution of hydrates between the matrix grains by integrating the vibrational bands of the matrix and methane hydrate for each mapping coordinate. Maps showing the intensity of the selected signal as function of the position in the sample can be reconstituted.

These same samples were analyzed by INS on the neutron spectrometer IN1 at ILL. The choice of INS to probe the nanoscale of our samples comes from a study of Jiménez *et al.* in which they identify the librational modes of water as a signature of the water confinement in the interlayer space of clay by using INS.²³⁴ In this way, the vibrational signatures of both synthetic and natural methane hydrates are investigated. The samples were cold-transferred into the cryostat set at 10 K and the spectra were collected at the same temperature. Rotational bands of methane, translational and librational modes of water are compared for all the samples.

All the experiments and results dedicated to the nano- and micro- distribution of methane hydrate into the clay-rich sedimentary matrices are summarized in the Chapter 5.

**CHAPTER 3:
Raman and
neutron
diffraction of
pure and mixed
gas hydrates.**

I. INTRODUCTION.

Natural gas hydrates are mainly composed of microbial gases consisting of ~99.9% of methane. In few areas (e.g. Marmara Sea), hydrate deposits are formed from thermogenic gases which usually contains not only methane gas, but also carbon dioxide, ethane, propane, butane and longer hydrocarbon gaseous species.²⁶ The purpose of this chapter is to investigate the structural, and thermodynamics properties as well as the chemical composition of gas hydrates formed with a single gas species and with gas mixtures. In the following chapters of the manuscript, clay-rich sediments - characterizing 90 % of these natural hydrate deposits^{235,236} – will be taken into account in the investigations.

As described in chapter 1, the nature of the gas species is one factor governing the formed clathrate structure. Let recall that in nature, three main structures occur: the cubic structure sI, the cubic structure sII and the hexagonal structure sH.^{40,237} Neutron diffraction is an appropriated technique to investigate hydrate structural properties.^{93,238} The Bragg peaks positions of the collected diffractograms are characteristic of the formed unit cell – allowing the straight determination of the formed clathrate structure (sI, sII sH, etc). The Bragg peak intensities analysis yields the determination of the space groups (extinction rules) and through a Rietveld refinement (as described in chapter 2), the structural model (especially with the crystallographic positions of “hydrogenated” species) can be determined. To characterize these structures and their chemical composition, Raman spectroscopy has also proven to be an appropriated techniques.⁵⁶ The short acquisition times, as well as the coupling with a confocal microscope, make this technique particularly attractive for in-situ experiments under controlled temperature and pressure.²³⁹ Raman spectroscopy provides access to intramolecular vibration (guest and host molecular vibrations), enabling not only to disentangle the various involved phases (gas, liquid and hydrate phases), but also to determine the chemical composition (and cage occupancy) of the investigated hydrates. The spectroscopic signatures of gaseous hydrocarbons (stretching and bending modes) are specific to each gaseous species and exhibits a frequency shift when confined into the hydrate cages compared to the free gas state. This shift may also depend on the investigated structure (sI, sII, sH). Indeed, the cage in which the guest molecule is located differs in size, modifying the water-guest molecule interactions and thus, the associated spectroscopic signatures.

The study of gas hydrates from small to larger hydrocarbons gas molecules is required to characterize natural gas hydrates especially to explore the structures formed in presence of

complex natural gas mixture and the possible variation of gas compositions and coexisting phases.^{26–28} In this chapter, Raman spectroscopy and Neutron diffraction experiments are detailed for selected gas hydrates of interest in natural environments. The series of analyzed gas hydrates is listed in **Table 8**.

Gaseous species	Formed structure	Raman scattering data	Neutron diffraction (ND) or X-ray (XRD) data
Pure gas			
CH ₄	sI	This work, Uchida <i>et al.</i> ²⁴⁰ , Subramanian <i>et al.</i> ²⁴¹ , Sum <i>et al.</i> ⁵⁶ , Schicks <i>et al.</i> ²³⁹	This work (ND), Davidson <i>et al.</i> ⁹³ (XRD), Kirchner <i>et al.</i> ²⁴² (XRD)
C ₂ H ₆	sI	This work, Subramanian <i>et al.</i> ^{241,243,244} , Uchida <i>et al.</i> ^{96,240} , Schicks <i>et al.</i> ²³⁹	Udachin <i>et al.</i> ²⁴⁵ (XRD), Murshed <i>et al.</i> ²⁴⁶ (XRD)
C ₃ H ₈	sII	This work, Subramanian <i>et al.</i> ²⁴¹ , Sum <i>et al.</i> ⁵⁶ , de Menezes <i>et al.</i> ²⁴⁷ , Kumar <i>et al.</i> ⁹⁵ , Schicks <i>et al.</i> ²³⁹	This work (ND), Rawn <i>et al.</i> ²⁴⁸ (ND), Kirchner <i>et al.</i> ²⁴² (XRD)
iso-C ₄ H ₁₀ (liquid)	sII	This work, Takeya <i>et al.</i> ²⁴⁹ , Subramanian <i>et al.</i> ²⁴¹ , Uchida <i>et al.</i> ⁹⁶ , Hester <i>et al.</i> ²⁷ , Petrov <i>et al.</i> ²⁵⁰ , Schicks <i>et al.</i> ²³⁹	Takeya <i>et al.</i> ²⁴⁹ (XRD)
CO ₂	sI	Sum <i>et al.</i> ⁵⁶ , Qin <i>et al.</i> ²³³ , Chazallon <i>et al.</i> ²⁵¹ , Petuya ²⁵²	This work (ND), Henning <i>et al.</i> ⁷⁷ (ND)
Gas Mixture			
CH ₄ +C ₂ H ₆	sII	This work, Murshed <i>et al.</i> ^{246,253} , Ohno <i>et al.</i> ²⁵⁴ , Hester <i>et al.</i> ²⁷	Murshed <i>et al.</i> ^{246,253} (ND, XRD)
CH ₄ +n-C ₄ H ₁₀	sII	This work, Luzi <i>et al.</i> ²⁵⁵	Takeya <i>et al.</i> ²⁴⁹ (XRD), Kida <i>et al.</i> ²⁵⁶ (XRD)

Table 8. List of gas (pure and mixed) hydrates studied in the present chapter by means of Raman scattering and/or neutron diffraction.

II. PURE GAS HYDRATES.

a. Methane hydrate (sI)

Methane hydrates are the most abundant gas hydrates on earth with an amount of methane trapped in the overall deposits reaching 600 to 10000 billion tons.^{104,105,227} The analysis of synthetic pure methane hydrate is required to get a reference system used for comparing the structure and composition with natural methane hydrates.

The sample was synthesized in the lab before the experiment. Crushed deuterated ice was pressurized at 273 K and 200 bar during 13 days and then, stored in liquid nitrogen before being cold-transferred to the cryostat of the diffractometer at 150 K. The neutron powder diffractogram (**Figure 43**) was collected on the D20 diffractometer at ILL ($\lambda_0 = 2.41 \text{ \AA}$).

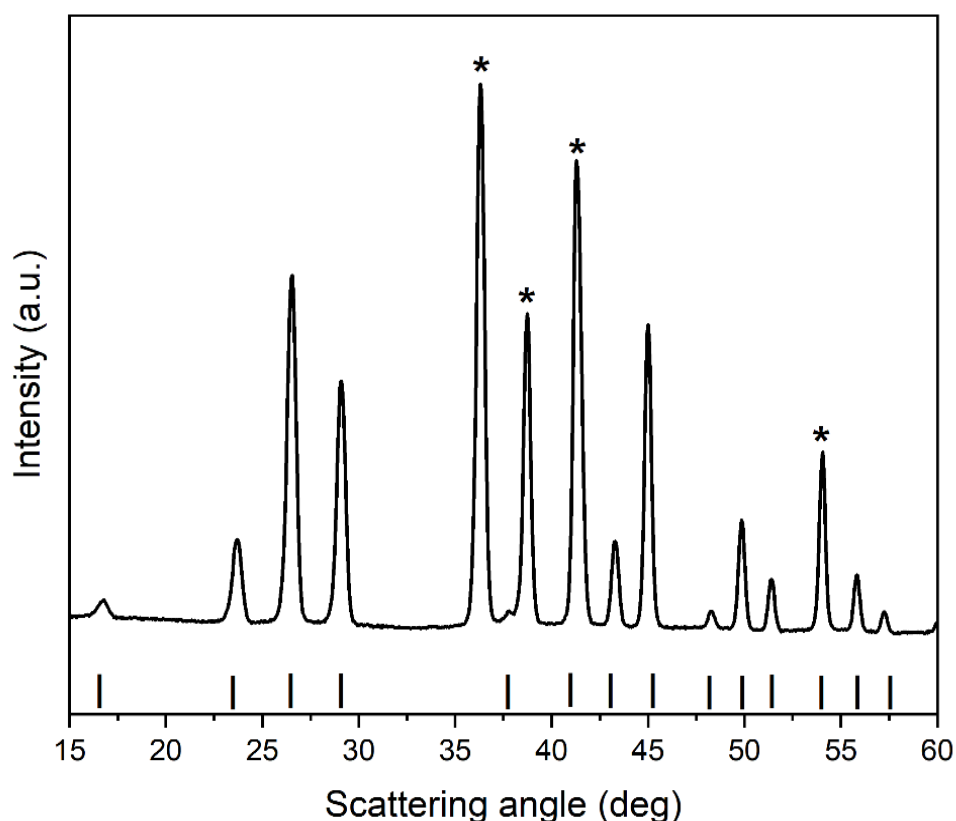


Figure 43. Powder diffractogram of methane hydrate structure sI collected at 150 K and 1 bar with D20 diffractometer at ILL-Grenoble, FR ($\lambda_0 = 2.41 \text{ \AA}$). Vertical ticks and stars indicate the Bragg peaks of structure sI hydrate and ice Ih, respectively.

The positions of the Bragg peaks on the diffractogram indicate the presence of methane hydrate in structure sI (vertical ticks) as well as of hexagonal ice Ih (stars). The analysis of these phases has been treated by a Rietveld refinement by using two phases: the methane hydrate structure sI and the hexagonal ice Ih.²³² The structural model used for each phase is given in **APPENDIX 1, Table S1 and Table S2**. The resulting comparison of the calculated and measured diffractograms is shown in **APPENDIX 2, Figure S1**.

The **Figure 44** shows the Raman spectra of CH₄ in gas and in hydrate phases. The spectrum of CH₄ (green) is collected at room temperature and 97 bar. The CH stretching of CH₄ gas is a single band observed at 2917 cm⁻¹.⁵⁶ The other Raman band assignments of CH₄ gas are detailed in **Table 9**.^{27,56,257–259} The spectrum of structure sI CH₄ hydrate can be decomposed into two parts: the spectroscopic signatures of water molecules and the CH stretching of methane in hydrate phase. The spectroscopic signatures between 200 and 400 cm⁻¹ are attributed to the H₂O lattice modes (involving hydrogen-bonded O-O intermolecular stretching) and the O-H stretching intramolecular modes corresponds to the spectral region between 3000 and 3800 cm⁻¹. The signal of CH₄ hydrate sI is characterized by Raman bands associated to the CH₄ molecule in two different types of sI cages. The bands at 2903 cm⁻¹ and 2914 cm⁻¹ are attributed to the signal of methane inside the LCs (5¹²6²) and SCs (5¹²), respectively.^{3,233,240} This attribution is related to the intensity ratio between the SCs and the LCs. According to the density of the cavities per unit cell of sI (2 SCs and 6 LCs), this ratio should be very close to 1:3.⁵⁶ Here, the measured ratio (by integrating each band) is 0.28.

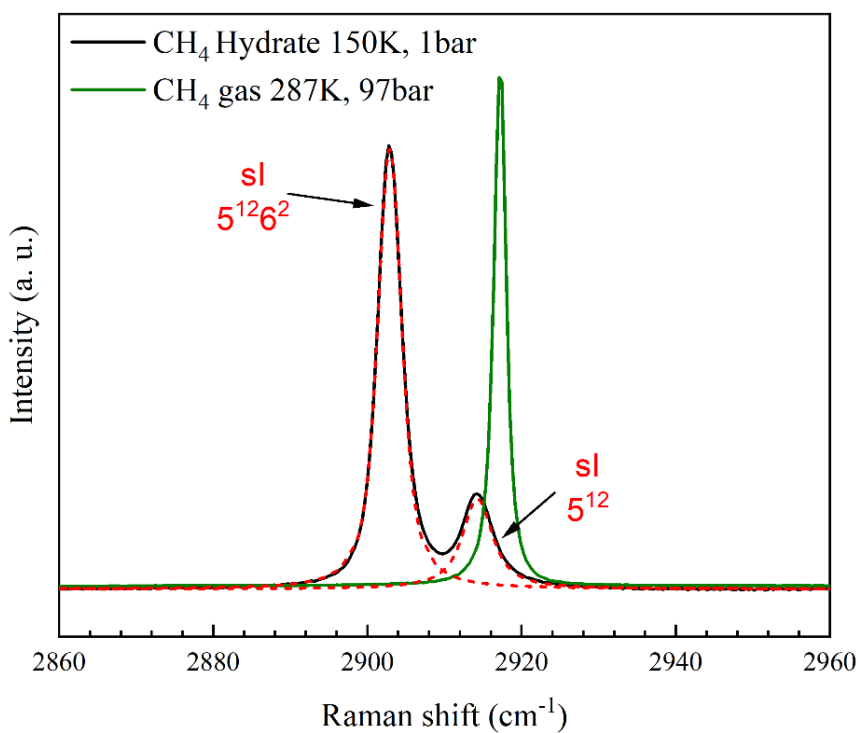
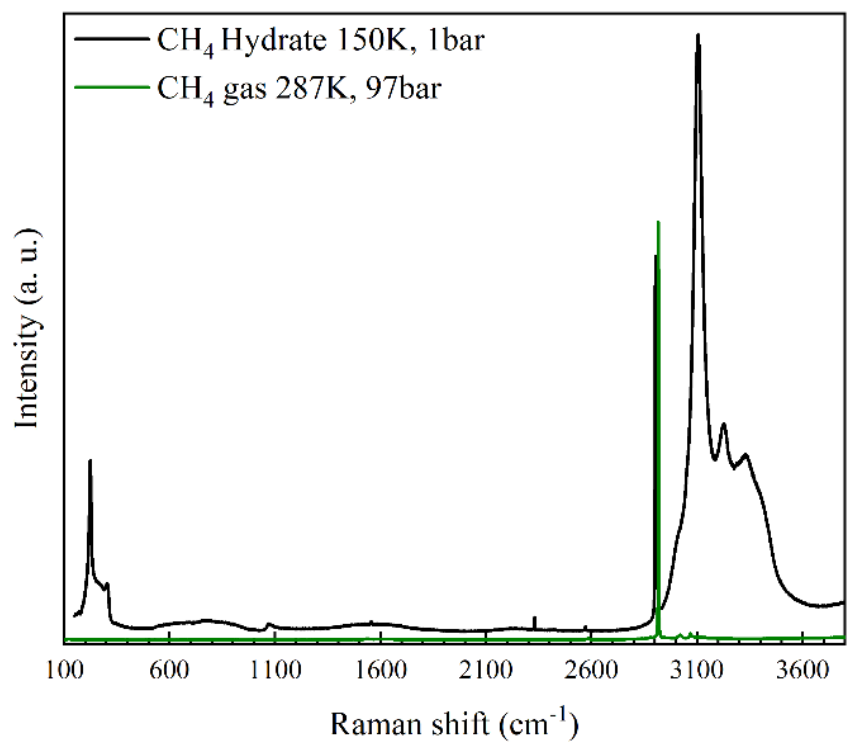


Figure 44. Full Raman spectra of CH₄ gas at 287 K and 97 bar and CH₄ hydrates at 150 K and 1bar (Top). Raman spectra for the stretching modes of CH₄ in gas (287 K and 97 bar) and hydrate (150 K and 1bar) phases (Bottom).

According to the thermodynamics conditions in marine environments, gas hydrates formed from methane gas in natural environment also adopt the structure sI.¹⁵³ In the following chapters, the results collected on synthetic methane hydrates formed in various clay matrices and natural methane hydrate samples recovered in the Black Sea will be compared to this reference synthetic pure methane hydrate data.

Table 9. Raman vibrational modes of CH₄ gas and CH₄ hydrate structure sl: frequencies and assignments. (d: degenerated, s: symmetric)

Gas Molecule	Phase	Type of cage	Vibrational modes	Assignment	Raman shift		P-T conditions		References
					(cm ⁻¹)	(cm ⁻¹)	Previous work (cm ⁻¹)	conditions	
CH ₄	Gas		v ₂	CH-d-bending	1535	287K, 97bar	1534	Not reported	257
			2v ₄	Overtone CH d-bending	~2580	287K, 97bar	2580	275 K, 77bar	27
			v ₁	CH-s-stretching	2917	287K, 97bar	2917.6	293 K, 33.6bar	56
			v ₃	CH-d-stretching	3018	287K, 97bar	3020	293 K, 2-79bar	259
			2v ₂	Overtone CH d-bending	3066	287K, 97bar	3070	293 K, 2-79bar	259
			sl			CH-d-bending	1555.8	150K, 1bar	-
			2v ₄	Overtone CH d-bending	2571.1	150K, 1bar	2570.3	113K, 1bar	233
			5 ¹²	CH-s-stretching	2903	150K, 1bar	2902	150 K, 1bar	240
			5 ¹² 6 ²	CH-s-stretching	2914	150K, 1bar	2912	150 K, 1bar	240
			2v ₂	Overtone CH d-bending	3050	150K, 1bar	3050.1	113K, 1bar	233

b. Ethane hydrate (sI)

Pure ethane gas forms sI hydrate crystals and occupies the LCs ($5^{12}6^2$).^{240,243} The Raman spectrum of C_2H_6 gas, collected at 286 K and 30 bar, is composed of two major signatures: one band at $\sim 994.1\text{ cm}^{-1}$ related to the C-C stretching mode and the C-H Fermi resonance modes given rise to a doublet at $\sim 2899\text{ cm}^{-1}$ and $\sim 2955\text{ cm}^{-1}$ (**Figure 45**).^{243,258} The ethane hydrate sample was synthesized *in-situ* at 277 K and 10 bar. To minimize the Raman signal of free gas, the Raman spectrum of C_2H_6 hydrate was collected at 150 K and 1 bar (by staying in the stability zone of the gas hydrate when decreasing the pressure and the temperature). The Raman signature at $\sim 1000.9\text{ cm}^{-1}$, 2888.6 cm^{-1} and 2943.9 cm^{-1} are attributed to the signatures of C_2H_6 molecules inside LCs ($5^{12}6^2$). Two additional bands of C_2H_6 hydrates were observed at 2735.5 cm^{-1} and 2768.4 cm^{-1} . Minor bands for C_2H_6 hydrates or gas are observed and attributed to combinations of vibrational modes or overtones (detailed in **Table 10**).^{241,243,258}

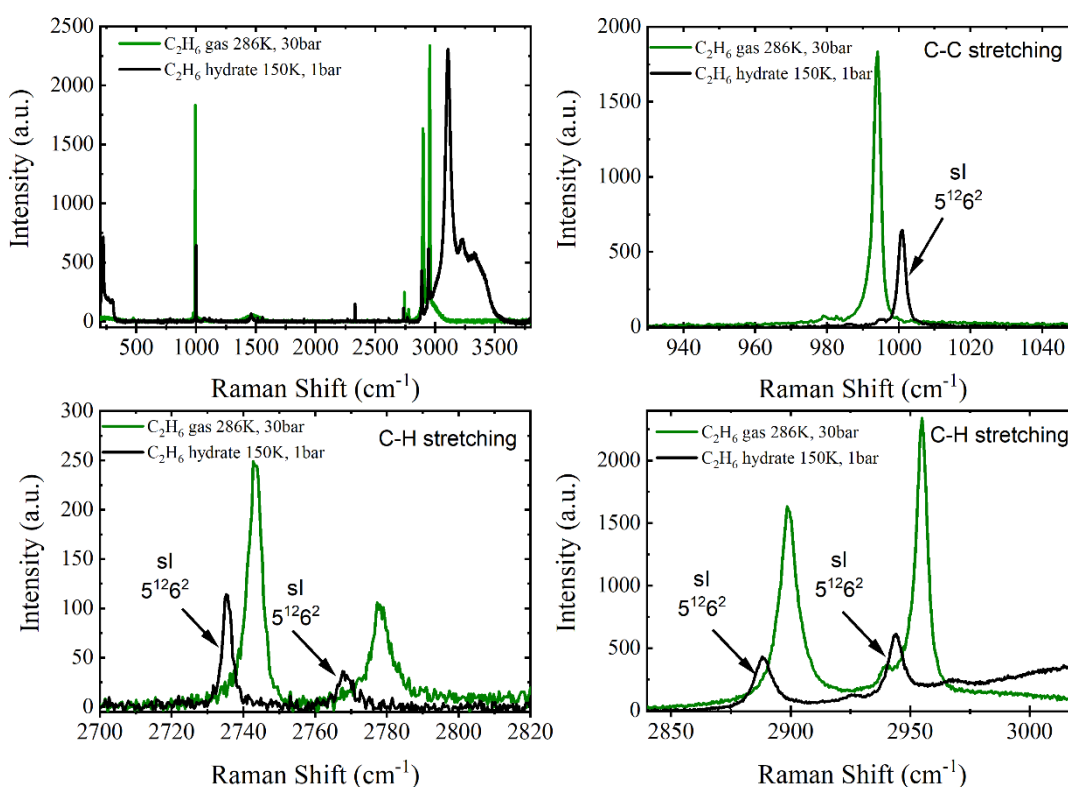


Figure 45. Full Raman spectra of C_2H_6 gas at 286 K and 30 bar, and of C_2H_6 hydrates at 150 K and 1 bar (Top left). Raman spectra for the CC- and CH-stretching modes of C_2H_6 in gas (286 K and 30 bar) and hydrate (150 K and 1bar) phases are represented respectively in top right and bottom spectra.

Table 10. Raman vibrational modes of C₂H₆ gas and C₂H₆ hydrate sI: frequencies and assignments. (a: anti-symmetric, s: symmetric, d: degenerated)

Gas Molecule	Phase	Type of cage	Vibrational modes	Assignment	Raman shift		Raman shift		References
					(cm ⁻¹)	P-T conditions	Previous work (cm ⁻¹)	P-T conditions	
C ₂ H ₆	Gas		v ₃	CC-stretching	994.1	286K, 30bar	994.4	278 K, 21bar	243
			2v ₆	Overtone CH ₃ s-bending	2743.2	286K, 30bar	2744	Gas flame (300-900 K)	258
			2v ₂	Overtone CH ₃ s-bending	2778.3	286K, 30bar	2779	Gas flame (300-900 K)	258
			v ₁ +v ₅	CH- Fermi resonance	2899	286K, 30bar	2900.4	278 K, 21bar	243
			(v ₈ +v ₁₁) or v ₁₀	CH ₃ or CH	2955	286K, 30bar	2955.6		
					2939.9	286K, 30bar	2944.3	278 K, 21bar	243
sI	5 ¹²		v ₃	CC-stretching	1000.9	150K, 1bar	1000.9	274 K, 10bar	243
			2v ₆	Overtone CH ₃ s-bending	2735.5	150K, 1bar	-		
			2v ₂	Overtone CH ₃ s-bending	2768.4	150K, 1bar	-		
			v ₁ +v ₅	CH- Fermi resonance	2888.6	150K, 1bar	2891.2	274 K, 10bar	243
					2943.9	150K, 1bar	2946.2	274 K, 10bar	243
					2925.4	150K, 1bar	2926.5	274 K, 10bar	243

c. Propane (sII)

The neutron powder diffraction experiments (at ILL Powder Diffractometer D1B - $\lambda_0 = 2.52$ Å). conducted in collaboration with B. Bouillot (EMSE, Saint-Etienne, France) on C_3D_8 hydrate structure are analyzed in this section. To form the hydrate, the sample made of glass wool soaked with deuterated water was pressurized at 277 K and 7 bar in a high-pressure cell for 1.5 days. Then, the sample temperature was cooled down to 249 K for 1.5 days and warmed up to 277 K (at constant pressure) for 10 days. The sample was recovered and stored into liquid nitrogen until the neutron experiment. The diffractogram was collected at 150 K and 1 bar by cold transferring under inert atmosphere the powdered hydrate sample into the neutron diffraction cylindrical container (made of vanadium). The C_3D_8 hydrate adopts the structure II.^{56,95,241,247} A Le Bail refinement was used to describe the phases according to the space group of sII hydrate ($Fd\bar{3}m$) and hexagonal ice ($P 6_3/mmc$).²⁶⁰ On the diffractogram, the Bragg peaks are attributed to structure sII hydrate (vertical ticks on **Figure 46**) and hexagonal ice Ih (stars on **Figure 46**). The high intensity of the ice Bragg peaks shows a low conversion of water into hydrate phase.

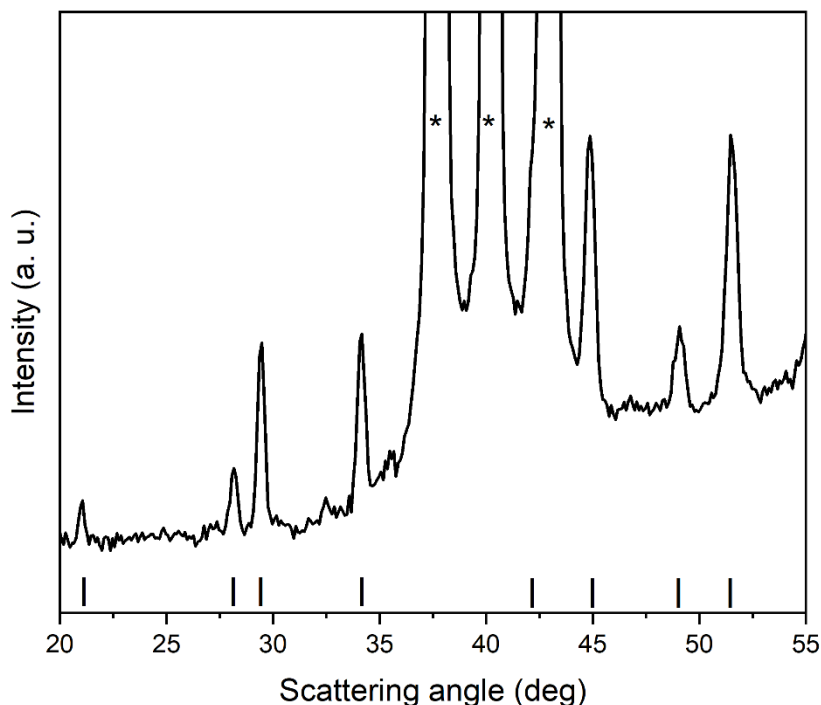


Figure 46. Powder diffractometer of propane hydrate sII collected at 150 K and 1 bar with D1B diffractometer at ILL-Grenoble, FR ($\lambda_0 = 2.52$ Å). Vertical ticks and stars indicate the Bragg peaks of sII hydrate and ice Ih, respectively.

The C₃H₈ hydrate sample was also synthesized *in-situ* at 274 K and 3.4 bar for Raman analysis. The Raman spectroscopic signature of C₃H₈ in the gas phase and in the hydrate, phase are shown in **Figure 47**. The gas spectrum of C₃H₈ is characterized by a band at ~871 cm⁻¹ attributed to the C-C stretching and multiple bands in the C-H stretching regions with a dominant peak at 2887 cm⁻¹ attributed to the symmetric stretching modes of CH₂ (ν_3), and CH₃ (ν_{16}).^{56,258,261} At higher frequencies the spectrum shows several Raman bands related to asymmetric stretching modes of CH₃, symmetric and asymmetric stretching modes of CH₂, as well as several combination and overtone modes (detailed in **Table 11**).^{56,258,261} The C-C stretching modes of C₃H₈ hydrate are observed at 878.1 cm⁻¹ and 1054.4 cm⁻¹.⁹⁵ In the spectral range between 1157 cm⁻¹ and 3000 cm⁻¹, there are multiple Raman signature assigned to the CH vibrational modes of C₃H₈ hydrate (detailed in **Table 12**) with two remarkable bands at 2870.3 cm⁻¹ and 2878.8 cm⁻¹.⁹⁵ Compared to methane (4.36 Å) or ethane (5.5 Å) molecules, propane molecules are very large (6.28 Å) and cannot fit into the small sII cages.³ These large molecules only stabilize the large cavities of the sII structure. Thus, the Raman signatures are attributed to propane signatures within the 5¹²6⁴ cages only.^{95,241,247}

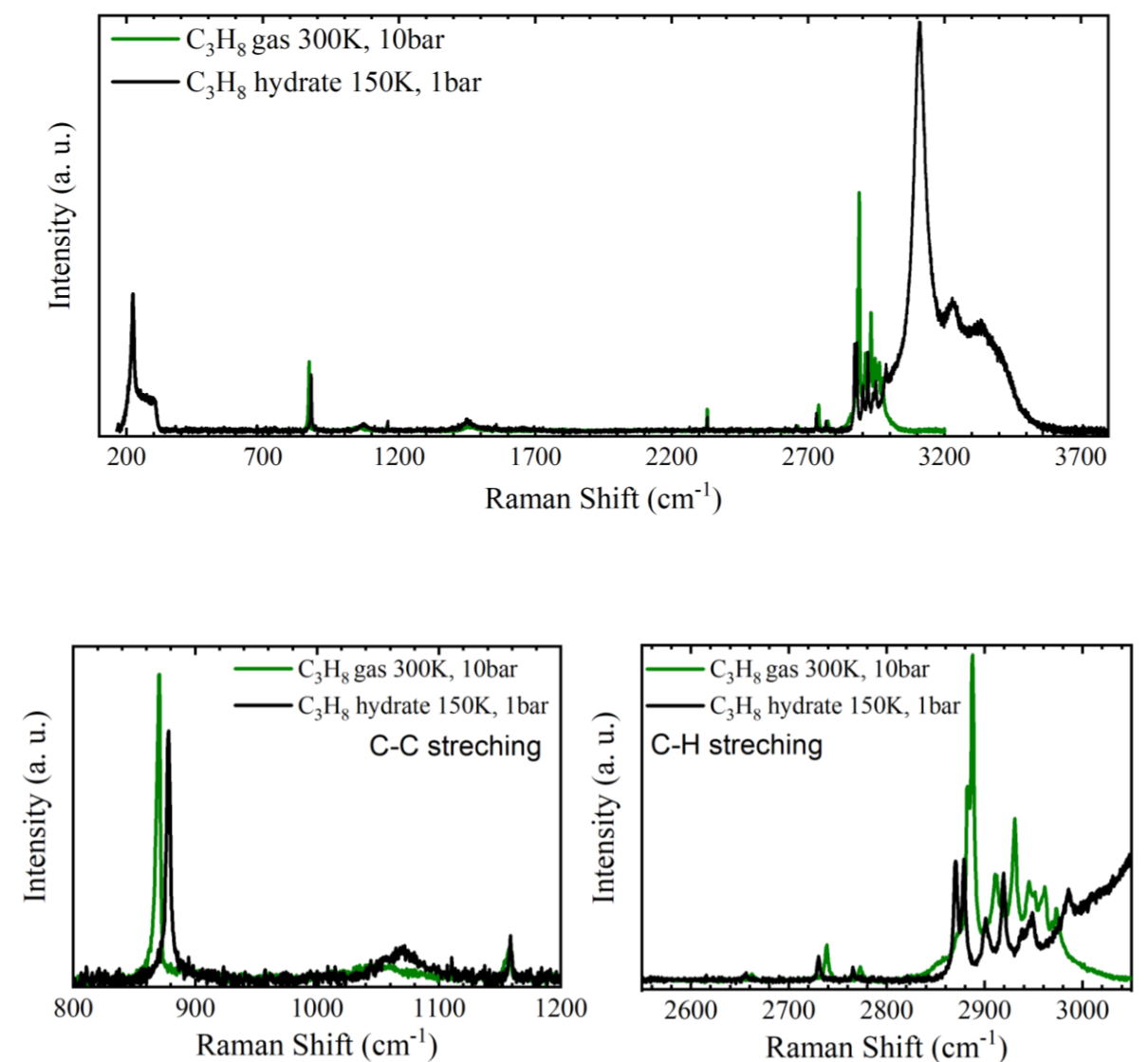


Figure 47. Full Raman spectra of C_3H_8 gas at 300 K and 10 bar and C_3H_8 hydrates at 150 K and 1 bar (Top). Raman spectra for the CC- and CH-stretching modes of C_3H_8 in gas (300 K and 10 bar) and hydrate (150 K and 1 bar) phases are represented respectively in bottom left and right spectra.

Table 11. Raman vibrational modes of C₃H₈ gas: frequencies and assignments. (* uncertain, s: symmetric, d: degenerated)

Gas Molecule	Phase	Vibrational modes	Assignment	Raman shift			References	
				Raman shift (cm ⁻¹)	P-T conditions	Previous work (cm ⁻¹)		
C ₃ H ₈	Gas	v ₈	CC-stretching	870.7	300K, 10bar	871	274 K, 6bar	56
		v ₇	CH ₃ rocking	1157.4	300K, 10bar	1057	Gas flame (300-900 K)	258
		(v ₅ +v ₁₂)*	CH ₂ scissoring + twisting	2738.9	300K, 10bar	2738	Gas flame (300-900 K)	258
		(v ₁₈ +v ₆)*	CH ₃ s-bending	2773.5	300K, 10bar	2771	Gas flame (300-900 K)	258
		v ₁₆	CH ₃ -s-stretching	2882.6	300K, 10bar	2883	300 K	261
		v ₁₆ , v ₃	CH ₃ , CH ₂ s-stretching	2887.7	300K, 10bar	2887	Gas flame (300-900 K)	258
		N.A	-	2911.6	300K, 10bar	2910	Gas flame (300-900 K)	258
		N.A	-	2931.1	300K, 10bar	2929	Gas flame (300-900 K)	258
		N.A	-	2946.6	300K, 10bar	-		
		v ₂	CH ₃ -s-stretching	2961.3	300K, 10bar	2962	Gas flame (300-900 K)	258
		v ₁₀ , v ₁₅	CH ₃ d-stretching	2968.8	300K, 10bar	2967	Gas flame (300-900 K)	258
		v ₂₂	CH ₃ d-stretching	2972.8	300K, 10bar	2973	Gas flame (300-900 K)	258

Table 12. Raman vibrational modes of C₃H₈ hydrate sII: frequencies and assignments. (s: symmetric)

Gas Molecule	Phase	Type of cage	Vibrational modes	Assignment	Raman shift				
					Raman shift (cm ⁻¹)	P-T conditions	Previous work (cm ⁻¹)	P-T conditions	References
C ₃ H ₈	sII	5 ¹² 6 ⁴	ν_8	CC-stretching	878.1	150K, 1bar	878.5	283 K, 28bar	96
		5 ¹² 6 ⁴	ν_7	CH ₃ rocking	1158.7	150K, 1bar	1157.5	283 K, 28bar	96
		5 ¹² 6 ⁴	N.A	-	2656.2	150K, 1bar	-	283 K, 28bar	
		5 ¹² 6 ⁴	N.A	-	2730.4	150K, 1bar	-		
		5 ¹² 6 ⁴	N.A	-	2765.2	150K, 1bar	-		
		5 ¹² 6 ⁴	N.A	-	2870.3	150K, 1bar	2870	283 K, 28bar	96
		5 ¹² 6 ⁴	ν_{16}	CH ₃ -s-stretching	2878.8	150K, 1bar	2878.5	283 K, 28bar	96
		5 ¹² 6 ⁴	ν_{16}, ν_3	CH ₃ , CH ₂ s-stretching	2900.9	150K, 1bar	2900	283 K, 28bar	96
		5 ¹² 6 ⁴	N.A	-	2919.2	150K, 1bar	2920	283 K, 28bar	96
		5 ¹² 6 ⁴	N.A	-	2938.4	150K, 1bar	-		
5 ¹² 6 ⁴	N.A	-	2947.7	150K, 1bar	-				
5 ¹² 6 ⁴	N.A	-	2985.2	150K, 1bar	2984	283 K, 28bar	96		

d. Iso-Butane (sII)

Figure 49 shows the Raman spectrum of pure iso-butane sII hydrate (273 K and 1.5 bar), and the spectrum of liquid iso-butane gas (258 K and 4 bar). The sample was synthesized *in-situ* in a spherical glass capillary with a diameter of 200 μm gas filled with Milli Q water and liquid iso-butane (**Figure 48**). The capillary is placed inside a heating-cooling stage (Linkam CAP500) connected to the pressure device ensuring a constant pressure during the whole experiment (see chapter 2). The spectrum of the liquid iso-butane is collected at 258 K and 4 bar. Then, the temperature and pressure are decreased to 273 K and 1.5 bar. These p-T conditions ensures iso-C₄H₁₀ hydrate formation in presence of iso-C₄H₁₀ gas only.²⁴¹

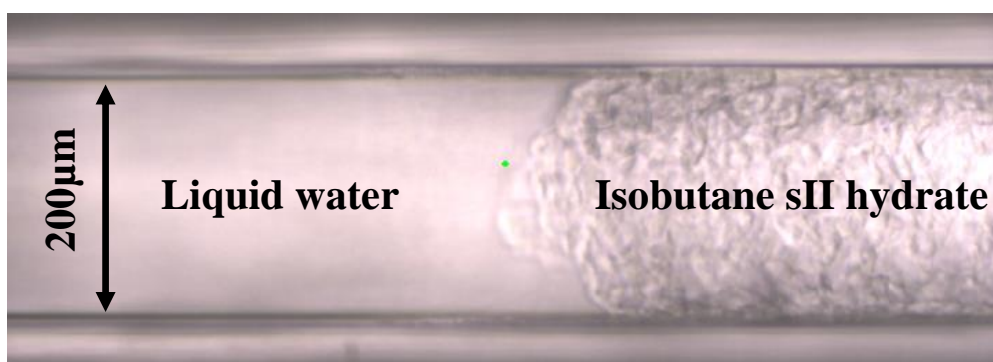


Figure 48. Glass capillary of isobutane hydrate. The water phase is seen on the left of the capillary. The hydrate phase is observed on the right side of the capillary.

The spectrum of liquid iso-C₄H₁₀ shows numerous Raman bands (**Figure 49**). The two most intense bands are observed at 797.5 cm^{-1} (ν_7 symmetric C-C stretching vibrational mode) and at 2870.5 cm^{-1} (ν_3 C-H stretching vibrational mode).²⁶² All the additional signatures are detailed on the **Table 13**.²⁶² The same vibrations are observed at 809.6 cm^{-1} and 2873.9 cm^{-1} , when iso-C₄H₁₀ is trapped in the sII hydrate (see **Figure 49**).⁹⁶ Similarly to propane molecules, the molecular size of iso-C₄H₁₀ only allows the stabilization of the LCs of sII hydrate cages. Hence, all the Raman signatures are assigned to iso-C₄H₁₀ in the large 5¹²6⁴ cavity of sII hydrate (**Table 14**).^{96,241} The shift observed between the ν_7 symmetric C-C stretching mode of iso-butane liquid compared to hydrate phase is 12.1 cm^{-1} . For propane, the shift of the ν_8 C-C stretching mode between the propane gas and hydrate in the 5¹²6⁴ cage is 7.4 cm^{-1} .

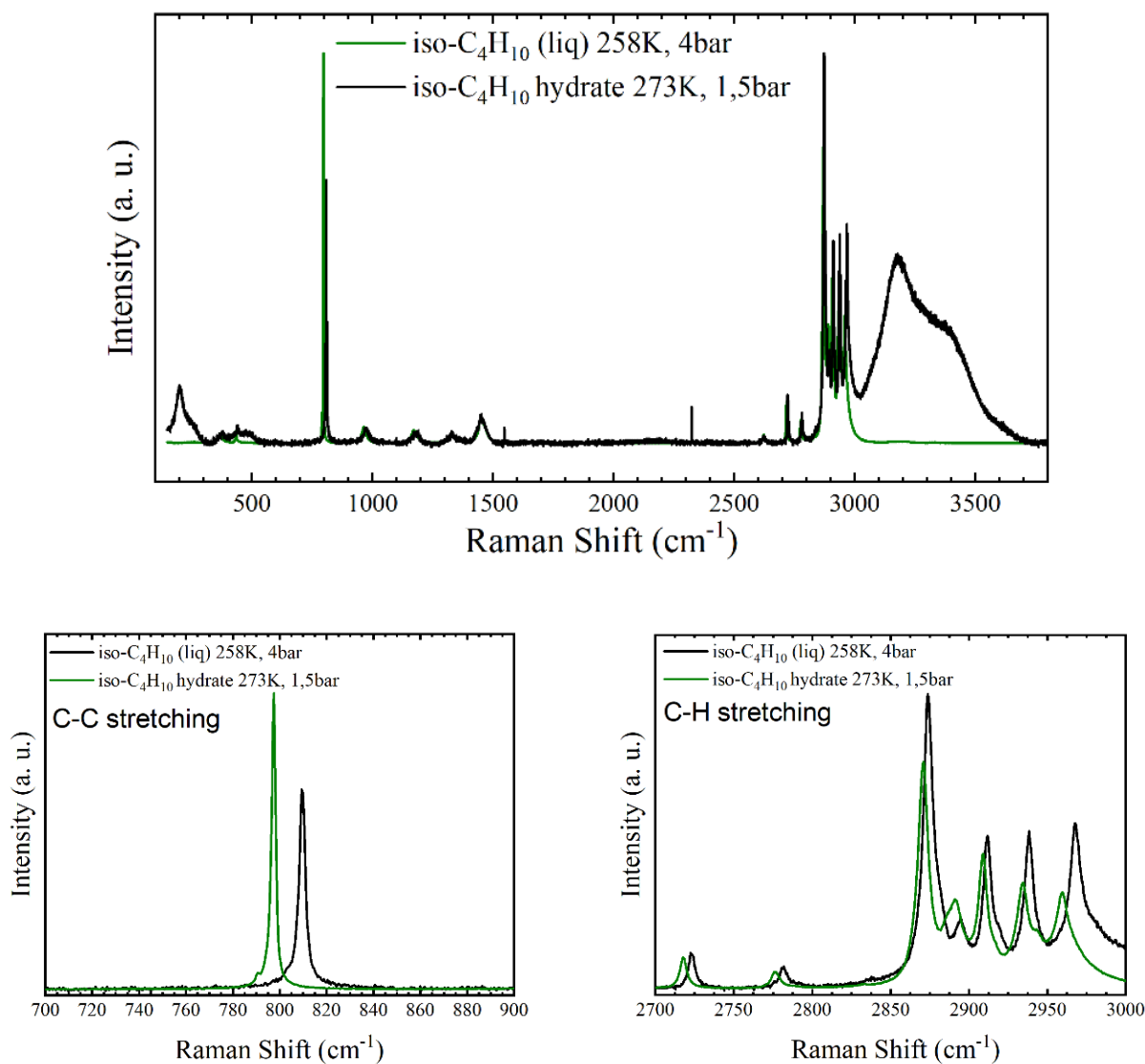


Figure 49. Full Raman spectra of iso-C₄H₁₀ liquid at 258K, 3bar and iso-C₄H₁₀ hydrates at 273 K and 1.5 bar (Top). Raman spectra for the CC- and CH-stretching modes of iso-C₄H₁₀ in liquid (258 K and 3 bar) and hydrate (273 K and 1.5 bar) phases are represented respectively in bottom left and right spectra.

Table 13. Raman vibrational modes of iso-C₄H₁₀ liquid: frequencies and assignments. (a: anti-symmetric, s: symmetric)

Gas Molecule	Phase	Vibrational modes	Assignment	Raman shift (cm ⁻¹)	P-T conditions	Raman shift Previous work (cm ⁻¹)	P-T conditions	References
i-C ₄ H ₁₀	Liquid	v ₁₉	CCC-bending	369	258K, 4bar	367	203 K, 1bar	262
		v ₈	CCC-bending	434.9	258K, 4bar	433	203 K, 1bar	262
		v ₇	CC-stretching	797.2	258K, 4bar	799	203 K, 1bar	262
		v ₁₈	CC-stretching	915.6	258K, 4bar	917	203 K, 1bar	262
		v ₁₇	CCH ₃ -bending	964.2	258K, 4bar	966	203 K, 1bar	262
		v ₁₆	CCH ₃ -bending	1171.3	258K, 4bar	1169	203 K, 1bar	262
		v ₆	CCH ₃ -bending	1184.7	258K, 4bar	1184	203 K, 1bar	262
		v ₁₅	CH-bending	1328.7	258K, 4bar	1327	203 K, 1bar	262
		v ₁₄	CH ₃ -s-bending	1369.4	258K, 4bar	~1373	203 K, 1bar	262
		v _{12, v13}	CH ₃ -a-bending	1451.4	258K, 4bar	1450	203 K, 1bar	262
		v ₄	CH ₃ -a-bending	1464.7	258K, 4bar	~1468	203 K, 1bar	262
		2v ₁₄	Overtone CH ₃ -s-bending	2717.6	258K, 4bar	2716	203 K, 1bar	262
		2v ₁₂	Overtone CH ₃ -a-bending	2776.6	258K, 4bar	2783	203 K, 1bar	262
		v ₃	CH-stretching	2870.5	258K, 4bar	2869	203 K, 1bar	262
		2v ₁₂ or 2v ₁₃	Overtone CH ₃ -a-bending	2890.8	258K, 4bar	2889	203 K, 1bar	262
		v ₂	CH-s-stretching	2908.8	258K, 4bar	2907	203 K, 1bar	262
		v ₁	CH-a-stretching	2934.4	258K, 4bar	2933	203 K, 1bar	262
v _{9, v10, v11}	CH-a-stretching, CH-s-stretching	2959.6	258K, 4bar	2958	203 K, 1bar	262		

Table 14. Raman vibrational modes of iso-C₄H₁₀ hydrate sII: frequencies and assignments. (a: anti-symmetric, s: symmetric)

Gas Molecule	Phase	Type of cage	Vibrational modes	Assignment	Raman shift (cm ⁻¹)		P-T conditions	Raman shift (cm ⁻¹)		References
								Previous work	conditions	
i-C ₄ H ₁₀	sII	5 ¹² 6 ⁴	v ₁₉	CCC-bending	378.2	-	273K, 1.5bar	-	-	
			v ₈	CCC-bending	440.7	-	273K, 1.5bar	-	-	
			v ₇	CC-stretching	809.6	810	273K, 1.5bar	200 K, 10bar	61	
			v ₁₇	CCH ₃ -bending	974.2		273K, 1.5bar			
			-	CCH ₃ -bending	1182.1		273K, 1.5bar			
			v ₁₅	CH-bending	1329		273K, 1.5bar			
			v ₁₂ , v ₁₃	CH ₃ -a-bending	1452.9		273K, 1.5bar			
			2v ₁₄	Overtone CH ₃ -s-bending	2723.2		273K, 1.5bar			
			2v ₁₂	Overtone CH ₃ -a-bending	2781.7		273K, 1.5bar			
			v ₃	CH-stretching	2873.9	2872	273K, 1.5bar	200 K, 10bar	61	
			2v ₁₂ or 2v ₁₃	Overtone CH ₃ -a-bending	2894.5	2890	273K, 1.5bar	200 K, 10bar	61	
			v ₂	CH-s-stretching	2911.7	2910	273K, 1.5bar	200 K, 10bar	61	
			v ₁	CH-a-stretching	2938.3	2938	273K, 1.5bar	200 K, 10bar	61	
v ₉ , v ₁₀ , v ₁₁	CH-a-stretching, CH-s-stretching	2967.8	2969	273K, 1.5bar	200 K, 10bar	61				

e. Carbon dioxide (sI)

CO₂ hydrate structure was analyzed by neutron powder diffraction at ILL (Powder Diffractometer D1B – $\lambda_0 = 2.52 \text{ \AA}$). The sample was prepared prior to the experiment by soaking fiberglass wool with deuterated water in a high-pressure cell at 277 K and 20 bar during 1.5 days. Then, the temperature of the sample was cooled down to 249 K for 1.5 days and warmed up to 277 K during 10 days (in the stability p-T region of the gas hydrate). The sample was recovered and stored into liquid nitrogen until the neutron experiment. The diffractogram was collected at 130 K and 1 bar by cold transferring under inert atmosphere the powdered hydrate sample into the neutron diffraction cylindrical container (made of vanadium). Similarly to CH₄, the hydrate formed from CO₂ gas adopts the structure sI.⁵⁶ Bragg peaks of the diffractograms are attributed to sI hydrate (vertical ticks on **Figure 50**) and hexagonal ice Ih (stars on **Figure 50**). The Bragg peaks of ice are extremely intense, since only a small amount of deuterated water has been converted into sI hydrate.

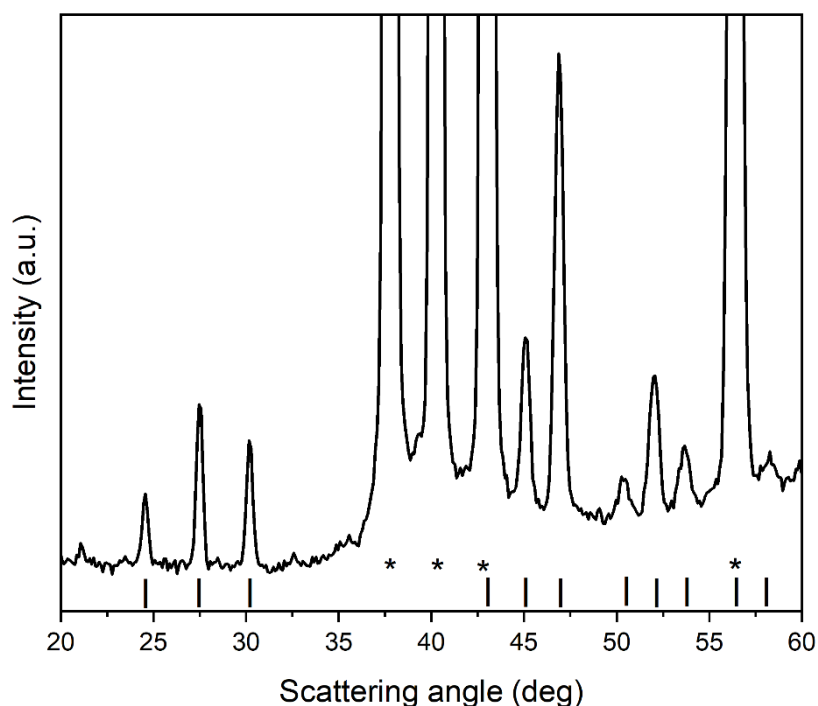


Figure 50. Powder diffractometer of carbone dioxide hydrate sI collected at 130 K and 1 bar with D1B diffractometer at ILL-Grenoble, FR ($\lambda_0 = 2.52\text{\AA}$). Vertical ticks and stars indicate the Bragg peaks of sII hydrate and ice Ih respectively.

The Raman spectrum of CO₂ hydrate in **Figure 51** was taken from the PhD work of Dr. C. Petuya.²⁵² The sample was formed in-situ at 270 K, 25 bar during several hours. The spectrum of CO₂ gas is constituted of two major bands observed at 1286 cm⁻¹ and 1389 cm⁻¹ and two minor bands at 1266 cm⁻¹ and 1410 cm⁻¹, respectively called the Fermi diad and hot bands, which are coupled through Fermi resonance.⁵⁶ The Raman bands related to the formation of CO₂ hydrate sI are broader and shifted to lower frequencies at 1276.9 cm⁻¹ and 1381.8 cm⁻¹, due the confinement of the CO₂ molecules within the cages. It should be noted that the frequency difference for CO₂ molecules in LCs and in SCs could not be resolved in the present experiment. The difference between these two vibrational signatures is within 1 cm⁻¹ according to IR absorption experiments.⁵⁹ All the band attribution are detailed in **Table 15**.

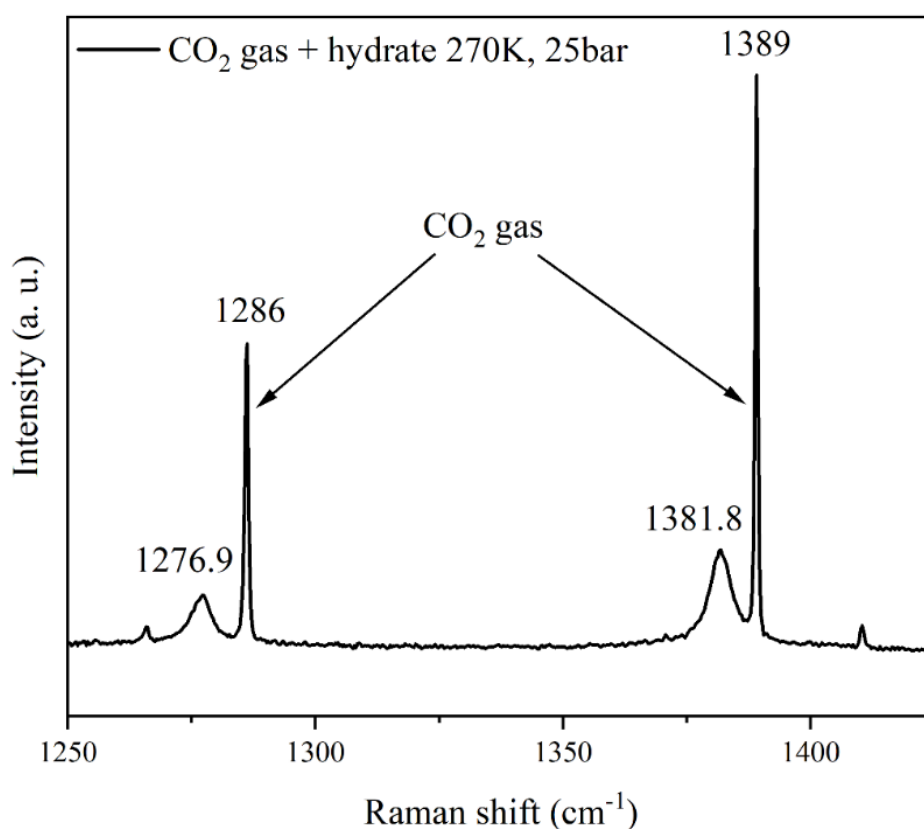


Figure 51. Raman spectrum of Fermi resonance of CO₂ gas and CO₂ trapped in sI hydrate at 270 K, 25 bar.

Table 15. Raman vibrational modes of CO₂ gas and CO₂ hydrate sI: frequencies and assignments.

Gas Molecule	Phase	Type of cage	Vibrational modes	Assignment	Raman shift		P-T conditions		References
					(cm ⁻¹)	(cm ⁻¹)			
CO ₂	Gas		ν ₁ +2ν ₂	Fermi resonance (s-stretching + bending overtone)	1286	1286	270K, 25bar	293 K, 33.6bar	56
					1389	1389		293 K, 33.6bar	56
sI		5 ¹² , 5 ¹² 6 ²	ν ₁ +2ν ₂	Fermi resonance (s-stretching + bending overtone)	1276.9	1277	270K, 25bar	Not reported	56
					1381.8	1382		Not reported	56

III. MIXED GAS HYDRATES.

a. Methane – Ethane (sII)

In natural environments, hydrates rarely form in the presence of pure gas; the composition of natural gas varies and thus, their composition and their structure also. Methane remains the main gaseous component, closely followed by ethane.^{3,263} As described on the previous sections, both methane and ethane form sI hydrate. Models dedicated to the prediction of structures formed as a function of gas composition initially assumed that the methane-ethane mixture would form the sI hydrate. However, experimental work by Holder and Hand showed inconsistencies with the results predicted by the theoretical models.²⁶⁴ Work was then carried out on the methane-ethane system with different mixture compositions in order to highlight the formation of hydrates in structure sII.²⁶⁵ Thermodynamics²⁵⁴, Raman and NMR investigations²⁴³ have led to confirm the formation of the structure sII for methane ethane mixture constituted of 72.2 mol.% and 75 mol.% of methane. In this work, structure II hydrates were formed at 274 K and 84bar with a gas mixture constituted of 93mol.% of CH₄ and 7mol.% of C₂H₆. According to Ohno *et al.*, this mixture yields the formation of the thermodynamically stable sII structure.²⁵⁴ Once formed *in-situ*, the pressure and temperature were decreased to 150 K and 1bar to preserve the hydrates and to minimize the Raman signatures of free gas. The Raman spectra collected are represented in **Figure 52** and all Raman signatures are detailed in **Table 16**. In the region between 970 and 1020 cm⁻¹, the main band related to the ethane molecule in the gas phase (300K and 83bar) is observed at 993cm⁻¹.^{56,243} As described previously, this band is attributed to CC-stretching modes. This band, in the case of pure ethane hydrate is observed at 1000.9 cm⁻¹ and corresponds to the signature of the hydrate in structure sI. In the case of CH₄ – C₂H₆ gas mixture, this signature is observed at lower frequency (991.4 cm⁻¹), constituting a Raman signature of the formation of structure sII hydrate. The CH-stretching region between 2850 cm⁻¹ and 2975 cm⁻¹, contains the methane and ethane signatures in both gas and hydrate phases. The Raman signature of methane gas is observed at ~2916 cm⁻¹ at 300 K and 83 bar. In the CH₄ – C₂H₆ mixed hydrate phase at 150K, three methane bands are observed. At ~2917 cm⁻¹, remaining methane gas signal is observed. The two other bands at 2902.8 cm⁻¹ and 2913.5 cm⁻¹, are attributed to the signal of methane molecules in the LCs (5¹²6⁴) and SCs (5¹²), respectively. The frequency of these bands could be related to the formation of sII hydrate with both type of cages filled with methane. The intensities ratio between the SCs and the LCs Raman signatures helps also to confirm this hypothesis, since it

is below 1. Let recall that for the methane hydrate in structure sI, the ratio between the LCs and the SCs is 3:1 due to the relative abundance of large cavities (leading to a LC to SC Raman ratio of *ca.* 3 as shown in section I.a) of this chapter). For the structure sII a LC to SC ratio of 1:2 is expected (they are 8 LCs and 16 SCs in sII hydrate)., leading to a LC to SC Raman intensities ratio less than one – as observed in the present experiment and previous work.³ The other bands observed in this region of the spectrum are related to ethane molecule. At 300 K, and 83 bar, the spectrum of the CH₄ – C₂H₆ gas mixture shows two bands at 2898.5 cm⁻¹ and 2954.2 cm⁻¹ attributed to CH-Fermi resonance of ethane molecule. These signatures are shifted to lower frequencies at 2885.1 cm⁻¹ and 2940.2 cm⁻¹, and assigned to ethane hydrates in structure II. As these two bands did not exhibit any splitting characteristic of the confinement in the two types of cages, it is highly probable that C₂H₆ molecule occupies only the large 5¹²6⁴ cavity in the mixed hydrate. Compare to pure ethane sI hydrate, the C–H region resonance doublet band frequencies of C₂H₆ differ by 4 cm⁻¹ towards the lower frequencies in sII. Again, this constitutes a typical Raman signature of the formation of sII hydrate containing ethane molecule.

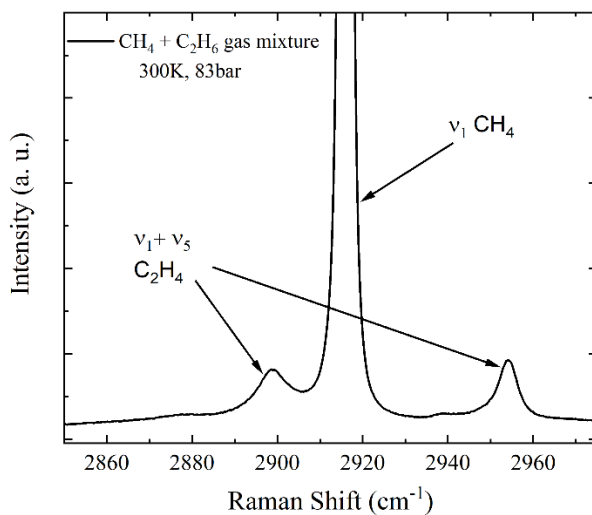
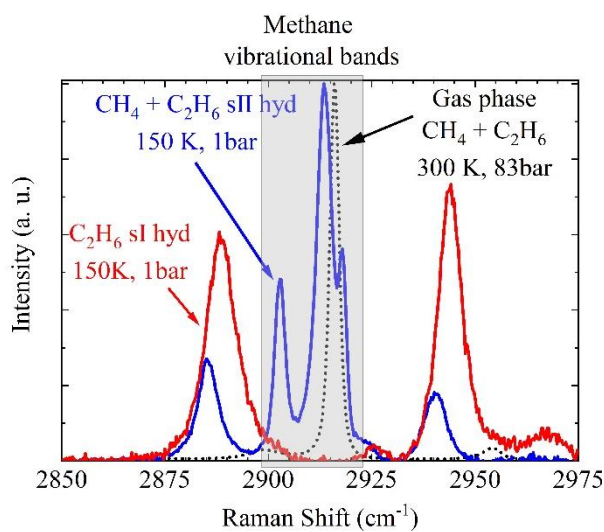
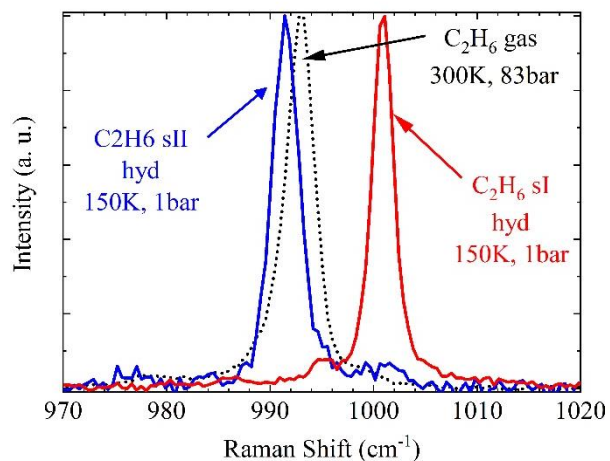


Figure 52. Raman spectra for the CC- and CH-stretching modes of mixed $\text{CH}_4 - \text{C}_2\text{H}_6$ hydrate sII (150 K and 1 bar) compared to the Raman signatures of gas mixture (300 K and 83 bar) and pure C_2H_6 sI hydrate.

Table 16. Raman vibrational modes of CH₄ – C₂H₆ gas mixture and mixed CH₄ – C₂H₆ hydrate sII: frequencies and assignments. (s: symmetric)

Gas Molecule	Phase	Type of cage	Vibrational modes	Assignment	Raman shift		P-T conditions	References	
					(cm ⁻¹)	(cm ⁻¹)			
CH₄-C₂H₆									
C ₂ H ₆ (gas)	C ₂ H ₆ (gas)		v ₃	CC-stretching	993	994.4	300K, 83bar	298 K, 21bar	243
	CH ₄ (gas)		v ₁	CH-s-stretching	2916	2917.9	300K, 83bar	298K, 21bar	56
	C ₂ H ₆ (gas)		v ₁ +v ₅	CH- Fermi resonance	2898.5	2900.4	300K, 83bar	298 K, 21bar	243
	C ₂ H ₆ (gas)				2954.2	2955.6	300K, 83bar		
C ₂ H ₆ (sII)	C ₂ H ₆ (sII)	5 ¹² 6 ⁴	v ₃	CC-stretching	991.4	992.2	150K, 1bar	274K, 15bar	243
	CH ₄ (sII)	5 ¹²	v ₁	CH-s-stretching	2902.8	2903.7	150K, 1bar	274K, 15bar	243
	CH ₄ (sII)	5 ¹² 6 ⁴	v ₁	CH-s-stretching	2913.5	2913.7	150K, 1bar	274K, 15bar	243
	C ₂ H ₆ (sII)	5 ¹² 6 ⁴	v ₁ +v ₅	CH- Fermi resonance	2885.1	2887.3	150K, 1bar	274K, 15bar	243
	C ₂ H ₆ (sII)	5 ¹² 6 ⁴			2940.2	2942.3	150K, 1bar	274K, 15bar	243

b. *n*-Butane – Methane (sII)

The methane – *n*-butane mixture was used to record the Raman signatures of *n*-butane hydrates structure II. Compared to the previous hydrocarbons studied in this work, *n*-butane has the characteristic of having two rotational isomers, the *trans* and *gauche* forms. It is well known in the literature that these two forms exhibit distinct Raman signatures, allowing to clearly identified the preferred encapsulation of one of the conformers in the hydrate.

A gas mixture constituted of 95mol.% CH₄ and 5mol.% *n*-C₄H₁₀ was used to form sII *n*-butane hydrate. The spectrum of the gas mixture was collected at 300 K and 19 bar (**Figure 53**). In the spectral region between 400 and 1200 cm⁻¹, Raman bands can be assigned to both *gauche* (g) and *trans* (t) *n*-butane. The CC stretching vibrations of the two forms are represented by two bands at 829.1 cm⁻¹ (ν₃₂, g) and 1077.6 cm⁻¹ (ν₁₃, g) for the *gauche* conformer, and at 838.8 cm⁻¹ (ν₁₀, t) and 1060 cm⁻¹ (ν₉, t) for the *trans* conformer.^{56,257,266} The other bands in this region may be either attributed to *gauche* or *trans*. The *trans* *n*-butane shows two bands at 430.5 cm⁻¹ (ν₁₁, t) and 1150.2 cm⁻¹ (ν₈, t) assigned to CCC deformation and CH₃ rocking modes, respectively. The bands at 475.5 cm⁻¹ (ν₃₅, g), 750.3 cm⁻¹ (ν₃₄, g), 789.6 cm⁻¹ (ν₁₆, g) and 982 cm⁻¹ (ν₃₂, g) correspond to the *gauche* form.^{56,257,266} The CH-stretching region of the spectrum is extremely complex with multiple bands due to classic Fermi resonance between symmetric, antisymmetric stretching and overtones deformations, but especially by the fact that *n*-butane consists of two conformers, leading to more than 20 bands in this spectral region.²⁶⁶ All the maxima are detailed in the **Table 17** and **Table 18**.

The mixed hydrate was synthesized from the mixture 95mol.% CH₄ and 5mol.% *n*-C₄H₁₀ at 274 K and 19 bar and the Raman spectrum was collected 150 K and 1bar to minimize free gas Raman signatures. What can be identified first on the hydrate spectra is the presence of only one Raman band at 836.9 cm⁻¹ and 1080.8 cm⁻¹ where two pairs of bands (*trans* and *gauche*) were observed in the gas phase. The band at 1080.8 cm⁻¹ is shifted to higher frequencies compared to the same signature in the gas phase for the *gauche* form. The proximity of these signals suggest *gauche* *n*-butane would be preferentially encapsulated in the LCs (5¹²6⁴) of sII hydrate compared to *trans* *n*-butane. The other bands related to sII *n*-butane hydrates are also shifted to higher frequencies compared to those in the gas-phase spectrum and are attributed to the *gauche* form of *n*-butane. Whenever the gas spectrum showed signatures of *trans* *n*-butane, there are no hydrate signature which confirms *trans* *n*-butane does not participate to sII hydrate formation. The same Raman observations were detailed by Subramanian *et al.* confirming the

hypothesis of Davidson *et al.* on the possibility that *trans* n-butane (7.9 Å) may be too large to enter the $5^{12}6^4$ cages compared to the *gauche* form (7.1 Å).^{241,267} The CH-region of the spectrum is constituted of only four bands for sII n-butane hydrates at 2864.3 cm^{-1} (CH_2 s-stretching), 2884.9 cm^{-1} , 2937.7 cm^{-1} and 2947.8 cm^{-1} . The other signal in this region is assigned to the signatures of methane sII hydrate with two Raman bands at 2901.9 cm^{-1} and 2911.5 cm^{-1} attributed respectively to methane in SCs (5^{12}) and LCs ($5^{12}6^4$). The Raman vibrational modes are detailed in **Table 19**.

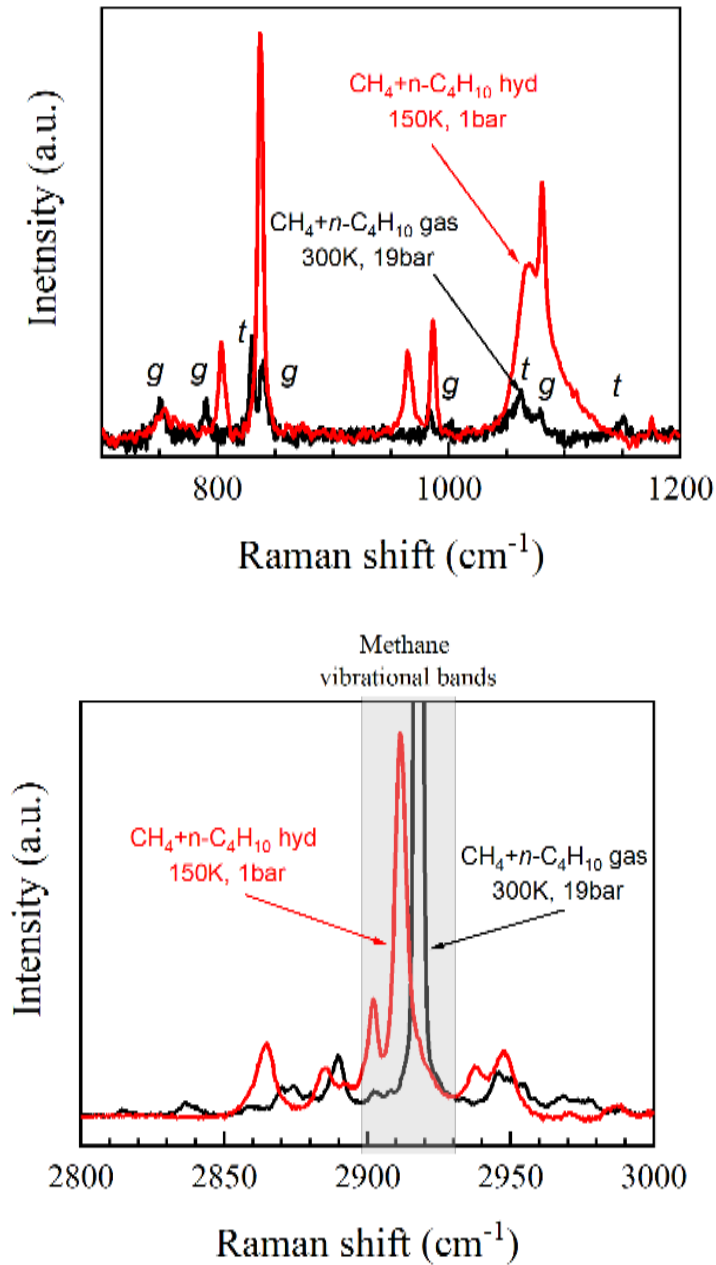


Figure 53. Raman spectra for the CC- and CH-stretching modes of mixed CH₄ – n-C₄H₁₀ cryo-hydrate sII (150K and 1 bar) compared to the Raman signatures of gas mixture *trans* (*t*) and *gauche* (*g*) (300 K and 19 bar).

Table 17. Raman vibrational modes of CH₄ – *n*-C₄H₁₀ gas mixture: frequencies and assignments. (* uncertain, N.A not attributed, t: trans, g: gauche, a: anti-symmetric, s: symmetric)

Gas Molecule	Phase	Vibrational modes	Assignment	Raman shift (cm ⁻¹)	P-T conditions	Raman shift		References
						Previous work (cm ⁻¹)	P-T conditions	
CH₄								
<i>n</i> -C ₄ H ₁₀								
<i>n</i> -C ₄ H ₁₀ (gas)	N.A		-	418	300K, 19bar	-	-	-
<i>n</i> -C ₄ H ₁₀ (gas)	v ₁₁ , t	CCC bending		430.5	300K, 19bar	430	293K, 1bar	266
<i>n</i> -C ₄ H ₁₀ (gas)	v ₃₅ , g	CCC bending		475.5	300K, 19bar	469	Gas flame (300-900 K)	258
<i>n</i> -C ₄ H ₁₀ (gas)	v ₃₄ , g	CH ₂ rocking		750.3	300K, 19bar	747	Gas flame (300-900 K)	258
<i>n</i> -C ₄ H ₁₀ (gas)	v ₁₆ , g	CH ₂ rocking		789.6	300K, 19bar	789	293K, 1bar	266
<i>n</i> -C ₄ H ₁₀ (gas)	v ₁₅ , g	CC-stretching		829.1	300K, 19bar	829.5	293K, 1bar	266
<i>n</i> -C ₄ H ₁₀ (gas)	v ₁₀ , g	CC-stretching		838.8	300K, 19bar	837.2	293K, 1bar	266
<i>n</i> -C ₄ H ₁₀ (gas)	v ₃₂ , g	CH ₃ rocking		982.6	300K, 19bar	982	293K, 1bar	266
<i>n</i> -C ₄ H ₁₀ (gas)	v ₉ , t	CC-stretching		1060	300K, 19bar	1062	293K, 1bar	266
<i>n</i> -C ₄ H ₁₀ (gas)	v ₁₃ , g	CC-stretching		1077.6	300K, 19bar	1079	293K, 1bar	266
<i>n</i> -C ₄ H ₁₀ (gas)	v ₈ , t	CH ₃ rocking		1150.2	300K, 19bar	1151	293K, 1bar	266
<i>n</i> -C ₄ H ₁₀ (gas)	N.A	-		2814.7	300K, 19bar	-	-	-
<i>n</i> -C ₄ H ₁₀ (gas)	N.A	-		2837.4	300K, 19bar	-	-	-
<i>n</i> -C ₄ H ₁₀ (gas)	-	CH ₂ -a-stretching*		2859.6	300K, 19bar	2860	Gas flame (300-900 K)	258
<i>n</i> -C ₄ H ₁₀ (gas)	N.A	-		2869.9	300K, 19bar	-	-	-
<i>n</i> -C ₄ H ₁₀ (gas)	v ₂ , t	CH ₃ -s-stretching*		2874.3	300K, 19bar	2872	Gas flame (300-900 K)	258
<i>n</i> -C ₄ H ₁₀ (gas)	N.A	-		2879.9	300K, 19bar	-	-	-
<i>n</i> -C ₄ H ₁₀ (gas)	N.A	-		2889.6	300K, 19bar	-	-	-
<i>n</i> -C ₄ H ₁₀ (gas)	N.A	-		2902.5	300K, 19bar	-	-	-
<i>n</i> -C ₄ H ₁₀ (gas)	N.A	-		2907.9	300K, 19bar	-	-	-

Table 18. Raman vibrational modes of CH₄ – *n*-C₄H₁₀ gas mixture: frequencies and assignments. (* uncertain, N.A not attributed, t: trans, g: gauche, a: anti-symmetric, s: symmetric)

Gas Molecule	Phase	Vibrational modes	Assignment	Raman shift		P-T conditions	References
				(cm ⁻¹)	(cm ⁻¹)		
CH₄- <i>n</i>-C₄H₁₀	<i>n</i> -C ₄ H ₁₀ (gas)	$\nu_{21, t}$	CH ₂ -a-stretching*	2912.5	2912	300K, 19bar Gas flame (300-900 K)	258
	CH ₄ (gas)	ν_1	CH-s-stretching*	2917.8	2917.6	300K, 19bar 298 K, 21bar	56
	<i>n</i> -C ₄ H ₁₀ (gas)	-	CH ₂ -a-stretching*	2924.9	2920	300K, 19bar Gas flame (300-900 K)	258
	<i>n</i> -C ₄ H ₁₀ (gas)	$\nu_{13, t}$	CH ₂ -a-stretching*	2932.2	2930	300K, 19bar Gas flame (300-900 K)	258
	<i>n</i> -C ₄ H ₁₀ (gas)	N.A	-	2939.3	-	300K, 19bar	-
	<i>n</i> -C ₄ H ₁₀ (gas)	N.A	-	2945.5	-	300K, 19bar	-
	<i>n</i> -C ₄ H ₁₀ (gas)	N.A	-	2950.2	-	300K, 19bar	-
	<i>n</i> -C ₄ H ₁₀ (gas)	N.A	-	2954.1	-	300K, 19bar	-
	<i>n</i> -C ₄ H ₁₀ (gas)	N.A	-	2959	-	300K, 19bar	-
	<i>n</i> -C ₄ H ₁₀ (gas)	-	CH ₃ bending*	2968	-	300K, 19bar Gas flame (300-900 K)	258
	<i>n</i> -C ₄ H ₁₀ (gas)	N.A	-	2977.2	-	300K, 19bar	-
	<i>n</i> -C ₄ H ₁₀ (gas)	N.A	-	2989.8	-	300K, 19bar	-
	<i>n</i> -C ₄ H ₁₀ (gas)	N.A	-	2999.2	-	300K, 19bar	-
	<i>n</i> -C ₄ H ₁₀ (gas)	N.A	-	3018	-	300K, 19bar	-
<i>n</i> -C ₄ H ₁₀ (gas)	N.A	-	3022.3	-	300K, 19bar	-	

Table 19. Raman vibrational modes of mixed $\text{CH}_4 - n\text{-C}_4\text{H}_{10}$ hydrate sII: frequencies and assignments. (* uncertain, N.A not attributed, t: trans, g: gauche, a: anti-symmetric, s: symmetric)

Gas Molecule	Phase	Type of cage	Vibrational modes	Assignment	Raman shift (cm^{-1})	P-T conditions	Raman shift Previous work (cm^{-1})	P-T conditions	References
CH_4 - $n\text{-C}_4\text{H}_{10}$	$n\text{-C}_4\text{H}_{10}(\text{sII})$	$5^{12}6^4$	g	CCC bending*	419.9	150K, 1bar	-	-	-
	$n\text{-C}_4\text{H}_{10}(\text{sII})$	$5^{12}6^4$	ν_{35} , g	CCC bending	475.7	150K, 1bar	-	-	-
	$n\text{-C}_4\text{H}_{10}(\text{sII})$	$5^{12}6^4$	ν_{34} , g	CH_2 rocking	756.5	150K, 1bar	-	-	-
	$n\text{-C}_4\text{H}_{10}(\text{sII})$	$5^{12}6^4$	ν_{16} , g	CH_2 rocking	803.5	150K, 1bar	806	274K, 19.3bar	241
	$n\text{-C}_4\text{H}_{10}(\text{sII})$	$5^{12}6^4$	ν_{10} , g	CC-stretching	836.9	150K, 1bar	838.7	274K, 19.3bar	241
	$n\text{-C}_4\text{H}_{10}(\text{sII})$	$5^{12}6^4$	ν_{32} , g	CH_3 rocking	986.2	150K, 1bar	986.7	274K, 19.3bar	241
	$n\text{-C}_4\text{H}_{10}(\text{sII})$	$5^{12}6^4$	N.A	CC-stretching	1067.1	150K, 1bar	-	-	-
	$n\text{-C}_4\text{H}_{10}(\text{sII})$	$5^{12}6^4$	ν_{13} , g	CC-stretching	1080.8	150K, 1bar	1081.6	274K, 19.3bar	241
	$n\text{-C}_4\text{H}_{10}(\text{sII})$	$5^{12}6^4$	N.A	-	2864.3	150K, 1bar	-	-	-
	$n\text{-C}_4\text{H}_{10}(\text{sII})$	$5^{12}6^4$	N.A	-	2884.9	150K, 1bar	-	-	-
	$\text{CH}_4(\text{sI})$	5^{12}	ν_1	CH-s-stretching	2902.8	150K, 1bar	2903.7	274K, 19.3bar	241
	$\text{CH}_4(\text{sI})$	$5^{12}6^4$	ν_1	CH-s-stretching	2913.5	150K, 1bar	2913.7	274K, 19.3bar	241
	$n\text{-C}_4\text{H}_{10}(\text{sII})$	$5^{12}6^4$	N.A	-	2937.7	150K, 1bar	-	-	-
	$n\text{-C}_4\text{H}_{10}(\text{sII})$	$5^{12}6^4$	N.A	-	2947.8	150K, 1bar	-	-	-

IV. CONCLUSION.

In this chapter, the structural signatures of sI and sII hydrates were investigated for pure and mixed gas species using two complementary methods. Neutron diffraction was used to characterize the crystal structure of pure methane and carbon dioxide hydrates formed in the sI type and propane hydrates in the sII type.

Raman spectroscopic measurements were used to study both the vibrational signatures of sI and sII hydrates for small gas species (CO_2 , CH_4) to larger hydrocarbons (C_2H_6 , C_3H_8 , iso- C_4H_{10} , n- C_4H_{10}) and gas mixtures. This study validated the occupancy of SCs and LCs cages in structure sI for CO_2 , CH_4 and C_2H_6 . The spectrum of CH_4 hydrate structure sII (formed in the case of mixed hydrates) shows the ν_1 bands, attributed to the occupancy of the SCs and LCs of the hydrate, shifted with respect to the signatures of structure sI. Moreover, the intensity ratio of the two bands is close to 1:2, due to the presence of 8 LCS for 16 SCs in the sII structure. In the sII mixed hydrates formed with methane and large hydrocarbons, methane molecules occupy both types of cages, while the Raman band analysis suggests that only the large cages $5^{12}6^4$ are occupied by the large hydrocarbon molecules.

The knowledge of all these signatures for hydrates of various hydrocarbons allows to consider the contribution of Raman spectroscopy to estimate the gas composition of natural gas hydrates and to compare it with the composition of the natural gas mixture where hydrates are formed. This will contribute not only to the assessment of potential molecular selectivity (i.e., chemical composition differences between the natural gas reservoir and the natural gas hydrates), but also to the determination of the hydrates structure formed in natural environments. On a longer perspective, all these results contribute to a better quantification of the resources encapsulated in the sea floor.

CHAPTER 4:
Kinetics of methane
hydrate formation:
Impact of
sedimentary media
and salinity.

I. INTRODUCTION.

Gas hydrates are crystalline structures from which cages resulting from the hydrogen bonding of water molecules (host) enclose relatively small gas molecules (guest), such as hydrogen, methane and other small hydrocarbons.³ Gas hydrates occur naturally on continental margins and in the permafrost regions where low temperature and/ or high pressure conditions are favorable for their formation and stability. Methane hydrates represent the largest natural reservoir of methane on Earth (600-10000 GT).^{104,105} However, large uncertainties remain about the amount of methane bound in these deposits, and the mechanisms governing the fate of the released methane, limiting the conclusions about climate impacts and implications.^{15,268}

The crystalline structure of methane hydrate is called structure sI (as described in chapter 1). Two types of cages characterize this structure, two small cages 5^{12} (denoted SC) build up from 12 pentagons and 6 large cages $5^{12}6^2$ (denoted LC) composed of 12 pentagons and 2 hexagons.^{3,36} One methane molecule can be engaged inside each type of cages. The structural stability of hydrates, between the guest and host molecules, is ensured by weak van der Waals interactions.³⁷

Over the last decades, a significant piece of work has been carried on the structural characterization and the thermodynamic stability of gas hydrates.^{3,36,269} Nowadays, attention of researchers is being focused toward understanding their kinetic properties. The study on the kinetic behavior of gas hydrate formation is a complex phenomenon. Let recall the description provided in chapter 1. Such a process is commonly describes as a two steps process: a stochastic hydrate nucleation process followed by a hydrate growth process.^{36,60} The first step, stochastic hydrate nucleation, is characterized by an induction time where nucleation begins. In this step the first hydrate crystals appear. However, not all the hydrate crystals grow during this period because of their metastability. The second step, called hydrate growth, integrated three periods: first, the adsorption phase where gas hydrates grow quickly and a large amount of gas is consumed and the crystal size increases. Then, the water and gas molecule consumption decreases, leading to the flattening out of the reaction. Finally, the system tends to reach a thermodynamically stable state. This final step can be explained by either the complete consumption of one of the hydrate-forming components (i.e., water or gas) or by the limitation of mass or heat transfer from the molecular species (i.e., water or gas) to the hydrate-forming interface, resulting in low driving forces and an almost negligible rate of hydrate formation.⁶⁰

In the past years, kinetic studies were mainly focused on bulk phase systems^{63,270,271} and a few studies are dedicated to the formation kinetics of gas hydrate in sediments (see chapter 1). However several scientific cruises have collected samples of natural gas hydrates and highlighted that a large part of natural gas hydrates are present in porous media, especially in marine sediments, mainly composed of clay-rich sediments.^{8,10,26,155,272} There is a need to study the influence of sediments on methane hydrate formation at laboratory scale to better elucidate the formation/dissociation process of natural hydrate. Many substrates have been considered. The kinetic influence of the size of sand grains on the methane hydrate formation was conducted by Heeschen *et al.* in 2016.¹⁴³ The fine grains act as promoters of gas hydrate formation compared to the coarse grains. Silica beads and silica gels were also used as silica substrates to mimic natural sediments.^{94,273} Seo *et al.*²⁷³ reported the enhancement of the formation kinetics of hydrate when dispersing water inside the pores of silica gels. Métais *et al.*⁹⁴ studied the effect of silica beads size on CO₂, CH₄, and mixed hydrates formation and observed the ice-to-hydrate conversion in few minutes in the nano-silica beads while in few hours for the larger beads sizes. Another major interest of studying gas hydrates in their natural environment is to increase hydrate formation rate using porous media with pore diameter ranging from more than 50 nm (macropores) to less than 2 nm (nanopores). Such substrates present large specific surface area, which increases the available water-gas interaction surfaces for hydrate formation. Liu *et al.*, investigated methane hydrate formation in mesoporous MCM-41.¹⁶⁸ Other sedimentary porous analogs were used as gas hydrates matrices such as activated carbons^{169,170}, carbon nanotubes¹⁶² and metal organic frameworks (MOFs)¹⁷¹. It turns out that both hydrate macro-properties and kinetics highly depend on the sample microstructure including the matrix composition, pore structure, water and gas transport, as well as the hydrate morphology.⁹⁸ However, it is still necessary to understand the mechanisms that govern the formation of hydrates in clay sediments, both for economic purposes with the exploitation of gas hydrate resources, but also to prevent possible environmental risks and geohazards.²⁷⁴

Clays present a layered structure, which provides a multiscale distribution of the pore size. In presence of water, cation solvation can occur in the interlayer space of clay. Crystalline swelling takes place: it is the case of smectite clay.²⁷⁵ The complexity of these structured materials attracts the scientific interest. Na-montmorillonite, smectite clay in which the interlayer space can reach 2 nm, has been used to synthesize methane hydrate.^{30,32,34,35} To determine whether stable methane clathrates could in principle form in the interlayers of hydrated montmorillonite, computational methods and X-ray diffraction experiments were carried out: these main studies

on the formation of gas hydrates in the presence of clay have confirmed a favorable interaction between the water molecules and the clay surface, as such an interaction promotes their formation.^{30,32,34,35} Recent work was conducted on natural sediments from Krishna-Godavari, Mahanadi and Andaman basin in India where hydrates are encountered in clay-rich sediments.¹⁹⁷ They observed significant decrease of the pressure needed for hydrate formation compared to formation in bulk water. Besides, MD simulations were performed on the dissociation of methane hydrates in illite, and reveal a combined effect of the confinement, the surface and the composition of illite layers leading to the production of gas nanobubbles in the nanopores. Moreover, the gas production from illite reservoir is better than that from silica reservoir.²¹⁷ All of these cited studies were devoted to investigating the origin and stability of natural gas hydrates in an environment mimicking marine sediments and permafrost regions where large quantities of natural gas are present and mechanism of formation remains unknown.

In addition, when considering marine gas hydrates, it is important to take into account the presence of dissolved salt within the hydrate-forming pore fluid, and therefore investigate the effect of salt in the formation process. The formation of gas hydrate in pure water or NaCl solution in bulk phase has been investigated for decades, mainly to evaluate the hydrate thermodynamic stability field.^{276,277} Mekala, *et al.* and Chong *et al.* focused on the formation kinetics and dissociation mechanisms of methane hydrates in seawater and NaCl solution in presence of silica sand.^{209,218} They reported a significant kinetics inhibition effect on hydrate formation in presence of NaCl that resulted in a lower conversion of water into hydrate phase. In a recent work, the effect of montmorillonite, sand and NaCl concentration on methane hydrate was been investigated. They observed for a low NaCl concentration of 0.2 mol/L and a low montmorillonite content range of 10–25 wt% the induction time of hydrate formation was reduced compared to a higher concentration of NaCl and montmorillonite where the induction time significantly increased. They also suggested that the effect of montmorillonite content on the induction time is smaller than NaCl.²²⁰

The dissociation of gas hydrate is also a complex process.^{278,279} One major and very intriguing result discovered during hydrate dissociation is the metastability, *e.g.* the self-preservation effect.^{3,280–282} During this process, it was observed that hydrates may dissociate in anomalous slow rates and in a different range of temperature far from stable thermodynamic equilibrium. “Self-preservation” phenomenon remains not well understood, it occurs on a temperature range of 242–271 K.³ Neutron diffraction and SEM experiments conducted by Kuhs *et al.*²⁸³ suggest that extensive annealing of ice stacking defects (ice defects) at about 240 K would allow "self-

preservation" of the hydrate. The impact of several factors such as guest gas composition, sample morphology and size, and salt concentrations have been reported to affect the dissociation rate of gas hydrates outside the equilibrium region. Because natural gas hydrates are primarily found in marine sediments with either constant or variable salt concentrations and in porous environments, increasing attention is devoted to the effect of NaCl and sediments on the dissociation and metastability of methane hydrates.^{282,284} Most of these studies have been conducted at pressure-induced phase transformation.²⁸⁵

In this chapter, methane hydrate formation kinetics was for the first time investigated by time-dependent *in-situ* neutron diffraction technique in presence of clay-rich matrix with pure water and NaCl deuterated solution. The dissociation of the subsequently formed hydrates was also investigated using *in-situ* neutron diffraction at constant pressure (1bar) with increasing temperature from 150 K to 300 K. The selected substrate is made of 60 % clay and 40 % of other minerals (quartz and plagioclase) constituted by a mixture of Fontainebleau sand and Montmorillonite. The aim of this study being to reproduce the natural environment of gas hydrates (p, T, salinity, sediments) and to investigate the effect of salt and swelling clay on the kinetics of formation of methane hydrate. In the second part, *ex-situ* neutron diffraction is used to characterize the formation of methane hydrates in clay media. The formation kinetics in Illite and natural sediments from the Black Sea are compared to the data collected in montmorillonite. The effects of particle size, specific surface area and clay composition are investigated.

II. KINETICS OF METHANE HYDRATE FORMATION IN MONTMORILLONITE: SALINITY EFFECT (NaCl).

a. Abstract

The estimation of methane trapped in gas hydrates motivates the scientific community to get more insight on the formation and dissociation of gas hydrates in natural environments. These quantities represent both a high potential as a future energy source and geological hazards due to the dissociation of methane hydrates. In this work, the natural environment of methane hydrates was reproduced *in-situ* in order to study the formation kinetics and dissociation using neutron diffraction. For this purpose, a sedimentary matrix consisting of 60 % montmorillonite and 40 % quartz was used. The salinity conditions were reproduced by using an aqueous solution with a low concentration of NaCl (2.2 wt% NaCl). The results show that

montmorillonite is a promoter of methane hydrate formation. The first Bragg peaks of methane hydrate are observed after 10min of pressurization and the conversion of water to hydrate reaches 80% after less than 40 min. However, salt slows the formation of methane hydrate, with Bragg peaks observed after 15min of pressurization, but does not affect the conversion rate. The curve of dissociation of the pure methane hydrates as an anomalous tendency with increasing temperature. After the beginning of the dissociation, the curves show a re-formation of the hydrate between 221 and 237 K, before the restart of its dissociation at 237 K. This effect is not observed in the presence of salt. However, its presence limits the formation of ice from the water released by the melting of the hydrate due to a lower melting temperature than pure water.

b. Materials and methods

In-situ neutron diffraction experiments were performed at constant temperature (282 K) and pressure (70 bar) with methane (CH₄) gas (Figure 54) on the high-intensity 2-axis neutron diffractometer D20 at ILL, Grenoble. D20 is a medium- to high-resolution diffractometer providing a very high flux at the sample position and allows probing of the sample over a volume of ~2 cm³. It has 1536 detection cells of a stationary and a curved linear position sensitive detector (PSD) covering a 2θ range of 153.6°. D20 is ideal for *in-situ* diffraction studies with acquisition times below 1s allowing the investigation of fast changes in the sample (2 cm³). Aluminum cell, with a highly pressure-temperature controlled set-up, is filled with the partially-saturated systems using either deuterated water or salted deuterated water (2.2 wt% NaCl). A mixture of 60 % Montmorillonite K10 (Sigma Aldrich) and 40 % Fontainebleau sand is used as hydrate formation matrix. The matrix is homogeneously mixed with the aqueous solutions under inert atmosphere. The amount of aqueous solution added into the matrix is determined from the amount of solution required to hydrate 5 cm³ of sand at 75 % considering a free space of 40 %. Then, this same amount of deuterated water or salted deuterated water is added into 5 cm³ of montmorillonite. The hydrated sample is connected to a gas injection pump and placed in the orange cryostat for temperature control. Time-dependent diffraction acquisition starts when the gas is filled into the cell (defined at t = 0). Diffraction patterns of hydrate formation along time were collected using a wavelength of $\lambda_0 = 2.414 \text{ \AA}$. The reaction of gas (at constant pressure and temperature) with the hydrated matrices was followed over a period of typically 2-5 h with a diffractogram collected every 1min. The methane hydrate formation is detected on the diffractograms by the apparition of the Bragg peaks characteristic of the structure I (cubic structure with a $\approx 12 \text{ \AA}$).²⁸⁶ The hydrate growth reveals itself by an

increase of the Bragg intensities, which starts extremely fast after the application of gas pressure, and increases with time when water is converted into hydrate until it stabilizes. The dissociation of methane hydrate in the pure and salted samples was recorded by continuously increasing the temperature from 150 K to 300 K (Figure 54, 2→3) according to 3 K/min and a diffractogram was recorded every 3 minutes.

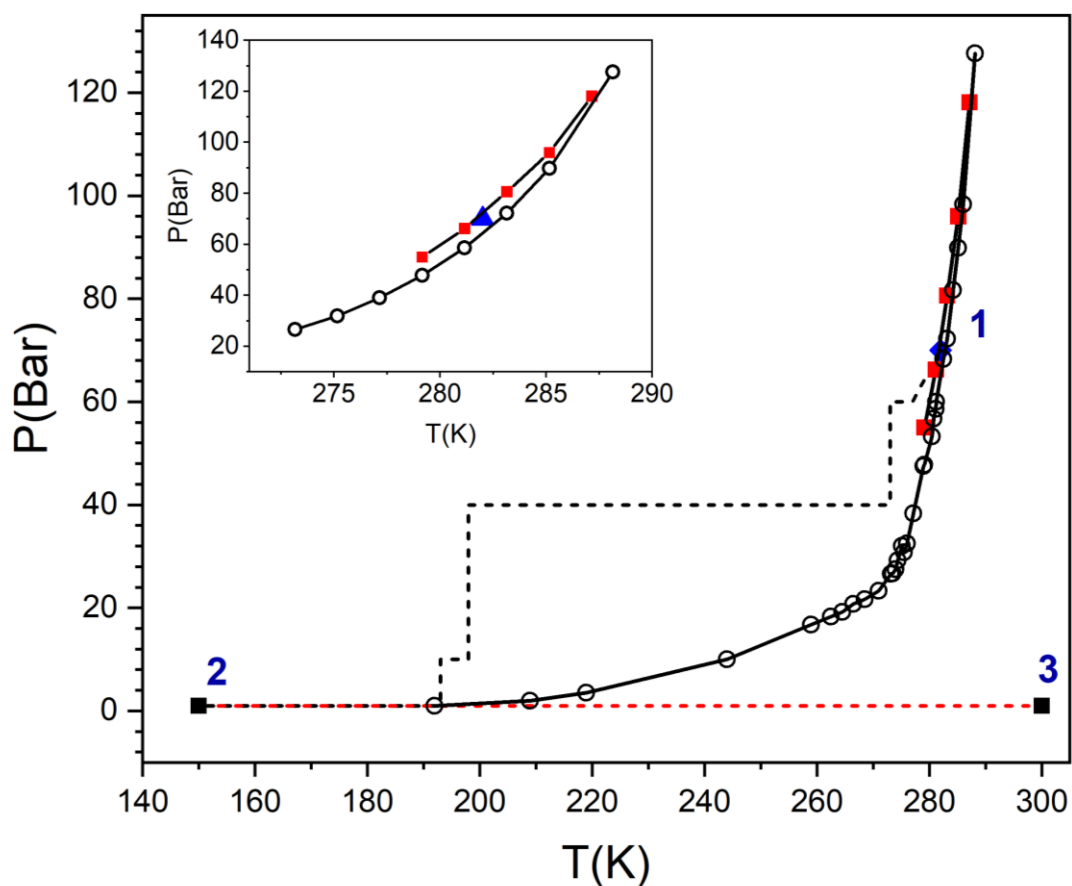


Figure 54. Thermodynamic equilibrium curves of pure CH₄ hydrate (black line with rounds) and 2.2 wt% NaCl CH₄ hydrate (black line with red squares). The blue triangle (Point 1) corresponds to the P,T conditions of the hydrate formation in this study.

c. Experimental results

i. Kinetics of formation

Two series of the *in-situ* neutron diffraction experiments were performed with montmorillonite hydrated with D₂O and salty NaCl D₂O (2.2 wt% NaCl). The pores are interconnected and partially filled with water allowing the circulation of gas into the matrix and increasing the water-gas contact surface to form gas hydrate.^{201,210} **Figure 55** shows examples of diffractograms recorded during the methane hydrate formation inside montmorillonite with pure deuterated water. At $t = 0$ min, when methane gas is injected onto the hydrated mixture of montmorillonite and Fontainebleau sand at 282 K, the diffractogram only exhibits the Bragg peaks related to the matrix (indicated on the **Figure 55**). After less than 10 minutes, the methane hydrate formation is detected by the apparition of Bragg peaks related to the structure I (sI). Then, the intensities of the hydrate's peaks keep increasing along time. After 5.5 hours, the recorded diffractograms no longer exhibit significant evolution and the methane hydrate formation is stabilized. To evaluate the amount of deuterated water converted into methane hydrate sI, the sample was cooled to 150 K, and the pressure release at 1bar by following the thermodynamics pathway denoted (1→2) in **Figure 54**, to ensure the stability of the formed gas hydrate. The red diffractogram on the top of **Figure 54** is recorded at 150 K and 1bar: it shows a broad signal between 35° and 45°. This signal is related to the remaining deuterated water into the sample. It is composed of a broad peak that may be assigned to an unorganized water network, an ice with lower crystallinity, which could be present in the interlayer space of montmorillonite. The ice with low crystallinity may be named as “short-range ice”.²⁸⁷ Two weak Bragg peaks can also be distinguish at 36.4° and 38.7°. They are attributed to crystallized bulky ices (Ih and Ic). Rietveld refinements reveal a combination of methane hydrate sI, cubic ice (Ic) and hexagonal ice (Ih) (**APPENDIX 3, Figure S1 and Figure S2**). Similar signals of water into confined cylindrical nano pores have already been observed in MCM-41.²⁸⁷

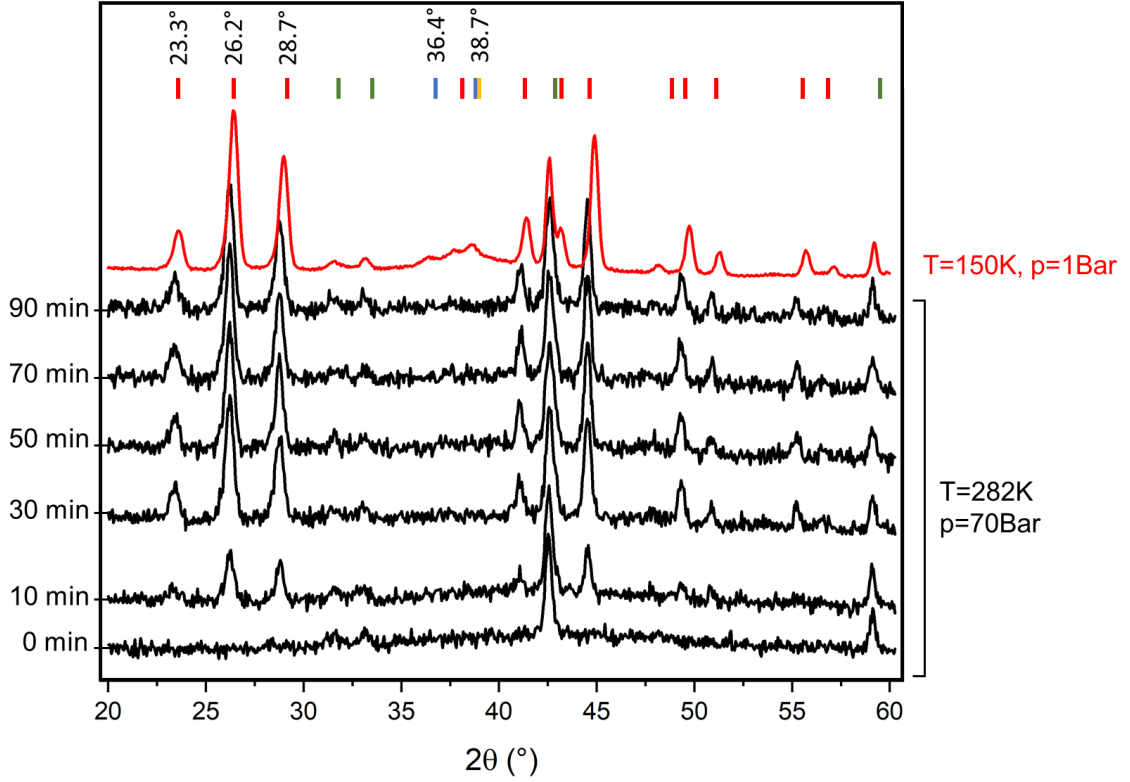


Figure 55. Recorded diffraction patterns of the formation of pure CH₄ hydrate over time (Black) at 70 bar and 282 K. Recorded diffraction pattern at 1 bar and 150 K after 5.5 hours of pressurization at constant pressure and temperature (Red). Rietveld refinements peak positions for hydrate sI, the matrix, the cubic ice (Ic) and the hexagonal ice (Ih) are represented by red, green, yellow and blue coloured bars respectively.

To estimate the amount of water converted into hydrate phase on the diffractogram collected at 150 K after hydrate formation, the areas of the water signal and hydrate peaks have been integrated for both pure and salted methane hydrate. Not all the peaks of the diffractograms have been considered for this analysis. The water signal, noted $A_{ice}^{150K}(t_f)$ was determined by integrating the diffraction signatures previously described and observed between the scattering angles $2\theta = 35^\circ$ and $2\theta = 40^\circ$. $A_{ice}^{150K}(t_f)$ can be determined according to the following equation:

$$A_{ice}^{150K}(t_f) = \int_{35^\circ}^{40^\circ} I_{ice}^{150K}(t_f) d2\theta \quad (27)$$

Where $I_{ice}^{150K}(t_f)$ refers to the intensity of the ice signal on the diffractogram collected at 150 K at the end of pressurization time t_f . For the pure and salted methane hydrate, $t_f = 95$ min and $t_f = 332$ min respectively.

Concerning the hydrate phase, only the three peaks located at 23.3°, 26.2°, 28.7° (Fig. 2) were considered as they are the most intense. $A_{hyd}^{150K}(t_f)$ can be calculated according to this equation:

$$A_{hyd}^{150K}(t_f) = \sum_{i=1}^3 A_i^{150K} \quad (28)$$

Where $i = 1, 2, 3$ corresponds to the hydrate Bragg peaks 23.3°, 26.2°, 28.7°.

The fraction of water converted into hydrate reached at the end of the pressurization time t_f was determined by combining equations (27) and (28):

$$\alpha^{150K}(t_f) = \frac{A_{hyd}^{150K}(t_f)}{A_{hyd}^{150K}(t_f) + A_{ice}^{150K}(t_f)} \quad (29)$$

The values of pure and salted methane hydrate are reported in Table 1.

The kinetic curves are obtained by estimating the areas of the three main first Bragg peaks of sI hydrate (23.3°, 26.2°, 28.7°) for each diffractogram over time.

$$A_{hyd}(t) = \sum_{i=1}^3 A_i(t) \quad (30)$$

Where $i = 1, 2, 3$ corresponds to the hydrate Bragg peaks 23.3°, 26.2°, 28.7°.

The conversion rate of methane hydrate over time is estimated according to the following equation:

$$\alpha(t) = \frac{A_{hyd}(t)}{\lim_{t \rightarrow \infty} A_{hyd}(t)} \alpha^{150K}(t_f) \quad (31)$$

Figure 56 represents the kinetic curves $\alpha(t)$ of pure and salted methane hydrate over time. The kinetic curves can be divided into three steps, which described the processes involved in hydrate formation. The hydrate nucleation referring to the induction time is followed by the adsorption phenomenon where gas hydrates grow quickly and the long diffusion process required to reach the final conversion rate.⁶⁰ All these steps, characteristic of hydrate formation, can be observed over times ranging from a few minutes to several hours or even days/months. Indeed, many parameters are involved in the formation of gas hydrates and can impact the formation times (e.g., the experimental procedure, the thermodynamic conditions, the gas composition, the addition of substrates or kinetic promoters and inhibitors). The induction time corresponds to the time required to reach the apparition and detection of the first hydrate crystal nuclei. In the

case of the methane hydrate synthesized from pure deuterated water, this time is short and the hydrate formation starts after less than 10 minutes. However, in presence of salt, the hydrate formation is slower and the induction time takes 12 minutes before the formation starts. The presence of salt seems to have an inhibitor effect on the hydrate formation in montmorillonite. In 2015, Chong *et al.* described the effect of NaCl salt on the hydrate formation in porous Toyoura sand.²¹⁸ They observed a significantly slower kinetics in the presence of NaCl as compared to experiments conducted without the presence of salts, affirming the significant kinetic inhibition effect of NaCl on methane hydrate formation in porous media. To go further on the interpretation of the effect of salt on the methane hydrate kinetics of formation, the adsorption phase and the diffusion process are investigated. The adsorption step is represented on the curve by a steep slope, while diffusion corresponds to the third part of the curve, which tends towards a plateau. Using the boundary nucleation and growth model, denoted BNG, the data are fitted to study gas hydrate formation kinetics. The BNG model was developed to describe transformations in polycrystalline materials, where nucleation occurs at grain boundaries, rather than scattered throughout the volume.²⁸⁸ This model is based on the assumptions that the nucleation and growth rates are constant throughout the process. The model has been generalized to allow anisotropic growth from a constant number of nuclei or with a constant nucleation rate.²⁸⁹ The BNG model has been for the first time used and adapted by Métais *et al.*⁹⁴ to study formation kinetics of gas hydrates from ice in presence of silica beads.

The BNG model is expressed by this equation:

$$\alpha(t) = A \left\{ 1 - \exp \left[-2k_2(t - t_0) \left(1 - \frac{F_D[k_1(t - t_0)]}{k_1(t - t_0)} \right) \right] \right\} + (1 - A) \{ 1 - \exp[-k_3(t - t_0)] \} \quad (32)$$

Where $F_D(x)$ is the Dawson function, defined as:

$$F_D(x) = \exp(-x^2) \int_0^x \exp(y^2) dy \quad (33)$$

In the BNG model, α represents the rate of conversion of water to hydrate at time t . The constant A corresponds to the fraction of water converted to the hydrate layer at the water-gas interface, it is related to the absorption process. Then, the first part of the equation describes the surface formation of a hydrate layer at the water-gas interface. k_1 represents the heterogeneous nucleation of gas hydrate at the interface water-gas, and leads the formation of a hydrate layer

of limited thickness characterized by the kinetic constant k_2 . The second part of the equation is a "phenomenological" term. It describes the diffusive part, and is characterized by the constant k_3 . This part is associated with the growth of the hydrate at the hydrate-water interface involving the diffusion of gas molecules through the hydrate layer, as well as at the hydrate-gas interface, due to the diffusion of water molecules into the gas phase.

To resume, in this model, the hydrate formation is composed of three main stages: a first stage of heterogeneous and anisotropic nucleation water-gas interface, followed by formation of a hydrate layer at the interface, and a third stage corresponding to the mass growth of this layer.

All the kinetic data could be successfully fitted using the above model and the excellent agreement is shown in **Figure 56**.

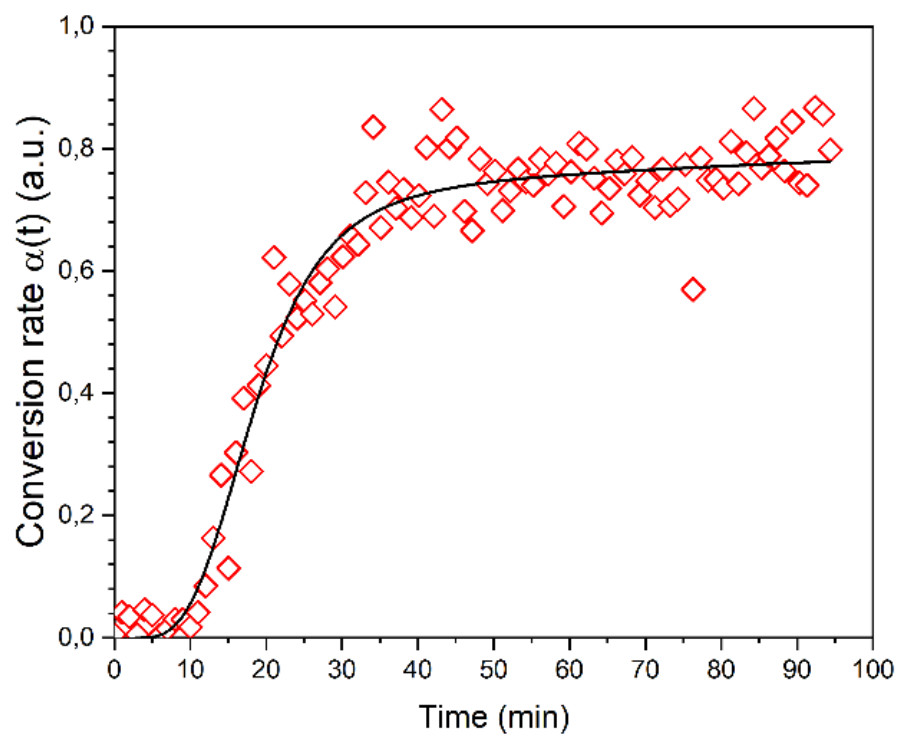
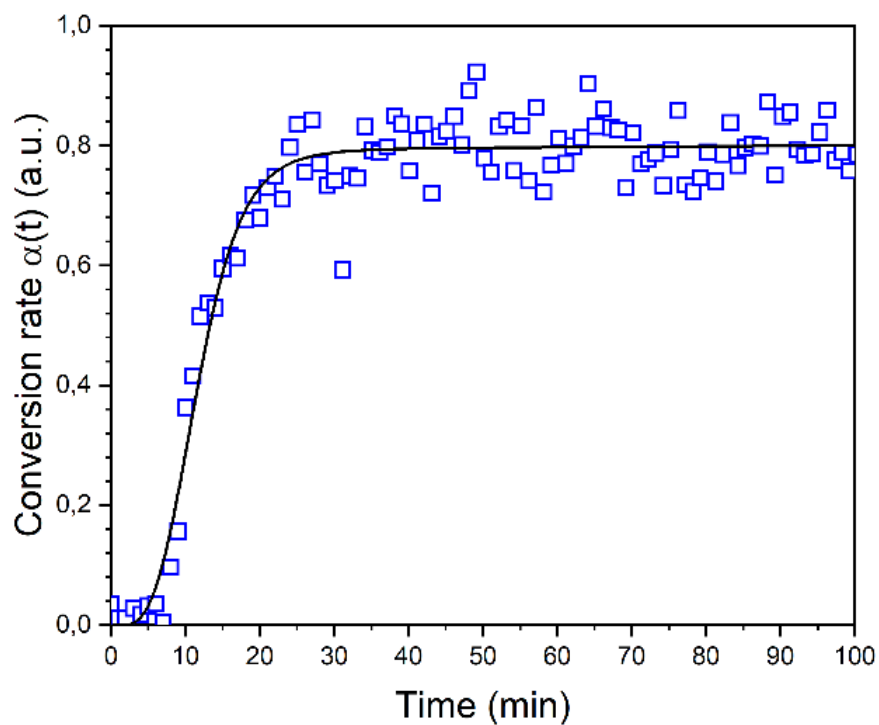


Figure 56. Kinetic curves of pure CH_4 hydrates (top) and CH_4 hydrates with 2.2wt% NaCl (bottom) in MS. The black lines represent the fits of the experimental data (symbols) with the modified BNG model. (See text for the details)

	Pure CH ₄ hydrate	CH ₄ hydrate 2,2w% NaCl
$\alpha^{150K}(t_f)$	0.81	0.80
t_0	1.23 ± 1.07 min	3.64 ± 1.01 min
A	0.8 ± 0.01	0.7 ± 0.03
k₁	8.0 ± 0.003 x 10 ⁻² min ⁻¹	6.7 ± 1.4 x 10 ⁻² min ⁻¹
k₂	9.3 ± 2.0 x 10 ⁻² min ⁻¹	5.1 ± 1.0 x 10 ⁻² min ⁻¹
k₃	3.9 ± 3.1 x 10 ⁻⁴ min ⁻¹	2.4 ± 1.7 x 10 ⁻³ min ⁻¹

Table 20. Kinetic parameters from the modeling of the kinetic curves using the BNG model from pure CH₄ hydrates and CH₄ hydrates with 2.2 wt% NaCl in MS.

The kinetic parameters of the BNG model provide valuable information on the process of hydrate formation inside clay matrices. All the parameters are reported in the **Table 20**. The conversion constant A is high and quite close for both samples. As a reminder, it corresponds to the amount of water converted into hydrate before the diffusive process starts. The kinetic constant k₁, characteristic of the heterogeneous nucleation of hydrate at the water-gas interface, is also very similar for pure water and salted water. This result means that the presence of salt does not influence the hydrate germination. However, the kinetic constant k₂ is significantly higher in the sample formed without NaCl salt. Knowing that this kinetic constant is characteristic of the formation of a hydrate layer at the water-gas interface, the presence of salt seems to prevent expansion of hydrate layer. Numerous studies show that electrolytes can be considered as inert inhibitors as they affect the phase equilibrium of hydrate, but do not enter the hydrate phase.^{18,290} Following these assumptions, the methane hydrate formation may faces three competitive processes. The exclusion of salt ions from hydrate structure and the thermodynamic inhibitor effect of NaCl on hydrate formation and the effect of NaCl on the swelling of montmorillonite. The exclusion of salt ions from hydrate structure may causes an increase of the local salt concentration at the interface between gas hydrates and the unconverted salted water, which limits hydrate conversion and slows down the surface hydrate layer growth at the water-gas interface. Moreover, the presence of salt is known to change the methane hydrate phase diagram. As the concentration of salt increases, the phase equilibrium curve is shifted to higher pressure and lower temperature. This change of the thermodynamic conditions lower the driving force and slow down the hydrate formation.^{191–195} Tao *et al.* have shown that NaCl salt ions influenced the water content of montmorillonite decreases with

increasing the salt concentration by affecting the intercalation of water molecules and limiting clay swelling.¹⁹⁸ All these effects combined could inhibit the promoting effect of montmorillonite on the formation of gas hydrate. Finally, the constant k_3 is characteristic of the diffusive process. This diffusive process is slow. In pure methane hydrate, the plateau is almost achieved after less than 40 minutes and the rate of hydrate conversion reaches 80 %. In the sample that contains 2.2 wt% NaCl, the constant k_3 is one order of magnitude slower than in pure D₂O and the plateau is not reach yet after 90 minutes of pressurization. However, the acheived hydrate conversion rate is 80 %. The interpretation of these observations with the BNG model show that the anisotropic hydrate layer growth is faster in the sample without salt and grow slowly in presence of salt towards the complete growth. This process can be extremely slow (days, months, years) and is limited by the amount of water still available is the samples to be converted into hydrate or the limited mass and heat transfer. The general trend observed as a function of the presence of salt is its kinetic inhibitor effect on the hydrate growth but it does not influence the rate of hydrate conversion compared to the sample without salt.

ii. Dissociation

Figure 57 represents the dissociation of CH₄ hydrates and the formation of ice as function of temperature between 150 K and 300 K. The dissociation curves of pure and salted methane hydrate are obtained by integrating the Bragg peaks of sI hydrate (23.3°, 26.2°, 28.7°) as followed:

$$A_{hyd}(T) = \sum_{i=1}^3 A_i(T) \quad (34)$$

Where $i = 1, 2, 3$ corresponds to the three hydrate Bragg peaks considered and T is the temperature.

The ice formation curves are determined by integrated the area of the signal of ice between the scattering angles $2\theta = 35^\circ$ and $2\theta = 40^\circ$.

$$A_{ice}(T) = \int_{39^\circ}^{42^\circ} I_{ice}(T) d2\theta \quad (35)$$

By looking at these data, the effect of salt on hydrate dissociation is clearly observed. Dissociation of pure methane hydrate appears to occur in three steps while methane hydrate in

the presence of NaCl dissociates homogeneously with increasing temperature. However, in both samples, the gas hydrates show abnormal stability outside its thermodynamic stability limits (**Figure 54**) and are preserved with the increase in temperature until more than 272 K. This phenomenon is known as self-preservation zone²⁸⁴. The precise explanation for the mechanism remains unknown, in this work, self-preservation behavior of methane hydrates synthesized with pure water (0.0wt% NaCl), mild salt solutions (2.2 wt% NaCl) is investigated.

For the pure CH₄ hydrate in montmorillonite (**Figure 57** On the top), the hydrate dissociation begins at 207 K. According to Brodskaya *et al.*, this temperature corresponds to the melting of the hydrate shell.²⁹¹ The Bragg peaks of sI hydrate start decreasing and the signal of water becomes narrower, the Bragg peaks intensities of Ic and Ih ices increase. This formation of ice arises from the melting the hydrate surface. The more the hydrate melts, the more the water released is loaded with methane dissolved at the hydrate-ice interface. At 220 K, in **Figure 57**, it can be observed that the ice signal stops increasing and the hydrate dissociation stabilizes between 221 K and 237 K. This phenomenon can be explained by the possible re-formation of hydrate crystals. Indeed, a local pressure is created at the ice-hydrate interface, linked to the decomposition of the external layer of hydrate crystals. These local thermodynamic conditions, favorable to the formation of methane hydrates, allow the methane-laden ice to reorganize its structure into hydrate cages. The temperature keeps increasing to 240 K, the signal of hydrate decreases, hydrates are melting again and the amount of ice in the sample increases. This temperature corresponds to the hydrate core melting.²⁹¹ It can be observed on the diffractogram, the increase of the intensity of ice Bragg peaks. The signature of “short range ice”, i.e., the broad signal under the ice Bragg Peaks, remains stable. At 258 K, the sample contains the maximum of ice. Rietveld refinement (**APPENDIX 3, Figure S3**) was used to determine the fraction of ice in the sample at this temperature. The Bragg peaks of sI hydrate, Ic and Ih ices were refined. The sample is composed of 95 % of different types of ice: Ih, Ic and confined “short-range ice” and a small amount of hydrate structure sI. Then, at 264 K, methane hydrates are completely dissociated. Finally, the signal of confined water decreases and is converted into ice before the complete melt of the sample at 282 K.

The presence of NaCl in small concentration modifies the dissociation of gas hydrates. Methane hydrates synthesized in 2.2 wt% NaCl begin to dissociate at 218 K. At this temperature, the molten water released by hydrate dissociation turns to ice. Since salt does not penetrate the hydrate cages, a local salt concentration is created outside the hydrate crystals. This concentration at the hydrate-ice interface appears to prevent hydrate reformation that could be

observed in the sample containing no salt. Indeed, on the **Figure 57** (bottom), the fraction of ice in the sample increases at the same temperature than the dissociation of methane hydrate (i.e., diminution of hydrate fraction). Between 240 K and 270 K, the fraction of ice is almost stable while the fraction of methane hydrate is decreasing. Indeed, at 252 K, the melting point of salted ice is reached and the water liberated by the dissociation of gas hydrates will not anymore be converted into ice but will remain in the liquid phase. The maximum fraction of ice in the sample is reached at 257 K. Rietveld refinement (**APPENDIX 3, Figure S4**) was used to determine the fractions of each phase. The sample is composed of 94% of different types of ice: Ih, Ic, and confined “short range ice” and a small amount of hydrate structure sI. At 270 K, methane hydrates are completely dissociated and ice melts at 280.5 K.

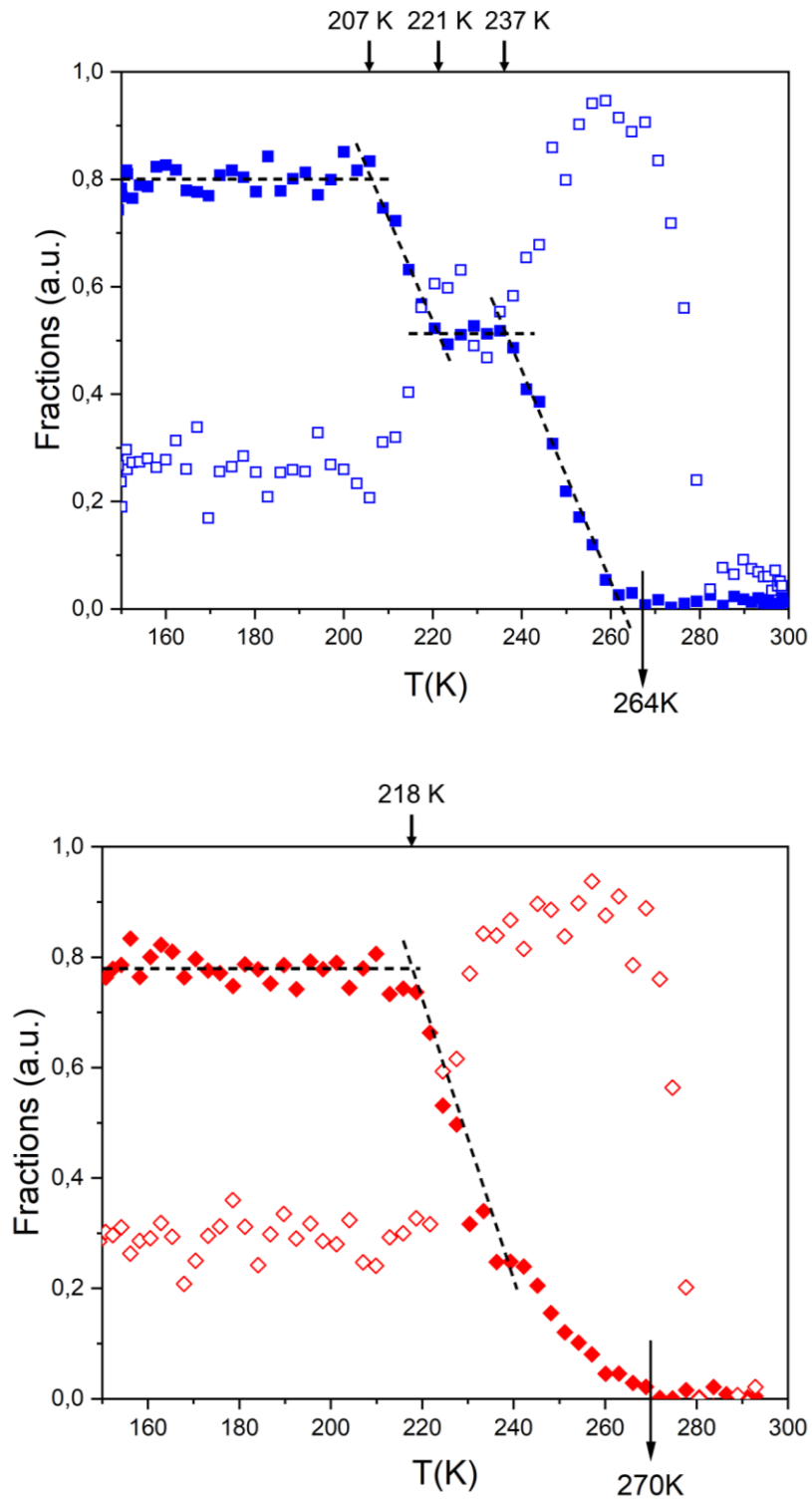


Figure 57. Hydrate dissociation (filled squares) and evolution of ice signal (empty squares) as function of temperature for pure CH₄ hydrates (top) and CH₄ hydrates with 2.2wt% NaCl (bottom).

d. Conclusion

In summary, the influence of montmorillonite clay and the presence of NaCl salt on the formation kinetics and dissociation of CH₄ hydrates have been investigated by neutron powder diffraction. 60 % Montmorillonite with 40 % quartz constituted the hydrate substrate to substitute natural sediments. Both pure and salted samples have undergone the same temperature and pressure conditions for all the analyses.

Montmorillonite appears to act as a kinetic promotor of methane hydrate with an almost complete conversion of water into hydrate after less than 60min of pressurization (70 bar) at constant temperature (282K). Similar timescales were observed for sediments analogues like silica beads with a size smaller than 100nm.⁹⁴ Several physicochemical parameters can explain these very short induction and formation times. First, the first parameter is the particle size. Heeschen *et al.* have shown that gas hydrate formation in presence of a high concentration of fine grains (clays) <125 µm have a faster hydrate conversion than methane hydrate in coarse grains and sand. The major parameter is highly connected to the atomic structure of clays. Several studies highlighted the promoted effect of clay surfaces with the presence of hydroxylated edge sites to induce hydrate nucleation.^{35,214} The last parameters involves the thermodynamics with a larger driving force provided by the presence of smectite clays like bentonite which shortened the induction time.^{213,292} Montmorillonite, smectite clay, with particles size ~14 µm, and inter-layer cations causing the swelling of the structure provides a good nucleation site for hydrate formation.

For 2.2 wt% NaCl system, the CH₄ hydrate formation is slower and starts after 15min of pressurization, the water to hydrate conversation rate is lower and comes with a long diffusion process. The kinetic inhibitor effect of salt is well-known from the community. Chong *et al.* described this effect on the hydrate formation in porous Toyoura sand and presented the lower thermodynamic driving force during hydrate formation²¹⁸. Similarly, very recent experimental study on the coupling effect of montmorillonite and NaCl shows that when the concentration of NaCl and Montmorillonite is high, the induction time increases.²²⁰ However, the indicated induction times in their study range between less than 5 hours to 50 hours, which is 5 to 50 times higher than the times observed in this work.

The study of the dissociation of CH₄ hydrates in both pure and salted samples exhibits the self-preservation mechanism. However, different phenomena occur in each sample. The dissociation of pure CH₄ hydrate includes hydrate re-formation due to local pressure at the

hydrate-ice interface, the high concentration of dissolved methane concentration in water from the melted hydrate and the restructuration of water molecules from hydrate and “short range ice” to ice and melted water. The presence of salt prevents hydrate re-formation due to the possible presence of high local concentration of salt around hydrate cages, which were excluded out of the cages during hydrate formation. However, self-preservation is still observed with a hydrate melting point reaching 270K.

III. KINETICS OF METHANE HYDRATE FORMATION IN SYNTHETIC AND NATURAL SEDIMENTS FROM BLACK SEA: EFFECT OF CLAY PROPERTIES.

a. Abstract

In the marine sediments of continental margins, large quantities of methane hydrates are found. Marine sediments, mainly composed of sand and clays, constitute a porous medium where the distribution of water and gas, as well as the physico-chemical properties of the mineral species influence the formation of hydrates. In this work, the effect of two artificial and one natural matrix composed of 60 % clay and 40 % other mineral species (mainly quartz) is studied on the kinetics of methane hydrate formation. The clay fraction of each matrix has a variable mineralogical composition composed of smectite, illite and kaolinite. Time-dependent neutron diffraction has allowed to follow the kinetics of methane hydrate formation. The mineralogical composition of the matrices has a strong impact on hydrate formation with hydrate conversion rates ranging from less than 15 minutes to several days/months. The crystal structure of smectite provides large specific surface area, which promotes methane hydrate formation. Conversely, illite and kaolinite do not appear to promote hydrate formation. Furthermore, methane hydrate formation is favored in the large pores of clays (mesoporous and macroporous) and/or in the inter-particle spaces.

b. Materials and methods

i. Sediment

Black Sea sediments collected during the GHASS¹²⁶ cruise in 2015 are used for the first time to synthesize methane hydrate in the lab. Black Sea is known as a major methane hydrate reservoir on earth and it is thus a large-scale natural lab to understand methane hydrate

formation and implication on geohazards. These sediments were collected on the Romanian margin of the Black Sea, and analyzed at Ifremer (Brest) by XRD. The sediment is mainly composed of clay (60 %) and 40 % of other minerals (mainly quartz, calcite and plagioclase) (**Table 21**). This matrix is denoted as BS in this paper.

Illite clay (Argiletz, France) is the last matrix used in this study. It was identified as a good sedimentary analog to reproduce Black Sea sediments. Illite, characterized by XRD at Ifremer (Brest), is composed of 60 % clays and 40 % other minerals like quartz and calcite (**Table 21**). Illite is a non-swelling clay, its structure is very similar to that of 2:1 mica, where two tetrahedral sheets sandwich an octahedral one to build up the T–O–T unit.²⁹³ This matrix is denoted as IS in this paper.

Montmorillonite (Montmorillonite K10, Sigma Aldrich) was selected as the representative smectite clay mineral for this study. It consists of aluminosilicate layers stacked in the perpendicular direction.^{294–296} It is a 2:1 clay mineral part of the smectite group. The clay layers are constituted of an octahedral sheet sandwiched between two tetrahedral sheets. Due to tetrahedral substitutions, smectite layer are negatively charged. This charge is compensated by the presence of interlayer cations located in the interlayer space. Due to their strong affinity with water, water molecules can fill the interlayer space and cause the swelling of the crystal lattice. This characteristic layered structure provide extremely large specific surface area, which is known as a kinetic promotor for gas hydrate.^{32,235} Montmorillonite K10 is composed of 70 % of clay and 30 % of other mineral. To mimic the natural Black Sea sediment composition, montmorillonite is mixed with Fontainebleau sand to reach a composition of 60 % clays and 40 % of other minerals (**Table 21**). This mixture is denoted as MS in this paper.

The three matrices (BS, IS, MS) are hydrated with deuterated water (Sigma Aldrich) under nitrogen atmosphere at room temperature prior neutron diffraction experiments. The amount of deuterated water added onto the mixture is determined from the free space volume of sand. A volume of 5 cm³ is filled with sand. The free space volume is approximated at 40%. The samples are prepared with a saturation level of 75 % of the free space volume according to the sand, which correspond to added 1.5 cm³ of deuterated water in 5 cm³ of each matrix. According to experimental studies on hydrate formation in silica sand, fine sand and glass beads, an optimal value of water saturation is around 70 %.^{203,211,212} This saturation keeps the pores interconnected and creates channels for gas circulation, which provides a large surface contact between water and gas, and consequently favors hydrate formation.

The methane gas (99.995 % of purity), used for hydrate formation in all the experiments presented here, is supplied by Air Liquid.

Properties	Montmorillonite (MS)	Illite (IS)	Black Sea sediments (BS)
Particle size (D_{mean})	14 μm	4.5 μm	2.75 μm
BET Surface area	240.8 m^2/g	66.5 m^2/g	63.1 m^2/g
Global mineralogy			
Quartz	30 %	25 %	14 %
Argiles / micas	60 %	60 %	60 %
Calcite	-	14 %	5 %
Plagioclase	10 %	-	8 %
Clay fraction mineralogy			
Smectite	82 %	< 5 %	5-10 %
Illite	15 %	77 %	60 %
Kaolinite	< 5 %	17 %	20 %
Chlorite	< 5 %	< 5 %	10 %

Table 21. Main properties of the sediments used in this study.

ii. Experimental procedure.

In-situ neutron diffraction experiments is used to study methane hydrate formation in clay sediments. Experiments are conducted on the 2-axis high intensity neutron diffractometer of ILL, Grenoble, D20, at constant methane pressure (70 bar) and temperature (282 K). These thermodynamic conditions were chosen to reproduce the natural environment of the Black Sea where the methane hydrates have been collected at around 700 m water depth (70bars), where the seafloor temperature is close to 282 K.¹⁰ D20 is a high resolution diffractometer which provides a very high neutron flux at the sample position. An aluminum cell is filled with the different systems partially saturated with deuterated water. A gas injection pump and an orange cryostat control the pressure and temperature. The same procedure is applied to all three matrices. The diffraction recording starts once the gas is in contact to the sample. The hydrate formation is recorded over time with a wavelength of $\lambda = 2.414 \text{ \AA}$. A diffractogram is collected every minute over a period of typically 2-5 h to follow the reaction of the gas (at constant pressure and temperature) with the hydrated matrices.

In parallel, methane hydrates samples were synthesized at the laboratory prior the experiment in IS and BS. The sediments partially saturated with D_2O are pressurized prior to diffraction experiments during five different pressurization times. The samples were pressurized with CH_4

at 200 bar at constant temperature $T = 282$ K during 1, 7, 30, 75 and 110 days. Samples were then stored in liquid nitrogen to ensure the stability of the formed hydrate until analyses. Neutron diffraction experiments on these *ex-situ* methane hydrate samples have been performed at ILL, Grenoble using the high intensity two-axis powder diffractometer D1B with an incident wavelength of 2.52 Å. Its high efficiency position sensitive detector (PSD) covers a 2θ scattering angles range from 0.8° to 128.8° . The methane hydrate samples were cold-transferred to the orange cryostat at constant temperature (150 K). Diffractograms were collected at constant temperature with acquisition time of *ca.* 2 h. The conversion rate of water into hydrate is estimated by Rietveld refinement.²³²

c. Experimental results

i. Monitoring the methane hydrate formation.

Figure 58 presents the diffractograms recorded during the formation of methane hydrate within the three different matrices: MS, IS and BS. The diffractograms are presented over a period of 100 min for a better comparison but some of the diffractograms have been recorded over several hours. The apparition of the Bragg peaks characteristic of the structure I hydrate (cubic structure $a \approx 12$ Å) is the signature of methane hydrate on the diffractograms.²⁸⁶ As the methane hydrates begin to grow, the intensity of the Bragg peaks increases. In the presence of montmorillonite, the hydrate is formed within few minutes after the application of gas pressure. The hydrate peaks intensity continues to increase with the amount of water converted into hydrate. After one hour, the intensity of the Bragg peaks reaches a plateau. Either the sample has reached complete consumption of one of water within the matrix, or the mass transfer of the molecular species (water or gas) to the hydrate-forming interface is limited, resulting in low driving forces and a slow rate of hydrate formation.⁶⁰ Conversely, in the case of methane hydrate formation in IS and BS, no Bragg peaks related to the presence of gas hydrate appeared during the time of pressurization (more than 3 hours). From the observation of the diffractograms, it is already possible to conclude about the effect of the sediment composition on the gas hydrates formation kinetics. Indeed, the water-to-hydrate conversion occurs very quickly (within 10 minutes) in the MS matrix. Compare to IS and BS, MS contains a large portion of smectite clay. The presence of smectite provides a largest surface area (**Table 21**), which is known as a kinetic promotor for gas hydrate formation. In IS and BS, the hydrate formation takes longer than 3

hours of pressurization. Samples prepared *ex-situ* during longer pressurization times are needed to study the hydrate formation kinetics inside these matrices.

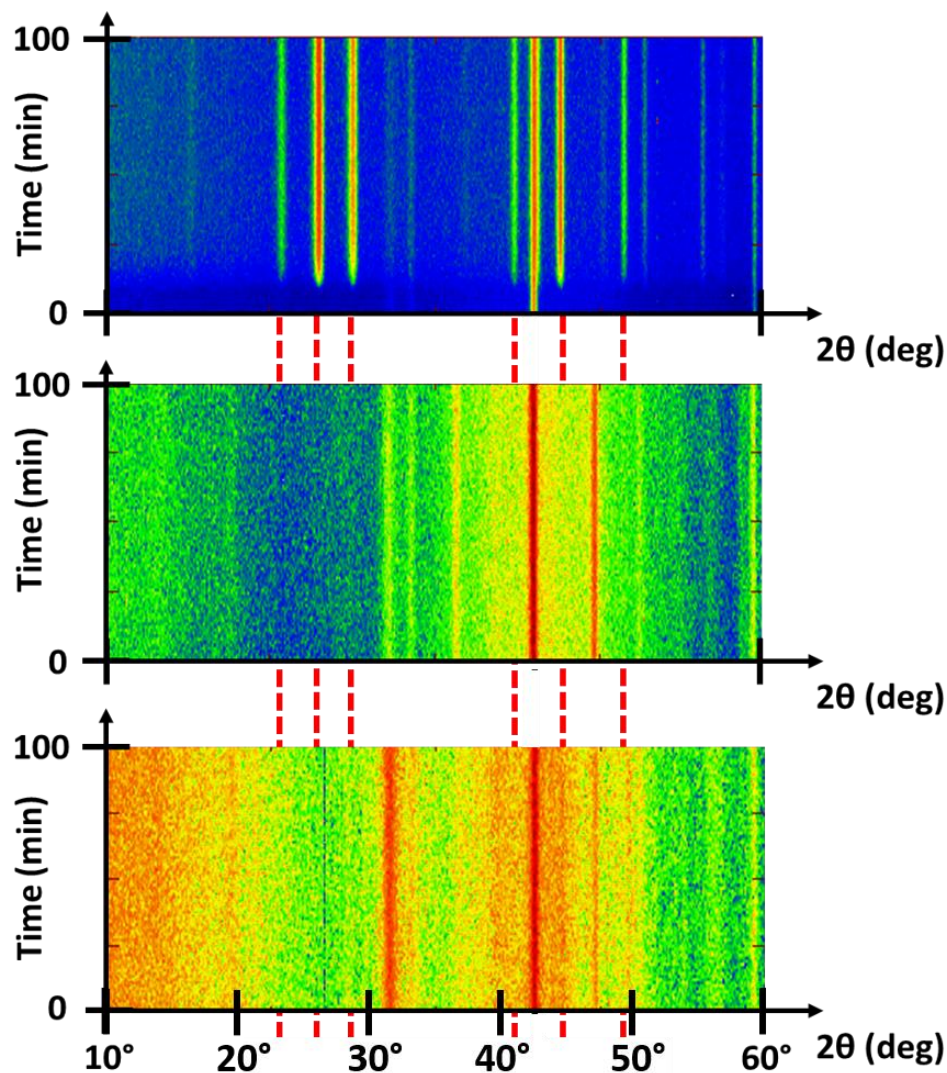


Figure 58. Time evolution of the structure of methane hydrate formed at 282 K and 70 bar within MS (top), IS (middle) and BS (bottom) over 100 minutes. The red dashed lines indicate type I hydrate Bragg.

Methane hydrates were synthesized in IS and BS in the lab prior neutron experiments. The samples were prepared at constant pressure (200 bar) and temperature (282 K) during 1, 7, 30, 75 and 110 days. A diffractogram is collected for both matrices on each sample with different pressurization time (**Figure 59**). In both matrices, Bragg peak related to methane hydrate sI can be observed after one day of pressurization. However, their intensity is extremely small compared to the intensity of ice peaks. When the number of pressurization days increases, it

can be observed that the fraction of ice in the sample decreases while the Bragg peaks of sI hydrate increases. The free water available in the sample decreases to form methane hydrate. In BS, the Bragg peaks of sI hydrate are more intense than in IS, and the signal of ice disappears. In order to quantify and understand these differences, a kinetic model is applied to the experimental data collected with neutron diffraction.

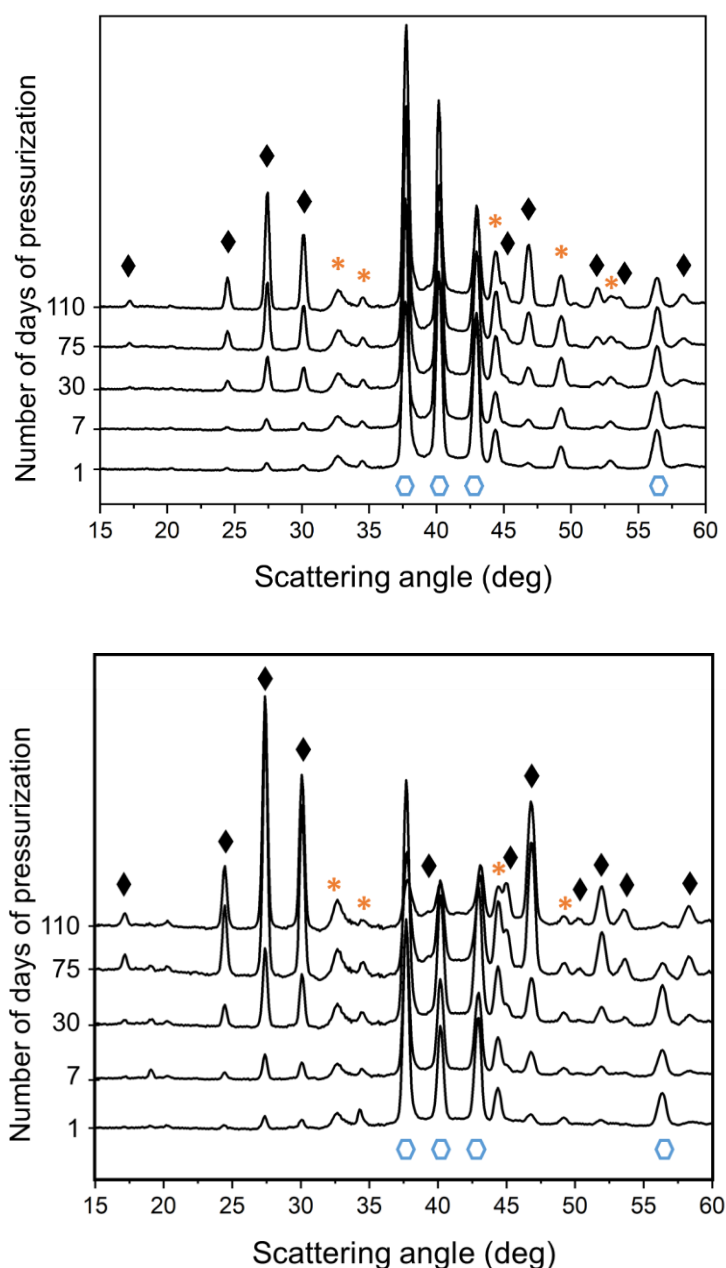


Figure 59. Diffractograms of methane hydrate in IS (top) and in BS (bottom) for different pressurization time (1, 7, 30, 75, 110 days). Bragg peaks of methane hydrate structure sI, ice and the matrices are tagged by the black diamonds, the blue hexagons and the orange stars, respectively.

ii. Quantifying the methane hydrate formation kinetics.

The quantitative analysis of the gas hydrate formation kinetics has been carried out for subsequent modeling. Rietveld refinement for each pressurization times and each sample has been conducted to measure the fraction of water converted into hydrate (called gas hydrate “conversion rate” $\alpha(t)$) defined as:

$$\alpha(t) = \frac{A_{hydrate}(t)}{A_{ice}(t) + A_{hydrate}(t)} \quad (36)$$

Where $A_{hydrate}(t)$ and $A_{ice}(t)$ are the integrated area of the Bragg peaks of hydrate and ice respectively as function of the time of pressurization t , as measured with Rietveld refinements (**APPENDIX 4, Figure S1 and Figure S2**). The Bragg peaks of each fraction are attributed by Rietveld refinement according to their space group. The cubic crystalline structure (Pm-3n) is used to refine the Bragg peaks of methane hydrate sI. Ice Bragg peaks are characterized by a fraction of cubic ice (Ic) and hexagonal ice (Ih), Fd-3m and P63/mmc structures respectively. The conversion rate for IS and BS as function of time plotted in **Figure 60** and compared to the methane hydrate formation kinetics in MS.

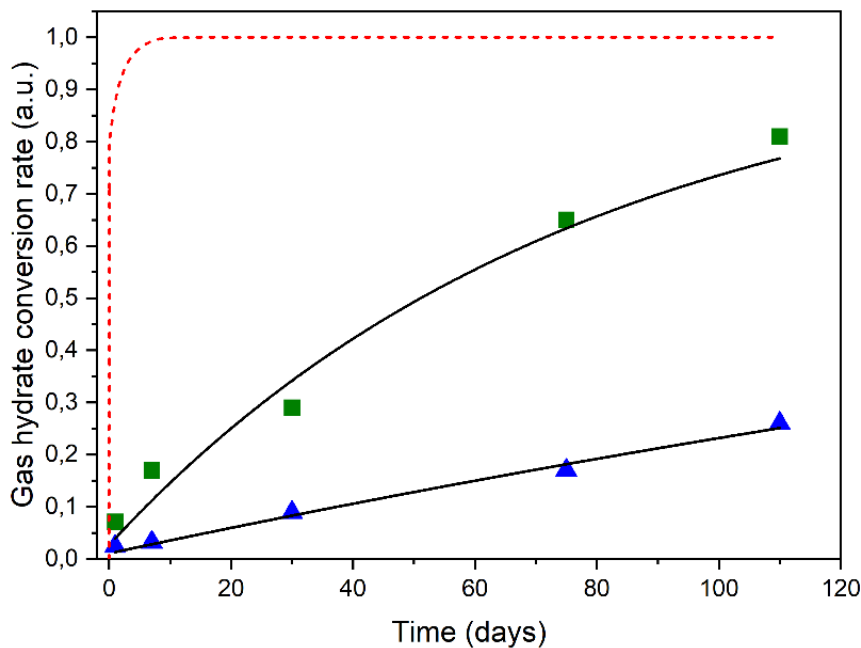


Figure 60. Experimental kinetic curves of CH₄ hydrates in BS (green square) and IS (blue triangle) synthesized ex-situ at 200 bar and 282 K. The black lines represent the fitted data with the modified BNG model in IS and BS and the red dashed line is the fitted curve of the kinetics of methane hydrates in MS from **Figure 56**.

The fraction of water converted into hydrate phase is very low (less than *ca.* 10%) for the sample pressurized during one day. This result was expected as the D20 *in-situ* neutron diffraction experiments did not show any Bragg peak of methane hydrate sI after more than 5 hours of pressurization for the methane hydrates synthesized in these matrices. After 110 days of pressurization, the fraction of methane hydrate has greatly increased. In the IS, the fraction of water converted into hydrates is still very low (less than *ca.* 35%). In the natural sediments from Black Sea (BS), the fraction of hydrate in the sample is higher, with more than 80% of the water converted into hydrate. The methane hydrate formation kinetics in MS have been studied into details in a previous paper. The presence of smectite in large quantity promotes hydrate formation. At 70 bar, 282 K, methane hydrate formation into MS occurs in less than 15min, reaching an almost complete conversion in less than one hour.

While in montmorillonite, the large specific surface area seems to play a major role in promoting hydrate formation, the kinetic difference between IS and BS cannot be explained in the same way, as these two matrices have very similar specific surface areas (**Table 21**). Particle size is also known to be a property involved in the mechanisms and kinetics of hydrate formation. Métais *et al.*⁹⁴ in 2021 used silica beads ranging from 70 nm to 210 μm . They observed a strong variation of the formation kinetics of the gas hydrates with the size of the sediment analogues particles, going from a very fast ice-to-hydrate conversion with the 70 nm silica nanoparticles to a very slow hydrate formation with silica particles larger than 50 μm . They therefore concluded that gas hydrate formation is faster when formed in presence of smaller sediment size.⁹⁴ Only a small difference in particle size is observed when comparing illite and natural Black Sea sediments, 530 nm and 275 nm respectively (**Table 21**). This difference could play a role in the faster water-to-hydrate conversion in natural sediments (BS) compared to IS, but is not sufficient to explain a conversion of up to 80% in BS for only 35% in IS. The impact of clay composition is now considered. The sample synthesized in IS, exhibits an impeding effect on the formation of gas hydrates. Moreover, a low conversion rate is reached after 110 days of pressurization. This commercially available illite matrix (IS) matrix contains 77% of illite clay and almost 20 % of kaolinite clay. The natural sediments from the Black Sea (BS) are composed of 60 % illite clay, 20 % kaolinite clay and between 5-10 % of smectite clay. Methane hydrate formation in kaolinite was previously investigated by Li *et al.*²¹⁶ in 2020. Molecular dynamics simulations demonstrated two nucleation processes, first, the bulk-like formation and then the formation of semi-clathrate at the siloxane surface of kaolinite clay.²¹⁶ As the second nucleation process occur at the nanoscale of clay when CH_4 is in close contact

with siloxane surface only, it can be concluded that experimentally, methane hydrate formation in presence of kaolinite mainly occurs in the time scale of bulk phase formation. Kaolinite, being in similar proportion in IS and BS, cannot explain the kinetic difference observed in this work. Here, the proportion of smectite inside the natural matrix draws attention. In our previous work, methane hydrate formation performed in montmorillonite (smectite clay) demonstrated the promoting effect of such clay mineral with an extremely fast nucleation (less than an hour) with almost complete water-to-hydrate conversion. Thus, the faster kinetics in the natural Black Sea sediments (BS) can be explained by the presence of smectite. Illite would then act as an inhibitor of methane hydrate formation. In BS, the fraction of illite is larger than the fraction of smectite. Hence, the methane hydrate formation will be shorter IS but longer than MS.

iii. Modeling the methane hydrate formation kinetics.

The modified Grain Boundary Nucleation (GBN) model was used to reproduce the kinetic data recorded during *ex-situ* neutron diffraction experiment on the two different matrices studied during this work: IS and BS (**Figure 60**). This model is applicable to the study of transformations in polycrystalline materials, especially when nucleation occurs at grain boundaries.²⁸⁸ Nucleation and growth rates are assumed constant throughout the process. Improvements to the model have been made to allow anisotropic growth from a constant number of nuclei or with a constant nucleation rate.²⁸⁹ The BNG model was first used and adapted by Métais *et al.*⁹⁴ to study the kinetics of gas hydrate formation from ice in the presence of silica beads. Most recently, it was used to adjust kinetics data of methane hydrate formation in presence of montmorillonite.

The BNG model follows this expression:

$$\alpha(t) = A \left\{ 1 - \exp \left[-2k_2(t - t_0) \left(1 - \frac{F_D[k_1(t - t_0)]}{k_1(t - t_0)} \right) \right] \right\} + (1 - A) \{ 1 - \exp[-k_3(t - t_0)] \} \quad (37)$$

$F_D(x)$ is the Dawson function, defined as:

$$F_D(x) = \exp(-x^2) \int_0^x \exp(y^2) dy \quad (38)$$

Where (t) corresponds to the conversion rate of water into hydrate at time t . t_0 corresponds to the time when the diffusion process starts. A is a constant related to the water fraction converted

into a hydrate layer at the water-gas interface. The first part of the above equation is devoted to the description of the formation of a hydrate surface layer at the water-gas interface. At the water-gas interface, the heterogeneous nucleation of the gas hydrate is controlled by the constant k_1 . Then, a hydrate layer forms with a limited thickness characterized by the kinetic constant k_2 . A "phenomenological" term is used in the second part of the equation and describes the diffusion process associated with hydrate growth. It is characterized by the constant k_3 : hydrate growth occurs at the hydrate-water interface where gas molecules diffuse through the hydrate layer and water molecules diffuse at the hydrate-gas interface into the gas phase.

The above model successfully fitted the kinetic data and the fitted curves are shown in **Figure 7**. Valuable data on the hydrate formation process in clay matrices could be obtained. All parameters are listed in **Table 22**.

	MS	IS	BS
A	0.8 ± 0.01	0	0
k₁	$8.0 \pm 0.003 \times 10^{-2} \text{ min}^{-1}$	0	0
k₂	$9.3 \pm 2.0 \times 10^{-2} \text{ min}^{-1}$	0	0
k₃	$3.9 \pm 3.1 \times 10^{-4} \text{ min}^{-1}$	$1.7 \pm 0.1 \times 10^{-6} \text{ min}^{-1}$	$9.0 \pm 1.4 \times 10^{-6} \text{ min}^{-1}$

Table 22. Kinetic parameters of the modified BNG model for methane hydrate formation in MS, IS and BS.

Kinetics modeling of the data recorded in IS and BS allows highlighting a unique phenomenon involved in the formation of methane hydrate. Indeed, compared to the hydrate formation in the presence of MS where the kinetics consists of three major steps. A rapid heterogeneous germination followed by the growth of a hydrate layer at the water/gas interface and a diffusion stage reached rapidly. The kinetics of hydrate formation in these two matrices are dominated by the diffusion phenomenon exclusively. This formation is therefore similar to the formation of bulky hydrate.^{297,298} The surface of these clays does not seem to modify the hydrate formation mechanism; however, the difference observed between the two matrices can be explained by the effect of the mineral composition. Both IS and BS have a large proportion of illite clay. Illite is a non-swelling clay with K^+ cations in the interlayer layer: K^+ cation has an extremely weak interaction with water and does not allow the initiation of solvation and swelling. This means that water in the matrices will only have access to the mesopores and macropores of the clays and the inter-particle space between clay and sand grains. As the kinetic rate of hydrate formation is similar to hydrate formation from pure liquid water^{297,298}, it can be concluded that

the multiscale distribution of pores in clays does not play a role in the promotion of methane hydrates and hydrate formation may occur in the inter-particle space. This result is supported by Wu *et al.*²¹⁵ who highlighted that it is much easier to form hydrate in bulk phase than in pores suggesting that hydrate formation may favor the formation in larger pore sizes. However, the presence of smectite in small proportion in BS may promote hydrate formation over IS. In the study of the kinetics of methane hydrate formation in MS, methane hydrate formation occurs in less than 15 minutes, highlighting the promoter effect of smectite clay. Besides the mineral composition, the large specific surface area provided by the smectite particles (**Table 18**) seems to be the main reason that favors hydrate formation in MS and BS compared to IS. Large specific surface area is known as a promoter effect of hydrate formation by improving the water-gas reaction. Furthermore, this work tends to state that hydrate formation in these matrices does not take place in the interstitial space but in larger pores or between the particles.

d. Conclusion.

In this work, the formation of methane hydrates in the presence of a commercially available illite matrix (IS) and natural Black Sea sediments (BS) was studied by neutron diffraction. Diffraction patterns of each sample synthesized from 1 day to 110 days at constant pressure and temperature in these two matrices were collected. Analysis of the diffractograms allowed the study of the structure of the hydrate formed and the kinetics of formation. No structural differences were observed in the two matrices. The kinetic study was performed by determining the intensity variation of the Bragg peaks related to the sI methane hydrate. The significant presence of illite (>60 %) in both matrices seems to have an inhibitory effect on hydrate kinetics. This results in a low hydrate conversion rate (<30 %) after 110 days in IS as well as a diffusion rate close to bulk hydrate formation. Methane hydrate formation in the presence of natural Black Sea sediments is more rapid and reaches a conversion rate of almost 85 % after 110 days. The presence of smectite in this sample (~10 %) and comparison with previous work on montmorillonite confirm the promoting effect of smectite due to the large specific surface area of smectite clay. This work is a significant advance in the understanding of the mechanisms governing the formation of methane hydrates in sedimentary environments.

CHAPTER 5:
Hydrate formation
in clays:
investigation of
confinement
signatures.

I. INTRODUCTION.

The significant natural occurrence of methane hydrates in deep marine sediments and permafrost regions draws strong attention to the estimation of these marine carbon resources but also to the geotechnical and geoclimatic consequences of such quantities in a complex and changing environment. As of today, the amount of energy stored in CH₄ hydrates is estimated to be twice that contained in conventional fossil fuels, with values ranging from 600 to 10,000 billion tons of methane trapped in hydrates.^{104,227} This large range requires a better understanding of the mechanisms of hydrate formation in natural environments, accumulation and storage capacity. This information is even more important in the field of geohazards. In the context of climate change, recent studies underlined the possible effects of the increase in seabed temperature, leading to hydrates destabilization, submarine land-slides and tsunami waves formations.¹⁰ In longer timescales, this could participate in ocean acidification and released-methane may reached the atmosphere.¹⁰ These climatic consequences motivate the scientific community to explore and bring new insights on methane hydrates formation in natural environment.

Nonstoichiometric crystalline compounds, methane hydrates are constituted by hydrogen-bonded water (host) cages in which methane (guest) molecules are trapped. The stability of the guest-host organization is handled by Van-der-Waals interactions.³ It exists three main gas hydrate crystalline structures: sI, sII and sH characterized by the assembly of different types and sizes of cages.³ Methane hydrate is known to form the structure sI hydrate. This cubic unit cell (space group Pm $\bar{3}$ n with a lattice constant $a = 11.77 \text{ \AA}$ at $T = 100 \text{ K}$ ⁹²) is formed with six $5^{12}6^2$ large cages (12 pentagons and 2 hexagons) and two 5^{12} small cages (12 pentagons)³, both types of cage being filled with methane molecule.

In natural environments, methane hydrates are found in fine-grained clay-rich sediments mixed mainly with silica materials like plagioclase, quartz and feldspars.^{235,236} Initially, in order to study the formation of methane hydrates in natural environments, the scientific community focused on the formation in the presence of various surrogates. Silica sand with various particle size ranging from 50 to 500 μm were used as sediments analogs. Liu *et al.*¹⁵⁸, investigated the influence of sand particle size on cage occupancy and hydration number and observed similar results compared with bulk hydrate, indicating the lack of influence of the particle size on hydrate composition. Magnetic resonance imaging performed by Bagherzadeh *et al.*, in 2011, showed a heterogeneous distribution of hydrates in a bed of silica particles and provides a

correlation between low water content and enhanced gas transport that improves water-gas contact.¹⁶¹ The understanding of hydrate formation also requires the study of the formation kinetics and in particular the impact of the sedimentary environment on the kinetics. Experiments conducted by Heeschen *et al.*¹⁴³ have shown that sediments particle size effect have a strong effect on the kinetics of gas hydrate formation, especially, medium or coarse sands conducted to a slower gas hydrate formation compared to a high concentration of fine grains <125 μm . Similar results have been observed by Métais *et al.*⁹⁴ with gas hydrates in presence of glass beads. They have shown the promotor effect of nanoparticules silica beads with hydrate formation starting in few minutes.⁹⁴ In addition to the effect of particle size on hydrate formation, experiments devoted to the study of hydrate formation in porous media, more similar to the natural system; have explored the effect of porosity on the kinetics. In particular, the surface of porous materials provides new nucleation sites and ensures a better gas–water contact resulting in a better hydrate formation kinetics compared to other matrices (quartz, sand).^{19,201}

From these studies emerged a major question, where does the formation of methane hydrate in porous media occur? This ambitious objective has led to original experiments including the study of the formation of gas hydrates in mesoporous MCM-41¹⁶⁸, activated carbons and carbon nanotubes^{162,169,170} and metal organic frameworks (MOFs)¹⁷¹. Despite the information obtained on the macro-properties of the hydrates and the effects on the kinetics, the techniques used did not allow to identify the formation of hydrates in confined nanoporous spaces.

Inelastic Neutron Scattering (INS) has proven its major role in the study of hydrogenated samples and in particular its performance in the study of the dynamics of atoms as well as the signal of confined molecules.^{299,300} Thus, pure methane hydrate was the subject of numerous studies, notably dedicated to the signatures of the guest molecule with mainly the identification of the methane rotation bands in the SC and LC of structure sI.^{301,302} Studies were then carried out on the analysis of guest-host interactions and the attribution of signatures of the translational modes and librational modes of water molecules in ice or as part of networks constituting the cages of the hydrate.^{303–307} One study investigated a sample of natural methane hydrate collected on the Pacific sea-floor where they identified the signatures of the three first rotational transitions of methane trapped in hydrate cages.³⁰⁸ Recently inelastic neutron spectroscopy studies have been performed on hydrate samples formed in the presence of porous activated carbons and in MOFs^{162,163}. The rotational signature identified in the samples are similar to those observed in the natural methane hydrate of the Pacific sea-floor and would be the first

evidence of hydrate formation in nanoporous spaces. These studies reported a minimum confined size of 1.6 nm necessary for methane hydrate formation.^{162,309} However, this dimension evaluated by Uchida *et al.*³¹⁰, would exhibit a minimum of 3 nm in for maintaining the hydrate stability.

All the experiments carried out on these sedimentary analogues have extended the physicochemical information on the formation of hydrates. However, in order to go further, it is necessary to reproduce the natural environment by taking into account its diversity, in particular by studying the influence of clayey sediments on the formation of hydrates. Clays are layered crystalline materials characterized by the structure of the layers and its stacking organization. According to their nature, clays are classified by their swelling properties in the presence of water characterized by the interlayer distance d_{001} . For swelling clays, smectites, this distance can vary between 10 and 20 Å.³¹¹ Conversely, non-swelling clays are characterized by a fixed and specific d_{001} depending on the type of clay ($d_{001}(\text{Kaolinite}) = 7 \text{ \AA}$, $d_{001}(\text{Illite}) = 10 \text{ \AA}$).³¹² In addition to this interlayer space, the structure of clays is composed of a multiscale porous network ranging from 20 to more than 500 Å constituted of mesopores and macropores.³¹³ This provides the clays a large specific surface area and raises questions about the impact on gas hydrate formation. Today, the majority of projects dedicated to this study use molecular simulation techniques. Only few studies have investigated the formation of methane hydrates in the presence of non-swelling clay. Molecular dynamic simulations focusing on the kaolinite effect shows that hydrate nucleation is affected by water and gas contacts with the surfaces of the clay layers, resulting in two nucleation events: in the bulk phase and near clay surfaces.²¹⁶ The adsorption of cations on the clay surface would be involved in the formation of methane nanobubbles at the liquid water/hydrate interface during decomposition. Molecular dynamics simulations conducted by Fang *et al.*²¹⁷ have identified this effect. The majority of studies focuses on the effect of swelling clays on the formation of gas hydrates and mainly on Montmorillonite. Molecular dynamics simulations have allowed the formation of methane hydrate in the interlayer space of montmorillonite. In particular, a study conducted by Yan *et al.* shows that the interlayer distance required to form the hydrate is 24 Å, which would correspond to 6 layers of water intercalated.²⁹ It is suggested that methane hydrate adopts a distorted structure constituted with the basal oxygen atoms of the silicate rings and intercalated H₂O molecules.²⁹⁻³² However, experimental studies of methane hydrate formation in the interlayer space of Na-Montmorillonite are inconsistent. X-ray diffraction experiments highlight the formation of the methane hydrate in the interlayer space, formation characterized

by a d_{001} equal to 22 Å.^{33,34} Conversely, the study conducted by Kim *et al.*³⁵ affirms that the formation of the hydrate structure in this space is physically impossible and identifies the formation in noninterlamellar voids like mesopores and macropores. Nevertheless, experimental and theoretical studies show that the surface of clays helps to provide a stabilizing influence of gas hydrate formation.^{31,35} On the contrary, Wu *et al.*²¹⁵ indicate that it is much easier to form hydrate in bulk phase than in pores.

Other question arises from these results: could there be potential impact of the clay matrix on the formed structure of hydrate and does it influence hydrate cage occupancy?

In this work, the influence of the nature of the clay sediment on the structure of the hydrate formed, the cage occupancy and the distribution from the micro- to the nano-scale is investigated. Neutron diffraction (ND), Raman spectroscopy (RS) and Inelastic Neutron Scattering (INS) were selected in this work to provide new original data on synthetic and natural methane hydrate. The collected information of the synthetic samples made in illite, kaolinite, montmorillonite and Black Sea natural sediments are compared to the natural sample collected in Black Sea in September 2021 during the GHASS2 cruise.

II. MATERIALS AND METHODS.

a. Sample preparation

Synthetic methane hydrate samples were prepared in presence of Black Sea natural sediments, Illite, Kaolinite and Montmorillonite. All the matrices are constituted with 60 % clay and 40 % of other minerals (mainly quartz).

Black Sea sediments were collected during the GHASS cruise in 2015 on the Romanian sector.¹²⁶ Black Sea sediments are denoted BS in this work. These sediments have been analyzed by XRD and are naturally composed of clay (60 %) and 40 % of other minerals (mainly quartz, calcite and plagioclase). The mineralogical analysis of the clay composition indicates the average presence of 60 % illite, <10% smectite, 20 % kaolinite and 10 % chlorite.

The illite matrix commercialized by Argiletz (FR) will be denoted IS in this work. Its mineral composition makes this matrix an excellent sedimentary analogue of the natural sediments of the Black Sea since it is composed of 60 % clay and 40% other minerals (quartz, calcite). Illite is a 2:1 dioctahedral clay mineral characterized by the structure of its layers, which consists of

two tetrahedral sheets which intercalate an octahedral sheet to constitute the T-O-T unit.³¹² The K^+ cations are present in the interlayer space and confer to this clay a non-swelling behavior.

The kaolinite matrix is commercialized by Argiletz (FR). It is a non-swelling clay made up with two types of layers: a tetrahedral silica sheet and an octahedral alumina sheet. Hydrogen bonds provide the connection between the two types of sheets and avoid water molecules to enter in the interlayer space.³¹² To reproduce the mineral fraction of the natural sediments, kaolinite was mixed with Fontainebleau sand (Laboratoires Humeau, FR) to constitute a matrix with 60 % clay and 40 % quartz, denoted KS.

Montmorillonite (Montmorillonite K10, Sigma Aldrich) is a smectite clay. It is a naturally abundant material and is chemically modified by the cation-exchange method. Like illite clays, it is a 2:1 dioctahedral mineral clay. However, its swelling behavior differs by the nature of the intercalated cations (Na^+ , Mg^{2+} , Ca^{2+} , Li^+) which in the case of montmorillonite, provides a suitable environment for water molecules to access the interlayer space and gives to this clay an extremely large specific surface area and swelling capacity.³¹¹ The swelling properties of this montmorillonite clay was analyzed thanks to neutron diffraction by determining the scattering angle of the Bragg peak attributed to the (001) plane used to estimate of d_{001} distance (see **APPENDIX 5, Figure S1**) and the supplementary information. A matrix made with a mixture of Montmorillonite and Fontainebleau sand (Laboratoires Humeau, FR) constitutes a reference swelling matrix for this study with 60 % clay and 40 % sand, denoted MS.

The main physicochemical properties of the four matrices BS, IS, KS, MS are detailed in **Table 23**.

Properties	Montmorillonite (MS)	Illite (IS)	Kaolinite (KS)	Black Sea sediments (BS)
Particle size (D_{mean})	14 μm	4.5 μm	5.8 μm	2.75 μm
BET Surface area	240.8 m^2/g	66.5 m^2/g	17.5 m^2/g	63.1 m^2/g
Global mineralogy				
Quartz	30 %	25 %	40 %	14 %
Argiles / micas	60 %	60 %	60 %	60 %
Calcite	-	14 %	-	5 %
Plagioclase	10 %	-	-	8 %
Clay fraction mineralogy				
Smectite	82 %	< 5 %	-	5-10 %
Illite	15 %	77 %	< 5 %	60 %
Kaolinite	< 5 %	17 %	84 %	20 %
Chlorite	< 5 %	< 5 %	14 %	10 %

Table 23. Main physicochemical properties and mineral composition of the four clay-rich matrices used as methane hydrate substrates.

To form methane hydrates, at room temperature, the four matrices were homogeneously hydrated with deuterated water (D_2O) or purified MilliQ water (H_2O) for neutron diffraction and spectroscopy experiments, respectively. For a same volume of each matrix, the amount D_2O or H_2O corresponding to 30 % of this same volume was injected and then, manually mixed with each sediment. Once hydrated, the matrices are placed inside home-made aluminum pressured-cells connected to a gas pump to control gas pressure. The cells pressure and temperature are fixed during 14 days for hydrate formation at 200 bar and 282 K. The temperature is controlled by a water bath. After 14 days, the hydrate samples are collected and stored in liquid nitrogen until analyses.

Natural methane hydrate samples were collected on the Romanian sector of the Black Sea in September 2021 during the scientific cruise GHASS2²¹. The samples investigated in this study were recovered from core CS05 collected 345 cm below the seafloor at the top of the crest line near gas flares. In this core, X-ray diffraction analysis of the sediments revealed a composition close to 60 % clay including kaolinite, smectite and illite.

b. Techniques

Neutron Diffraction (ND).

Structural analysis of synthetic deuterated methane hydrates in clay matrices was performed on the 2-axis high intensity neutron powder diffractometer D20 at Institute Laue-Langevin (ILL), Grenoble (FR). IS, KS, BS and MS are the matrices selected as hydrate-forming sediments to mimic natural hydrate formation in marine environments. Deuterated hydrate samples are cold transferred in liquid nitrogen to an aluminum cell prior the experiments. Diffractograms are collected at 150 K and 1 bar with a wavelength of $\lambda = 2.41 \text{ \AA}$.

Raman spectroscopy (RS).

Raman spectroscopic experiments were conducted on the LabRam HR Evolution Raman microspectrometer (Horiba Jobin Yvon, Villeneuve d'Ascq, France) using a $\lambda_0 = 405 \text{ nm}$ wavelength laser as the excitation source. A long-working distance objective 50x is used for an optimum spatial resolution to focus the incident laser beam on the sample and to collect the Raman scattering. The Raman scattering is dispersed by a holographic grating of 1800 lines/mm (high resolution) and analyzed by a Peltier-cooled CCD detector (Andor, Belfast, UK). The intensity of different wavelengths of the spectrum are measured with a spectral resolution of 2.5 cm^{-1} (full width at half-maximum). The calibration of the spectrometer was done using the 520.7 cm^{-1} mode of a silicon sample. The data were collected on a spectral range from 150 to 3800 cm^{-1} . Crushed hydrate samples are placed on a Peltier plate in an optical Linkam cell (Linkam Scientific Instruments Ltd., UK) with a glass window on top, which allows microscopic investigation and Raman spectroscopic measurements. Crushed synthetic hydrogenated and natural samples (CS05) collected in Black Sea during the GHASS2 cruise are characterized by Raman micro mapping at 150 K and 1 bar. This technique allows phase identification and 2D chemical distribution at the micrometer scale.

Inelastic Neutron Scattering (INS).

INS was used to identify and attribute the hydrogen vibrational signatures in synthetic hydrogenated and natural samples from the Black Sea (CS05). Spectra were measured at 10 K in the range of energy transfers from 10 to 140 meV ($80 \text{ to } 1200 \text{ cm}^{-1}$) on the IN1-Lagrange neutron spectrometer at ILL. Hydrate samples were cold transferred into aluminum cells under inert atmosphere and connected to a sample-changer designed at ILL. The raw INS spectra were

pre-treated by subtracting the background spectrum from the cryostat and an empty sample holder.

III. RESULTS AND DISCUSSION.

a. Structural analysis and cage occupancy

The influence of a clay-rich matrix on two characteristic properties of methane hydrates was investigated. Neutron diffraction was used to characterize the crystalline structure of the synthetic formed hydrate and Raman micro-spectroscopy contributed to evaluate the cage occupancy of synthetic and natural hydrates, all according to the four selected matrices (IS, BS, MS, KS). Synthetic pure methane hydrate was used as a reference system.

Neutron diffraction is used to study the structure of methane hydrates formed in the presence of clay minerals. On a previous paper, this technique was used to determine the impact of clay minerals on methane hydrate formation kinetics. Unlike X-ray diffraction, commonly used for the study of methane hydrates in the presence of Na-Montmorillonite³⁴, activated carbons¹⁶² or MOFs¹⁶³, neutron diffraction allows to better access the deuterated aqueous substructure (ice, hydrate) due to the coherent scattering cross-section of the deuterium compared to the signal of the matrix (clay, sand). Thus, this study focuses on the analysis of the structure of clays and of the formed hydrate.

The diffractograms collected at 150 K and 1 bar of the synthetic samples made in MS, IS, KS and BS are represented in **Figure 61** and compared to the diffractogram of pure synthetic methane hydrate. The analysis of the Bragg peaks of the sedimentary matrices is focused on the (001) diffraction plane, which is used to determine the interlayer distance (corresponding to d_{001} as described in **APPENDIX 5 and APPENDIX 5, Table S1**). They are measured for kaolinite and illite as $7.11 \pm 0.03 \text{ \AA}$ and $9.81 \pm 0.56 \text{ \AA}$, respectively. On the diffractogram of the Black Sea natural sediments, these two peaks are also observed, which is in agreement with the mineral composition of the natural sediments. Finally, the d_{001} of montmorillonite is broadened, which makes the determination of the interlayer distance difficult in the presence of hydrate. The broad peak is observed at $8.42 \pm 0.15^\circ$, which corresponds to a d_{001} of $16.44 \pm 0.15 \text{ \AA}$ and the study of the d_{001} of montmorillonite before and after the addition of deuterated water for hydrate formation shows a d_{001} distance of $14.61 \pm 0.06 \text{ \AA}$ and $19.01 \pm 0.1 \text{ \AA}$, respectively (**APPENDIX 5, Figure S1**). The interlayer distance of montmorillonite is

contracted in presence of methane hydrate in the sample. This contraction phenomenon was previously reported with X-ray diffraction when investigating the effect of freezing on the swelling of Na-montmorillonite interlayer.³¹⁴ They observed the decreased of the interlayer space due to the formation of solid water structure outside this space, causing the compression of water molecules.³¹⁴ These values were also observed by Kim *et al.*³⁵ and Guggenheim *et al.*³⁴ regarding the formation of methane hydrate inside the interlayer space of Na-montmorillonite. The Bragg peaks of methane hydrate in structure sI are labeled on the diffractograms in the **Figure 61**. The three most intense and isolated peaks are observed at $23.58 \pm 0.01^\circ$, $26.42 \pm 0^\circ$, $28.99 \pm 0^\circ$. By comparing the data collected, it can be observed that the position and the width of the peaks in the four matrices are similar to the Bragg peaks of the diffractogram of the pure bulky hydrate. However, the intensity of the Bragg peaks varies depending on the fraction of water converted into hydrate in the samples. In MS, the Bragg peaks of hexagonal ice Ih are weak compared to the Bragg peaks of structure sI hydrate, most of the water available have been converted into hydrate. In the contrary, in IS, BS and KS, the Bragg peaks of Ih are more intense than the Bragg peaks of structure sI hydrate. According to these observations, the presence of clay does not influence the crystalline structure of the formed hydrate but the presence of methane hydrate in MS modifies the interlayer distance. Does it mean that methane hydrate is formed in the interlayer space or outside of it, involving the lattice contraction of MS?

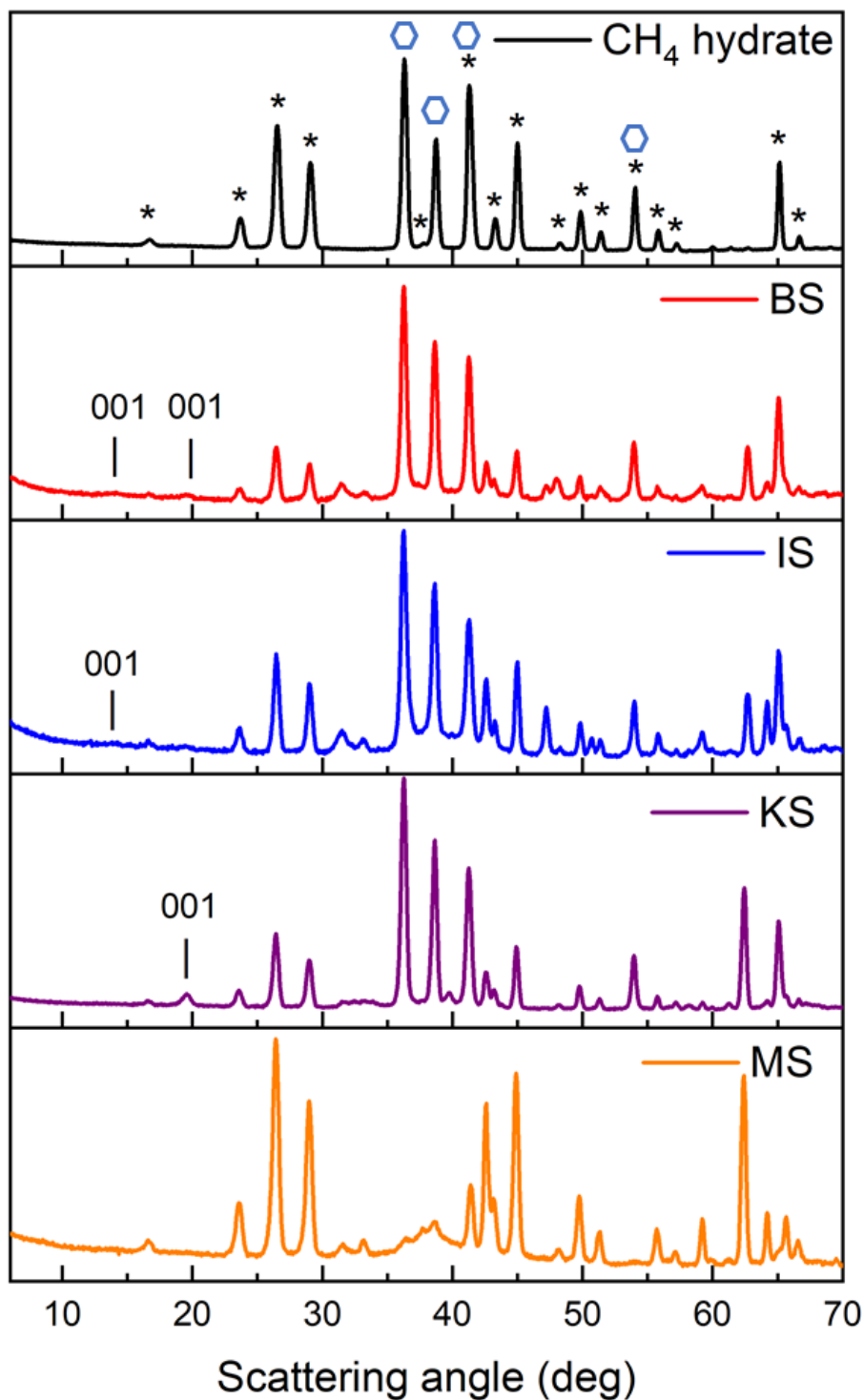


Figure 61. Diffractograms recorded at 150K, 1bar of the pure bulky synthetic methane hydrate (top-Black) and methane hydrate formed in presence of BS (position 2-red), IS (position 3-Blue), KS (position 4-Purple) and MS (Bottom-Orange). Bragg peaks of structure sI hydrate and hexagonal ice Ih are identified by black stars and bleu hexagons, respectively.

Before answering this question, the impact of the matrix on the vibrational signatures and cage occupancy of methane hydrate is studied. Raman spectroscopic measurements on the crushed pure hydrogenated synthetic methane hydrate, on the hydrate samples formed in the four clays matrices (KS, MS, BS, IS) and on natural hydrate sample CS05 collected in the Black Sea in September 2021 were performed at 150 K and 1 bar. Examples of the collected spectra are shown in **Figure 62**.

The typical spectra collected can be detailed into three main contributions of methane hydrate. The bands at 200-400 cm^{-1} corresponds to H_2O lattice modes, and the O-H stretching bands are observed between 3000 and 3800 cm^{-1} .⁴² These two signals exhibit similar features for ice and structure sI hydrate in the sample.⁴⁴ The last region, 2700-3000 cm^{-1} , corresponds to the stretching modes of methane molecules trapped in hydrate cages: two Raman bands centered at $\sim 2905 \text{ cm}^{-1}$ and $\sim 2916 \text{ cm}^{-1}$ are attributed to the C-H stretching of methane trapped in the large cage (LC) and the small cage (SC), respectively.⁵⁶ These spectroscopic signatures are in agreement with the formation of structure sI hydrate in Black Sea, as reported by Chazallon *et al.*¹⁵³. Besides these signals, two weak bands at $\sim 2570 \text{ cm}^{-1}$ and $\sim 3050 \text{ cm}^{-1}$ are attributed to the overtone of C-H asymmetric bending mode ($2\nu_4$) and the first overtone of the C-H bending mode ($2\nu_2$) of methane in hydrate lattice, respectively (**APPENDIX 5, Figure S2**).²³³

The spectra collected in the sediment-rich zone show a large background signal related to the fluorescence signal of clays. Moreover, numerous peaks are present in the range of 400-1500 cm^{-1} related to clay layers (Si-, Al-, -OH).³¹⁵ Spectra also showed a Raman band at $\sim 465 \text{ cm}^{-1}$ characteristic of the presence of quartz in the sample.³¹⁶ Additional signatures are observed at higher frequencies for Kaolinite clay, identified by five distinct Raman bands at 3620, 3652, 3670, 3685 and 3693 cm^{-1} assigned to the O-H stretching modes of the three inner surface hydroxyl groups at clay layers.³¹⁷

Regarding the frequencies of the Raman bands attributed to LC and SC, the comparison of all the spectra recorded for the various synthetic and natural samples shows that the composition of the clay matrices does not change the frequency of the bands within the accuracy limit of the spectrometer.

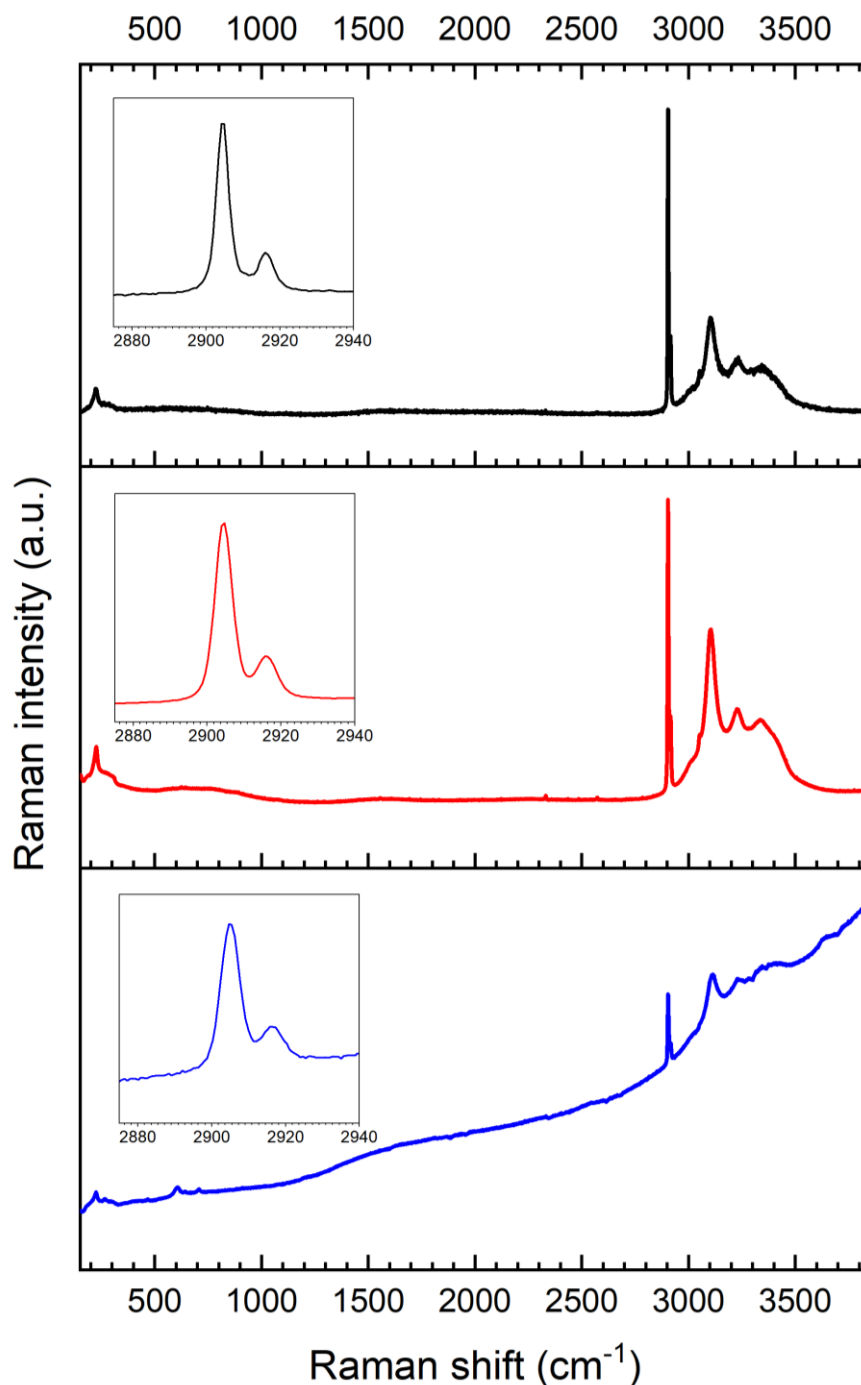


Figure 62. Raman spectra of pure methane hydrate (top), natural methane hydrate CS05 (middle) and methane hydrate in MS (bottom), recorded at 150K and 1bar. The inserts show the CH-stretching bands of methane molecules in the LCs (2905 cm^{-1}) and SCs (2916 cm^{-1}), respectively.

The evaluation of cage occupancy of the methane hydrate can be done by using the vibrational signature of methane molecules in the LCs and SCs. The synthetic samples made in clay rich-matrices (IS, BS, MS and KS) are compared to the pure synthetic methane hydrate sample and

the natural sample collected in Black Sea (CS05) with similar a clay composition (**Figure 63**). The cage occupancy is estimated from the ratio of the integrated Raman signal of the LC (A_{LC}) and SC (A_{SC})^{56,318}:

$$\frac{A_{LC}}{A_{SC}} = 3 \frac{\theta_{LC}}{\theta_{SC}} \left(\frac{\sigma_{LC}}{\sigma_{SC}} \right)^2 \quad (39)$$

θ_{LC} and θ_{SC} represent the CH_4 occupancy and σ_{LC} and σ_{SC} are the Raman scattering cross sections of methane in LC and in SC, respectively. They are assumed to be similar in the pure structure sI methane hydrate.^{56,233}

Several spectra are collected over the sediment-free sample area and the average of the ratio of the LC and SC band areas of each spectrum is taken to estimate the cage occupancy of each sample. The number of spectra collected for each sample is summarized in the supplementary information (**APPENDIX 5, Table S2**). The A_{LC}/A_{SC} ratio is ranging from 2.8 and 3.7 (**Figure 63**), which is closed to the value expected for structure sI methane hydrate.^{153,233,319} Comparison of cage occupancy ratios A_{LC}/A_{SC} in the various clay matrices, in the natural Black Sea sample and in pure methane hydrate suggests a low impact of sediments on the cage occupancy of the investigated hydrate. Furthermore, this result suggests that the samples formed in the laboratory accurately reproduce the formation of natural hydrates of the Black Sea.

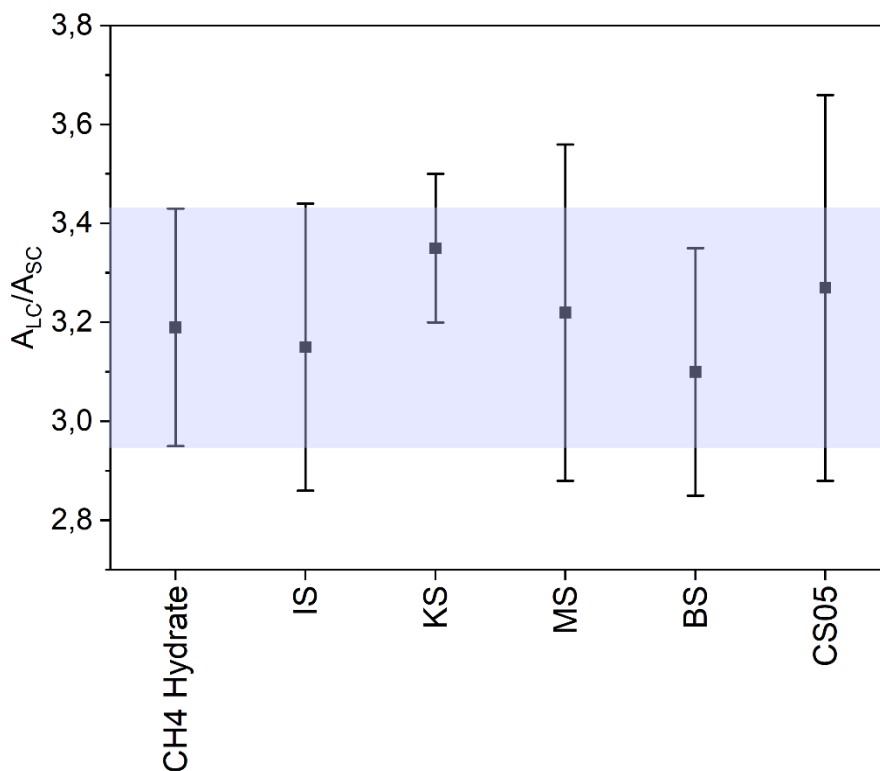


Figure 63. Estimation of cage occupancy of pure methane hydrate, methane hydrate in the synthetic samples made with typical clays present in Black Sea and the natural sample CS05 with similar clay composition. The error bars are calculated by the standard deviation measured from the average of Raman spectra collected for each sample (**APPENDIX 5, Table S2**).

In order to interpret these results in favor of the formation of methane hydrate in the interlayer space of montmorillonite, four hypotheses can be formulated.

- The formation of methane hydrate in the interlayer space leads to isotropic compression of the montmorillonite and hydrate lattices. This is visible on a diffractogram by the shift of all the Bragg peaks to smaller or larger angles.
- Conversely, the formation of methane hydrate in this space leads to an anisotropic compression of the montmorillonite and hydrate lattices. This can lead to the loss of the cubic symmetry of the hydrate lattice, the formation of a distorted hydrate structure, resulting in the appearance of additional Bragg peaks on the diffractogram.
- The formation of this hydrate confined in this nano-metric space can also create a disorder, observed on the diffractogram by the broadening of the Bragg peaks.
- Finally, the presence of interlayer cations could enter in the hydrate cages, replace methane molecules and thus lead to a variation of the occupancy rate of the confined hydrate cages observed with Raman spectroscopy. These observations have been made

by Yeon *et al.* who showed the abnormal cage occupancy of clathrate hydrate intercalated with the substitution of Na⁺ and CH₄ in 45 % of the small cages.^{17,320}

Several studies have been dedicated to the formation of methane hydrate in the interlayer space of swelling clays and the community is still unable to reach an agreement. Molecular Dynamics simulations tend towards the intercalation of a new intercalated clathrate hydrate structure composed of the silicate ring of 2:1 silicate layers of swelling clays and interlayer water molecules.^{29-32,321} Their results is supported by experimental studies on Na- and Ca-Montmorillonite by Koster Van Groos *et al.*³³ and Guggenheim *et al.*³⁴, which attributed the contraction of the d_{001} to the presence of methane hydrate in the interlayer space. Inversely, studies conducted by Kim *et al.*³⁵, based on the size of a hydrate cage compared to the interlayer space of swelling clays, concluded that structuring a complete hydrogen-bonded cage in this space is almost physically impossible. Furthermore, MD simulations dedicated to the effect of 1 to 8 water layers on the formation of methane hydrate in montmorillonite suggests that interlayer space with 6 H₂O layers is the most suitable to form CH₄ hydrate, which corresponds to a interlayer distance $d_{001} = 24 \text{ \AA}$. The hydrate cages formed in this space would be irregular with deformation and defects.²⁹

In this present work, the d_{001} of montmorillonite varies from 14 and 20 Å, which suggests the intercalation of less than 4 water layers³¹¹, the formation of methane hydrate in the interlayer space of montmorillonite appear to be physically impossible similarly to the work of Kim *et al.*³⁵. Furthermore, from the collected diffractograms, the hypotheses of the formation of a distorted hydrate structure and isotropic or anisotropic compression of the methane hydrate lattice are not supported. No deformation or displacement of the characteristic Bragg peaks of methane hydrate in sI structure are observed, and no additional peaks are found. The Raman spectroscopic analysis did not show any variation of the cage occupancy in presence of montmorillonite. The formation of the methane hydrate probed with these two techniques does not take place in the interlayer space of montmorillonite in the MS matrix. However, methane hydrate can form in the multiple non-intercalated spaces of clays, consisting of mesopores (2-50 nm) and macropores (>50 nm) and the obtained results show that these meso- or macro-hydrates have similar characteristics to pure bulky methane hydrate. Moreover, it is important to note that Raman spectroscopy does not probe the mesoporous spaces of clays. Therefore, it is not possible to determine the role of clays on cage occupancy at all pore scales with this technique.

In order to complete the understanding of methane hydrate formation in clay-rich matrices and to discuss the possibility of hydrate formation in confined environments, it is necessary to access the distribution of hydrates in clay matrices and to explore the nanoscale. For this purpose, Raman and Neutron spectroscopic experiments have been performed.

b. Hydrate distribution from micrometer to nanometer scales

Raman micro-spectroscopy was used to probe the distribution of the sI methane hydrate structure in all samples made in IS, MS, BS, KS, pure bulky methane hydrate, and the natural sample (CS05). 2D Raman imaging was obtained by collecting multiple Raman spectra, over a pre-selected area of the sample, where the Raman signal of the hydrate is high. Then, the methane hydrate and matrix signal is integrated and plotted against position on the sample to reconstruct Raman maps. The methane hydrate integrated signal consists of the two Raman bands attributed to the CH-stretching of the methane molecule in the LC and SC, after background subtraction. The matrix signal is integrated between 560 and 623.6 cm^{-1} taking into account the background signal, which is related to the presence of clays. This technique allows access to the micrometric distribution of the sI methane hydrate and sediment structure in the samples.

In **Figure 64**, the Raman mapping of methane hydrate sI and the matrix of BS are represented. The area probed measured 70 x 50 μm and 110 spectra have been collected every 3.2 μm . The combination of these two Raman maps reveals the presence of hydrates primarily in areas where the sediment matrix signal is absent (**Figure 64**). The same observation was made for all the synthetic and natural sample containing clay-rich sediments. Two hydrate pore-habits could explain this result. In clay-rich sediments, methane hydrate can nucleates on sediment grain boundaries and grow freely into pore spaces without altering the structure of the sediments, this hydrate pore habit is called pore-filling.⁹⁸ In contrast, hydrate nucleation can happen between grains and induce sediment grain-displacing to form “bulky” hydrate lenses and nodules.³²² The identification of these pore habits in the samples investigated is extremely challenging mainly due to the heterogeneities of the water and gas distribution in the various pore sizes in the matrices. This could lead to an heterogeneous hydrate formation at the grain scale and at the sample scale.^{165,323} The *in-situ* observation of the formation and distribution of the hydrate in clay sediments at the microscopic or nanoscale is required to complete these results. Recently, the formation and dissociation of Xenon hydrate in sand and a mixture of sand and

montmorillonite was observed experimentally using X-ray micro-tomography and observed hydrate nucleation at the water-gas interface and hydrate grows around sediments grains.²⁰⁴ However, this technique does not provide information on the distribution at the nanoscale and in particular does not allow the study of the interlayer space of clays.

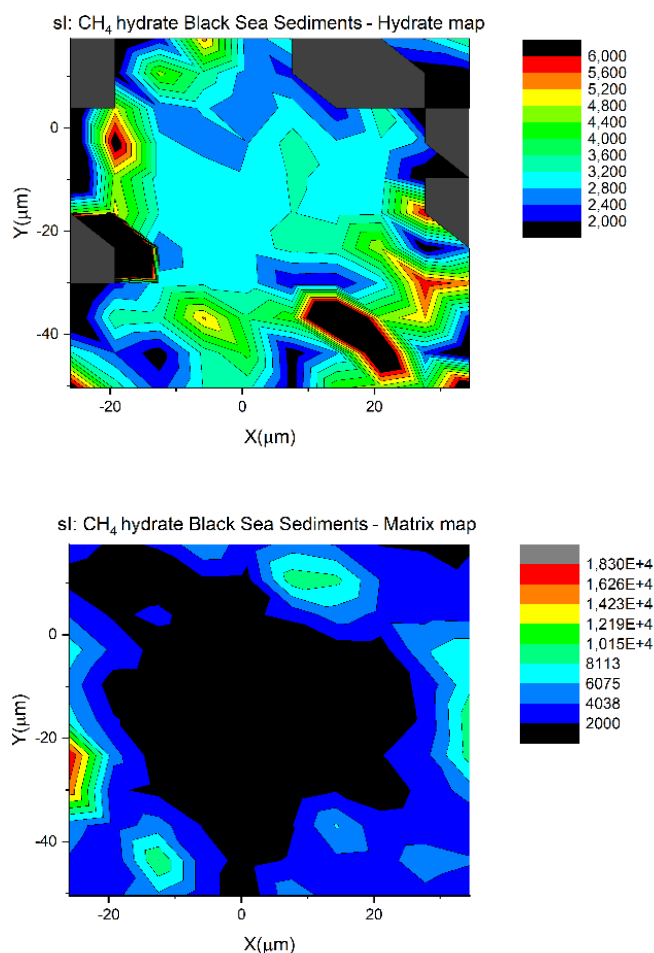


Figure 64. Optical microscope capture of methane hydrate sample formed in Black Sea natural sediments (x50 objective). The white square defines the area analyzed by 2D Raman mapping (top). Two 2D Raman maps of the sample are represented: the integrated signal of the Raman

bands of SCs (2916 cm^{-1}) and LCs (2905 cm^{-1}) of methane hydrate (middle) and the integrated signal related to the sediment ($560 - 623.6\text{ cm}^{-1}$) (bottom).

The study of confinement phenomena at the nanoscale is extremely challenging. In this work, Inelastic Neutron Scattering (INS) were performed on the crushed synthetic and natural samples previously analyzed with Raman spectroscopy at 10 K and 1 bar. INS is a powerful technique to access the molecular self-dynamics. The translational and librational modes of water as cage-forming molecules or ice particles and the rotational modes of methane molecules trapped in hydrate cages are investigated.

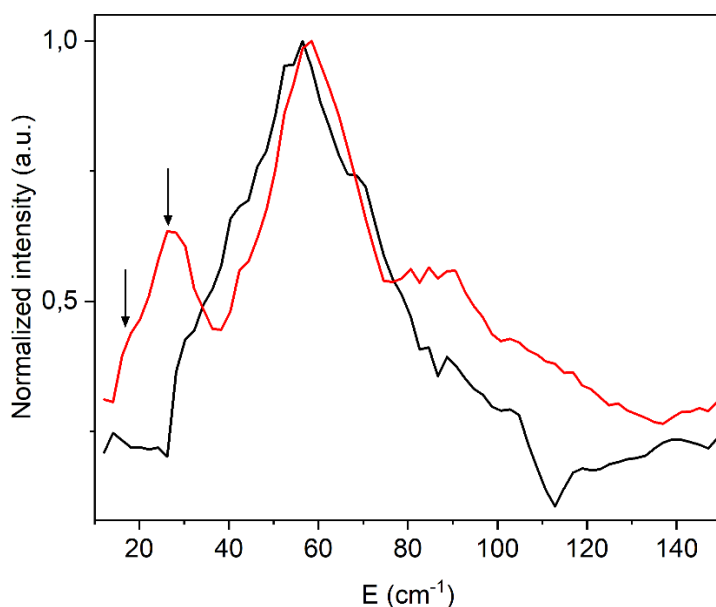
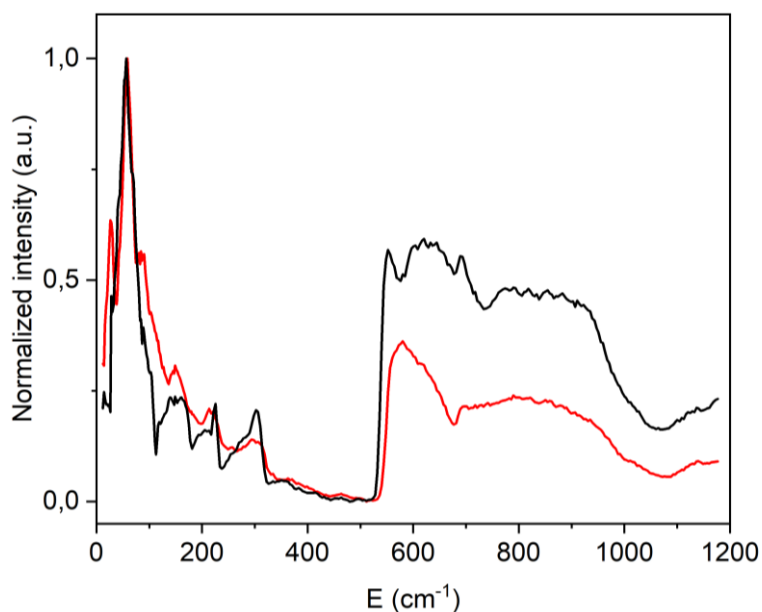


Figure 65. Inelastic neutron scattering spectra of ice Ih (black) and pure methane hydrate (red) (top). Rotational bands of methane in structure sI hydrate (Black arrows) and translational modes of water molecules in ice and structure sI methane hydrate are represented on the bottom spectra. Spectra are collected at 10 K and 1 bar.

The spectra of hexagonal ice Ih and pure methane hydrate structure sI are shown in the **Figure 65**. The spectra of Ih shows translational modes of water represented by a sharp peak at 55.5 cm^{-1} , a hump around 107 cm^{-1} , a broad peak around 153 cm^{-1} , and two sharp peaks at 226 and 304 cm^{-1} .³²⁴ The spectral range between 550 and 1100 cm^{-1} is related to the librational modes of water molecules.³²⁴ The librational spectrum of Ih is characterized by a left edge around 540

cm^{-1} , two minimums at 570 cm^{-1} and 735 cm^{-1} , and a right edge at around 975 cm^{-1} .³²⁴ The spectra of pure methane hydrate structure sI is characterized by two peak at 17.8 cm^{-1} and 26.2 cm^{-1} which are attributed to the rotational modes of methane trapped inside water cages.³⁰¹ These two peaks are assigned to the rotational transition from $J=1$ to $J=2$ and $J=0$ to $J=2$, respectively. The transition from $J=0$ to $J=1$ at 7.9 cm^{-1} ^{325,326} cannot be observed in the present experiment (out of spectral range). The peaks at 58 cm^{-1} and between 75 and 90 cm^{-1} are attributed to the transverse acoustic host lattice dynamics^{305,327}. The methane vibrations inside the small cages influences the signal between 75 and 90 cm^{-1} .^{305,327} A sharp peak, at around 580 cm^{-1} , characterizes the librational mode of methane hydrate and a broad signal between 678 cm^{-1} and 975 cm^{-1} .³⁰⁷

The spectra of ice Ih and pure methane hydrate are compared to the synthetic and natural samples formed in presence of clay-rich sediments (**Figure 66** and **Figure 67**). In **Figure 66**, the spectra of synthetic and natural hydrate samples show methane hydrate signatures similar to the pure methane hydrate spectrum with the two rotational bands at $\sim 17.8 \text{ cm}^{-1}$ and $\sim 26.2 \text{ cm}^{-1}$ and the peak at $\sim 58 \text{ cm}^{-1}$ attributed to the host lattice dynamics.³²⁴ The latter peak, depending on the sample, has a variable width and is notably wider depending on the amount of ice present in the sample. As a reminder, the ice Ih presents this same peak at shifted to 55.5 cm^{-1} .³⁰³ It related to the translational modes of water molecules.³⁰³ In **Figure 67**, are represented the librational modes, between 500 and 1100 cm^{-1} . In this spectral range, the signal is complex, constituted of signatures of both ice Ih and methane hydrate structure sI depending on the fraction of each phase in the samples. The comparison of the spectra of ice Ih, pure methane hydrate and the synthetic methane hydrates in IS, KS and BS show signatures similar to the spectra of Ih with a band at around 555 cm^{-1} , two broad signals between 570 cm^{-1} and 735 cm^{-1} , and between 735 cm^{-1} and 975 cm^{-1} . A weak methane hydrate signal is identified at $\sim 580 \text{ cm}^{-1}$. The strong similarity of the synthetic methane hydrate spectra to the Ih ice spectrum rather than the pure methane hydrate spectrum indicates the presence of a significant ice fraction in the samples. This result is not surprising because studies of methane hydrate formation kinetics performed on these same matrices (with the exception of KS) show that only a small amount of the water in the matrix is converted into hydrate after 14 days of pressurization (*i.e.* $< 20 \%$ in BS and $< 10 \%$ in IS).³²⁸

The librational spectrum of the natural sample (CS05) shows a stronger methane hydrate signature at $\sim 580 \text{ cm}^{-1}$ compared to the synthetic samples. However, the librational signatures

between 592 cm^{-1} and 975 cm^{-1} indicate the presence of ice Ih in the sample. The only difference between the spectra of ice Ih and CS05 is a minimum at 694 cm^{-1} , where there is a maximum on the Ih ice spectrum. The presence of ice in CS05 can be explained by the conditions of recovery of natural hydrate in the Black Sea. Between the time when the sample is removed from the seabed and its recovery on the ship at room temperature, the surface of the sample is destabilized before storage in liquid nitrogen, while the core of the sample is preserved. Once crushed, the sample collected is constituted of a mixture of ice, resulting from hydrate dissociation, and preserved methane hydrate during hydrate recovery.

Analysis of the INS spectra collected by probing the synthetic methane hydrate samples in IS, KS, and BS, shows the presence of the methane hydrate structure sI with characteristic signatures of methane molecules rotational motion in SC and LC. However, these spectra show many similarities to the Ih ice spectrum, evidence for the presence of a large ice fraction in the samples. The natural methane hydrate sample collected in the Black Sea (CS05) contains both Ih ice and methane hydrate structure sI. This ice fraction is the result of the dissociation during hydrate recovery.

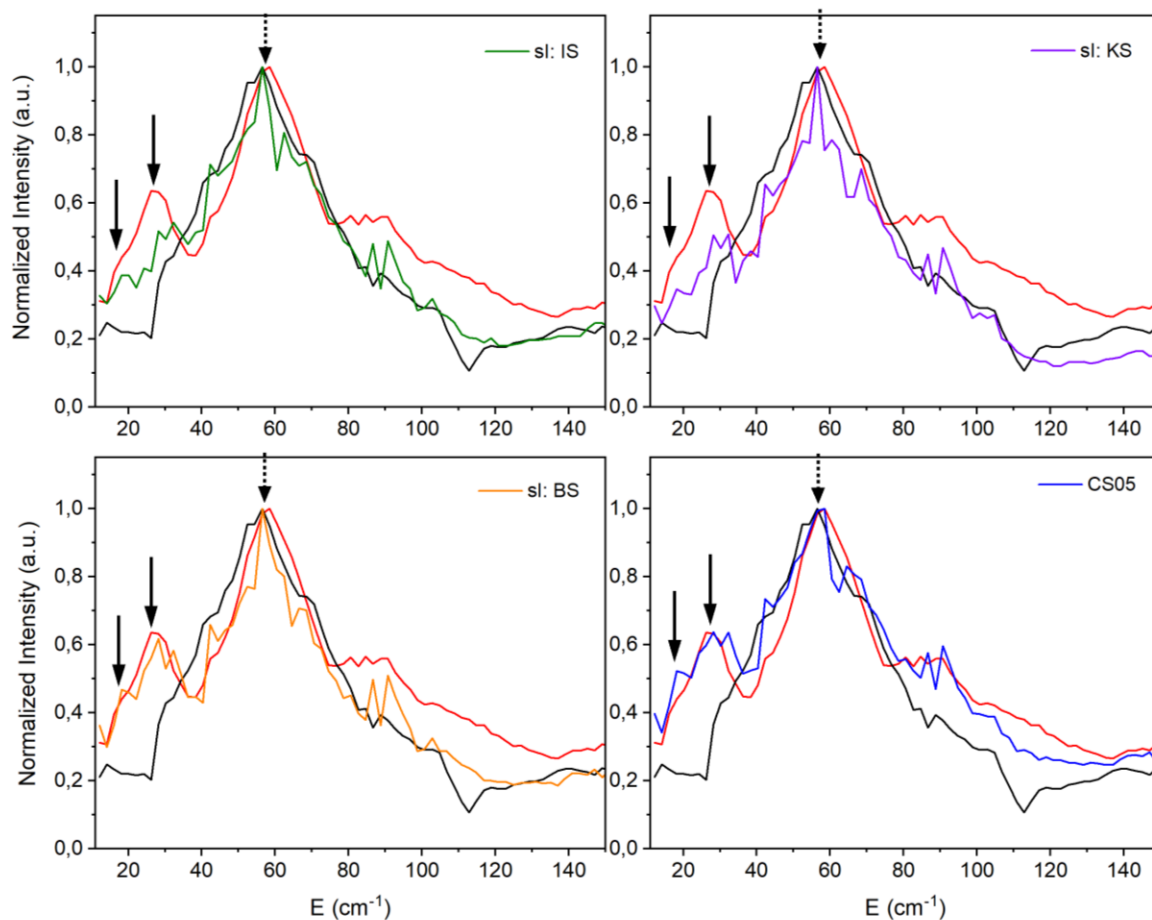


Figure 66. Inelastic neutron scattering spectra of ice (black) and pure methane hydrate sI (red) compared to methane hydrate in IS (top left), KS (top right), BS (bottom left) and natural methane hydrate CS05 (bottom right). Full black arrows represent rotational bands of methane in structure sI hydrate and the dotted black arrow represents translational mode of water molecules in methane hydrate, slightly shifted from the translational modes of water molecules in ice. Spectra are collected at 10 K and 1 bar.

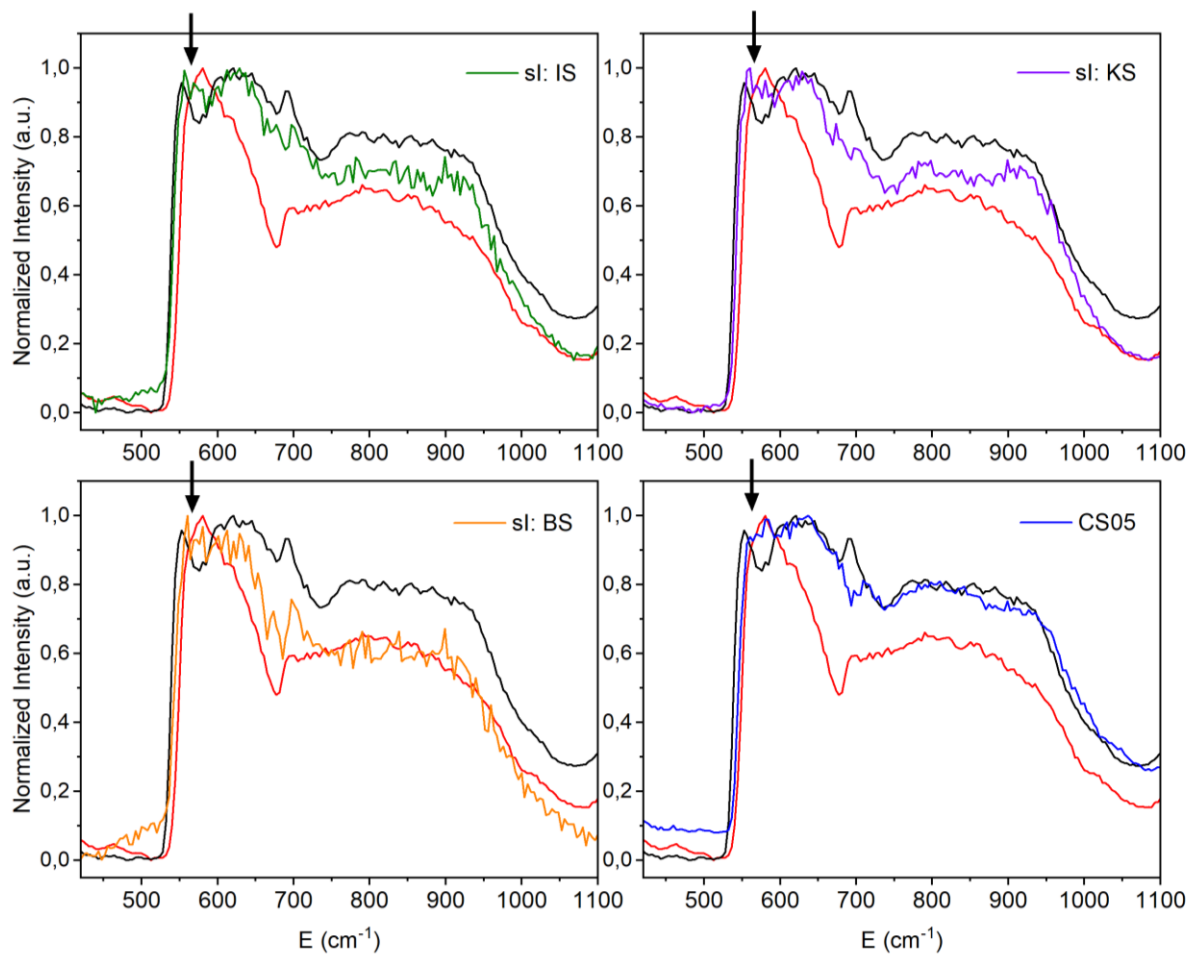


Figure 67. Librational spectra of ice (black) and pure methane hydrate structure sI (red) are compared to methane hydrate in IS (top left), KS (top right), BS (bottom left) and natural methane hydrate CS05 (bottom right). Full black arrows represent the librational signal of water molecules as host molecules of structure sI. Spectra are collected at 10 K and 1 bar.

In a second step, INS was used to study the distribution of methane hydrates in the MS and probe the interlayer space. The objective was to examine the presence of additional signatures, on the INS spectra, possibly related to hydrate growth in a confined environment. INS experiments on swelling saponite clay, conducted by Jiménez-Ruiz *et al.* show a shift to higher energies of librational bands related to the presence of confined water between layers.²³⁴ According to this paper, the INS signal of MS (undried), hydrated MS, and methane hydrate in MS are compared to ice Ih and pure methane hydrate structure sI to look for a similar signature of ice or methane hydrate confined (**Figure 68**). The signatures of methane hydrate structure sI in MS are observed at $\sim 17.8 \text{ cm}^{-1}$ and $\sim 26.2 \text{ cm}^{-1}$ corresponding to the two rotational bands of methane molecule in hydrates cages and a peak at $\sim 58 \text{ cm}^{-1}$ attributed to the host lattice dynamics.³²⁴ The spectrum of methane hydrate in MS and pure methane hydrate exhibit similar

signatures and intensities, with the exception of the first rotational band at 17.8 cm^{-1} that has a lower intensity. The peak at 58 cm^{-1} is shifted from the peak of ice Ih, which appear at 55.5 cm^{-1} . This shift is the evidence of the low fraction of ice Ih in the sample of methane hydrate in MS. This first observation confirm the result obtained with neutron diffraction for the deuterated sample of methane hydrate in MS formed in the same conditions: almost all available water phase has been converted into methane hydrate.³²⁹ Between 30 and 113 cm^{-1} , the signal related to the translational modes of water is identical for pure ice Ih, non-hydrated MS and hydrated MS. In the librational region of the spectra, compared to pure ice Ih and pure methane hydrate structure sI, all the spectra collected in presence of MS exhibit an additional signal around 512 cm^{-1} , which could be related to the presence of water in the interlayer of montmorillonite.²³⁴ The signal of undried MS and ice are very similar between 530 and 1100 cm^{-1} , evidence of the presence of residual water molecules on the non-hydrated MS. When water is added onto MS, the spectrum of hydrated MS shows an extra signal at $\sim 670\text{ cm}^{-1}$. The latter signal could be evidence of the signature of confined ice in the montmorillonite. Now the question remains, are similar signatures of molecular confinement observed in the methane hydrate sample synthesized in MS? The librational region of the collected spectrum of methane hydrate in MS is similar to the spectrum of pure methane hydrate with the exception of three weak signals: at ~ 512 , ~ 550 and $\sim 670\text{ cm}^{-1}$. When compared to hydrated MS and pure ice Ih, these signatures are all attributed the libration of water molecules into ice Ih structure. Thus, it can be concluded from this experiment that methane hydrate did not form in the interlayer space of the MS, most of the water was converted to bulky hydrate, and the remaining water molecules contribute to the spectroscopic signature of ice Ih. All synthetic and natural methane hydrates studied in this paper, exhibit spectroscopic signatures similar to those of the bulky hydrate structure sI and pure ice Ih. These hydrate structures form between clay grains or in the meso- and macropores of clays.

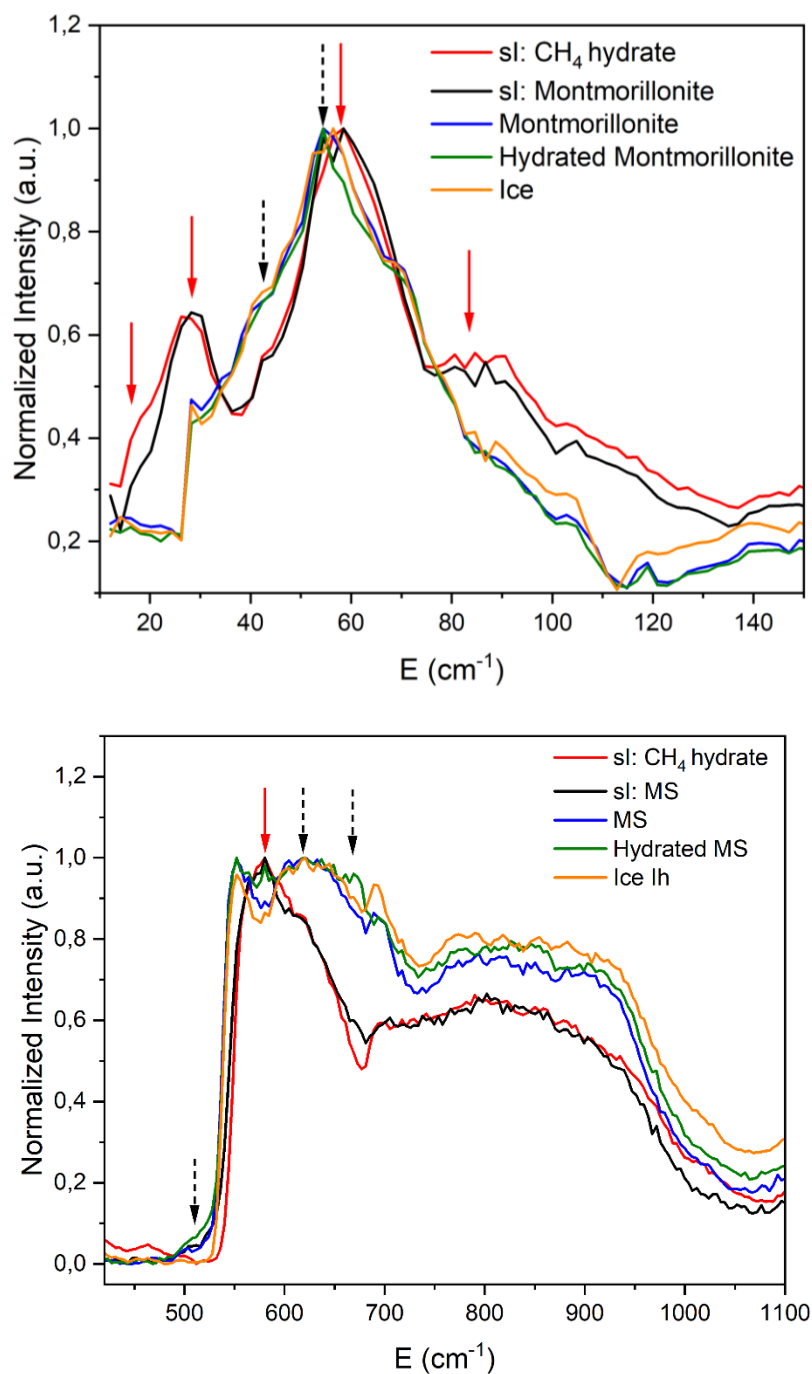


Figure 68. Rotational modes of methane molecules in structure sI hydrate, translational and librational modes of water in ice, in hydrate substructure and in MS are compared. Red full arrows are the signature of methane hydrate structure sI. Black dotted arrows are the signature of water molecules in ice and in confined space of MS. Spectra are collected at 10 K and 1 bar.

IV. CONCLUSION.

In this chapter, an original experimental approach has been carried out for investigating the formation of methane hydrate at scales ranging from the micrometer to the nanometer. The investigation has been conducted by comparing lab-made methane hydrate samples (formed in clayey matrices reproducing the natural sediments) with natural methane hydrate samples collected in the Black Sea. The strategy developed to understand the effect of these matrices on the structure, the cage occupancy and the multiscale distribution of the formed hydrate combines neutron diffraction, Raman spectroscopy and Inelastic Neutron Scattering.

Montmorillonite, a so-called swelling clay, has been the subject of a few studies, dedicated to the plausible formation of methane hydrate in the interlayer space.^{29,30,32–35} Two controversial results are reported: (i) the formation of a new distorted hydrate structure in the nano-space³⁴ and (ii) the physical impossibility of forming the hydrate in this space, thus privileging the formation in the mesoporous and macroporous spaces³⁵. In this study, neutron diffraction reveals no structural differences between pure methane hydrate structure sI and methane hydrate formed in IS, KS, BS or MS. A deeper analysis of the latter, in particular the study of the variation of the d_{001} interlayer space, indicates results similar to the literature with a swelling reaching 20 Å and a decrease of this space once the hydrate is formed. Combining these results with the information collected with Inelastic Neutron Scattering seems to favor the hypothesis of the methane hydrate formation outside this nano-space. The spectrum of methane hydrate in MS is similar to that of pure methane hydrate with no signature of confined water molecules. Furthermore, this data also reveals that almost all the water available for hydrate formation has been converted and the decrease observed on the d_{001} may be related to the water desorption to be converted into hydrate.

Inelastic neutron scattering on the synthetic methane hydrate in IS, KS, BS and the natural sample CS05 collected in Black Sea in September 2021 show similar spectroscopic signatures. CS05 presents a great signal of methane hydrate sI with the identification of the two rotational bands of methane in SCs and LCs of structure sI, and of translational and librational signatures: all neutron spectroscopic signals are similar to the one measured in pure methane hydrate (i.e., formed without sediments). However, similarly to the synthetic samples with IS, KS, BS, numerous spectroscopic signatures are assigned to the presence of water in the samples, indicating a lower conversion rate for synthetic samples in these clays and the probable presence of a fraction of the dissociated sample related to the recovery method for CS05.

Finally, Raman spectroscopy allowed the study of the distribution of methane hydrates in the sedimentary matrix by highlighting a heterogeneous distribution of the matrix and the hydrate phase. The mapped areas exhibit a high methane hydrate signal where the matrix signal was low or non-existent. This provides microscopic evidence that hydrate forms between sediment grains, consistent with pore-filing and pore-displacing models.⁹⁸

Raman signal analysis was also used to estimate methane hydrate cage occupancy for different matrices. Despite large uncertainties related to the heterogeneities of the analyzed samples and the quality of the collected spectra at each mapping positions, the relative occupancies of the LCs and SCs in the presence of the various matrices seem similar to the one measured in the pure methane hydrate. There would not be a significant impact of the sediments onto the cage occupancy.

This study constitutes a new approach to study the formation of methane hydrates in natural environments and could contribute to the improvement of models related to the quantification of methane contained in natural hydrates and thus improve environmental predictions in case of destabilization of these structures.

General conclusion & Perspectives

In the context of the study of gas hydrate formation in natural environment, three complex parameters were taken into account during this PhD work: the composition of the natural gas available to form gas hydrates, the water salinity and the nature of the marine sedimentary environment present in the gas hydrate stability zones. The crystal structures and the chemical composition of mixed hydrates formed with various gaseous species existing in geological sites suitable for gas hydrate formation, have been studied by means of Raman spectroscopy and neutron diffraction. In order to study the influence of salinity and the presence of clayey sediments on the methane formation kinetics (as well as dissociation mechanism), samples were synthesized in the laboratory - mimicking the natural marine environment - and analyzed by time-dependent neutron diffraction. In addition, neutron diffraction combined with Raman and neutron spectroscopy allowed to study the impact of sediments on the structural properties, the cage occupancy and the distribution from micrometer to nanometer scales. Moreover, the results obtained by spectroscopic methods on lab-made gas hydrates are compared to the ones obtained on natural methane hydrate samples, collected in the Black Sea during the GHASS2 scientific campaign. This PhD works thus provide a range of new information by identifying key physical-chemistry factors affecting the cage occupancy, the crystalline structure, the distribution, and therefore the ability of hydrates to store methane in natural environment.

In order to address the first problematic, the structural and vibrational signatures of synthetic gas hydrates formed from pure molecules CH_4 , C_2H_6 , C_3H_8 , *iso*- C_4H_{10} , CO_2 and gas mixtures $\text{CH}_4+\text{C}_2\text{H}_6$, $\text{CH}_4+n\text{-C}_4\text{H}_{10}$, have been studied by Raman spectroscopy and neutron diffraction. Neutron diffraction was used to characterize the crystal structure of pure methane and carbon dioxide hydrates, which adopts the structure sI and propane hydrates in the structure sII. Raman spectroscopic measurements were used to study both the vibrational signatures of structure sI and structure sII hydrates for small gas species (CO_2 , CH_4), larger hydrocarbons (C_2H_6 , C_3H_8 , *iso*- C_4H_{10} , *n*- C_4H_{10}) and gas mixtures ($\text{CH}_4+\text{C}_2\text{H}_6$, $\text{CH}_4+n\text{-C}_4\text{H}_{10}$). This study confirmed the occupancy of both SCs and LCs with CO_2 , CH_4 and C_2H_6 molecules in structure sI. The study of the structure sII formed by mixed gas hydrates with methane and larger hydrocarbons reveals that methane molecules occupy both types of cages, while the Raman band analysis suggests that only the LCs ($5^{12}6^4$) are occupied by the large size hydrocarbon molecules. The spectra of CH_4 hydrate structure sI and structure sII (formed in the case of mixed hydrates) show two characteristic Raman bands (ν_1), attributed to the CH-stretching of methane in both SCs and LCs. In the structure sII, these signatures are shifted towards lower energy with respect to the signatures of structure sI. Moreover, the intensity ratio of the two bands is close to 1:2, due to

the presence of 8 LCS for 16 SCs in the structure sII, while it is close to 1:3 due to the presence of 2 SCs and 6 LCs in the structure sI.

In order to address the impact of salt combined with the presence of clay on methane hydrate formation kinetics and dissociation mechanisms, samples were synthesized and analysed by *in-situ* time-dependent neutron diffraction. A mixture of 60 % swelling clay, Montmorillonite, and 40 % quartz was chosen as the mineralogical surrogate of natural environments for this study. This mixture is designated by the acronym MS. Methane hydrate samples were synthesized in presence of pure deuterated water and salted water (22 wt% NaCl). Montmorillonite acts as a kinetic promotor of methane hydrate with an almost complete conversion of water into hydrate after less than 60min of pressurization (70 bar) at constant temperature (282 K). Similar timescales were observed for sediments analogues like silica beads with a size smaller than 100nm.⁹⁴ Several physicochemical parameters can explain these very short induction and formation times. The first parameter is the particle size. Heeschen *et al.* have shown that gas hydrate formation in presence of a high concentration of fine grains (clays) <125 μm have a faster hydrate conversion than methane hydrate in coarse grains and sand. The major parameter is highly connected to the atomic structure of clays. Several studies highlighted the promoted effect of clay surfaces with the presence of hydroxylated edge sites to induce hydrate nucleation.^{35,214} The last parameters involves the thermodynamics conditions with a larger driving force provided by the presence of smectite clays like bentonite, which shortened the induction time.^{213,292} Montmorillonite, a smectite clay, with particles size $\sim 14 \mu\text{m}$, and interlayer cations causing the swelling of the structure possesses favorable nucleation sites for hydrate formation. For 2.2 wt% NaCl system, the CH₄ hydrate formation is slower and starts after 15min of pressurization, the water to hydrate conversation rate is lower and comes with a long diffusion process. The kinetic inhibitor effect of salt is well-known from the literature. Chong *et al.* described this effect on the hydrate formation in porous Toyoura sand and presented the lower thermodynamic driving force during hydrate formation.²¹⁸ Similarly, very recent experimental study on the coupling effect of montmorillonite and NaCl shows that when the concentration of NaCl is high, the induction time increases.²²⁰ However, the indicated induction times in their study range from less than 5 hours to 50 hours, which is 5 to 50 times higher than the times observed in this work. The study of the dissociation of CH₄ hydrates in both pure and salted samples exhibits characteristics of the self-preservation phenomenon. In addition, other phenomena may be considered as hypothesis to explain the observed behaviors. First, the dissociation of pure CH₄ hydrate may involve hydrate re-formation probably due to

the increased concentration of dissolved methane from the melted hydrate leading to the creation of methane “high-pressure” bubbles at interfaces (hydrate/ice or hydrate/clays); such phenomenon have been reported in the literature.^{217,330} A second process that may be involved in this re-formation is probably related with the restructuration of water molecules from hydrate and “short range ice” to ice and melted water, as experimentally observed on the neutron diffractograms. The presence of salt prevents hydrate re-formation due to the possible presence of high local concentration of salt around hydrate cages, which were excluded out of the cages during hydrate formation. However, self-preservation is still observed with a hydrate melting point reaching 270 K.

In a second step, in order to compare the effect of the nature of the clay on the methane hydrate formation kinetics, two clay-rich matrices were selected: a commercial sample consisting mainly of illite (denominated IS) and natural sediments from the Black Sea (denominated BS). The formation kinetics of methane hydrates formed within these two matrices were studied by time-dependent neutron diffraction and then, compared to the result obtained for samples formed within MS from pure water. Diffraction patterns of each sample synthesized from 1 day to 110 days at constant pressure and temperature in these two matrices were collected. Analysis of the diffractograms as a function of the pressurization time yield the quantitative determination of the fraction of formed hydrate and thus, the formation kinetics to be monitored (by measuring the Bragg peaks intensity of the sI methane hydrate as a function of the pressurization time). No structural differences (compared to methane hydrate formed without clays) were observed for the two matrices. The significant presence of illite (> 60 %) in both matrices seems to have an impeding – even inhibiting - effect on hydrate formation compared with the formation of MS methane hydrate. This results in a low hydrate conversion rate (< 30 %) after 110 days in IS as well as a diffusion rate close to bulk hydrate formation.^{297,298} Methane hydrate formation in the presence of natural Black Sea sediments is more efficient than in IS and reaches a conversion rate of almost 85 % after 110 days. The presence of smectite in this sample (~10 %) and comparison with previous work on Montmorillonite confirm the promoting effect of smectite clay surface.³⁵

The last part of the manuscript was dedicated to the comparison of synthetic methane hydrate samples, formed in the laboratory in the presence of clayey matrices, and of natural methane hydrate samples collected in the Black Sea. The strategy developed aimed at understanding the effect of these matrices on the formed structure, the cage occupancy and the hydrate distribution

at the micro- and nanoscale. This strategy is based on the combination of neutron diffraction, Raman spectroscopy and Inelastic Neutron Scattering experiments. The structural analysis was performed with neutron diffraction and Raman spectroscopy. Both techniques reveal no structural differences between pure bulky methane hydrate structure sI and methane hydrate formed in IS, KS, BS or MS. Moreover, Raman signal analysis was also used to estimate methane hydrate cage occupancy in the natural and synthetic matrices. Despite large uncertainties related to the non-uniform shape of the samples analyzed and the quality of the spectra collected at each mapping positions, the cage occupancy of the LCs and SCs in the presence of the matrices is similar to pure bulky methane hydrate. Gas hydrate distribution at the micro- and nanoscale was studied with Raman imaging and inelastic neutron scattering, respectively. At the microscale, the study of the distribution of methane hydrates in the sedimentary matrix highlighted a heterogeneous distribution of the matrix and of the hydrate phase. The mapped areas exhibited a high methane hydrate signal in micrometer areas where the matrix Raman signal was negligible. This provides microscopic evidence that hydrate forms between sediment grains, consistent with pore-filing and pore-displacing models⁹⁸. At the nanoscale, the spectra collected with the inelastic neutron scattering (INS) technique show similar spectroscopic signatures for natural and synthetic methane hydrate samples. The natural sample, collected in Black Sea, exhibits strong methane hydrate sI signals characterized with the two rotational bands of methane in SCs and LCs of structure sI, and with the translational and librational bands of water molecules. The natural sample exhibit INS signals very similar to those of pure methane hydrate. The synthetic samples made in IS, KS, BS exhibit weak methane hydrate signatures. However, numerous spectroscopic signatures in these spectra are assigned to the presence of unconverted water in the samples, evidencing the low conversion rate observed for these synthetic samples. Moreover, the combination of these techniques brings new element to answer the question of the hypothetical intercalation of methane hydrate in swelling Montmorillonite (MS). The study of the variation of the d_{001} interlayer space with neutron diffraction is in agreement with published results^{30,35}, reporting a decrease of the interlayer (reaching 20 Å before hydrate formation) space once the hydrate is formed. Both Raman and neutron spectra of methane hydrate in MS exhibit similar signatures to pure bulky methane hydrate structure sI with no specific signatures of confined water molecules or of confined hydrate. These results suggest that the methane hydrate formation occur outside the interlayer space, i.e. in the meso- and macro- pores of clay allowing the formation of methane hydrate structure sI with properties similar to bulky hydrate phase.

This PhD work provides new information regarding the formation of methane hydrates in natural environments.

First, the study of the effect of gas composition on hydrate structure was conducted. The knowledge of all the vibrational signatures of gas hydrates of various hydrocarbons shows the effective contribution of Raman spectroscopy to estimate the gas composition of natural gas hydrates, and the resulting structure. To extend this study, Raman spectroscopy can be used to investigate the vibrational signatures of natural gas hydrates formed from complex gas mixtures and to determine the adopted preferential structures. This will contribute not only to the assessment of potential molecular selectivity (i.e., chemical composition differences between the natural gas reservoir and the natural gas hydrates), but also to the determination of the hydrates structure formed in natural environments. A preliminary study was carried out *in-situ* to compare the spectrum of the hydrate formed from natural gas recovered from the Marmara Sea and the spectrum of the hydrate formed from a mixture of synthetic gas (Standard-1B) with a composition close to the natural one, all under identical thermodynamic conditions. The presence of several hydrocarbons makes the analysis of the Raman spectra complex, with several signatures around 2900 cm^{-1} attributed to the C-H vibrational modes. The obtained results seem to indicate only vibrational signatures of gas hydrates in structure sII. Further analysis of the relative intensities, positions and widths of the Raman bands could allow to determine the single, multiple or mixed encapsulation of gas molecules within the cages. This study is the subject of a collaboration with Olivia Fandino-Torres (IFREMER).

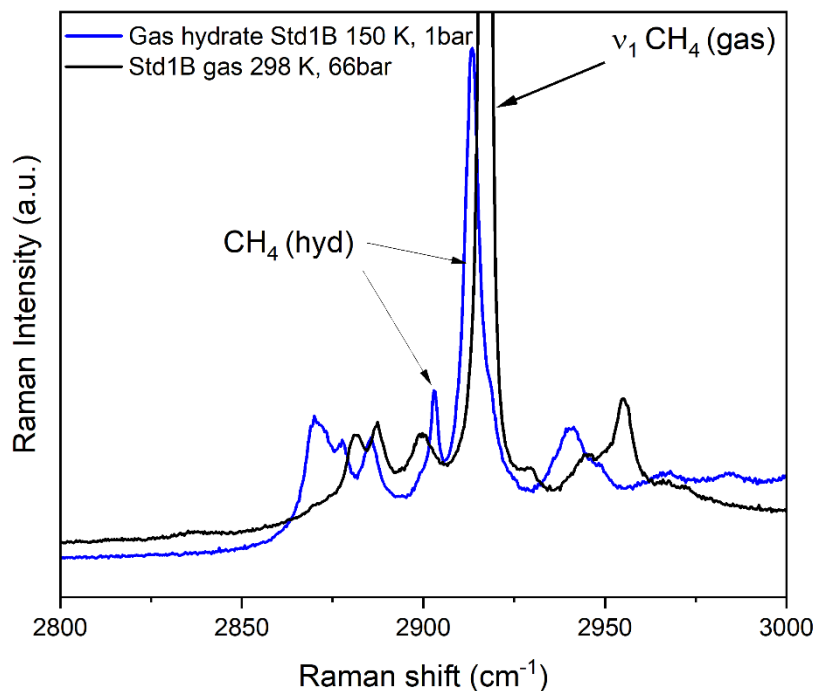


Figure 69. Raman spectra of Standard-1B gas (298 K, 66bar) and hydrate (150 K, 1bar). ($\lambda_0 = 532$ nm).

Then, the main challenge of this PhD work was to study the formation of gas hydrates in a clay-rich sedimentary environment. The variability of the chemical and structural nature of the clay, of the morphology and of the particle size provide a large range of parameters that could influence hydrate formation. Raman spectroscopy, inelastic neutron scattering and neutron diffraction have shown the strong effect of the nature of the clays on the kinetics of synthetic methane hydrate formation: Montmorillonite, providing a large specific surface area, acts as a kinetic promoter allowing methane hydrate formation in less than 15 minutes. Conversely, Illite, present in majority in the commercial matrix and in the natural matrix collected from the Black Sea, slows down the rate of methane hydrate formation on scales reaching several days. Furthermore, studies conducted on synthetic samples have shown that sediments have no impact on the structure of the hydrates formed, their distribution at the microscopic scale and no vibrational signatures of confinement have been observed. The structure of the natural samples collected in the Black Sea could not be analyzed by neutron diffraction. Indeed, due to their high hydrogen content, the diffractograms only showed a large incoherent background. X-ray diffraction experiments would allow characterization of the structure of natural hydrates and comparison with the structures of synthetic hydrates. In addition, a neutron proposal on the tomograph (NEXT) at ILL aimed at coupling X-ray and neutron tomography to probe the distribution of natural and synthetic samples within sedimentary matrices at the microscale

(unfortunately, this proposal has not been accepted due to the strong overload on NEXT before the long ILL shutdown in 2022). Moreover, in this work, a huge effort was dedicated to the investigation the hypothetical formation of methane hydrate in the nano- spaces of clays by the use of inelastic neutron scattering. With this technique, it was extremely challenging to observed any signatures of possible confinement. Other techniques could be used to probe the samples at the nanoscale. Preliminary experiments were conducted using Tip Enhanced Raman spectroscopy (TERS) on clay grains. TERS allows to probe nanometric signatures of materials through the amplification of the Raman signal by specific enhancement mechanisms that occur on a metal nanotip.³³¹ Such experiments are extremely challenging for various reasons: the sample preparation – deposition of thin clay flakes to allow TERS enhancement, the control of the sample environment – design a cell which allows temperature and gas control, and the preparation of effective AFM-tips for such samples. Nano X-ray tomography could also be used to observe the formation of methane hydrate in clays on pore scale and to quantify hydrate saturation, pore structure parameters. Nano-focused X-ray computed tomography has already been used in sands by Li *et al.*³³² (**Figure 70**).

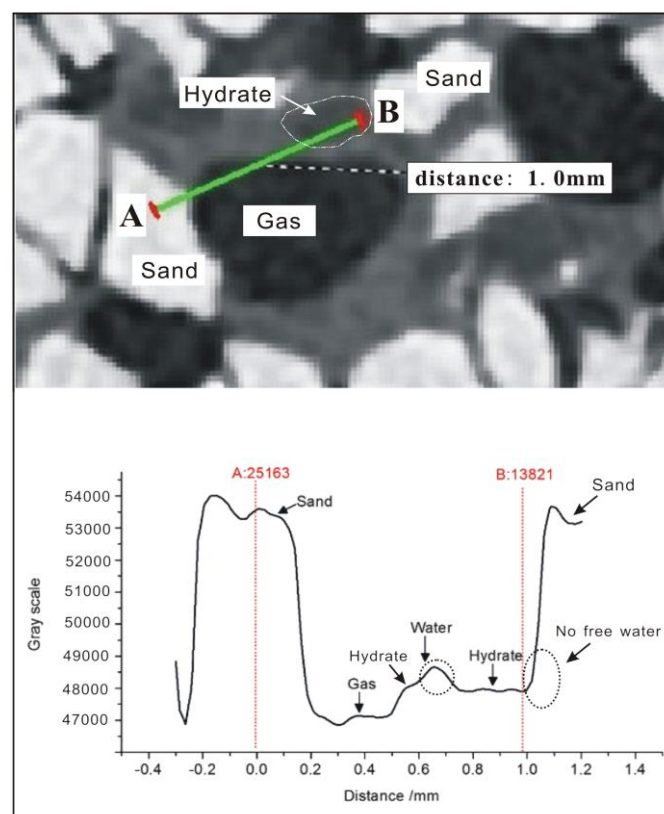


Figure 70. Gray value curve from position A to B in the X-ray computed tomography image (From Li *et al.*³³²).

On a longer perspective, all these results contribute to the improvement of geophysical models dedicated to the quantification of methane trapped in natural hydrates and thus, could improve environmental predictions in case of destabilization of these systems in deep ocean seafloors.

Appendix

APPENDIX 1

Content

- Structural models of methane hydrate structure sI, ice Ih, ice Ic, SiO₂

STRUCTURAL MODEL OF METHANE HYDRATE STRUCTURE SI

Unit cell: $a = b = c = 11.90 \pm 0.03 \text{ \AA}$; $\alpha = \beta = \gamma = 90^\circ$

Space Group: Pm $\bar{3}$ n

Table S1. Atomic fractional coordinates, site occupancy and site symmetries of methane hydrate structure sI.

Atom	Atom Type	x	y	z	Occupancy	Cristallographic site and multiplicity
O1	O	0.00000	0.30703	0.11394	0.50000	
O2	O	0.18431	0.18431	0.18431	0.33333	
O3	O	0.25000	0.00000	0.50000	0.12500	
D1	D	0.23910	0.23910	0.23910	0.16667	
D2	D	0.00000	0.42685	0.19737	0.25000	
D3	D	0.00000	0.37757	0.16421	0.25000	
D4	D	0.00000	0.32501	0.03372	0.25000	
D5	D	0.06942	0.25439	0.13827	0.50000	
D6	D	0.11220	0.22689	0.15595	0.50000	
C1	C	0.00000	0.00000	0.00000	0.04167	2a (2SC)
H1	H	0.00000	0.10643	0.08000	0.16670	24k/3
C2	C	0.25000	0.50000	0.00000	0.12500	6d (6LC)
H2	H	0.26389	0.50000	0.11830	0.25000	24k/2
H3	H	0.18594	0.50000	0.04298	0.25000	24k/2

STRUCTURAL MODEL OF ICE Ih

Unit cell: $a = b = 4.497 \pm 0.001 \text{ \AA}$; $c = 7.352 \pm 0.002 \text{ \AA}$; $\alpha = \beta = 90^\circ$; $\gamma = 120^\circ$

Space Group: $P6_3/mmc$

Table S2. Atomic fractional coordinates and site occupancy of hexagonal ice Ih.

Space group $P6_3/mmc$					
Atom	Atom Type	x	y	z	Occupancy
O1	O	0.33333	0.66667	0.15779	0.16667
D1	D	0.33333	0.66667	0.45453	0.08333
D2	D	0.46505	0.93005	0.01008	0.25000

STRUCTURAL MODEL OF ICE Ic

Unit cell: $a = b = c = 6.37 \pm 0.01 \text{ \AA}$; $\alpha = \beta = \gamma = 90^\circ$

Space Group: $Fd\bar{3}m$

Table S3. Atomic fractional coordinates and site occupancy of cubic ice Ic.

Space group $Fd\bar{3}m$					
Atom	Atom Type	x	y	z	Occupation
O1	O	0.37500	0.37500	0.37500	1.00000
D1	D	0.46700	0.46700	0.46700	0.50000

STRUCTURAL MODEL OF SiO₂

Unit cell: $a = b = 4.92 \text{ \AA}$; $c = 5.42 \text{ \AA}$; $\alpha = \beta = 90^\circ$, $\gamma = 120^\circ$

Space Group: $Fd\bar{3}m$

Table S4. Atomic fractional coordinates and site occupancy of quartz SiO₂.

Space group $Fd\bar{3}m$					
Atom	Atom Type	x	y	z	Occupation
Si	Si	0.46900	0.00000	0.66667	0.50000
O	O	0.40300	0.25300	0.78900	1.00000

APPENDIX 2

Content

- Rietveld refinement of pure CH₄ hydrate at 150K and 1bar

RIETVELD REFINEMENT OF PURE CH₄ HYDRATE AT 150K AND 1 BAR

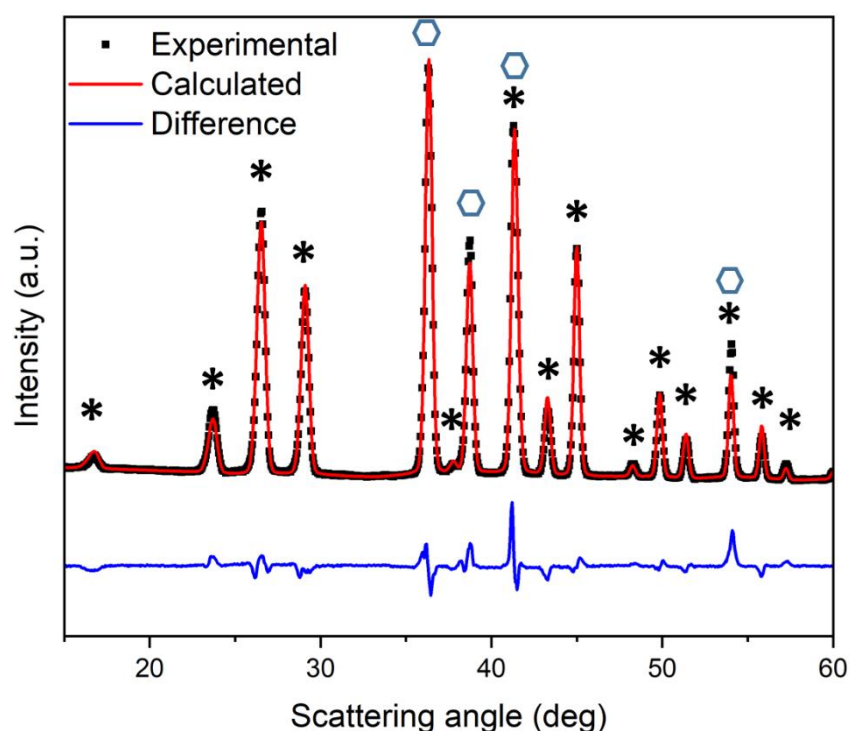


Figure S1. Rietveld refinement of pure CH₄ hydrate at 150K and 1bar ($\lambda_0 = 2.41 \text{ \AA}$). Rietveld refinements peak positions for hydrate sI ($Pm\bar{3}n$) and the hexagonal ice (Ih) ($P6_3/mmc$) are represented by black stars and blue hexagons, respectively. ($\chi^2 = 105$)

Fitted unit cell parameters:

Methane hydrate sI: $a = b = c = 11.9117 \pm 0.0003 \text{ \AA}$; $\alpha = \beta = \gamma = 90^\circ$

Ice Ih: $a = b = 4.5171 \pm 0.0001 \text{ \AA}$; $c = 7.3545 \pm 0.0003 \text{ \AA}$; $\alpha = \beta = 90^\circ$; $\gamma = 120^\circ$

APPENDIX 3

Content

- Rietveld refinement of pure CH₄ hydrate in MS at 150 K and 1 bar
- Rietveld refinement of CH₄ hydrate in MS with 2.2wt% NaCl at 150 K and 1 bar
- Rietveld refinement of pure CH₄ hydrate in MS at 258 K and 1 bar
- Rietveld refinement of CH₄ hydrate in MS with 2.2wt% NaCl at 257 K and 1 bar

RIETVELD REFINEMENT OF PURE CH₄ HYDRATE IN MS AT 150 K AND 1 BAR.

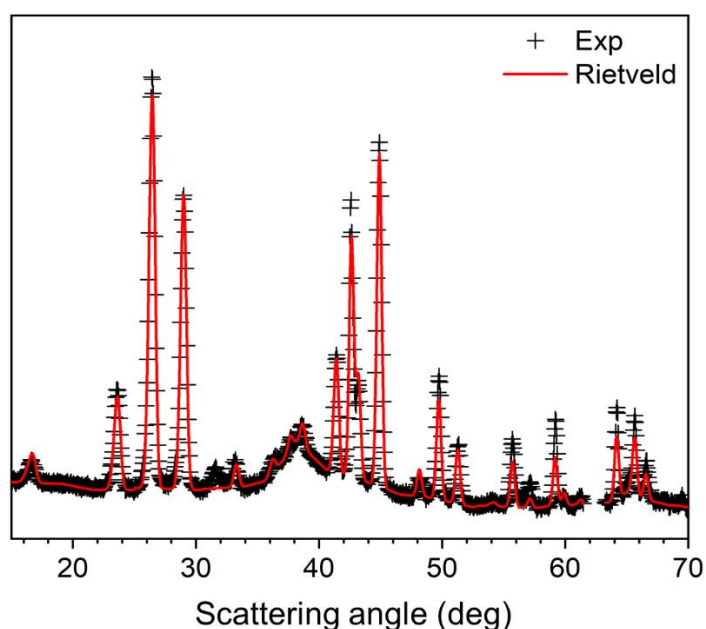


Figure S1. Rietveld refinement of pure CH₄ hydrate in MS at 150 K and 1 bar ($\lambda_0 = 2.41 \text{ \AA}$). Rietveld refinements peak positions for hydrate sI ($Pm\bar{3}n$), the matrix, the cubic ice (Ic) ($Fd\bar{3}m$) and the hexagonal ice (Ih) ($P6_3/mmc$) are represented by red, green, purple and blue colored bars respectively.

RIETVELD REFINEMENT OF CH₄ HYDRATE IN MS WITH 2.2 wt% NaCl AT 150 K AND 1 BAR.

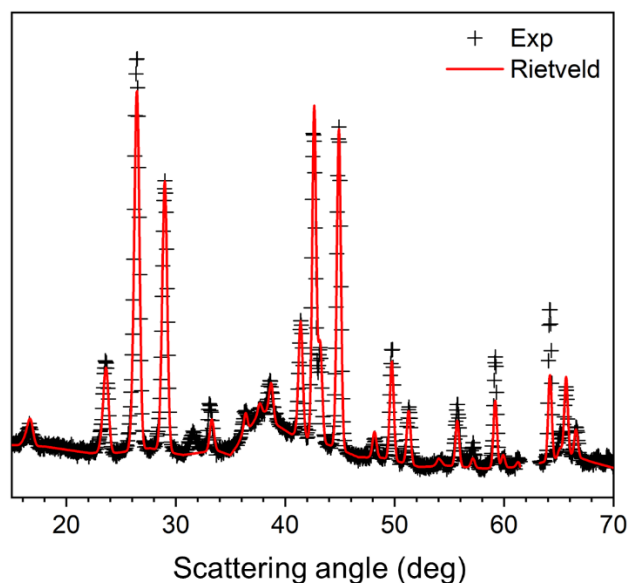


Figure S2. Rietveld refinement of CH₄ hydrate in MS with 2.2wt% NaCl at 150 K and 1 bar ($\lambda_0 = 2.41 \text{ \AA}$). Rietveld refinements peak positions for hydrate sI ($Pm\bar{3}n$), the matrix, the cubic ice (Ic) ($Fd\bar{3}m$) and the hexagonal ice (Ih) ($P6_3/mmc$) are represented by red, green, purple and blue colored bars respectively.

RIETVELD REFINEMENT OF PURE CH₄ HYDRATE IN MS AT 258 K AND 1 BAR.

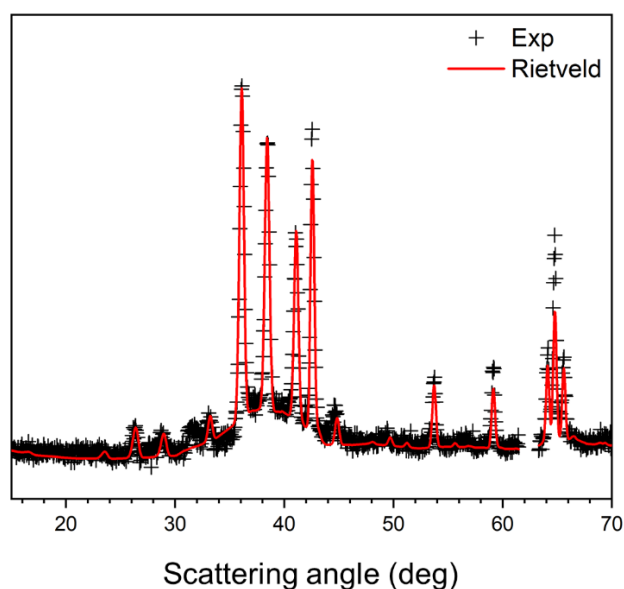


Figure S3. Rietveld refinement of pure CH₄ hydrate in MS at 258 K and 1 bar ($\lambda_0 = 2.41 \text{ \AA}$). Rietveld refinements peak positions for hydrate sI ($Pm\bar{3}n$), the matrix, the cubic ice (Ic) ($Fd\bar{3}m$)

and the hexagonal ice (Ih) ($P6_3/mmc$) are represented by red, green, purple and blue colored bars respectively.

RIETVELD REFINEMENT OF CH₄ HYDRATE IN MS WITH 2.2wt% NaCl AT 257 K AND 1 BAR.

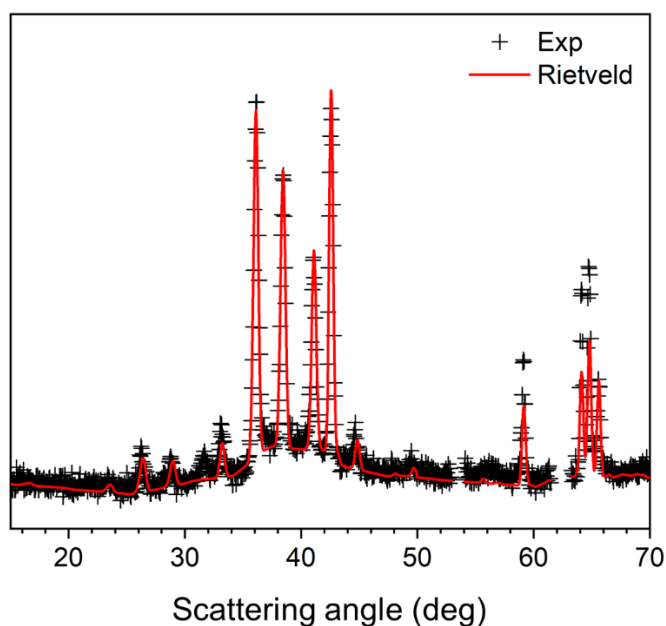


Figure S4. Rietveld refinement of CH₄ hydrate in MS with 2.2wt% NaCl at 257 K and 1 bar ($\lambda_0 = 2.41 \text{ \AA}$). Rietveld refinements peak positions for hydrate sI ($Pm\bar{3}n$), the matrix, the cubic ice (Ic) ($Fd\bar{3}m$) and the hexagonal ice (Ih) ($P6_3/mmc$) are represented by red, green, purple and blue colored bars respectively.

APPENDIX 4

Content

- Rietveld refinement of the neutron powder diffraction data of methane hydrate structure sI pressurized during 110 days with CH₄ in IS matrix at 150K and 1bar
- Rietveld refinement of the neutron powder diffraction data of methane hydrate structure sI pressurized during 110 days with CH₄ in BS matrix at 150K and 1bar

RIETVELD REFINEMENT OF THE NEUTRON POWDER DIFFRACTION DATA OF METHANE HYDRATE STRUCTURE sI PRESSURIZED DURING 110 DAYS WITH CH₄ IN IS MATRIX AT 150 K AND 1 BAR.

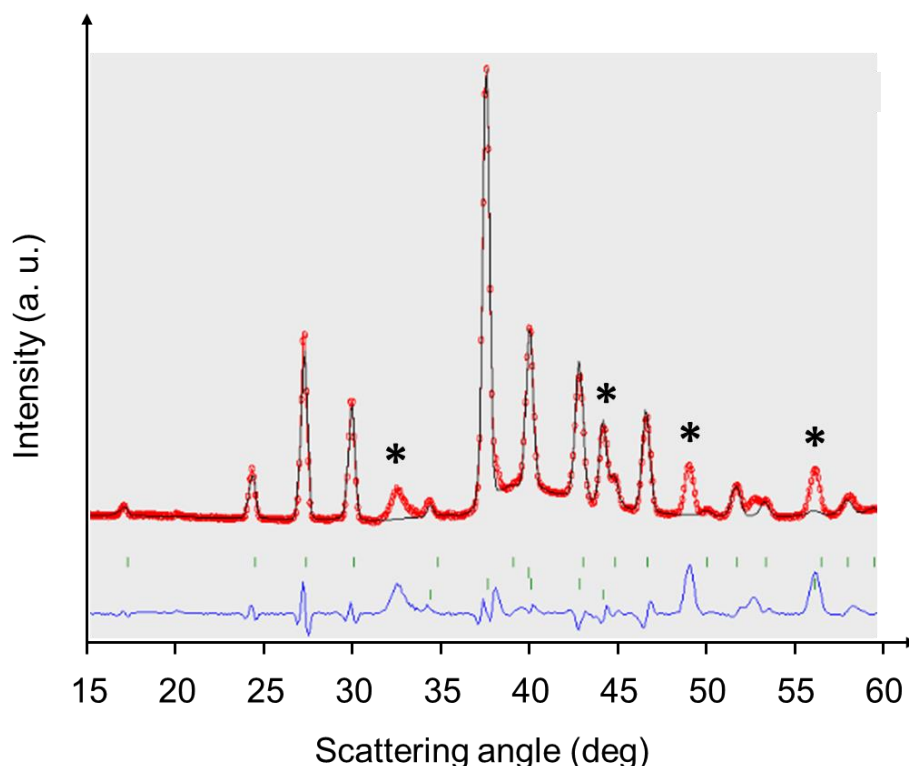


Figure S1. Rietveld refinement of the neutron powder diffraction data of methane hydrate structure sI after 110 days of CH₄ pressurization in IS matrix at 150 K and 1 bar ($\lambda_0 = 2.52 \text{ \AA}$). Tick marks indicate phase reflection related to the type I hydrate ($Pm\bar{3}n$), the cubic ice ($Fd\bar{3}m$), the hexagonal ice ($P63/mmc$) and the SiO₂ ($P3221$). Bragg peaks of the matrix are marked by black stars. The difference line (blue) is shown between the data and the fitted curve.

RIETVELD REFINEMENT OF THE NEUTRON POWDER DIFFRACTION DATA OF METHANE HYDRATE STRUCTURE sI PRESSURIZED DURING 110 DAYS WITH CH₄ IN BS MATRIX AT 150 K AND 1 BAR.

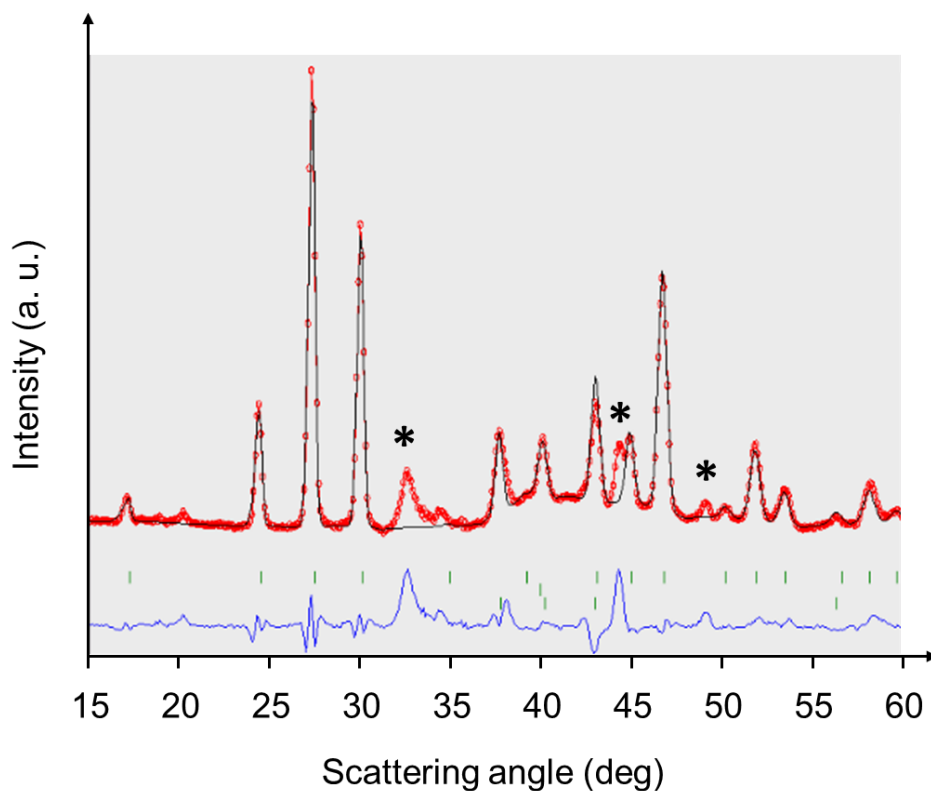


Figure S2. Rietveld refinement of the neutron powder diffraction data of methane hydrate structure sI after 110 days of CH₄ pressurization in BS matrix at 150 K and 1 bar ($\lambda_0 = 2.52 \text{ \AA}$). Tick marks indicate phase reflection related to the type I hydrate ($Pm\bar{3}n$), the cubic ice ($Fd\bar{3}m$) and the hexagonal ice ($P63/mmc$). Bragg peaks of the matrix are marked by black stars. The difference line (blue) is shown between the data and the fitted curve.

APPENDIX 5

Content

- Comparison d_{001} clay-rich matrices KS, IS, BS and MS
- Overtones Raman signatures of methane molecules
- Raman mapping parameters

COMPARISON OF d_{001} OF CLAY-RICH MATRICES KS, IS, BS AND MS.

The nature of clay mineral can be characterized in diffraction by the d spacing (basal spacing). It corresponds to the d_{001} diffraction plane, which is related to the distance between the centers of two neighboring clay layers³³³. This distance can be calculated using Bragg's Law applied to the scattering angle value of the (001) Bragg peak. The scattering angle (2θ) is determined by fitting a pseudo void function of the (001) Bragg peak.

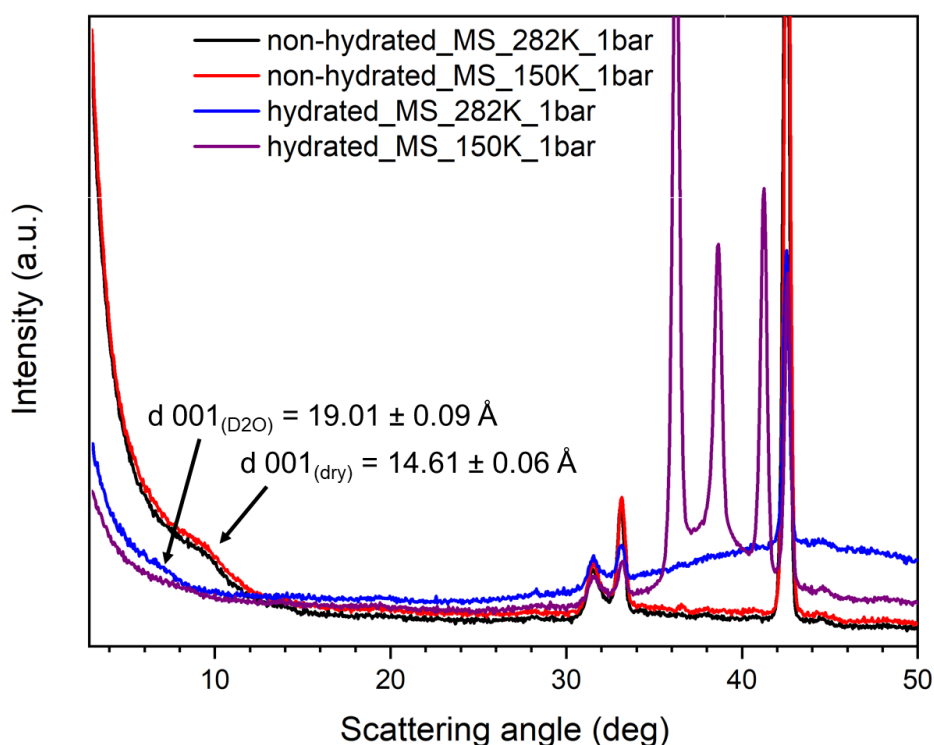


Figure S1. Diffractograms representing the evolution of the d_{001} of MS before and after adding deuterated water at 150 K and 282 K and 1bar ($\lambda_0 = 2.41 \text{ \AA}$).

	Scattering angle (001) (deg)	d_{001} (Å)
Non-hydrated MS	9.48 ± 0.06	14.61 ± 0.06
Hydrated MS	7.28 ± 0.09	19.01 ± 0.09
MS with structure sI methane hydrate	8.42 ± 0.15	16.44 ± 0.15
KS with structure sI methane hydrate	19.58 ± 0.03	7.11 ± 0.03
IS with structure sI methane hydrate	13.78 ± 0.56	9.81 ± 0.56

Table S1. Summary of the d_{001} values calculated for each matrix ($\lambda_0 = 2.41$ Å).

OVERTONES RAMAN SIGNATURES OF METHANE MOLECULES.

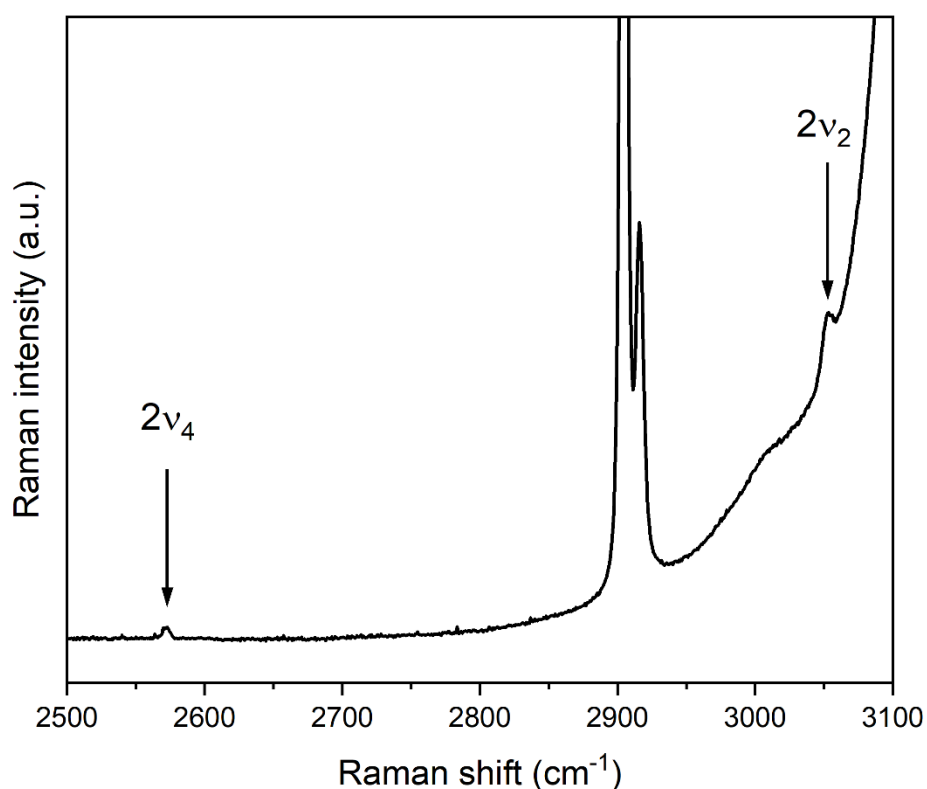


Figure S2. Raman spectrum of methane hydrate structure sI ($\lambda_0 = 405$ nm). The two weak bands at ~ 2570 cm^{-1} and ~ 3050 cm^{-1} are attributed to the overtone of C-H asymmetric bending mode ($2\nu_4$) and the first overtone of the C-H bending mode ($2\nu_2$) of methane in hydrate lattice, respectively²³³. Two Raman bands centered at ~ 2905 cm^{-1} and ~ 2916 cm^{-1} are attributed to the C-H stretching of methane trapped in the large cage (LC) and the small cage (SC), respectively⁵⁶.

RAMAN MAPPING PARAMETERS

	x (μm)	y (μm)	Step size (μm)	Total number of points	Number of points accounted for A_{LC}/A_{SC}
Pure CH₄ hydrate	40	50	5.2	99	42
KS	20	15	4	30	17
IS	40	30	5	63	20
BS	70	60	7	110	25
MS	30	26	2.6	121	66
CS05	30	40	3.2	130	130

Table S2. Parameters of the Raman maps collected on the synthetic and natural methane hydrate samples.

References

- (1) Hammerschmidt, E. G. Formation of Gas Hydrates in Natural Gas Transmission Lines. *Industrial & Engineering Chemistry* **1934**, 26 (8), 851–855.
- (2) Von Stackelberg, M. Feste Gashydrate. *Naturwissenschaften* **1949**, 36, 327–333.
- (3) Sloan Jr, E. D.; Koh, C. A. *Clathrate Hydrates of Natural Gases*; CRC press, 2007.
- (4) Boswell, R.; S. Collett, T. Current Perspectives on Gas Hydrate Resources. *Energy & Environmental Science* **2011**, 4 (4), 1206–1215. <https://doi.org/10.1039/C0EE00203H>.
- (5) Kvenvolden, K. A. A Primer on the Geological Occurrence of Gas Hydrate. *Geological Society, London, Special Publications* **1998**, 137 (1), 9–30. <https://doi.org/10.1144/GSL.SP.1998.137.01.02>.
- (6) Wallmann, K.; Pinero, E.; Burwicz, E.; Haeckel, M.; Hensen, C.; Dale, A.; Ruepke, L. The Global Inventory of Methane Hydrate in Marine Sediments: A Theoretical Approach. *Energies* **2012**, 5 (7), 2449–2498.
- (7) Ruppel, C. D.; Waite, W. F. Timescales and Processes of Methane Hydrate Formation and Breakdown, with Application to Geologic Systems. *Journal of Geophysical Research: Solid Earth* **2020**, 125 (8), e2018JB016459.
- (8) Ruffine, L.; Broseta, D.; Desmedt, A. *Gas Hydrates 2: Geoscience Issues and Potential Industrial Applications*; John Wiley & Sons, 2018.
- (9) Ruppel, C. D.; Kessler, J. D. The Interaction of Climate Change and Methane Hydrates. *Reviews of Geophysics* **2017**, 55 (1), 126–168.
- (10) Riboulot, V.; Ker, S.; Sultan, N.; Thomas, Y.; Marsset, B.; Scalabrin, C.; Ruffine, L.; Boulart, C.; Ion, G. Freshwater Lake to Salt-Water Sea Causing Widespread Hydrate Dissociation in the Black Sea. *Nature communications* **2018**, 9 (1), 1–8.
- (11) Kennett, J. P.; Cannariato, K. G.; Hendy, I. L.; Behl, R. J. Methane Hydrates in Quaternary Climate Change: The Clathrate Gun Hypothesis, Volume 54. In *Special Publications Series, American Geophysical Union, Washington, DC*; Wiley Online Library, 2003.
- (12) Maslin, M.; Owen, M.; Betts, R.; Day, S.; Dunkley Jones, T.; Ridgwell, A. Gas Hydrates: Past and Future Geohazard? *Philosophical Transactions of the Royal Society A: Mathematical, Physical and Engineering Sciences* **2010**, 368 (1919), 2369–2393.
- (13) Ker, S.; Thomas, Y.; Riboulot, V.; Sultan, N.; Bernard, C.; Scalabrin, C.; Ion, G.; Marsset, B. Anomalously Deep BSR Related to a Transient State of the Gas Hydrate System in the Western Black Sea. *Geochemistry, Geophysics, Geosystems* **2019**, 20 (1), 442–459.

- (14) Helgerud, M. B.; Dvorkin, J.; Nur, A.; Sakai, A.; Collett, T. Elastic-wave Velocity in Marine Sediments with Gas Hydrates: Effective Medium Modeling. *Geophysical Research Letters* **1999**, *26* (13), 2021–2024.
- (15) Milkov, A. V. Global Estimates of Hydrate-Bound Gas in Marine Sediments: How Much Is Really out There? *Earth-science reviews* **2004**, *66* (3–4), 183–197.
- (16) Merey, S.; Sinayuc, C. Investigation of Gas Hydrate Potential of the Black Sea and Modelling of Gas Production from a Hypothetical Class 1 Methane Hydrate Reservoir in the Black Sea Conditions. *Journal of Natural Gas Science and Engineering* **2016**, *29*, 66–79.
- (17) Yeon, S.-H.; Seol, J.; Koh, D.-Y.; Seo, Y.; Park, K.-P.; Huh, D.-G.; Lee, J.; Lee, H. Abnormal Methane Occupancy of Natural Gas Hydrates in Deep Sea Floor Sediments. *Energy & Environmental Science* **2011**, *4* (2), 421–424.
- (18) Seol, J.; Koh, D.-Y.; Cha, M.; Shin, W.; Lee, Y.-J.; Kim, J.-H.; Lee, J.; Lee, H. Experimental Verification of Anomalous Chloride Enrichment Related to Methane Hydrate Formation in Deep-Sea Sediments. *AIChE Journal* **2012**, *58* (1), 322–328. <https://doi.org/10.1002/aic.12555>.
- (19) Wang, Z.; Duan, J.; Chen, S.; Fu, Y.; Li, X.; Wang, D.; Zhang, M.; Zhang, Z.; Liu, D.; Wang, F. A Review on High-Density Methane Storage in Confined Nanospace by Adsorption-Hydration Hybrid Technology. *Journal of Energy Storage* **2022**, *50*, 104195. <https://doi.org/10.1016/j.est.2022.104195>.
- (20) Dickens, G. R.; O’Neil, J. R.; Rea, D. K.; Owen, R. M. Dissociation of Oceanic Methane Hydrate as a Cause of the Carbon Isotope Excursion at the End of the Paleocene. *Paleoceanography* **1995**, *10* (6), 965–971.
- (21) RIBOULOT Vincent; Stéphanie, D.; Stéphan, K.; Nabil, S. GHASS2 Cruise, Pourquoi Pas ? R/V. **2021**. <https://doi.org/10.17600/18001358>.
- (22) Milkov, A. V.; Etiope, G. Revised Genetic Diagrams for Natural Gases Based on a Global Dataset Of > 20,000 Samples. *Organic Geochemistry* **2018**, *125*, 109–120.
- (23) Whiticar, M. J. Correlation of Natural Gases with Their Sources: Chapter 16: Part IV. Identification and Characterization. **1994**.
- (24) Whiticar, M. J. Stable Isotope Geochemistry of Coals, Humic Kerogens and Related Natural Gases. *International Journal of Coal Geology* **1996**, *32* (1–4), 191–215.
- (25) Whiticar, M. J.; Faber, E.; Schoell, M. Biogenic Methane Formation in Marine and Freshwater Environments: CO₂ Reduction vs. Acetate Fermentation—Isotope Evidence. *Geochimica et Cosmochimica Acta* **1986**, *50* (5), 693–709.

- (26) Bourry, C.; Chazallon, B.; Charlou, J. L.; Donval, J. P.; Ruffine, L.; Henry, P.; Geli, L.; Çagatay, M. N.; İnan, S.; Moreau, M. Free Gas and Gas Hydrates from the Sea of Marmara, Turkey: Chemical and Structural Characterization. *Chemical Geology* **2009**, *264* (1–4), 197–206.
- (27) Hester, K. C.; Dunk, R. M.; White, S. N.; Brewer, P. G.; Peltzer, E. T.; Sloan, E. D. Gas Hydrate Measurements at Hydrate Ridge Using Raman Spectroscopy. *Geochimica et Cosmochimica Acta* **2007**, *71* (12), 2947–2959. <https://doi.org/10.1016/j.gca.2007.03.032>.
- (28) Chazallon, B.; Focsa, C.; Charlou, J.-L.; Bourry, C.; Donval, J.-P. A Comparative Raman Spectroscopic Study of Natural Gas Hydrates Collected at Different Geological Sites. *Chemical geology* **2007**, *244* (1–2), 175–185.
- (29) Yan, K.; Li, X.; Xu, C.; Lv, Q.; Ruan, X. Molecular Dynamics Simulation of the Intercalation Behaviors of Methane Hydrate in Montmorillonite. *Journal of molecular modeling* **2014**, *20* (6), 1–11.
- (30) Cygan, R. T.; Guggenheim, S.; Koster van Groos, A. F. Molecular Models for the Intercalation of Methane Hydrate Complexes in Montmorillonite Clay. *The Journal of Physical Chemistry B* **2004**, *108* (39), 15141–15149.
- (31) Martos-Villa, R.; Guggenheim, S.; Mata, M. P.; Sainz-Díaz, C. I.; Nieto, F. Interaction of Methane Hydrate Complexes with Smectites: Experimental Results Compared to Molecular Models. *American Mineralogist* **2014**, *99* (2–3), 401–414.
- (32) Park, S.-H.; Sposito, G. Do Montmorillonite Surfaces Promote Methane Hydrate Formation? Monte Carlo and Molecular Dynamics Simulations. *The Journal of Physical Chemistry B* **2003**, *107* (10), 2281–2290.
- (33) Van Groos, A. K.; Guggenheim, S. The Stability of Methane Hydrate Intercalates of Montmorillonite and Nontronite: Implications for Carbon Storage in Ocean-Floor Environments. *American Mineralogist* **2009**, *94* (2–3), 372–379.
- (34) Guggenheim, S.; van Groos, A. F. K. New Gas-Hydrate Phase: Synthesis and Stability of Clay–Methane Hydrate Intercalate. *Geology* **2003**, *31* (7), 653–656. [https://doi.org/10.1130/0091-7613\(2003\)031<0653:NGPSAS>2.0.CO;2](https://doi.org/10.1130/0091-7613(2003)031<0653:NGPSAS>2.0.CO;2).
- (35) Kim, D.; Ahn, Y.-H.; Kim, S.-J.; Lee, J. Y.; Lee, J.; Seo, Y.; Lee, H. Gas Hydrate in Crystalline-Swelled Clay: The Effect of Pore Dimension on Hydrate Formation and Phase Equilibria. *The Journal of Physical Chemistry C* **2015**, *119* (38), 22148–22153.
- (36) Broseta, D.; Ruffine, L.; Desmedt, A. *Gas Hydrates 1: Fundamentals, Characterization and Modeling*; John Wiley & Sons, 2017.

- (37) Hashimoto, S.; Murayama, S.; Sugahara, T.; Sato, H.; Ohgaki, K. Thermodynamic and Raman Spectroscopic Studies on H₂+ Tetrahydrofuran+ Water and H₂+ Tetra-n-Butyl Ammonium Bromide+ Water Mixtures Containing Gas Hydrates. *Chemical Engineering Science* **2006**, *61* (24), 7884–7888.
- (38) Goel, N. In Situ Methane Hydrate Dissociation with Carbon Dioxide Sequestration: Current Knowledge and Issues. *Journal of Petroleum Science and Engineering* **2006**, *51* (3), 169–184. <https://doi.org/10.1016/j.petrol.2006.01.005>.
- (39) Lu, H.; Seo, Y.; Lee, J.; Moudrakovski, I.; Ripmeester, J. A.; Chapman, N. R.; Coffin, R. B.; Gardner, G.; Pohlman, J. Complex Gas Hydrate from the Cascadia Margin. *Nature* **2007**, *445* (7125), 303–306.
- (40) Ripmeester, J. A.; Tse, J. S.; Ratcliffe, C. I.; Powell, B. M. A New Clathrate Hydrate Structure. *Nature* **1987**, *325* (6100), 135–136.
- (41) Strobel, T. A.; Hester, K. C.; Koh, C. A.; Sum, A. K.; Sloan Jr, E. D. Properties of the Clathrates of Hydrogen and Developments in Their Applicability for Hydrogen Storage. *Chemical physics letters* **2009**, *478* (4–6), 97–109.
- (42) Chazallon, B.; Noble, J. A.; Desmedt, A. Spectroscopy of Gas Hydrates: From Fundamental Aspects to Chemical Engineering, Geophysical and Astrophysical Applications. In *Gas Hydrates 1*; John Wiley & Sons, Ltd, 2017; pp 63–112. <https://doi.org/10.1002/9781119332688.ch2>.
- (43) *The Fascination of Crystals and Symmetry*. <https://crystalsymmetry.wordpress.com/2018/04/01/ice-ih/>.
- (44) Schicks, J. M.; Erzinger, J.; Ziemann, M. A. Raman Spectra of Gas Hydrates—Differences and Analogies to Ice 1h and (Gas Saturated) Water. *Spectrochimica Acta Part A: Molecular and Biomolecular Spectroscopy* **2005**, *61* (10), 2399–2403. <https://doi.org/10.1016/j.saa.2005.02.019>.
- (45) Klobes, B.; Desmedt, A.; Sergueev, I.; Schmalzl, K.; Hermann, R. ¹²⁹Xe Nuclear Resonance Scattering on Solid Xe and ¹²⁹Xe Clathrate Hydrate. *EPL (Europhysics Letters)* **2013**, *103* (3), 36001.
- (46) Plummer, P. L. M.; Chen, T. S. A Molecular Dynamics Study of Water Clathrates. *J. Phys. Chem.* **1983**, *87* (21), 4190–4197. <https://doi.org/10.1021/j100244a043>.
- (47) Moore Plummer, P.; Chen, T. Investigation of Structure and Stability of Small Clusters: Molecular Dynamics Studies of Water Pentamers. *The Journal of chemical physics* **1987**, *86* (12), 7149–7155.
- (48) Pauling, L. Hydrogen Bonding. *London* **1959**, 1–6.

- (49) Geiger, A.; Stillinger, F. H.; Rahman, A. Aspects of the Percolation Process for Hydrogen-bond Networks in Water. *J. Chem. Phys.* **1979**, *70* (9), 4185–4193. <https://doi.org/10.1063/1.438042>.
- (50) Sasaki, S.; Hori, S.; Kume, T.; Shimizu, H. Microscopic Observation and in Situ Raman Scattering Studies on High-Pressure Phase Transformations of a Synthetic Nitrogen Hydrate. *The Journal of chemical physics* **2003**, *118* (17), 7892–7897.
- (51) Shimizu, H. High-Pressure Raman and Brillouin Studies of Single Crystalline Gas Hydrates. *Canadian journal of physics* **2003**, *81* (1–2), 127–133.
- (52) Sugahara, K.; Sugahara, T.; Ohgaki, K. Thermodynamic and Raman Spectroscopic Studies of Xe and Kr Hydrates. *Journal of Chemical & Engineering Data* **2005**, *50* (1), 274–277.
- (53) Ratcliffe, C. I.; Irish, D. E. Vibrational Spectral Studies of Solutions at Elevated Temperatures and Pressures. 5. Raman Studies of Liquid Water up to 300.Degree.C. *J. Phys. Chem.* **1982**, *86* (25), 4897–4905. <https://doi.org/10.1021/j100222a013>.
- (54) Walrafen, G. E. Raman Spectral Studies of the Effects of Electrolytes on Water. *J. Chem. Phys.* **1962**, *36* (4), 1035–1042. <https://doi.org/10.1063/1.1732628>.
- (55) Hare, D. E.; Sorensen, C. M. Interoscillator Coupling Effects on the OH Stretching Band of Liquid Water. *J. Chem. Phys.* **1992**, *96* (1), 13–22. <https://doi.org/10.1063/1.462852>.
- (56) Sum, A. K.; Burruss, R. C.; Sloan, E. D. Measurement of Clathrate Hydrates via Raman Spectroscopy. *The Journal of Physical Chemistry B* **1997**, *101* (38), 7371–7377.
- (57) Kaye, G.; Laby, T. In *Tables of Physical and Chemical Constants*; 1986; p 219.
- (58) Uchida, T.; Hirano, T.; Ebinuma, T.; Narita, H.; Gohara, K.; Mae, S.; Matsumoto, R. Raman Spectroscopic Determination of Hydration Number of Methane Hydrates. *AIChE journal* **1999**, *45* (12), 2641–2645.
- (59) Dartois, E.; Schmitt, B. Carbon Dioxide Clathrate Hydrate FTIR Spectrum-Near Infrared Combination Modes for Astrophysical Remote Detection. *Astronomy & Astrophysics* **2009**, *504* (3), 869–873.
- (60) Yin, Z.; Khurana, M.; Tan, H. K.; Linga, P. A Review of Gas Hydrate Growth Kinetic Models. *Chemical Engineering Journal* **2018**, *342*, 9–29.
- (61) Bishnoi, P. R.; Natarajan, V. Formation and Decomposition of Gas Hydrates. *Fluid phase equilibria* **1996**, *117* (1–2), 168–177.
- (62) Ke, W.; Svartaas, T. M.; Chen, D. A Review of Gas Hydrate Nucleation Theories and Growth Models. *Journal of Natural Gas Science and Engineering* **2019**, *61*, 169–196.

- (63) Englezos, P.; Kalogerakis, N.; Dholabhai, P. D.; Bishnoi, P. R. Kinetics of Formation of Methane and Ethane Gas Hydrates. *Chemical Engineering Science* **1987**, *42* (11), 2647–2658. [https://doi.org/10.1016/0009-2509\(87\)87015-X](https://doi.org/10.1016/0009-2509(87)87015-X).
- (64) Englezos, P.; Kalogerakis, N.; Dholabhai, P.; Bishnoi, P. Kinetics of Gas Hydrate Formation from Mixtures of Methane and Ethane. *Chemical engineering science* **1987**, *42* (11), 2659–2666.
- (65) Khurana, M.; Yin, Z.; Linga, P. A Review of Clathrate Hydrate Nucleation. *ACS Sustainable Chemistry & Engineering* **2017**, *5* (12), 11176–11203.
- (66) Mullin, J. W. *Crystallization*; Elsevier, 2001.
- (67) Koh, C. A.; Sloan, E. D.; Sum, A. K.; Wu, D. T. Fundamentals and Applications of Gas Hydrates. *Annu. Rev. Chem. Biomol. Eng* **2011**, *2* (1), 237–257.
- (68) Buchanan, P.; Soper, A. K.; Thompson, H.; Westacott, R. E.; Creek, J. L.; Hobson, G.; Koh, C. A. Search for Memory Effects in Methane Hydrate: Structure of Water before Hydrate Formation and after Hydrate Decomposition. *The Journal of chemical physics* **2005**, *123* (16), 164507.
- (69) Lee, J. D.; Susilo, R.; Englezos, P. Methane–Ethane and Methane–Propane Hydrate Formation and Decomposition on Water Droplets. *Chemical Engineering Science* **2005**, *60* (15), 4203–4212.
- (70) Kashchiev, D.; Firoozabadi, A. Nucleation of Gas Hydrates. *Journal of crystal growth* **2002**, *243* (3–4), 476–489.
- (71) Long, J.; Sloan, E. Hydrates in the Ocean and Evidence for the Location of Hydrate Formation. *International journal of thermophysics* **1996**, *17* (1), 1–13.
- (72) Moon, C.; Taylor, P. C.; Rodger, P. M. Molecular Dynamics Study of Gas Hydrate Formation. *Journal of the American Chemical Society* **2003**, *125* (16), 4706–4707.
- (73) Radhakrishnan, R.; Trout, B. L. A New Approach for Studying Nucleation Phenomena Using Molecular Simulations: Application to CO₂ Hydrate Clathrates. *The Journal of chemical physics* **2002**, *117* (4), 1786–1796.
- (74) Long, J. Gas Hydrate Formation Mechanism and Its Kinetic Inhibition. *Colorado School of Mines* **1994**.
- (75) Kvamme, B. A New Theory for the Kinetics of Hydrate Formation; 1996; pp 139–146.
- (76) Jacobson, L. C.; Hujo, W.; Molinero, V. Amorphous Precursors in the Nucleation of Clathrate Hydrates. *Journal of the American Chemical Society* **2010**, *132* (33), 11806–11811.

- (77) Henning, R. W.; Schultz, A. J.; Thieu, V.; Halpern, Y. Neutron Diffraction Studies of CO₂ Clathrate Hydrate: Formation from Deuterated Ice. *The journal of physical chemistry A* **2000**, *104* (21), 5066–5071.
- (78) Wang, X.; Schultz, A. J.; Halpern, Y. Kinetics of Methane Hydrate Formation from Polycrystalline Deuterated Ice. *The Journal of Physical Chemistry A* **2002**, *106* (32), 7304–7309.
- (79) Staykova, D. K.; Kuhs, W. F.; Salamatin, A. N.; Hansen, T. Formation of Porous Gas Hydrates from Ice Powders: Diffraction Experiments and Multistage Model. *The Journal of Physical Chemistry B* **2003**, *107* (37), 10299–10311.
- (80) Kuhs, W. F.; Staykova, D. K.; Salamatin, A. N. Formation of Methane Hydrate from Polydisperse Ice Powders. *The Journal of Physical Chemistry B* **2006**, *110* (26), 13283–13295.
- (81) Falenty, A.; Salamatin, A.; Kuhs, W. Kinetics of CO₂-Hydrate Formation from Ice Powders: Data Summary and Modeling Extended to Low Temperatures. *The Journal of Physical Chemistry C* **2013**, *117* (16), 8443–8457.
- (82) Falenty, A.; Hansen, T. C.; Kuhs, W. F. Formation and Properties of Ice XVI Obtained by Emptying a Type SII Clathrate Hydrate. *Nature* **2014**, *516* (7530), 231–233.
- (83) Moudrakovski, I. L.; Sanchez, A. A.; Ratcliffe, C. I.; Ripmeester, J. A. Nucleation and Growth of Hydrates on Ice Surfaces: New Insights from ¹²⁹Xe NMR Experiments with Hyperpolarized Xenon. *The journal of physical chemistry B* **2001**, *105* (49), 12338–12347.
- (84) Sloan Jr, E.; Fleyfel, F. A Molecular Mechanism for Gas Hydrate Nucleation from Ice. *AIChE Journal* **1991**, *37* (9), 1281–1292.
- (85) Fletcher, N. H. Surface Structure of Water and Ice. *Philosophical Magazine* **1962**, *7* (74), 255–269.
- (86) Adamson, A. W.; Dormant, L. M.; Orem, M. Physical Adsorption of Vapors on Ice I. Nitrogen. *Journal of Colloid and Interface Science* **1967**, *25* (2), 206–217.
- (87) Orem, M. W.; Adamson, A. W. Physical Adsorption of Vapor on Ice: II. n-Alkanes. *Journal of Colloid and Interface Science* **1969**, *31* (2), 278–286.
- (88) Avrami, M. Kinetics of Phase Change. I General Theory. *The Journal of chemical physics* **1939**, *7* (12), 1103–1112.
- (89) Avrami, M. Kinetics of Phase Change. II Transformation-time Relations for Random Distribution of Nuclei. *The Journal of chemical physics* **1940**, *8* (2), 212–224.

- (90) Susilo, R.; Ripmeester, J. A.; Englezos, P. Methane Conversion Rate into Structure H Hydrate Crystals from Ice. *AIChE Journal* **2007**, *53* (9), 2451–2460.
- (91) Davidson, D. The Motion of Guest Molecules in Clathrate Hydrates. *Canadian Journal of Chemistry* **1971**, *49* (8), 1224–1242.
- (92) Davidson, D. W.; Garg, S. K.; Ratcliffe, C. I.; Tse, J. S.; Gough, S. R. Characterization of a Clathrate Hydrate of Nitrogen Trifluoride. *Can. J. Chem.* **1984**, *62* (7), 1229–1235. <https://doi.org/10.1139/v84-204>.
- (93) Davidson, D.; Handa, Y.; Ratcliffe, C.; Ripmeester, J.; Tse, J.; Dahn, J.; Lee, F.; Calvert, L. Crystallographic Studies of Clathrate Hydrates. Part I. *Molecular Crystals and Liquid Crystals* **1986**, *141* (1–2), 141–149.
- (94) Metais, C. Impact Des Analogues Sédimentaires et de La Stoechiométrie Sur La Métastabilité Structurale, La Cinétique de Formation et La Sélectivité Moléculaire Des Hydrates de Gaz : Une Étude Physico-Chimique Combinant Diffraction Neutronique, Spectroscopie Raman et Calculs Quantiques. These en préparation, Bourgogne Franche-Comté, 2018.
- (95) Kumar, R.; Linga, P.; Moudrakovski, I.; Ripmeester, J. A.; Englezos, P. Structure and Kinetics of Gas Hydrates from Methane/Ethane/Propane Mixtures Relevant to the Design of Natural Gas Hydrate Storage and Transport Facilities. *AIChE Journal* **2008**, *54* (8), 2132–2144. <https://doi.org/10.1002/aic.11527>.
- (96) Uchida, T.; Takeya, S.; Kamata, Y.; Ohmura, R.; Narita, H. Spectroscopic Measurements on Binary, Ternary, and Quaternary Mixed-Gas Molecules in Clathrate Structures. *Ind. Eng. Chem. Res.* **2007**, *46* (14), 5080–5087. <https://doi.org/10.1021/ie070153w>.
- (97) Kvenvolden, K. A.; Lorenson, T. D. The Global Occurrence of Natural Gas Hydrate. *Washington DC American Geophysical Union Geophysical Monograph Series* **2001**, *124*, 3–18. <https://doi.org/10.1029/GM124p0003>.
- (98) Waite, W. F.; Santamarina, J. C.; Cortes, D. D.; Dugan, B.; Espinoza, D. N.; Germaine, J.; Jang, J.; Jung, J. W.; Kneafsey, T. J.; Shin, H. Physical Properties of Hydrate-Bearing Sediments. *Reviews of geophysics* **2009**, *47* (4).
- (99) *Map of Gas Hydrates / U.S. Geological Survey.* <https://www.usgs.gov/media/images/map-gas-hydrates> (accessed 2022-07-11).
- (100) Yang, L.; Liu, Y.; Zhang, H.; Xiao, B.; Guo, X.; Wei, R.; Xu, L.; Sun, L.; Yu, B.; Leng, S. The Status of Exploitation Techniques of Natural Gas Hydrate. *Chinese Journal of Chemical Engineering* **2019**, *27* (9), 2133–2147.

- (101) Kirschke, S.; Bousquet, P.; Ciais, P.; Saunoy, M.; Canadell, J. G.; Dlugokencky, E. J.; Bergamaschi, P.; Bergmann, D.; Blake, D. R.; Bruhwiler, L.; Cameron-Smith, P.; Castaldi, S.; Chevallier, F.; Feng, L.; Fraser, A.; Heimann, M.; Hodson, E. L.; Houweling, S.; Josse, B.; Fraser, P. J.; Krummel, P. B.; Lamarque, J.-F.; Langenfelds, R. L.; Le Quéré, C.; Naik, V.; O'Doherty, S.; Palmer, P. I.; Pison, I.; Plummer, D.; Poulter, B.; Prinn, R. G.; Rigby, M.; Ringeval, B.; Santini, M.; Schmidt, M.; Shindell, D. T.; Simpson, I. J.; Spahni, R.; Steele, L. P.; Strode, S. A.; Sudo, K.; Szopa, S.; van der Werf, G. R.; Voulgarakis, A.; van Weele, M.; Weiss, R. F.; Williams, J. E.; Zeng, G. Three Decades of Global Methane Sources and Sinks. *Nature Geosci* **2013**, *6* (10), 813–823. <https://doi.org/10.1038/ngeo1955>.
- (102) Seol, J.; Lee, H. Natural Gas Hydrate as a Potential Energy Resource: From Occurrence to Production. *Korean J. Chem. Eng.* **2013**, *30* (4), 771–786. <https://doi.org/10.1007/s11814-013-0033-8>.
- (103) Sloan, E. D. Gas Hydrates: Review of Physical/Chemical Properties. *Energy & fuels* **1998**, *12* (2), 191–196.
- (104) Piñero, E.; Marquardt, M.; Hensen, C.; Haeckel, M.; Wallmann, K. Estimation of the Global Inventory of Methane Hydrates in Marine Sediments Using Transfer Functions. *Biogeosciences* **2013**, *10* (2), 959–975. <https://doi.org/10.5194/bg-10-959-2013>.
- (105) Stocker, T. *Climate Change 2013: The Physical Science Basis: Working Group I Contribution to the Fifth Assessment Report of the Intergovernmental Panel on Climate Change*; Cambridge university press, 2014.
- (106) Veluswamy, H. P.; Bhattacharjee, G.; Liao, J.; Linga, P. Macroscopic Kinetic Investigations on Mixed Natural Gas Hydrate Formation for Gas Storage Application. *Energy Fuels* **2020**, *34* (12), 15257–15269. <https://doi.org/10.1021/acs.energyfuels.0c01862>.
- (107) Linga, P.; Kumar, R.; Englezos, P. Gas Hydrate Formation from Hydrogen/Carbon Dioxide and Nitrogen/Carbon Dioxide Gas Mixtures. *Chemical engineering science* **2007**, *62* (16), 4268–4276.
- (108) Lee, H.-H.; Ahn, S.-H.; Nam, B.-U.; Kim, B.-S.; Lee, G.-W.; Moon, D.; Shin, H. J.; Han, K. W.; Yoon, J.-H. Thermodynamic Stability, Spectroscopic Identification, and Gas Storage Capacity of CO₂–CH₄–N₂ Mixture Gas Hydrates: Implications for Landfill Gas Hydrates. *Environmental science & technology* **2012**, *46* (7), 4184–4190.
- (109) Hovland, M.; Gardner, J. V.; Judd, A. G. The Significance of Pockmarks to Understanding Fluid Flow Processes and Geohazards. *Geofluids* **2002**, *2* (2), 127–136.

- (110) James, R. H.; Bousquet, P.; Bussmann, I.; Haeckel, M.; Kipfer, R.; Leifer, I.; Niemann, H.; Ostrovsky, I.; Piskozub, J.; Rehder, G. Effects of Climate Change on Methane Emissions from Seafloor Sediments in the Arctic Ocean: A Review. *Limnology and oceanography* **2016**, *61* (S1), S283–S299.
- (111) Schmale, O.; Greinert, J.; Rehder, G. Methane Emission from High-intensity Marine Gas Seeps in the Black Sea into the Atmosphere. *Geophysical Research Letters* **2005**, *32* (7).
- (112) McGinnis, D. F.; Greinert, J.; Artemov, Y.; Beaubien, S. E.; Wüest, A. Fate of Rising Methane Bubbles in Stratified Waters: How Much Methane Reaches the Atmosphere? *Journal of Geophysical Research: Oceans* **2006**, *111* (C9).
- (113) Collett, T. S.; Johnson, A.; Knapp, C. C.; Boswell, R. *Natural Gas Hydrates: Energy Resource Potential and Associated Geologic Hazards*, AAPG Memoir 89; AAPG, 2010; Vol. 89.
- (114) Riboulot, V.; Cattaneo, A.; Scalabrin, C.; Gaillot, A.; Jouet, G.; Ballas, G.; Marsset, T.; Garziglia, S.; Ker, S. Control of the Geomorphology and Gas Hydrate Extent on Widespread Gas Emissions Offshore Romania. *BSGF-Earth Sciences Bulletin* **2017**, *188* (4), 26.
- (115) Greinert, J.; Artemov, Y.; Egorov, V.; De Batist, M.; McGinnis, D. 1300-m-High Rising Bubbles from Mud Volcanoes at 2080 m in the Black Sea: Hydroacoustic Characteristics and Temporal Variability. *Earth and Planetary Science Letters* **2006**, *244* (1–2), 1–15.
- (116) Naudts, L.; Greinert, J.; Artemov, Y.; Staelens, P.; Poort, J.; Van Rensbergen, P.; De Batist, M. Geological and Morphological Setting of 2778 Methane Seeps in the Dnepr Paleo-Delta, Northwestern Black Sea. *Marine Geology* **2006**, *227* (3–4), 177–199.
- (117) Schmale, O.; Beaubien, S. E.; Rehder, G.; Greinert, J.; Lombardi, S. Gas Seepage in the Dnepr Paleo-Delta Area (NW-Black Sea) and Its Regional Impact on the Water Column Methane Cycle. *Journal of marine systems* **2010**, *80* (1–2), 90–100.
- (118) Robinson, A. G. *Regional and Petroleum Geology of the Black Sea and Surrounding Region: AAPG Memoir 68*; AAPG, 1997.
- (119) Baykara, S. Z.; Figen, E. H.; Kale, A.; Veziroglu, T. N. Hydrogen from Hydrogen Sulphide in Black Sea. *International journal of hydrogen energy* **2007**, *32* (9), 1246–1250.
- (120) Martinez-Lamas, R.; Toucanne, S.; Debret, M.; Riboulot, V.; Deloffre, J.; Boissier, A.; Cheron, S.; Pitel, M.; Bayon, G.; Giosan, L. Linking Danube River Activity to Alpine Ice-Sheet Fluctuations during the Last Glacial (ca. 33–17 Ka BP): Insights into the

- Continental Signature of Heinrich Stadials. *Quaternary Science Reviews* **2020**, 229, 106136.
- (121) Ballas, G.; Garziglia, S.; Sultan, N.; Pelleter, E.; Toucanne, S.; Marsset, T.; Riboulot, V.; Ker, S. Influence of Early Diagenesis on Geotechnical Properties of Clay Sediments (Romania, Black Sea). *Engineering Geology* **2018**, 240, 175–188. <https://doi.org/10.1016/j.enggeo.2018.04.019>.
- (122) Popescu, I.; Lericolais, G.; Panin, N.; De Batist, M.; Gillet, H. Seismic Expression of Gas and Gas Hydrates across the Western Black Sea. *Geo-Marine Letters* **2007**, 27 (2), 173–183.
- (123) Popescu, I.; De Batist, M.; Lericolais, G.; Nouzé, H.; Poort, J.; Panin, N.; Versteeg, W.; Gillet, H. Multiple Bottom-Simulating Reflections in the Black Sea: Potential Proxies of Past Climate Conditions. *Marine Geology* **2006**, 227 (3–4), 163–176.
- (124) Zander, T.; Haeckel, M.; Berndt, C.; Chi, W.-C.; Klauke, I.; Bialas, J.; Klaeschen, D.; Koch, S.; Atgün, O. On the Origin of Multiple BSRs in the Danube Deep-Sea Fan, Black Sea. *Earth and Planetary Science Letters* **2017**, 462, 15–25.
- (125) Chazallon, B.; Rodriguez, C.; Ruffine, L.; Carpentier, Y.; Donval, J.-P.; Ker, S.; Riboulot, V. Characterizing the Variability of Natural Gas Hydrate Composition from a Selected Site of the Western Black Sea, off Romania. *Marine and Petroleum Geology* **2021**, 124, 104785.
- (126) Stéphan, K.; RIBOULOT Vincent. GHASS Cruise, Pourquoi Pas? R/V. **2015**. <https://doi.org/10.17600/15000500>.
- (127) Bohrmann, G.; Ivanov, M.; Foucher, J.-P.; Spiess, V.; Bialas, J.; Greinert, J.; Weinrebe, W.; Abegg, F.; Aloisi, G.; Artemov, Y. Mud Volcanoes and Gas Hydrates in the Black Sea: New Data from Dvurechenskii and Odessa Mud Volcanoes. *Geo-Marine Letters* **2003**, 23 (3), 239–249.
- (128) Soulet, G.; Ménot, G.; Lericolais, G.; Bard, E. A Revised Calendar Age for the Last Reconnection of the Black Sea to the Global Ocean. *Quaternary Science Reviews* **2011**, 30 (9–10), 1019–1026.
- (129) Le Pichon, X.; Şengör, A. M. C.; Demirbağ, E.; Rangin, C.; Imren, C.; Armijo, R.; Görür, N.; Çağatay, N.; De Lepinay, B. M.; Meyer, B. The Active Main Marmara Fault. *Earth and Planetary Science Letters* **2001**, 192 (4), 595–616.
- (130) Le Pichon, X.; Chamot-Rooke, N.; Rangin, C.; Sengör, A. M. C. The North Anatolian Fault in the Sea of Marmara. *Journal of Geophysical Research: Solid Earth* **2003**, 108 (B4).

- (131) Henry, P.; Grall, C.; Kende, J.; Viseur, S.; Özeren, M. S.; Şengör, A. M. C.; Dupré, S.; Scalabrin, C.; Geli, L. A Statistical Approach to Relationships between Fluid Emissions and Faults: The Sea of Marmara Case. *Deep Sea Research Part II: Topical Studies in Oceanography* **2018**, *153*, 131–143.
- (132) Ruffine, L.; Çağatay, M. N.; Géli, L. *Fluids and Processes at the Seismically Active Fault Zone in the Sea of Marmara*; Elsevier, 2018; Vol. 153, pp 1–3.
- (133) Gasperini, L.; Polonia, A.; Del Bianco, F.; Etiope, G.; Marinaro, G.; Favali, P.; Italiano, F.; Çağatay, M. N. Gas Seepage and Seismogenic Structures along the North Anatolian Fault in the Eastern Sea of Marmara. *Geochemistry, Geophysics, Geosystems* **2012**, *13* (10).
- (134) Dupré, S.; Scalabrin, C.; Grall, C.; Augustin, J.; Henry, P.; Şengör, A. C.; Görür, N.; Çağatay, M. N.; Géli, L. Tectonic and Sedimentary Controls on Widespread Gas Emissions in the Sea of Marmara: Results from Systematic, Shipborne Multibeam Echo Sounder Water Column Imaging. *Journal of Geophysical Research: Solid Earth* **2015**, *120* (5), 2891–2912.
- (135) Geli, L.; Henry, P.; Zitter, T.; Dupré, S.; Tryon, M.; Çağatay, M. N.; de Lépinay, B. M.; Le Pichon, X.; Şengör, A. M. C.; Görür, N. Gas Emissions and Active Tectonics within the Submerged Section of the North Anatolian Fault Zone in the Sea of Marmara. *Earth and Planetary Science Letters* **2008**, *274* (1–2), 34–39.
- (136) Ruffine, L.; Ondreas, H.; Blanc-Valleron, M.-M.; Teichert, B. M.; Scalabrin, C.; Rinnert, E.; Birot, D.; Croguennec, C.; Ponzevera, E.; Pierre, C. Multidisciplinary Investigation on Cold Seeps with Vigorous Gas Emissions in the Sea of Marmara (MarsiteCruise): Strategy for Site Detection and Sampling and First Scientific Outcome. *Deep Sea Research Part II: Topical Studies in Oceanography* **2018**, *153*, 36–47.
- (137) HENRY Pierre; SENGOR Celal; CAGATAY Namik. MARNAUT Cruise, L'Atalante R/V. **2007**. <https://doi.org/10.17600/7010070>.
- (138) Libes, S. *Introduction to Marine Biogeochemistry*; Academic Press, 2011.
- (139) Udden, J. A. Mechanical Composition of Clastic Sediments. *Bulletin of the geological society of America* **1914**, *25* (1), 655–744.
- (140) Wentworth, C. K. A Scale of Grade and Class Terms for Clastic Sediments. *The journal of geology* **1922**, *30* (5), 377–392.
- (141) Gallagher, S. J.; Fulthorpe, C. S.; Bogus, K.; Auer, G.; Baranwal, S.; Castañeda, I. S.; Christensen, B. A.; De Vleeschouwer, D.; Franco, D. R.; Groeneveld, J. Expedition 356 Methods. **2017**.

- (142) Perkins, D. Mineralogy. *Open Educational Resources* **2020**.
<https://doi.org/10.31356/oers025>.
- (143) Heeschen, K. U.; Schicks, J. M.; Oeltzschner, G. The Promoting Effect of Natural Sand on Methane Hydrate Formation: Grain Sizes and Mineral Composition. *Fuel* **2016**, *181*, 139–147.
- (144) Aboudi Mana, S. C.; Hanafiah, M. M.; Chowdhury, A. J. K. Environmental Characteristics of Clay and Clay-Based Minerals. *Geology, Ecology, and Landscapes* **2017**, *1* (3), 155–161. <https://doi.org/10.1080/24749508.2017.1361128>.
- (145) Fomina, M.; Skorochod, I. Microbial Interaction with Clay Minerals and Its Environmental and Biotechnological Implications. *Minerals* **2020**, *10* (10), 861. <https://doi.org/10.3390/min10100861>.
- (146) Baldock, J. A.; Skjemstad, J. O. Role of the Soil Matrix and Minerals in Protecting Natural Organic Materials against Biological Attack. *Organic geochemistry* **2000**, *31* (7–8), 697–710.
- (147) Isson, T. T.; Planavsky, N. J. Reverse Weathering as a Long-Term Stabilizer of Marine PH and Planetary Climate. *Nature* **2018**, *560* (7719), 471–475.
- (148) Hendricks, S. B.; Alexander, L. T. Minerals Present in Soil Colloids: I. Descriptions and Methods for Identification. *Soil Science* **1939**, *48* (3), 257–272.
- (149) Hendricks, S. B. Concerning the Crystal Structure of Kaolinite, $\text{Al}_2\text{O}_3 \cdot 2\text{SiO}_2 \cdot 2\text{H}_2\text{O}$, and the Composition of Anauxite. *Zeitschrift für Kristallographie-Crystalline Materials* **1936**, *95* (1–6), 247–252.
- (150) Osacky, M.; Geramian, M.; Ivey, D. G.; Liu, Q.; Etsell, T. H. Influence of Nonswelling Clay Minerals (Illite, Kaolinite, and Chlorite) on Nonaqueous Solvent Extraction of Bitumen. *Energy & Fuels* **2015**, *29* (7), 4150–4159.
- (151) Bailey, S. X-Ray Diffraction Identification of the Polytypes of Mica, Serpentine, and Chlorite. *Clays and Clay minerals* **1988**, *36* (3), 193–213.
- (152) Middleton, V. *Encyclopedia of Sediments and Sedimentary Rocks*; Springer Netherlands, 2005.
- (153) Chazallon, B.; Rodriguez, C. T.; Ruffine, L.; Carpentier, Y.; Donval, J.-P.; Ker, S.; Riboulot, V. Characterizing the Variability of Natural Gas Hydrate Composition from a Selected Site of the Western Black Sea, off Romania. *Marine and Petroleum Geology* **2021**, *124*, 104785.
- (154) Ruffine, L.; Deusner, C.; Haeckel, M.; Kossel, E.; Toucanne, S.; Chéron, S.; Boissier, A.; Schmidt, M.; Donval, J.-P.; Scholz, F.; Guyader, V.; Ker, S.; Riboulot, V. Effects of

- Postglacial Seawater Intrusion on Sediment Geochemical Characteristics in the Romanian Sector of the Black Sea. *Marine and Petroleum Geology* **2021**, *123*, 104746. <https://doi.org/10.1016/j.marpetgeo.2020.104746>.
- (155) Max, M. D. *Natural Gas Hydrate in Oceanic and Permafrost Environments*; Springer Science & Business Media, 2003; Vol. 5.
- (156) Uchida, T.; Takeya, S.; Chuvilin, E. M.; Ohmura, R.; Nagao, J.; Yakushev, V. S.; Istomin, V. A.; Minagawa, H.; Ebinuma, T.; Narita, H. Decomposition of Methane Hydrates in Sand, Sandstone, Clays, and Glass Beads. *Journal of Geophysical Research: Solid Earth* **2004**, *109* (B5). <https://doi.org/10.1029/2003JB002771>.
- (157) Liang, S.; Rozmanov, D.; Kusalik, P. G. Crystal Growth Simulations of Methane Hydrates in the Presence of Silica Surfaces. *Physical Chemistry Chemical Physics* **2011**, *13* (44), 19856–19864.
- (158) Liu, C.; Lu, H.; Ye, Y.; Ripmeester, J. A.; Zhang, X. Raman Spectroscopic Observations on the Structural Characteristics and Dissociation Behavior of Methane Hydrate Synthesized in Silica Sands with Various Sizes. *Energy Fuels* **2008**, *22* (6), 3986–3988. <https://doi.org/10.1021/ef800440s>.
- (159) Zhou, Y.; Castaldi, M. J.; Yegulalp, T. M. Experimental Investigation of Methane Gas Production from Methane Hydrate. *Industrial & Engineering Chemistry Research* **2009**, *48* (6), 3142–3149.
- (160) Linga, P.; Haligva, C.; Nam, S. C.; Ripmeester, J. A.; Englezos, P. Gas Hydrate Formation in a Variable Volume Bed of Silica Sand Particles. *Energy & Fuels* **2009**, *23* (11), 5496–5507.
- (161) Bagherzadeh, S. A.; Moudrakovski, I. L.; Ripmeester, J. A.; Englezos, P. Magnetic Resonance Imaging of Gas Hydrate Formation in a Bed of Silica Sand Particles. *Energy Fuels* **2011**, *25* (7), 3083–3092. <https://doi.org/10.1021/ef200399a>.
- (162) Casco, M. E.; Silvestre-Albero, J.; Ramírez-Cuesta, A. J.; Rey, F.; Jordá, J. L.; Bansode, A.; Urakawa, A.; Peral, I.; Martínez-Escandell, M.; Kaneko, K.; Rodríguez-Reinoso, F. Methane Hydrate Formation in Confined Nanospace Can Surpass Nature. *Nat Commun* **2015**, *6* (1), 6432. <https://doi.org/10.1038/ncomms7432>.
- (163) Cuadrado-Collados, C.; Mouchaham, G.; Daemen, L.; Cheng, Y.; Ramirez-Cuesta, A.; Aggarwal, H.; Missyul, A.; Eddaoudi, M.; Belmabkhout, Y.; Silvestre-Albero, J. Quest for an Optimal Methane Hydrate Formation in the Pores of Hydrolytically Stable Metal–Organic Frameworks. *Journal of the American Chemical Society* **2020**, *142* (31), 13391–13397.

- (164) Ruffine, L. Exploring Methane-Hydrate Formation and Dissociation in Geologic Materials through Laboratory Experiments: Kinetic Behavior and Morphology. *Fuel* **2015**, *141*, 173–184.
- (165) Benmesbah, F. D.; Ruffine, L.; Clain, P.; Osswald, V.; Fandino, O.; Fournaison, L.; Delahaye, A. Methane Hydrate Formation and Dissociation in Sand Media: Effect of Water Saturation, Gas Flowrate and Particle Size. *Energies* **2020**, *13* (19), 5200.
- (166) Le, T. X.; Tang, A. M.; Aïmediou, P.; Bornert, M.; Chabot, B.; Rodts, S. Methane Hydrate-Bearing Sand-An Energy Resource? In *Vietnam Symposium on Advances in Offshore Engineering*; Springer, 2018; pp 158–163.
- (167) Le, T. X.; Rodts, S.; Hautemayou, D.; Aïmediou, P.; Bornert, M.; Chabot, B.; Tang, A. M. Kinetics of Methane Hydrate Formation and Dissociation in Sand Sediment. *Geomechanics for Energy and the Environment* **2020**, *23*, 100103. <https://doi.org/10.1016/j.gete.2018.09.007>.
- (168) Liu, X.; Liu, D.; Xie, W.; Cui, X.; Chen, Y. Methane Hydrate Uptake of MCM-41 Mesoporous Molecular Sieves with Preadsorbed Water. *J. Chem. Eng. Data* **2018**, *63* (5), 1767–1772. <https://doi.org/10.1021/acs.jced.8b00060>.
- (169) Govindaraj, V.; Mech, D.; Pandey, G.; Nagarajan, R.; Sangwai, J. S. Kinetics of Methane Hydrate Formation in the Presence of Activated Carbon and Nano-Silica Suspensions in Pure Water. *Journal of Natural Gas Science and Engineering* **2015**, *26*, 810–818.
- (170) Siangsai, A.; Rangsunvigit, P.; Kitiyanan, B.; Kulprathipanja, S.; Linga, P. Investigation on the Roles of Activated Carbon Particle Sizes on Methane Hydrate Formation and Dissociation. *Chemical Engineering Science* **2015**, *126*, 383–389.
- (171) Casco, M. E.; Rey, F.; Jordá, J. L.; Rudić, S.; Fauth, F.; Martínez-Escandell, M.; Rodríguez-Reinoso, F.; Ramos-Fernández, E. V.; Silvestre-Albero, J. Paving the Way for Methane Hydrate Formation on Metal–Organic Frameworks (MOFs). *Chemical science* **2016**, *7* (6), 3658–3666.
- (172) Borchardt, L.; Nickel, W.; Casco, M.; Senkowska, I.; Bon, V.; Wallacher, D.; Grimm, N.; Krause, S.; Silvestre-Albero, J. Illuminating Solid Gas Storage in Confined Spaces – Methane Hydrate Formation in Porous Model Carbons. *Physical Chemistry Chemical Physics* **2016**, *18* (30), 20607–20614. <https://doi.org/10.1039/C6CP03993F>.
- (173) Dai, S.; Santamarina, J. C.; Waite, W. F.; Kneafsey, T. J. Hydrate Morphology: Physical Properties of Sands with Patchy Hydrate Saturation. *Journal of Geophysical Research: Solid Earth* **2012**, *117* (B11).

- (174) Dvorkin, J.; Helgerud, M. B.; Waite, W. F.; Kirby, S. H.; Nur, A. Introduction to Physical Properties and Elasticity Models. In *Natural Gas Hydrate*; Springer, 2000; pp 245–260.
- (175) Yun, T. S.; Santamarina, J. C.; Ruppel, C. Mechanical Properties of Sand, Silt, and Clay Containing Tetrahydrofuran Hydrate. *Journal of geophysical research: solid earth* **2007**, *112* (B4).
- (176) Priest, J. A.; Rees, E. V.; Clayton, C. R. Influence of Gas Hydrate Morphology on the Seismic Velocities of Sands. *Journal of geophysical research: solid earth* **2009**, *114* (B11).
- (177) Sultaniya, A.; Priest, J.; Clayton, C. Measurements of the Changing Wave Velocities of Sand during the Formation and Dissociation of Disseminated Methane Hydrate. *Journal of Geophysical Research: Solid Earth* **2015**, *120* (2), 778–789.
- (178) Mahabadi, N.; Dai, S.; Seol, Y.; Jang, J. Impact of Hydrate Saturation on Water Permeability in Hydrate-Bearing Sediments. *Journal of Petroleum Science and Engineering* **2019**, *174*, 696–703.
- (179) Lv, J.; Zhao, J.; Jiang, L.; Liu, Y.; Mu, H. A Review of Micro Computed Tomography Studies on the Gas Hydrate Pore Habits and Seepage Properties in Hydrate Bearing Sediments. *Journal of Natural Gas Science and Engineering* **2020**, *83*, 103555. <https://doi.org/10.1016/j.jngse.2020.103555>.
- (180) Tréhu, A. M.; Long, P. E.; Torres, M. E.; Bohrmann, G.; Rack, F. R.; Collett, T. S.; Goldberg, D. S.; Milkov, A. V.; Riedel, M.; Schultheiss, P.; Bangs, N. L.; Barr, S. R.; Borowski, W. S.; Claypool, G. E.; Delwiche, M. E.; Dickens, G. R.; Gracia, E.; Guerin, G.; Holland, M.; Johnson, J. E.; Lee, Y.-J.; Liu, C.-S.; Su, X.; Teichert, B.; Tomaru, H.; Vanneste, M.; Watanabe, M.; Weinberger, J. L. Three-Dimensional Distribution of Gas Hydrate beneath Southern Hydrate Ridge: Constraints from ODP Leg 204. *Earth and Planetary Science Letters* **2004**, *222* (3), 845–862. <https://doi.org/10.1016/j.epsl.2004.03.035>.
- (181) Jung, J. W.; Jang, J.; Santamarina, J. C.; Tsouris, C.; Phelps, T. J.; Rawn, C. J. Gas Production from Hydrate-Bearing Sediments: The Role of Fine Particles. *Energy Fuels* **2012**, *26* (1), 480–487. <https://doi.org/10.1021/ef101651b>.
- (182) Zang, X.; Liang, D.; Wu, N. Research Progress on Methane Hydrate Formation Kinetics in Porous Media. *Advance in New and Renewable Energy,(2)* **2015**, 53–60.
- (183) Seshadri, K.; Wilder, J. W.; Smith, D. H. Measurements of Equilibrium Pressures and Temperatures for Propane Hydrate in Silica Gels with Different Pore-Size Distributions. *The Journal of Physical Chemistry B* **2001**, *105* (13), 2627–2631.

- (184) Kang, S.-P.; Lee, J.-W.; Ryu, H.-J. Phase Behavior of Methane and Carbon Dioxide Hydrates in Meso-and Macro-Sized Porous Media. *Fluid Phase Equilibria* **2008**, *274* (1–2), 68–72.
- (185) Li, M.; Fan, S.; Zhao, J. The Effect of Porous Media on the Formation of Natural Gas Hydrate. *Geophysical Prospecting for Petroleum* **2007**, *46* (1), 13–15.
- (186) Bhawangirkar, D. R.; Nair, V. C.; Prasad, S. K.; Sangwai, J. S. Natural Gas Hydrates in the Krishna-Godavari Basin Sediments under Marine Reservoir Conditions: Thermodynamics and Dissociation Kinetics Using Thermal Stimulation. *Energy Fuels* **2021**, *35* (10), 8685–8698. <https://doi.org/10.1021/acs.energyfuels.1c00162>.
- (187) Sun, S.-C.; Liu, C.-L.; Ye, Y.-G.; Liu, Y.-F. Phase Behavior of Methane Hydrate in Silica Sand. *The Journal of Chemical Thermodynamics* **2014**, *69*, 118–124.
- (188) Handa, Y. P.; Stupin, D. Y. Thermodynamic Properties and Dissociation Characteristics of Methane and Propane Hydrates in 70-Å Radius Silica Gel Pores. *The Journal of Physical Chemistry* **1992**, *96* (21), 8599–8603.
- (189) Yakushev, V. S. Experimental Modeling of Methane Hydrate Formation and Decomposition in Wet Heavy Clays in Arctic Regions. *Geosciences* **2018**, *9* (1), 13.
- (190) Turner, D. J.; Cherry, R. S.; Sloan, E. D. Sensitivity of Methane Hydrate Phase Equilibria to Sediment Pore Size. *Fluid Phase Equilibria* **2005**, *228*, 505–510.
- (191) Dickens, G. R.; Quinby-Hunt, M. S. Methane Hydrate Stability in Seawater. *Geophysical Research Letters* **1994**, *21* (19), 2115–2118. <https://doi.org/10.1029/94GL01858>.
- (192) Englezos, P.; Bishnoi, P. R. Prediction of Gas Hydrate Formation Conditions in Aqueous Electrolyte Solutions. *AIChE Journal* **1988**, *34* (10), 1718–1721. <https://doi.org/10.1002/aic.690341017>.
- (193) De Roo, J. L.; Peters, C. J.; Lichtenthaler, R. N.; Diepen, G. a. M. Occurrence of Methane Hydrate in Saturated and Unsaturated Solutions of Sodium Chloride and Water in Dependence of Temperature and Pressure. *AIChE Journal* **1983**, *29* (4), 651–657. <https://doi.org/10.1002/aic.690290420>.
- (194) Dholabhai, P. D.; Englezos, P.; Kalogerakis, N.; Bishnoi, P. R. Equilibrium Conditions for Methane Hydrate Formation in Aqueous Mixed Electrolyte Solutions. *The Canadian Journal of Chemical Engineering* **1991**, *69* (3), 800–805. <https://doi.org/10.1002/cjce.5450690324>.
- (195) Saw, V. K.; Ahmad, I.; Mandal, A.; Udayabhanu, G.; Laik, S. Methane Hydrate Formation and Dissociation in Synthetic Seawater. *Journal of natural gas chemistry* **2012**, *21* (6), 625–632.

- (196) Du, J.; Wang, X.; Liu, H.; Guo, P.; Wang, Z.; Fan, S. Experiments and Prediction of Phase Equilibrium Conditions for Methane Hydrate Formation in the NaCl, CaCl₂, MgCl₂ Electrolyte Solutions. *Fluid Phase Equilibria* **2019**, *479*, 1–8. <https://doi.org/10.1016/j.fluid.2018.09.028>.
- (197) Maiti, M.; Bhaumik, A. K.; Mandal, A. Geological Characterization of Natural Gas Hydrate Bearing Sediments and Their Influence on Hydrate Formation and Dissociation. *Journal of Natural Gas Science and Engineering* **2022**, *100*, 104491. <https://doi.org/10.1016/j.jngse.2022.104491>.
- (198) Tao, Y.; Yan, K.; Li, X.; Chen, Z.; Yu, Y.; Xu, C. Effects of Salinity on Formation Behavior of Methane Hydrate in Montmorillonite. *Energies* **2020**, *13* (1), 231.
- (199) Adeyemo, A.; Kumar, R.; Linga, P.; Ripmeester, J.; Englezos, P. Capture of Carbon Dioxide from Flue or Fuel Gas Mixtures by Clathrate Crystallization in a Silica Gel Column. *International Journal of Greenhouse Gas Control* **2010**, *4* (3), 478–485.
- (200) Linga, P.; Clarke, M. A Review of Reactor Designs and Materials Employed for Increasing the Rate of Gas Hydrate Formation. *Energy & Fuels* **2017**, *31* (1), 1–13.
- (201) Bhattacharjee, G.; Kumar, A.; Sakpal, T.; Kumar, R. Carbon Dioxide Sequestration: Influence of Porous Media on Hydrate Formation Kinetics. *ACS Sustainable Chem. Eng.* **2015**, *3* (6), 1205–1214. <https://doi.org/10.1021/acssuschemeng.5b00171>.
- (202) Chari, V. D.; Sharma, D. V.; Prasad, P. S.; Murthy, S. R. Methane Hydrates Formation and Dissociation in Nano Silica Suspension. *Journal of Natural Gas Science and Engineering* **2013**, *11*, 7–11.
- (203) Wang, S.; Yang, M.; Liu, W.; Zhao, J.; Song, Y. Investigation on the Induction Time of Methane Hydrate Formation in Porous Media under Quiescent Conditions. *Journal of Petroleum Science and Engineering* **2016**, *145*, 565–572.
- (204) Chaouachi, M.; Falenty, A.; Sell, K.; Enzmann, F.; Kersten, M.; Haberthür, D.; Kuhs, W. F. Microstructural Evolution of Gas Hydrates in Sedimentary Matrices Observed with Synchrotron X-Ray Computed Tomographic Microscopy. *Geochemistry, Geophysics, Geosystems* **2015**, *16* (6), 1711–1722.
- (205) Zhao, J.; Yang, L.; Liu, Y.; Song, Y. Microstructural Characteristics of Natural Gas Hydrates Hosted in Various Sand Sediments. *Physical Chemistry Chemical Physics* **2015**, *17* (35), 22632–22641.
- (206) Qin, Y.; Pan, Z.; Liu, Z.; Shang, L.; Zhou, L. Influence of the Particle Size of Porous Media on the Formation of Natural Gas Hydrate: A Review. *Energy Fuels* **2021**, *35* (15), 11640–11664. <https://doi.org/10.1021/acs.energyfuels.1c00936>.

- (207) Babu, P.; Kumar, R.; Linga, P. Pre-Combustion Capture of Carbon Dioxide in a Fixed Bed Reactor Using the Clathrate Hydrate Process. *Energy* **2013**, *50*, 364–373.
- (208) Babu, P.; Yee, D.; Linga, P.; Palmer, A.; Khoo, B. C.; Tan, T. S.; Rangsunvigit, P. Morphology of Methane Hydrate Formation in Porous Media. *Energy & Fuels* **2013**, *27* (6), 3364–3372.
- (209) Mekala, P.; Babu, P.; Sangwai, J. S.; Linga, P. Formation and Dissociation Kinetics of Methane Hydrates in Seawater and Silica Sand. *Energy Fuels* **2014**, *28* (4), 2708–2716. <https://doi.org/10.1021/ef402445k>.
- (210) Nambiar, A.; Babu, P.; Linga, P. CO₂ Capture Using the Clathrate Hydrate Process Employing Cellulose Foam as a Porous Media. *Canadian Journal of Chemistry* **2015**, *93*, 808–814. <https://doi.org/10.1139/cjc-2014-0547>.
- (211) Kumar, A.; Sakpal, T.; Roy, S.; Kumar, R. Methane Hydrate Formation in a Test Sediment of Sand and Clay at Various Levels of Water Saturation. *Canadian journal of chemistry* **2015**, *93* (8), 874–881.
- (212) Ge, B.-B.; Zhong, D.-L.; Lu, Y.-Y. Influence of Water Saturation and Particle Size on Methane Hydrate Formation and Dissociation in a Fixed Bed of Silica Sand. *Energy Procedia* **2019**, *158*, 5402–5407.
- (213) Prasad, P. S.; Chari, V. D.; Sharma, D. V.; Murthy, S. R. Effect of Silica Particles on the Stability of Methane Hydrates. *Fluid Phase Equilibria* **2012**, *318*, 110–114.
- (214) Yan, K.-F.; Li, X.-S.; Chen, Z.-Y.; Xia, Z.-M.; Xu, C.-G.; Zhang, Z. Molecular Dynamics Simulation of the Crystal Nucleation and Growth Behavior of Methane Hydrate in the Presence of the Surface and Nanopores of Porous Sediment. *Langmuir* **2016**, *32* (31), 7975–7984. <https://doi.org/10.1021/acs.langmuir.6b01601>.
- (215) Wu, G.; Ji, H.; Tian, L.; Chen, D. Effects of Salt Ions on the Methane Hydrate Formation and Dissociation in the Clay Pore Water and Bulk Water. *Energy & Fuels* **2018**, *32* (12), 12486–12494.
- (216) Li, Y.; Chen, M.; Song, H.; Yuan, P.; Liu, D.; Zhang, B.; Bu, H. Methane Hydrate Formation in the Stacking of Kaolinite Particles with Different Surface Contacts as Nanoreactors: A Molecular Dynamics Simulation Study. *Applied Clay Science* **2020**, *186*, 105439. <https://doi.org/10.1016/j.clay.2020.105439>.
- (217) Fang, B.; Lü, T.; Ning, F.; Pang, J.; He, Z.; Sun, J. Facilitating Gas Hydrate Dissociation Kinetics and Gas Migration in Clay Interlayer by Surface Cations Shielding Effects. *Fuel* **2022**, *318*, 123576. <https://doi.org/10.1016/j.fuel.2022.123576>.

- (218) Chong, Z. R.; Chan, A. H. M.; Babu, P.; Yang, M.; Linga, P. Effect of NaCl on Methane Hydrate Formation and Dissociation in Porous Media. *Journal of Natural Gas Science and Engineering* **2015**, *27*, 178–189. <https://doi.org/10.1016/j.jngse.2015.08.055>.
- (219) Chong, Z. R.; Koh, J. W.; Linga, P. Effect of KCl and MgCl₂ on the Kinetics of Methane Hydrate Formation and Dissociation in Sandy Sediments. *Energy* **2017**, *137*, 518–529. <https://doi.org/10.1016/j.energy.2017.01.154>.
- (220) Zeng, H.; Zhang, Y.; Zhang, L.; Chen, Z.; Li, X. Effects of the NaCl Concentration and Montmorillonite Content on Formation Kinetics of Methane Hydrate. *Journal of Marine Science and Engineering* **2022**, *10* (4), 548.
- (221) Lu, Z.; Zhu, Y.; Zhang, Y.; Wen, H.; Li, Y.; Liu, C. Gas Hydrate Occurrences in the Qilian Mountain Permafrost, Qinghai Province, China. *Cold Regions Science and Technology* **2011**, *66* (2), 93–104. <https://doi.org/10.1016/j.coldregions.2011.01.008>.
- (222) Lu, H.; Lorenson, T. D.; Moudrakovski, I. L.; Ripmeester, J. A.; Collett, T. S.; Hunter, R. B.; Ratcliffe, C. I. The Characteristics of Gas Hydrates Recovered from the Mount Elbert Gas Hydrate Stratigraphic Test Well, Alaska North Slope. *Marine and Petroleum Geology* **2011**, *28* (2), 411–418. <https://doi.org/10.1016/j.marpetgeo.2010.01.002>.
- (223) Ripmeester, J.; Lu, H.; Moudrakovski, I.; Dutrisac, R.; Wilson, L.; Wright, F.; Dallimore, S. Structure and Composition of Hydrate in Sediment Recovered from Mallik 5L-38, Mackenzie Delta, NWT, Canada: X-Ray Diffraction, Raman and Solid-State NMR Spectroscopy. *Bull. Geol. Surv. Can.* **2005**, 585.
- (224) Tung, Y.-T.; Chen, L.-J.; Chen, Y.-P.; Lin, S.-T. Molecular Dynamics Study on the Growth of Structure I Methane Hydrate in Aqueous Solution of Sodium Chloride. *J. Phys. Chem. B* **2012**, *116* (48), 14115–14125. <https://doi.org/10.1021/jp308224v>.
- (225) Palodkar, A. V.; Jana, A. K. Fundamental of Swapping Phenomena in Naturally Occurring Gas Hydrates. *Sci Rep* **2018**, *8* (1), 16563. <https://doi.org/10.1038/s41598-018-34926-2>.
- (226) Palodkar, A. V.; Jana, A. K. Growth and Decomposition Mechanism of Clathrate Hydrates in the Presence of Porous Media and Seawater: Experimental Validation. *Energy Fuels* **2019**, *33* (2), 1433–1443. <https://doi.org/10.1021/acs.energyfuels.8b03245>.
- (227) Archer, D. Methane Hydrate Stability and Anthropogenic Climate Change. *Biogeosciences* **2007**, *4* (4), 521–544. <https://doi.org/10.5194/bg-4-521-2007>.

- (228) Berrod, Q.; Lagrené, K.; Ollivier, J.; Zanotti, J.-M. Inelastic and Quasi-Elastic Neutron Scattering. Application to Soft-Matter. *EPJ Web of Conferences* **2018**, *188*, 05001. <https://doi.org/10.1051/epjconf/201818805001>.
- (229) Jiménez-Ruiz, M.; Ferrage, E.; Delville, A.; Michot, L. J. Anisotropy on the Collective Dynamics of Water Confined in Swelling Clay Minerals. *The Journal of Physical Chemistry A* **2012**, *116* (10), 2379–2387.
- (230) Rietveld, H. M. A Profile Refinement Method for Nuclear and Magnetic Structures. *Journal of Applied Crystallography* **1969**, *2* (2), 65–71. <https://doi.org/10.1107/S0021889869006558>.
- (231) Le Bail, A.; Duroy, H.; Fourquet, J. Ab-Initio Structure Determination of LiSbWO₆ by X-Ray Powder Diffraction. *Materials Research Bulletin* **1988**, *23* (3), 447–452.
- (232) Rodriguez-Carvajal, J. FULLPROF: A Program for Rietveld Refinement and Pattern Matching Analysis; Toulouse, France:[sn], 1990; Vol. 127.
- (233) Qin, J.; Kuhs, W. F. Quantitative Analysis of Gas Hydrates Using Raman Spectroscopy. *AIChE Journal* **2013**, *59* (6), 2155–2167.
- (234) Jiménez-Ruiz, M.; Ferrage, E.; Blanchard, M.; Fernandez-Castanon, J.; Delville, A.; Johnson, M. R.; Michot, L. J. Combination of Inelastic Neutron Scattering Experiments and Ab Initio Quantum Calculations for the Study of the Hydration Properties of Oriented Saponites. *The Journal of Physical Chemistry C* **2017**, *121* (9), 5029–5040.
- (235) Cha, S. B.; Ouar, H.; Wildeman, T. R.; Sloan, E. D. A Third-Surface Effect on Hydrate Formation. *The Journal of Physical Chemistry* **1988**, *92* (23), 6492–6494.
- (236) Meyer, D. W.; Flemings, P. B.; DiCarlo, D.; You, K.; Phillips, S. C.; Kneafsey, T. J. Experimental Investigation of Gas Flow and Hydrate Formation Within the Hydrate Stability Zone. *Journal of Geophysical Research: Solid Earth* **2018**, *123* (7), 5350–5371. <https://doi.org/10.1029/2018JB015748>.
- (237) Jeffrey, G.; McMullan, R. The Clathrate Hydrates. *John Wiley: New York* **1967**, *8*, 43–108.
- (238) Davidson, D.; Garg, S.; Gough, S.; Handa, Y.; Ratcliffe, C.; Tse, J.; Ripmeester, J. Some Structural and Thermodynamic Studies of Clathrate Hydrates. In *Clathrate Compounds, Molecular Inclusion Phenomena, and Cyclodextrins*; Springer, 1984; pp 231–238.
- (239) Schicks, J. M.; Pan, M.; Giese, R.; Poser, M.; Ismail, N. A.; Luzi-Helbing, M.; Bleisteiner, B.; Lenz, C. A New High-Pressure Cell for Systematic in Situ Investigations of Micro-Scale Processes in Gas Hydrates Using Confocal Micro-Raman Spectroscopy.

- Review of Scientific Instruments* **2020**, *91* (11), 115103.
<https://doi.org/10.1063/5.0013138>.
- (240) Uchida, T.; Takeya, S.; Kamata, Y.; Ikeda, I. Y.; Nagao, J.; Ebinuma, T.; Narita, H.; Zatssepina, O.; Buffett, B. A. Spectroscopic Observations and Thermodynamic Calculations on Clathrate Hydrates of Mixed Gas Containing Methane and Ethane: Determination of Structure, Composition and Cage Occupancy. *The Journal of Physical Chemistry B* **2002**, *106* (48), 12426–12431.
- (241) Subramanian, S.; Sloan, E. D. Trends in Vibrational Frequencies of Guests Trapped in Clathrate Hydrate Cages. *The Journal of Physical Chemistry B* **2002**, *106* (17), 4348–4355.
- (242) Kirchner, M. T.; Boese, R.; Billups, W. E.; Norman, L. R. Gas Hydrate Single-Crystal Structure Analyses. *J. Am. Chem. Soc.* **2004**, *126* (30), 9407–9412.
<https://doi.org/10.1021/ja049247c>.
- (243) Subramanian, S.; Kini, R. A.; Dec, S. F.; Sloan, E. D. Evidence of Structure II Hydrate Formation from Methane+ethane Mixtures. *Chemical Engineering Science* **2000**, *55* (11), 1981–1999. [https://doi.org/10.1016/S0009-2509\(99\)00389-9](https://doi.org/10.1016/S0009-2509(99)00389-9).
- (244) Subramanian, S.; Ballard, A. L.; Kini, R. A.; Dec, S. F.; Sloan, E. D. Structural Transitions in Methane+ Ethane Gas Hydrates—Part I: Upper Transition Point and Applications. *Chemical Engineering Science* **2000**, *55* (23), 5763–5771.
- (245) Udachin, K. A.; Ratcliffe, C. I.; Ripmeester, J. A. Single Crystal Diffraction Studies of Structure I, II and H Hydrates: Structure, Cage Occupancy and Composition. *Journal of Supramolecular Chemistry* **2002**, *2* (4), 405–408. [https://doi.org/10.1016/S1472-7862\(03\)00049-2](https://doi.org/10.1016/S1472-7862(03)00049-2).
- (246) Murshed, M. M.; Schmidt, B. C.; Kuhs, W. F. Kinetics of Methane-Ethane Gas Replacement in Clathrate-Hydrates Studied by Time-Resolved Neutron Diffraction and Raman Spectroscopy. *J. Phys. Chem. A* **2010**, *114* (1), 247–255.
<https://doi.org/10.1021/jp908016j>.
- (247) de Menezes, D. É. S.; Sum, A. K.; Desmedt, A.; de Alcântara Pessôa Filho, P.; Fuentes, M. D. R. Coexistence of SI and SII in Methane-Propane Hydrate Former Systems at High Pressures. *Chemical Engineering Science* **2019**, *208*, 115149.
- (248) Rawn, C. J.; Rondinone, A. J.; Chakoumakos, B. C.; Circone, S.; Stern, L. A.; Kirby, S. H.; Ishii, Y. Neutron Powder Diffraction Studies as a Function of Temperature of Structure II Hydrate Formed from Propane. *Canadian journal of physics* **2003**, *81* (1–2), 431–438.

- (249) Takeya, S.; Fujihisa, H.; Hachikubo, A.; Sakagami, H.; Gotoh, Y. Distribution of Butane in the Host Water Cage of Structure II Clathrate Hydrates. *Chemistry – A European Journal* **2014**, *20* (51), 17207–17213. <https://doi.org/10.1002/chem.201403575>.
- (250) Petrov, D.; Matrosov, I.; Zaripov, A. Raman Spectra of N-Butane, Isobutane, n-Pentane, and Isopentane in a Methane Environment. *Optics and Spectroscopy* **2018**, *125* (1), 5–9.
- (251) Chazallon, B.; Pirim, C. Selectivity and CO₂ Capture Efficiency in CO₂-N₂ Clathrate Hydrates Investigated by in-Situ Raman Spectroscopy. *Chemical Engineering Journal* **2018**, *342*, 171–183. <https://doi.org/10.1016/j.cej.2018.01.116>.
- (252) Pétuya-Poublan, C. Étude de La Stabilité, de l'occupation Des Cages et de La Sélectivité Moléculaire Des Hydrates de Gaz Par Spectroscopie Raman. **2017**.
- (253) Murshed, M. M.; Kuhs, W. F. Kinetic Studies of Methane–Ethane Mixed Gas Hydrates by Neutron Diffraction and Raman Spectroscopy. *J. Phys. Chem. B* **2009**, *113* (15), 5172–5180. <https://doi.org/10.1021/jp810248s>.
- (254) Ohno, H.; Strobel, T. A.; Dec, S. F.; Sloan, J., E. Dendy; Koh, C. A. Raman Studies of Methane–Ethane Hydrate Metastability. *The Journal of Physical Chemistry A* **2009**, *113* (9), 1711–1716.
- (255) Luzi, M.; Schicks, J. M.; Naumann, R.; Erzinger, J.; Udachin, K. A.; Moudrakovski, I. L.; Ripmeester, J. A.; Ludwig, R. Investigations on the Influence of Guest Molecule Characteristics and the Presence of Multicomponent Gas Mixtures on Gas Hydrate Properties. **2008**.
- (256) Kida, M.; Sakagami, H.; Watanabe, M.; Jin, Y.; Takahashi, N.; Nagao, J. Structural Properties of Methane and Butane Mixed-Gas Hydrates. *Chemical Engineering Science* **2016**, *140*, 10–15. <https://doi.org/10.1016/j.ces.2015.08.047>.
- (257) Shimanouchi, T. *Tables of Molecular Vibrational Frequencies*; US Government Printing Office, 1973.
- (258) Magnotti, G.; Kc, U.; Varghese, P. L.; Barlow, R. S. Raman Spectra of Methane, Ethylene, Ethane, Dimethyl Ether, Formaldehyde and Propane for Combustion Applications. *Journal of Quantitative Spectroscopy and Radiative Transfer* **2015**, *163*, 80–101. <https://doi.org/10.1016/j.jqsrt.2015.04.018>.
- (259) Hansen, S. B.; Berg, R. W.; Stenby, E. H. How to Determine the Pressure of a Methane-Containing Gas Mixture by Means of Two Weak Raman Bands, ν (3) and 2ν (2). *Journal of Raman Spectroscopy* **2002**, *33* (3), 160–164.
- (260) Snyder, R. L.; Fiala, J.; Bunge, H. J.; International Union of Crystallography. *Defect and Microstructure Analysis by Diffraction*; Oxford University Press Oxford, 1999; Vol. 200.

- (261) Atamas, N. A.; Yaremko, A. M.; Seeger, T.; Leipertz, A.; Bienko, A.; Latajka, Z.; Ratajczak, H.; Barnes, A. J. A Study of the Raman Spectra of Alkanes in the Fermi-Resonance Region. *Journal of Molecular Structure* **2004**, *708* (1–3), 189–195.
- (262) Evans, J. C.; Bernstein, H. J. The Vibrational Spectra of Isobutane and Isobutane-d 1. *Canadian Journal of Chemistry* **1956**, *34* (8), 1037–1045.
- (263) Brooks, J. M.; Cox, H. B.; Bryant, W. R.; Kennicutt II, M.; Mann, R. G.; McDonald, T. J. Association of Gas Hydrates and Oil Seepage in the Gulf of Mexico. *Organic Geochemistry* **1986**, *10* (1–3), 221–234.
- (264) Holder, G.; Hand, J. Multiple-phase Equilibria in Hydrates from Methane, Ethane, Propane and Water Mixtures. *AIChE Journal* **1982**, *28* (3), 440–447.
- (265) Hendriks, E.; Edmonds, B.; Moorwood, R.; Szczepanski, R. Hydrate Structure Stability in Simple and Mixed Hydrates. *Fluid phase equilibria* **1996**, *117* (1–2), 193–200.
- (266) Murphy, W.; Fernandez-Sanchez, J.; Raghavachari, K. Harmonic Force Field and Raman Scattering Intensity Parameters of N-Butane. *The Journal of Physical Chemistry* **1991**, *95* (3), 1124–1139.
- (267) Davidson, D.; Garg, S.; Gough, S.; Hawkins, R.; Ripmeester, J. Characterization of Natural Gas Hydrates by Nuclear Magnetic Resonance and Dielectric Relaxation. *Canadian journal of chemistry* **1977**, *55* (20), 3641–3650.
- (268) Klauda, J. B.; Sandler, S. I. Predictions of Gas Hydrate Phase Equilibria and Amounts in Natural Sediment Porous Media. *Marine and Petroleum Geology* **2003**, *20* (5), 459–470.
- (269) Khan, M. N.; Warriar, P.; Peters, C. J.; Koh, C. A. Review of Vapor-Liquid Equilibria of Gas Hydrate Formers and Phase Equilibria of Hydrates. *Journal of Natural Gas Science and Engineering* **2016**, *35*, 1388–1404.
- (270) Clarke, M.; Bishnoi, P. R. Determination of the Activation Energy and Intrinsic Rate Constant of Methane Gas Hydrate Decomposition. *The Canadian Journal of Chemical Engineering* **2001**, *79* (1), 143–147. <https://doi.org/10.1002/cjce.5450790122>.
- (271) Kim, H. C.; Bishnoi, P. R.; Heidemann, R. A.; Rizvi, S. S. H. Kinetics of Methane Hydrate Decomposition. *Chemical Engineering Science* **1987**, *42* (7), 1645–1653. [https://doi.org/10.1016/0009-2509\(87\)80169-0](https://doi.org/10.1016/0009-2509(87)80169-0).
- (272) Paull, C. K.; Dillon, W. P. Natural Gas Hydrates: Occurrence, Distribution, and Detection. *Washington DC American Geophysical Union Geophysical Monograph Series* **2001**, *124*.

- (273) Seo, Y.-T.; Moudrakovski, I. L.; Ripmeester, J. A.; Lee, J.; Lee, H. Efficient Recovery of CO₂ from Flue Gas by Clathrate Hydrate Formation in Porous Silica Gels. *Environmental science & technology* **2005**, *39* (7), 2315–2319.
- (274) Malagar, B. R.; Lijith, K. P.; Singh, D. N. Formation & Dissociation of Methane Gas Hydrates in Sediments: A Critical Review. *Journal of Natural Gas Science and Engineering* **2019**, *65*, 168–184.
- (275) Jullien, M.; Raynal, J.; Kohler, E.; Bildstein, O. Physicochemical Reactivity in Clay-Rich Materials: Tools for Safety Assessment. *Oil & gas science and technology* **2005**, *60* (1), 107–120.
- (276) Veluswamy, H. P.; Linga, P. Natural Gas Hydrate Formation Using Saline/Seawater for Gas Storage Application. *Energy Fuels* **2021**, *35* (7), 5988–6002. <https://doi.org/10.1021/acs.energyfuels.1c00399>.
- (277) Bai, D.; Wu, Z.; Lin, C.; Zhou, D. The Effect of Aqueous NaCl Solution on Methane Hydrate Nucleation and Growth. *Fluid Phase Equilibria* **2019**, *487*, 76–82.
- (278) Yang, M.; Fu, Z.; Zhao, Y.; Jiang, L.; Zhao, J.; Song, Y. Effect of Depressurization Pressure on Methane Recovery from Hydrate–Gas–Water Bearing Sediments. *Fuel* **2016**, *166*, 419–426. <https://doi.org/10.1016/j.fuel.2015.10.119>.
- (279) Zhao, J.; Zhu, Z.; Song, Y.; Liu, W.; Zhang, Y.; Wang, D. Analyzing the Process of Gas Production for Natural Gas Hydrate Using Depressurization. *Applied Energy* **2015**, *142*, 125–134. <https://doi.org/10.1016/j.apenergy.2014.12.071>.
- (280) Istomin, V. A.; Yakushev, V. S. Gas Hydrates in Nature. *Nedra, Moscow* **1992**.
- (281) Stern, L. A.; Circone, S.; Kirby, S. H.; Durham, W. B. Anomalous Preservation of Pure Methane Hydrate at 1 Atm. *The Journal of Physical Chemistry B* **2001**, *105* (9), 1756–1762.
- (282) Takeya, S.; Mimachi, H.; Murayama, T. Methane Storage in Water Frameworks: Self-Preservation of Methane Hydrate Pellets Formed from NaCl Solutions. *Applied Energy* **2018**, *230*, 86–93. <https://doi.org/10.1016/j.apenergy.2018.08.015>.
- (283) Kuhs, W.F., Genov, G., Staykova, D.K., Hansen, T. Proceedings of the Fifth International Conference on Gas Hydrates; Tapir forlag: Norway, 2005.
- (284) Prasad, P. S. R.; Kiran, B. S. Self-Preservation and Stability of Methane Hydrates in the Presence of NaCl. *Sci Rep* **2019**, *9* (1), 5860. <https://doi.org/10.1038/s41598-019-42336-1>.
- (285) Sun, R.; Yang, M.; Song, Y. Effect of NaCl Concentration on Depressurization-Induced Methane Hydrate Dissociation near Ice-Freezing Point: Associated with Metastable

- Phases. *Journal of Natural Gas Science and Engineering* **2021**, *96*, 104304. <https://doi.org/10.1016/j.jngse.2021.104304>.
- (286) Gutt, C.; Asmussen, B.; Press, W.; Johnson, M. R.; Handa, Y. P.; Tse, J. S. The Structure of Deuterated Methane–Hydrate. *The Journal of Chemical Physics* **2000**, *113* (11), 4713–4721. <https://doi.org/10.1063/1.1288789>.
- (287) Thangswamy, M.; Maheshwari, P.; Dutta, D.; K. Bera, A.; N. Singh, M.; K. Sinha, A.; M. Yusuf, S.; K. Pujari, P. Evolution of Confined Ice Nano Structures at Different Levels of Pore Filling: A Synchrotron Based X-Ray Diffraction Study. *Physical Chemistry Chemical Physics* **2020**, *22* (25), 14309–14317. <https://doi.org/10.1039/D0CP01988G>.
- (288) Cahn, J. W. Transformation Kinetics during Continuous Cooling. *Acta Metallurgica* **1956**, *4* (6), 572–575. [https://doi.org/10.1016/0001-6160\(56\)90158-4](https://doi.org/10.1016/0001-6160(56)90158-4).
- (289) Scherer, G. W.; Zhang, J.; Thomas, J. J. Nucleation and Growth Models for Hydration of Cement. *Cement and Concrete Research* **2012**, *42* (7), 982–993. <https://doi.org/10.1016/j.cemconres.2012.03.019>.
- (290) Simmons, B.; Bradshaw, R.; Dedrick, D.; Cygan, R.; Greathouse, J.; Majzoub, E. *Desalination Utilizing Clathrate Hydrates (LDRD Final Report)*; SAND2007-6565, 934586; 2008; pp SAND2007-6565, 934586. <https://doi.org/10.2172/934586>.
- (291) Brodskaya, E. N.; Sizov, V. V. Molecular Simulation of Nanoclusters of Gas Hydrates in a Water Shell. The Mechanical State of the System. *Colloid J* **2013**, *75* (4), 366–372. <https://doi.org/10.1134/S1061933X13030046>.
- (292) Kumar Saw, V.; Udayabhanu, G.; Mandal, A.; Laik, S. Methane Hydrate Formation and Dissociation in the Presence of Silica Sand and Bentonite Clay. *Oil Gas Sci. Technol. – Rev. IFP Energies nouvelles* **2015**, *70* (6), 1087–1099. <https://doi.org/10.2516/ogst/2013200>.
- (293) Wenk, H.-R.; Bulakh, A. Minerals. *Minerals* **2004**, 668.
- (294) Norrish, K. The Swelling of Montmorillonite. *Discussions of the Faraday society* **1954**, *18*, 120–134.
- (295) Karaborni, S.; Smit, B.; Heidug, W.; Urai, J.; Van Oort, E. The Swelling of Clays: Molecular Simulations of the Hydration of Montmorillonite. *Science* **1996**, *271* (5252), 1102–1104.
- (296) Morodome, S.; Kawamura, K. In Situ X-Ray Diffraction Study of the Swelling of Montmorillonite as Affected by Exchangeable Cations and Temperature. *Clays and Clay Minerals* **2011**, *59* (2), 165–175.

- (297) Fandiño, O.; Ruffine, L. Methane Hydrate Nucleation and Growth from the Bulk Phase: Further Insights into Their Mechanisms. *Fuel* **2014**, *117*, 442–449.
- (298) Subramanian, S.; Sloan Jr, E. D. Molecular Measurements of Methane Hydrate Formation. *Fluid Phase Equilibria* **1999**, *158*, 813–820.
- (299) Desmedt, A.; Bedouret, L.; Pefoute, E.; Pouvreau, M.; Say-Liang-Fat, S.; Alvarez, M. Energy Landscape of Clathrate Hydrates. *The European Physical Journal Special Topics* **2012**, *213* (1), 103–127.
- (300) Desmedt, A.; Bedouret, L.; Ollivier, J.; Petuya, C. Neutron Scattering of Clathrate and Semiclathrate Hydrates. In *Gas Hydrates 1*; John Wiley & Sons, Ltd, 2017; pp 1–61. <https://doi.org/10.1002/9781119332688.ch1>.
- (301) Tse, J. S.; Ratcliffe, C. I.; Powell, B. M.; Sears, V. F.; Handa, Y. P. Rotational and Translational Motions of Trapped Methane. Incoherent Inelastic Neutron Scattering of Methane Hydrate. *J. Phys. Chem. A* **1997**, *101* (25), 4491–4495. <https://doi.org/10.1021/jp963006c>.
- (302) Prager, M.; Press, W. Methane Clathrate: CH₄ Quantum Rotor State Dependent Rattling Potential. *The Journal of chemical physics* **2006**, *125* (21), 214703.
- (303) Schober, H.; Itoh, H.; Klapproth, A.; Chihaiia, V.; Kuhs, W. F. Guest-Host Coupling and Anharmonicity in Clathrate Hydrates. *Eur. Phys. J. E* **2003**, *12* (1), 41–49. <https://doi.org/10.1140/epje/i2003-10026-6>.
- (304) Tse, J. S.; Shpakov, V. P.; Belosludov, V. R.; Trouw, F.; Handa, Y. P.; Press, W. Coupling of Localized Guest Vibrations with the Lattice Modes in Clathrate Hydrates. *EPL (Europhysics Letters)* **2001**, *54* (3), 354.
- (305) Baumert, J.; Gutt, C.; Shpakov, V. P.; Tse, J. S.; Krisch, M.; Müller, M.; Requardt, H.; Klug, D. D.; Janssen, S.; Press, W. Lattice Dynamics of Methane and Xenon Hydrate: Observation of Symmetry-Avoided Crossing by Experiment and Theory. *Physical Review B* **2003**, *68* (17), 174301.
- (306) Baumert, J.; Gutt, C.; Johnson, M. R.; Tse, J. S.; Klug, D. D.; Press, W. The Structure of Methane Hydrate under Geological Conditions a Combined Rietveld and Maximum Entropy Analysis. *The Journal of chemical physics* **2004**, *120* (21), 10163–10171.
- (307) Celli, M.; Colognesi, D.; Ulivi, L.; Zoppi, M.; Ramirez-Cuesta, A. J. Phonon Density of States in Different Clathrate Hydrates Measured by Inelastic Neutron Scattering. In *Journal of Physics: Conference Series*; IOP Publishing, 2012; Vol. 340, p 012051.

- (308) Gutt, C.; Asmussen, B.; Press, W.; Merkl, C.; Casalta, H.; Greinert, J.; Bohrmann, G.; Tse, J. S.; Hüller, A. Quantum Rotations in Natural Methane-Clathrates from the Pacific Sea-Floor. *EPL (Europhysics Letters)* **1999**, *48* (3), 269.
- (309) Zhou, L.; Liu, J.; Su, W.; Sun, Y.; Zhou, Y. Progress in Studies of Natural Gas Storage with Wet Adsorbents. *Energy & fuels* **2010**, *24* (7), 3789–3795.
- (310) Uchida, T.; Ebinuma, T.; Takeya, S.; Nagao, J.; Narita, H. Effects of Pore Sizes on Dissociation Temperatures and Pressures of Methane, Carbon Dioxide, and Propane Hydrates in Porous Media. *The journal of physical chemistry B* **2002**, *106* (4), 820–826.
- (311) De Pablo, L.; Chávez, M. L.; Sum, A. K.; De Pablo, J. J. Monte Carlo Molecular Simulation of the Hydration of Na–Montmorillonite at Reservoir Conditions. *The Journal of chemical physics* **2004**, *120* (2), 939–946.
- (312) Bergaya, F.; Lagaly, G. General Introduction: Clays, Clay Minerals, and Clay Science. In *Developments in clay science*; Elsevier, 2013; Vol. 5, pp 1–19.
- (313) Li, J.; Li, X.; Wang, X.; Li, Y.; Wu, K.; Shi, J.; Yang, L.; Feng, D.; Zhang, T.; Yu, P. Water Distribution Characteristic and Effect on Methane Adsorption Capacity in Shale Clay. *International Journal of Coal Geology* **2016**, *159*, 135–154.
- (314) Pons, C.-H.; Tchoubar, C.; Tchoubar, D. Organisation Des Molécules d'eau à La Surface Des Feuilletés Dans Un Gel de Montmorillonite- Na. *Bulletin de Minéralogie* **1980**, *103* (3), 452–456.
- (315) Legodi, M. A.; De Waal, D. Raman Spectroscopic Study of Ancient South African Domestic Clay Pottery. *Spectrochimica Acta Part A: Molecular and Biomolecular Spectroscopy* **2007**, *66* (1), 135–142.
- (316) Kingma, K. J.; Hemley, R. J. Raman Spectroscopic Study of Microcrystalline Silica. *American Mineralogist* **1994**, *79* (3–4), 269–273.
- (317) Horváth, E.; Kristóf, J.; Frost, R. L. Vibrational Spectroscopy of Intercalated Kaolinites. Part I. *Applied Spectroscopy Reviews* **2010**, *45* (2), 130–147. <https://doi.org/10.1080/05704920903435862>.
- (318) Petuya, C.; Choukroun, M.; Vu, T. H.; Desmedt, A.; Davies, A. G.; Sotin, C. Cage Occupancy of Methane Clathrate Hydrates in the Ternary H₂O–NH₃–CH₄ System. *Chemical Communications* **2020**, *56* (82), 12391–12394.
- (319) Choukroun, M.; Morizet, Y.; Grasset, O. Raman Study of Methane Clathrate Hydrates under Pressure: New Evidence for the Metastability of Structure II. *Journal of Raman Spectroscopy: An International Journal for Original Work in all Aspects of Raman*

- Spectroscopy, Including Higher Order Processes, and also Brillouin and Rayleigh Scattering* **2007**, *38* (4), 440–451.
- (320) Yeon, S.-H.; Seol, J.; Seo, Y.; Park, Y.; Koh, D.-Y.; Park, K.-P.; Huh, D.-G.; Lee, J.; Lee, H. Effect of Interlayer Ions on Methane Hydrate Formation in Clay Sediments. *The Journal of Physical Chemistry B* **2009**, *113* (5), 1245–1248.
- (321) Rao, Q.; Xiang, Y.; Leng, Y. Molecular Simulations on the Structure and Dynamics of Water–Methane Fluids between Na-Montmorillonite Clay Surfaces at Elevated Temperature and Pressure. *The Journal of Physical Chemistry C* **2013**, *117* (27), 14061–14069.
- (322) Terzariol, M.; Park, J.; Castro, G. M.; Santamarina, J. C. Methane Hydrate-Bearing Sediments: Pore Habit and Implications. *Marine and Petroleum Geology* **2020**, *116*, 104302. <https://doi.org/10.1016/j.marpetgeo.2020.104302>.
- (323) Le, T.-X.; Bornert, M.; Aïmedieu, P.; Chabot, B.; King, A.; Tang, A.-M. An Experimental Investigation on Methane Hydrate Morphologies and Pore Habits in Sandy Sediment Using Synchrotron X-Ray Computed Tomography. *Marine and Petroleum Geology* **2020**, *122*, 104646.
- (324) Li, J. Inelastic Neutron Scattering Studies of Hydrogen Bonding in Ices. *The Journal of chemical physics* **1996**, *105* (16), 6733–6755.
- (325) Tse, J. S.; Klein, M. L.; McDonald, I. R. Molecular Dynamics Studies of Ice Ic and the Structure I Clathrate Hydrate of Methane. *The Journal of Physical Chemistry* **1983**, *87* (21), 4198–4203.
- (326) Tse, J. S.; Klein, M. L.; McDonald, I. R. Computer Simulation Studies of the Structure I Clathrate Hydrates of Methane, Tetrafluoromethane, Cyclopropane, and Ethylene Oxide. *The Journal of chemical physics* **1984**, *81* (12), 6146–6153.
- (327) Baumert, J. Structure, Lattice Dynamics, and Guest Vibrations of Methane and Xenon Hydrate, 2003.
- (328) Guimpier, C.; Agnissan, A.-C. C.; Nassif, V.; Hansen, T.; Cheron, S.; Boissier, A.; Ruffine, L.; Desmedt, A. Kinetic of Formation of Methane Hydrate in Clays and Natural Sediments from Black Sea: Matrix Effect (to Be Published). **2022**.
- (329) Guimpier, C.; Agnissan, A.-C. C.; Hansen, T.; Ruffine, L.; Desmedt, A. Kinetic of Formation of Methane Hydrate in Montmorillonite: Salinity Effect (to Be Published). **2022**.
- (330) Klapp, S. A.; Enzmann, F.; Walz, P.; Huthwelker, T.; Tuckermann, J.; Schwarz, J.; Pape, T.; Peltzer, E. T.; Mokso, R.; Wangner, D. Microstructure Characteristics during Hydrate

- Formation and Dissociation Revealed by X-Ray Tomographic Microscopy. *Geo-Marine Letters* **2012**, 32 (5), 555–562.
- (331) Yano, T.; Verma, P.; Saito, Y.; Ichimura, T.; Kawata, S. Pressure-Assisted Tip-Enhanced Raman Imaging at a Resolution of a Few Nanometres. *Nature Photonics* **2009**, 3 (8), 473–477.
- (332) Li, C.; Liu, C.; Hu, G.; Sun, J.; Hao, X.; Liu, L.; Meng, Q. Investigation on the Multiparameter of Hydrate-bearing Sands Using Nano-focus X-ray Computed Tomography. *Journal of geophysical research: solid earth* **2019**, 124 (3), 2286–2296.
- (333) Breen, C.; Adams, J. M.; Riekel, C. Review of the Diffusion of Water and Pyridine in the Interlayer Space of Montmorillonite: Relevance to Kinetics of Catalytic Reactions in Clays. *Clays and Clay Minerals* **1985**, 33 (4), 275–284.

